

Future Microwave Arrays Take Shape

Thesis by
Austin C. Fikes

In Partial Fulfillment of the Requirements for the
Degree of
Doctor of Philosophy

The logo for the California Institute of Technology (Caltech), featuring the word "Caltech" in a bold, orange, sans-serif font.

CALIFORNIA INSTITUTE OF TECHNOLOGY
Pasadena, California

2022
Defended 01/28/2022

© 2022

Austin C. Fikes

ORCID: 0000-0003-4889-5782

All rights reserved

ACKNOWLEDGEMENTS

Only a tiny fraction of PhD students have access to the resources and opportunities which have been made available to me during my PhD. In my time at CHIC lab, I have completed five tapeouts in advanced semiconductor processes and am set to launch a payload I designed to space. Tapeouts and space missions involve incredible technological and financial resources. Integrated circuit fabrication requires cutting edge manufacturing technology to create an object the size of a grain of rice with millions or billions of electronic components. For better or worse, these nanometer scale devices shape our relationships, lives, and brains in ways we have only begun to understand. When the fog of deadlines and specifications clears, I can occasionally fully appreciate integrated circuits as a wonder of the world and am awestruck. My flirtation with worlds of wonder did not stop there. My inconsequential satellite payload will be sent beyond the barriers which confined human society for millennia.

At moments, I am baffled why these incredible technologies have been entrusted to me. However, these opportunities are not what I am most grateful for in life. As lucky as I have been technologically, my fortune in the people I have met in life is many fold greater.

The path that lead me to where I am today began in 3rd grade when my mother started a two year homeschooling experiment with my sister and I. When I came back to public school for 5th grade, it was immediately apparent that she had given me an big advantage in math, science, and focus over my peers. The foundation she gave me probably determined more about my life today than any other factor. My mother was only part of a household well suited towards crafting a scientist and engineer. Despite his own PhD, when I think of my father's influence I think of his patience and kindness. I am at my best when I can channel those traits. The final member of the Fikes family is my sister. While it may be a small sample size and reflect personal bias, I strongly believe an older sister to be the best sibling pairing for a young man. Annie helped me develop an emotional maturity, respect for others, and kept my ego down. As we have become adults, I appreciate seeing someone else on the life-long journey of understanding and search for happiness.

My path from childhood to the Caltech High Speed Integrated Circuits (CHIC) Lab was dictated by hundreds of suggestions, nudges, and pushes whose effect was unknowable at the time. In retrospect, Phillip Huszar's every morning math club

at Stanley Middle School and the Science Olympiad team led by Sandra Mann at University City High School certainly had out-sized roles.

By the time I was an undergraduate at Harvey Mudd College, critical influences were much more apparent. Without David Harris' VLSI course and research group as well as Matthew Spencer developing a mixed-signal electronics course I almost certainly would not have been accepted in CHIC lab or succeeded once I was here. Additionally, Lori Bassman was a wellspring of perspective and warmth during a senior year of which I only realized how much of a toll it took on me in retrospect.

When I reflect on my PhD in a broad sense, I consider it successful. I am proud of my scientific contributions and have built connections with many people I respect and believe in the future of. I learned so much it is difficult to remember how little I knew coming in. Despite this success, I do not think I could have succeeded in every RF or integrated circuits lab. I came in with a general engineering degree, deficient in the EE and microwave background knowledge I probably should have had. However, CHIC lab in 2016 was an ideal place for someone with my strengths and weaknesses. CHIC lab and the Space Solar Power Project was choc-ful of veteran mentors who helped set me on a path to success. Florian Bohn, Behrooz Abiri, Amir Safaripour, and Matan Gal-Katziri all dedicated significant time to teaching me the technical fundamentals and professional research behavior. Mohammed Reza Hashemi was a great partner as I learned the ropes on my first projects. Alex Pai, Costantine Sideris, and Reza Fatemi's acknowledgement suffers because their influence occurred so early in my PhD but they were friends and mentors in my first years. I am always fascinated by how precisely non-overlapping Brian Hong's and my strengths are. Despite this, he is someone I respect immensely and enjoy a meaningful connection with outside of lab. Aroutin Khachaturian, Parham Khial, and Elliott Williams were at CHIC lab from the beginning to the end of my PhD. Aroutin is the CHIC lab elder statesman, with poise and institutional knowledge. Parham is a first-class researcher, a decent roommate, and the enviable holder of an infectious joviality. Elliott bent but never broke and I will always respect him for it. Craig Ives and Alex White were never my collaborators but always good friends. Samir Nooshabadi's intelligence, thoroughness, and patience sometimes makes me forget he is several years my junior in the lab. By the time I am defending, the Space Solar Power Project team has transitioned to the next generation of Ailec Wu, Alex Ayling, and Oren Mizrahi. Ailec brought a critical set of missing skills to SSPP, tackling the most frustrating tasks for our satellite payload. Alex is calm, adaptable, and far too generous as an

office-mate. The first months after I met Oren I vacillated between thinking he is an intelligent and highly driven researcher who I should make sure to partner with and thinking he is obstinate, short-sighted, and destined for solo research projects. Two years later I am firmly planted in the former camp and am glad to be able to call him a friend outside of lab. Also through SSPP, I enjoyed fruitful collaboration and friendship outside of CHIC Lab with Mike Kelzenberg from the Atwater Lab and Alex Wen, Charles Sommer, and Terry Gdoutos from the Pellegrino Lab. From CHIC lab, Parham, Matan, Samir, and Oren deserve another level of appreciation for their substantial contribution to the scientific work presented in the thesis. The concepts, systems, and illustrations that follow these acknowledgements would not be the same without them.

I have now reached the part of the acknowledgements where I am supposed to thank my advisor, Ali Hajimiri. While not explicitly, much of the acknowledgements have already done so. The opportunities discussed in the first paragraph, the long successful journey of my PhD, and the positive environment of CHIC lab are all credited to him above anyone else. Ali's balanced perspective on the importance of our work in life deserves a more nuanced treatment than I could provide here. However, I can say that this perspective is simultaneously motivating, calming, and fulfilling. I trust his wisdom inside and outside of lab.

The final person I need to thank is Amy Ngai. Many PhD students spend their time outside of lab conducting a desperate search for meaning and happiness. With Amy, I never searched.

Finishing this PhD is a significant accomplishment but still only a sign of potential rather than fulfillment of potential. In many ways, I have been insulated from the challenges and demands of the real world. When I face those obstacles, I need to prove the resources, knowledge, and love that have been invested in me were warranted.

ABSTRACT

Phased arrays provide high gain electronically steerable beams and are powerful systems for sensing and communication. Existing phased arrays are typically small, rigid, and planar which limits their possible use cases. This thesis describes the author's contributions to the creation of novel phased array architectures which can enable new phased array systems and applications. The first chapter describes the design, testing, and use of the scalable router. Scalable routers are a time delay array relay used to reroute signals a microwave frequencies. The second chapter describes the development of large scale flexible phased arrays, first in the context the Caltech Space Solar Power Project, and then in an exploration of a technique for determining the shape of arrays using only mutual coupling between elements. Finally, a guide for developing electronics for academic space payloads is included as an appendix.

PUBLISHED CONTENT AND CONTRIBUTIONS

- [1] Eleftherios Gdoutos et al. “A lightweight tile structure integrating photovoltaic conversion and RF power transfer for space solar power applications”. In: *2018 AIAA Spacecraft Structures Conference*. DOI: 10.2514/6.2018-2202. eprint: <https://arc.aiaa.org/doi/pdf/10.2514/6.2018-2202>. URL: <https://arc.aiaa.org/doi/abs/10.2514/6.2018-2202>.
A.C.F. participated in the design, integration, and testing of the system.
- [2] Matan Gal-Katziri, Austin Fikes, and Ali Hajimiri. “Flexible Smart Antenna Arrays”. In: *Submitted to Nature Partner Journal Flexible Electronics* (2022).
A.C.F. participated in concept development, designed the flexible carrier board, and prepared parts of the manuscript.
- [3] Parham P. Khial et al. “Multi-beam, Scalable 28 GHz Relay Array with Frequency and Spatial Division Multiple Access Using Passive, High-Order N-Path Filters”. In: *Submitted to Radio Frequency Integrated Circuits Symposium* (2022).
A.C.F. participated in concept development, designed parts of the RFIC, and prepared parts of the manuscript.
- [4] Austin Fikes, Oren S. Mizrahi, and Ali Hajimiri. “A Framework for Array Shape Reconstruction Through Mutual Coupling”. In: *IEEE Transactions on Microwave Theory and Techniques* 69.10 (2021), pp. 4422–4436. DOI: 10.1109/TMTT.2021.3097729.
A.C.F. participated in concept development, designed the flexible arrays and parts of the RFIC and parts of the PCB, took part in the measurement process, and prepared parts of the manuscript.
- [5] Austin Fikes et al. “Fully Collapsible Lightweight Dipole Antennas”. In: *Presented at IEEE International Symposium on Antennas and Propagation* (2021).
A.C.F. participated in concept development, designed pop-up radiator, and prepared parts of the manuscript.
- [6] Austin Fikes et al. “Programmable Active Mirror: A Scalable Decentralized Router”. In: *IEEE Transactions on Microwave Theory and Techniques* 69.3 (2021), pp. 1860–1874. DOI: 10.1109/TMTT.2020.3042516.
A.C.F. participated in concept development, designed parts of the RFIC and parts of the PCB, took part in the measurement process, and prepared parts of the manuscript.
- [7] Oren S. Mizrahi, Austin Fikes, and Ali Hajimiri. “Flexible Phased Array Shape Reconstruction”. In: *2021 IEEE MTT-S International Microwave Symposium (IMS)*. 2021, pp. 31–33. DOI: 10.1109/IMS19712.2021.

9574941.

A.C.F. participated in concept development, designed the flexible arrays and parts of the RFIC and parts of the PCB, took part in the measurement process, and prepared parts of the manuscript.

- [8] Matan Gal-Katziri et al. “Scalable, Deployable, Flexible Phased Array Sheets”. In: *2020 IEEE/MTT-S International Microwave Symposium (IMS)*. 2020, pp. 1085–1088. DOI: 10.1109/IMS30576.2020.9224066.

A.C.F. participated in concept development, designed the flexible carrier board, and prepared parts of the manuscript.

- [9] Austin Fikes et al. “Flexible, Conformal Phased Arrays with Dynamic Array Shape Self-Calibration”. In: *2019 IEEE IMS*. 2019, pp. 1458–1461.

A.C.F. participated in concept development, designed the flexible array and parts of the RFIC, performed the measurements, wrote the manuscript, and presented the material.

- [10] Mohammed Reza M. Hashemi et al. “A flexible phased array system with low areal mass density”. In: *Nature Electronics* 2.5 (May 2019), pp. 195–205. ISSN: 2520-1131. DOI: 10.1038/s41928-019-0247-9. URL: <https://doi.org/10.1038/s41928-019-0247-9>.

A.C.F. participated in concept development, designed the flexible carrier board, took part in the measurement process, and prepared parts of the manuscript.

- [11] Michael D. Kelzenberg et al. “Ultralight Energy Converter Tile for the Space Solar Power Initiative”. In: *2018 IEEE 7th World Conference on Photovoltaic Energy Conversion (WCPEC) (A Joint Conference of 45th IEEE PVSC, 28th PVSEC 34th EU PVSEC)*. 2018, pp. 3357–3359. DOI: 10.1109/PVSC.2018.8547403.

A.C.F. participated in the design, integration, and testing of the system.

TABLE OF CONTENTS

| | |
|--|------|
| Acknowledgements | iii |
| Abstract | vi |
| Published Content and Contributions | vii |
| Table of Contents | viii |
| List of Illustrations | x |
| List of Tables | xxi |
| Nomenclature | xxii |
| Chapter I: Introduction | 1 |
| 1.1 Trends Toward Distributed Electronic Systems | 1 |
| 1.2 Distributed Microwave Systems | 3 |
| 1.3 Thesis Outline | 5 |
| Chapter II: Microwave Array Fundamentals | 6 |
| Chapter III: Scalable Router | 15 |
| 3.1 Purpose and Principles | 15 |
| 3.2 Scalable Router Architecture | 16 |
| 3.3 System Analysis | 20 |
| 3.4 Scalable Router Initial Prototype | 41 |
| 3.5 Multiband Scalable Router | 52 |
| Chapter IV: Large Scale Flexible Arrays | 58 |
| 4.1 Introduction | 58 |
| 4.2 Caltech Space Solar Power Project | 61 |
| 4.3 Flexible Array Shape Calibration | 93 |
| Appendix A: Electronics Design for Academic Space Payloads | 124 |
| A.1 Introduction | 124 |
| A.2 Mission Opportunity | 125 |
| A.3 Project Planning | 131 |
| A.4 Electrical Design | 135 |
| A.5 Mechanical and Thermal Design of Circuit Boards | 138 |
| A.6 Space Environment | 141 |
| A.7 MAPLE Qualification Testing | 142 |
| A.8 Regulatory | 149 |
| A.9 Results and Conclusions | 151 |
| Bibliography | 153 |

LIST OF ILLUSTRATIONS

| <i>Number</i> | <i>Page</i> |
|---|-------------|
| 1.1 Figure from [128] showing the explosion of inexpensive computing from 1980-2010. | 3 |
| 2.1 (a) Array factor pattern for uniformly excited 8 element array. The pattern is normalized to the peak value. (b) Array beam-steering geometry (c) Array pattern when steered to 30° | 7 |
| 2.2 8 element phased array steering with isotropic pattern elements and with cosine squared pattern element. The plotted element pattern has been normalized to the array peak power. | 8 |
| 2.3 8 Element array with 4 different element pitches steered to 50° . Grating lobes appear on the other side of the field of view. | 9 |
| 2.4 8 element array Taylor patterns and weights for a variety of sidelobe levels. | 10 |
| 2.5 Two near-field focusing scenarios for an 8 element array. The broadside focusing location is 8λ away from the center of the array. The off-axis focusing location is 6λ up and 6λ to the right of the array center. | 11 |
| 2.6 Arrays of 16, 32, and 64 elements transmitting a 16-QAM signal steered to 70° . Carrier frequency is 10 GHz, and element pitch is $\lambda/2$. Prior to time delay degradation the SNR at the receiver is 20 dB. EVM degrades as symbol rate increases. | 12 |
| 2.7 Mutual coupling effects on adjacent element coupling and element patterns for center and edge elements. | 13 |
| 3.1 The scalable router can be formed by apertures spread across a variety of static and moving surfaces. It can extend the effective reach of basestations to greater distances or areas blocked by obstructions. . . | 17 |
| 3.2 (a) Bent pipe relay. (b) Centralized phased array implementation of bent pipe relay. (c) Scalable router system architecture. (d) Hybrid scalable router. | 18 |
| 3.3 Possible integrated circuit branch implementation using baseband time delay. A scalable router branch provides amplification, time delay, and filtering to the signal it receives and transmits. | 19 |

| | | |
|------|--|----|
| 3.4 | A 16 element scalable router synthesizes a microwave mirror (shown as transparent) which can be electronically steered. | 21 |
| 3.5 | (a) An 8 branch router arranged in 3D space (b) A 2D 8 branch router with equidistant branch spacing. That spacing is chosen to be $d = \lambda/2$ for the simulated patterns shown in Fig. 3.6. | 23 |
| 3.6 | Normalized linear magnitude pattern plot for 1D 8-branch linear array with $\lambda/2$ branch spacing, and branch delays programmed for an intended $\phi_{rx} = -30^\circ$ and $\phi_{tx} = 60^\circ$ | 24 |
| 3.7 | Contours showing the normalized maximum transmitted power in any \hat{R}_{tx} as a function of \hat{R}_{rx} for both a circular and square router of 9 branches with a fixed aperture size of λ^2 | 26 |
| 3.8 | Contours showing the normalized transmitted power in \hat{R}_{rx} as a function of \hat{R}_{tx} for both a circular and square router of 9 branches with a fixed aperture size of λ^2 | 27 |
| 3.9 | (a) A typical branch implementation includes down-conversion and up-conversion of the signal by an LO tone and the application of true time delay. (b) To avoid the image issues associated with single sideband mixing, separate I/Q paths may be used. (c) Visual representation of image rejection by the I/Q architecture. (d) Because the scalable router branches are independent and decentralized, the noise added within each branch is uncorrelated. | 29 |
| 3.10 | Radiative measurement of output spectrum of a branch with free running VCO and excited by an external source. The branch is digitally configured to maximize VCO leakage through up-conversion mixer for better observation of phase noise cancellation. | 31 |
| 3.11 | Simplified branch transfer function phase and amplitude as ideal, unity gain phase rotation occurs under presence of parasitic feedback. | 33 |
| 3.12 | Peak and RMS transfer function phase and amplitude error vs the open loop gain of the simplified branch model. | 33 |
| 3.13 | Architecture of IRS as presented in [178]. | 34 |
| 3.14 | Simplified relaying scenario. Square relay of side length l . Transmit antenna is a m away, receive antenna is b m away. Relay could be an IRS or scalable router. | 35 |

| | | |
|------|---|----|
| 3.15 | (a) Geometric loss from relaying for range of α . α is defined as the ratio of total relaying distance to relay aperture side length. (b) Contribution of position of relay between TX and RX antennas. Equidistant ($x = 1$) is highest loss. (c) Noise power vs bandwidth as calculated by: $P_n = 10 \log_{10}(\frac{kBT}{1mW})$. P_n is noise power in dBm. k is Boltzmann's constant. B is bandwidth in Hz. T is temperature in Kelvin. | 36 |
| 3.16 | EVM degradation due to time offsets for large relays and oblique steering angles. Modulation scheme is 16-QAM. Relays are 1D with $\lambda/2$ pitch at 28 GHz. | 38 |
| 3.17 | EVM of 16-QAM signal at various symbol rates vs steering angle for the small room relaying scenario. | 40 |
| 3.18 | (a) Branch integrated circuit architecture (b) LNA matching and Vector sum phase rotator performance (c) System linearity and PA output power. | 42 |
| 3.19 | Die photo of branch integrated circuit implemented in standard 65nm CMOS process. | 42 |
| 3.20 | Hybrid analog/digital time delay unit (HTDU). Coarse delay is controlled by the initial set/reset state of the NOCs. Medium delay adds or removes inverters and fine delay changes a voltage controlled delay line. | 44 |
| 3.21 | Coarse, medium, and fine true time delays and measured phase responses for span of coarse, medium, and fine delay settings. All measurements are referenced to the lowest delay setting. | 45 |
| 3.22 | (a) Fabricated branch transceiver PCB for radiative measurements of the designed branch integrated circuit. The TX and RX antennas are orthogonally polarized. (b) The simulated S-Parameters of the PCB. (c) The simulated radiation pattern of the designed patch antenna. | 45 |
| 3.23 | Radiative scalable router test set-up. Two pairs of branch circuits are excited by a horn antenna and their re-radiation is measured by the other horn antenna. The branches are not colocated and do not share a timing/phase reference. | 46 |
| 3.24 | Radiatively measured branch phase response and group delays with and without true time delay correction. | 46 |

| | | |
|------|---|----|
| 3.25 | Received eye diagrams/constellations for BPSK, 16-QAM and 64-QAM at 45 Msps with beamforming achieved via phase-only steering (left side) or true time delay (TTD) and phase steering (right side). . . | 48 |
| 3.26 | Dual beam test set-up. TX and RX antennas connect to VNA. RX antenna is mounted on a linear scanner. | 49 |
| 3.27 | Branch phase responses measured at the center and left RX probe positions for the router digital configuration which steers 24.9 GHz to the center and 25 GHz left. | 50 |
| 3.28 | Measured patterns at 24.9 and 25 GHz for three different steering configurations. Demonstrates simultaneous, independent control of two receive/transmit beam pairs. The powers are normalized to the same global maximum occurring on the 24.9 GHz beam during center/center steering. | 50 |
| 3.29 | Multi-beam scalable router use-cases and integrated circuit architecture. The 3-channel, 2-branch integrated circuit is symmetric about the reference distribution lines. | 53 |
| 3.30 | Baseband architecture that performs filtering, phase shifting, and true time delay with two different N-path filters. | 54 |
| 3.31 | The 3-Channel response, individual channel response and channel 2 phase and time delay control are shown for a single branch. Double N-Path filter accomplishes independent phase and time delay control. Channel 2 phase sweep isolation is also shown. | 55 |
| 3.32 | Branch scalable router demonstrating simultaneous, independent steering of three beams. Two separate patch antenna circuit boards are used to form the 4-branch router which is excited by a vector network analyzer (VNA). Channels 2 and 3 have had their grating lobes removed in the independent steering to improve readability. | 56 |
| 3.33 | Radiative demonstration of simultaneous 3-channel data transmission using 4-branch router. | 57 |
| 3.34 | Micrograph of multi-beam, two branch integrated circuit. | 57 |
| 4.1 | Flexible Phased Array Concepts and Prototypes. | 59 |
| 4.2 | (a) Caltech Space Solar Power Project folding concept. (b) System architecture. | 63 |
| 4.3 | Atmospheric loss for 45° line of sight from sea level. Reprinted from [134]. | 64 |

| | | |
|------|--|----|
| 4.4 | Size of ground segment needed to capture 84% of radiated power vs size of space system. The useful power after rectification is plotted on the right axis. | 65 |
| 4.5 | (a) Die photograph of the implemented RFIC. (b) Measured output power as a function of power control index. (c) Measured phase and amplitude of a PA versus phase rotator setting. (d) Block diagram of the RFIC architecture. (e) Block diagram of each power quadrant of the RFIC. CLK, clock; ADC, analog-to-digital converter; I/O, input/output; POR, power-on reset; CMU, clock multiplier unit. . . . | 68 |
| 4.6 | (a) Schematic of the radiator. (b) Cross-sectional view of the flexible layers stack. (c) Simulated (black curve) and measured (blue curve) return loss of the flexible radiator. Inset, top view of the working flexible FIMP radiator prototype. (d) Simulated impedance of the designed 75Ω flexible transmission-line. Inset, the transmission-line configuration. (e) Comparison of simulated and measured radiation patterns along the E plane ($\phi = 90^\circ$) and H plane ($\phi = 0^\circ$) for E_θ (left plot) and E_ϕ (right plot) at the resonance frequency. GND, ground; FPCB, flexible printed circuit board; TL, transmission-line; IC, integrated circuit. | 71 |
| 4.7 | High dielectric patch single element test board and matching. | 73 |
| 4.8 | A collapsible dipole antenna in its operational configuration with its components labelled. | 74 |
| 4.9 | Antenna collapsibility: (a) Collapsed, flat configuration, (b) Intermediate state during redeployment. (c) Operational configuration. | 74 |
| 4.10 | (a) Sandwich and finger overlap feed transmission line designs (b) FDTD simulation of s-parameters of the two transmission line designs. $\pm 50 \mu m$ alignment error is added from the nominal design dimensions. | 76 |
| 4.11 | Simulated and measured antenna input match. | 76 |
| 4.12 | (a) Simulated and measured collapsible pop-up dipole element patterns. (b) Simulated 3D pattern with scale and axis. | 77 |

- 4.13 (a) Simulated and measured radiation patterns of the total radiated E fields along the E plane ($\phi = 90^\circ$) and H plane ($\phi = 0^\circ$) for three scan angles, ($\phi = 0^\circ, \theta = 90^\circ$), ($\phi = 0^\circ, \theta = 30^\circ$) and ($\phi = 90^\circ, \theta = 30^\circ$), shown from left to right. (b) Measured EIRP. (c) Radiating element referencing. The near-fields, far-fields, and hologram plots are measured at $f = 9.8$ GHz. Each PA draws nearly 180 mA at 1.1 V. 79
- 4.14 (a) View of the radiator side of the tile. (b) View of the RFIC side of the tile. (c) PV concentrators of the integrated tile. Concentrators are mounted on the same side of the four-layer RF flexible board as the RFIC. (d) Side view of the integrated tile. RF feedlines and the antenna layer are isolated from the photovoltaics and concentrators. Collapsibility is maintained in the integrated tile. e, Radiator side of the integrated tile. (f) Demonstration of power collection and transmission. A solar simulator illuminates the tile, which radiates RF power to the rectenna, lighting an LED. 81
- 4.15 Antenna sheet structure. (a) This antenna sheet assembled on the back side of the base-design main board. (b) Printed antenna patterns and (c) antenna feed assembly. (d) Aluminum heat-spreaders. (e) Power receiver board with an example consumer device (a commercial pulse-oximeter) attached to it. 82
- 4.16 Antenna sheet array measurements. (a) Beam-steering, (b) deformation correction, (c) wireless power transfer of about 80 mW at 1 m away from the transmitter (top), expected power delivery distribution to the remote receiver at ~ 1.4 m away (center), and real-time powering of a pulse-oximeter (bottom). 84
- 4.17 Flexible and robust smart antenna design. (a) Main boards with (b) Discrete patch antennas. (c) The antenna feed via is used for impedance matching. (d) High voltage (up to 6 V) power delivery strap with local voltage regulator. (e) Low-profile heat spreaders. 85

| | | |
|------|---|-----|
| 4.18 | Flexible array measurements. (a) horizontal and vertical convex and concave flex capability to bend radii smaller than 23 cm. (b) Representative focusing and steering capabilities. (c) Compensation in software for damaged RFIC. At the top shown an array with four non-functional. Below, the resulting pattern of broadside phase settings. At the bottom, pattern after re-focusing. (d) Focusing of a wavy surface with non-working ICs. (e) Lobe-splitting by focusing to two different targets. Note the side-lobe combining between the two peaks.(f) Wireless power transfer to real-time power a pulse oximeter 40 cm away from the antenna. (g) Outdoor deployment and focusing to power an LED indicator. The LED is on when the receiver is at the focus point (right) and of when moved away from it (left). | 87 |
| 4.19 | MAPLE Engineering Model. (a) At mechanical testing facility. (b) Image of MAPLE with top removed. (c) MAPLE flexible array seen through sapphire window. (d) Image of MAPLE. | 88 |
| 4.20 | (a) Model of non-uniform grid ground plane backed dipole. (b) Model of Yagi-Uda antenna without ground plane. (c) Reference distribution diagram. | 91 |
| 4.21 | (a) Active tile mass projection. (b) Area mass projection for $j = k = 100$. (c) Area mass projection for $j = k = 256$ | 92 |
| 4.22 | LCOE plot from [47] with asymptotic projection from this work added to curve. | 94 |
| 4.23 | A 2D flexible phased array antenna sheet with 256 10 GHz patch antennas. | 95 |
| 4.24 | A block diagram of our framework for mutual coupling-based shape reconstruction. | 96 |
| 4.25 | (a) Antenna pair coupling study test set-up. Continuous ground plane is maintained for all antenna distances. (b) Coupling power measurement compared with two different propagation models. Measurement averaged over the bandwidth from 2.3 to 2.7 GHz. (c) Coupling phase measurement plot. Antenna pair measurements compared with far-field linear phase propagation model. Measurement is at 2.48 GHz. In both the power and phase plots linear model traces are normalized to the first measured distance. | 100 |

- 4.26 (a) Ground plane backed dipole array. (b) Unwrapped coupling phase measurement plot. In array measured phased is compared to antenna pair measurements and far-field linear phase propagation model. Measurement is at 2.48 GHz. Traces are normalized to the first pair measurement distance. 101
- 4.27 A visualization of forbidden and allowed regions of the $\theta_{mn} \otimes |l_{mn}^{\vec{}}|$ vector space for physically restricted phase arrays. The “constant curvature” line is shown in dashed blue in the center of the allowed region. We also illustrate an example of an shape that generates an allowed $\{\theta_{mn}, |l_{mn}^{\vec{}}|\}$ pair (top right) and a forbidden $\{\theta_{mn}, |l_{mn}^{\vec{}}|\}$ pair (bottom right). As we can see, the forbidden $\{\theta_{mn}, |l_{mn}^{\vec{}}|\}$ pair can only be generated if the array is cut in half. 103
- 4.28 A side view of a flexible phased array ($f = 2.5$ GHz, 0.6λ antenna spacing, quarter-wave dipole antennas) with constant curvature, $R = -0.222m$. Ground plane and dipole feed in black, antennas in red. . . 105
- 4.29 A visualization of the Spiral Match algorithm. In black, the coupling transfer function model, $H_{mn}(|l_{mn}^{\vec{}}|)$, for variable distance is given. The red “X” is our measured coupling, H_{mn}^{meas} . It is “projected” onto the model via the argmin function to give us the blue circle, which is the position on the model that corresponds to our predicted distance, E_{mn} 107
- 4.30 Test set-up for coupling measurements of connectorized arrays. . . . 111
- 4.31 (a) Folded dipole antenna design dimensions. (b) Measured and simulated folded dipole input matching and adjacent element coupling. 112
- 4.32 Shape reconstruction results for passive 2.5 GHz folded dipole phased arrays. a. Concave wooden frames with dipole antennas and curvature radii. b. EDM error heatmaps and mean EDM error (ΔE) for concave shapes. c. Reconstructed antenna shapes (red), true antenna shapes (black), and mean shape error (Δx) for concave shapes. d. Convex wooden frames with dipole antennas and curvature radii. e. EDM error heatmaps and mean EDM error (ΔE) for convex shapes. f. Reconstructed antenna shapes (red), true antenna shapes (black), and mean shape error (Δx) for convex shapes. 113
- 4.33 (a) Patch antenna design dimensions. The substrate extends 5 mm around the copper patch. (b) Measured and simulated patch antenna input matching and adjacent element coupling. 114

- 4.34 Shape reconstruction results for passive 2.5 GHz patch antenna phased arrays. (a) Concave wooden frames with patch antennas and curvature radii. (b) EDM error heatmaps and mean EDM error (ΔE) for concave shapes. (c) Reconstructed antenna shapes (red), true antenna shapes (black), and mean shape error (Δx) for concave shapes. (d) Convex wooden frames with patch antennas and curvature radii. (e) EDM error heatmaps and mean EDM error (ΔE) for convex shapes. (f) Reconstructed antenna shapes (red), true antenna shapes (black), and mean shape error (Δx) for convex shapes. 115
- 4.35 (a) Integrated circuit-based flexible phased array with 8 elements bent in hand with front shown. (b) Array back with feed network, chips, interposers, and circuitry shown. 116
- 4.36 Custom RFIC element circuit block diagram. 117
- 4.37 (a) RFIC die photo. (b) Interposer with RFIC. (c) 3 interposers mounted on flexible printed circuit board. 118
- 4.38 (a) Image of RFIC layout CAD file. PA output balun is shown in the center. The output leg which feeds receiver is boxed in orange. (b) Balun output leg is cut and large transistor switch is added. (c) Schematic of receiver circuit. Amplifier symbol represents an inverter. 119
- 4.39 Element Radiator. (a) Radiators mounted on flexible printed circuit board and radiator dimensions. The feet beneath the fold line are soldered to the circuit board. (b) Measured and simulated in-array element pattern for $\varphi = 0^\circ$ cut. Pattern is measured flat and when array is conformed to a 120 mm convex bend radius. (c) Measured and simulated in-array element pattern for $\varphi = 90^\circ$ cut. All measurements are normalized to their global maximum. 120
- 4.40 Shape reconstruction results for integrated 10 GHz phased arrays with dipole antennas for various radii of curvature. Left: EDM error heatmaps and error mean (ΔE). Right: Reconstructed antenna shapes (red), true antenna shapes (black), and shape error mean (Δx). . . . 122
- A.1 (a) Image of the high altitude balloon launch site take from the payload. (b) Image taken by the payload during flight. (c) Comparison of the planned flight path and the flight path measured by the onboard GPS. (d) External pressure and temperature data from the payload. . . 126

| | | |
|------|--|-----|
| A.2 | Details of LEO, MEO, and GEO orbits. The altitude ranges listed on the vertical axis represent approximate bounds as no strict boundaries are universally defined. The LEO, MEO, and GEO altitude lines are at 700 km, 15,000 km, and 36,000 km above the surface of the earth, respectively. | 128 |
| A.3 | (a) SpaceX Falcon 9 fairing from [158] (b) Rendering of Momentus Vigoride in stowed configuration from [156] (c) Rendering of Momentus Vigoride in flight configuration with solar panels deployed from [156]. Three hosted payloads sit on the payload deck. | 129 |
| A.4 | NASA Technology Readiness Level Table [166] | 132 |
| A.5 | NASA Mission Classes from [81] | 133 |
| A.6 | (a) MAPLE bench top model. Electrically functional but not ready for environmental testing. (b) Electrically functional MAPLE engineering model which has been successfully environmentally tested. FM assembly is in progress as this document is being prepared. | 135 |
| A.7 | (a) Sources representing MAPLE reference oscillators are DC-coupled, risking complete system failure if one fails such that its enable/disable digital pin no longer works. (b) Sources representing MAPLE reference oscillators are AC-coupled, allowing individual oscillators to fail as shorts to VDD or GND without effecting the other oscillators. | 138 |
| A.8 | (a) Strain relief consisting of two holes and a solder pad. Wire emerges for use on the camera side of the board. Thermal damage is evident in the stranded wire insulation. In later assemblies, insulation with better thermal property was used. (b) Wire strain relief seen from the opposite side of the board. (c) In later versions of the board the solder was enlarged and moved further from the holes. Additionally the ground pour around the wire holes was covered with mask to reduce risk of shorting. | 140 |
| A.9 | (a) Component level mechanical testing at Caltech. (b) Preliminary EM mechanical testing at Caltech. (c) EM mechanical testing at Exporior Labs. | 143 |
| A.10 | MAPLE EM Y-axis mechanical testing excitation and response. (a) Sine Vibration (b) Random Vibration (c) Sine Burst (d) Shock. | 144 |

| | | |
|------|--|-----|
| A.11 | (a) Thermal chamber. (b) MAPLE EM inside thermal chamber. (c) Voltage sensing, current sensing, temperature sensing, and wireless power transfer experiment logged measurements (from top to bottom). The thermistor of sensor 13 was disconnected during this experiment. | 147 |
| A.12 | Arducam images at a range of temperatures. White balance changes and artifacts appear. | 148 |
| A.13 | (a) In-house TVAC chamber components from [167]. (b) MAPLE aggregation panel and flex array TVAC testing. | 148 |
| A.14 | Expected TID for given shielding thickness for MAPLE mission as predicted by SPENVIS. | 150 |
| A.15 | Expected proton flux for MAPLE mission as predicted by SPENVIS. Integrated flux shows expected flux of particles at higher energy levels than shown on the x-axis. Differential flux is the derivative of integral flux. (a) Result with 1.8 mm of shielding. (b) Result with 18 mm of shielding. | 150 |
| A.16 | (a) One of the MAPLE component panels mounted on the proton beam set-up at TAMU. (b) MAPLE component test panel. Digitally controlled switches allow each component under test to be powered separately. This prevents a single failed component from pulling the entire panel's supply to ground. (c) Measured current for RFIC before and during proton testing. | 151 |
| A.17 | Several categorical breakdowns of the spending in the MAPLE project. | 152 |

LIST OF TABLES

| <i>Number</i> | <i>Page</i> |
|--|-------------|
| 3.1 Relaying scenario parameters. | 38 |
| 3.2 Performance of IRS and scalable router for relaying scenarios. | 39 |
| 4.1 Iterations of Spiral Match | 107 |
| 4.2 EDM Mask Matrix Structure Candidates | 111 |
| A.1 MAPLE Estimated Link Budget Quantities | 130 |
| A.2 Noise powers for given receive antenna noise temperature and band- width. | 130 |
| A.3 Price comparison for several COTS and space grade components. . . | 132 |

NOMENCLATURE

- ASC.** Array shape construction.
- CMOS.** Complementary metal oxide semiconductor.
- EDM.** Euclidean distance matrix.
- EIRP.** Effective isotropic radiated power.
- EVM.** Error vector magnitude.
- FDM.** Frequency domain multiplexed.
- FIMP.** Fractal inspired modified patch radiator.
- GaAs.** Gallium Arsenide.
- GPU.** Graphics Processing Unit.
- HAP.** High altitude platform.
- HDTU.** Hybrid analog/digital time delay unit.
- IIP3.** Input third order intercept point.
- IoT.** Internet of Things.
- IRS.** Intelligent reflecting surface.
- ISI.** Inter-symbol interference.
- LCOE.** Levelized cost of electricity.
- LNA.** Low noise amplifier.
- LO.** Local oscillator.
- MAPLE.** Microwave array for power transfer, low earth orbit experiment.
- MIMO.** Multiple-input multiple-output.
- PA.** Power amplifier.
- PA.** Power amplifier.
- PAE.** Power added efficiency.
- PCM.** Physical constraint mapping.
- PLL.** Phase locked loop.

QAM. Quadrature amplitude modulation.

RF. Radio frequency.

RFIC. Radio frequency integrated circuits.

SAR. Synthetic aperture radar.

SNR. Signal to noise ratio.

SSPP. Space Solar Power Project.

TID. Total ionizing dose.

TID. Total ionizing dose.

TTD. True time delay.

VCO. Voltage controlled oscillator.

VNA. Vector network analyzer.

Chapter 1

INTRODUCTION

1.1 Trends Toward Distributed Electronic Systems

The last 25 years or more of electronics development has seen computing systems transition from monolithic, singular, high power, high throughput systems, to many small, low-power, distributed units working together. The trend is well known in digital electronics where the “GHz wars” around the turn of the millennium (focused on maximizing clock speed of single-threaded operation [154]) gave way to multi-threaded operation, multiple cores, and parallel processors like GPUs . Decentralization is further exemplified by transitions to cloud storage and computing with many small user interface nodes offloading computation to server farms. The trend can also be seen in the tech news darling “Internet of Things” (IoT)[110]. IoT is a term as nebulous as the systems it describes, and which encompasses a wide variety of sensor nodes, smart appliances and machinery, and remote controlled actuators which can be wirelessly networked. The IoT vision of interlinked, distributed electronic systems is so pervasive it can seem there is no limitation to what objects can be stuck with an ARM processor and incorporated into a distributed digital network ¹

While the trajectory of technological development can never be attributed to a single economic, cultural, or scientific factor, we can identify forces which may have contributed to the rise of distributed electronic systems.

First and foremost of these forces is the availability of nm scale integrated circuits at incredible cost/complexity ratio. The decades of technology development that were envisioned by Moore in 1965 [113] led to ever cheaper and higher density integrated circuits. This period was economically and scientifically fruitful for circuit designers as costs fell and performance rose year after year. The result was the explosive growth of the microelectronics industry.

The improvement of semiconductor manufacturing sustained innovation and industry for decades but slowed at around 2010² in the face of fundamental physical

¹Lack of usefulness and user desire for IoT capability has not proven to be fatal for many applications [3] [21] [12].

²[160] [19] [135] all discuss the slowing or ceasing of Moore’s law with agreement about the broader trends and minor disagreements about the timeline and significance of certain developments.

challenges that hampered further scaling. The inter-related issues of increased transistor leakage density, thermal bottlenecks, reliability problems, and increased production costs have slowed the development and deployment of electrically and economically viable low-nm processes. However, while cutting edge development slowed, existing semiconductor processes grew in availability, infrastructure, and volume.

The proliferation of existing processes made computation sufficiently inexpensive to enable scientists and engineers to focus on computation heavy tools, theories, techniques, and systems that would have previously been infeasible. [128] presents the number of operations paid for by one dollar from 1980 to 2010 (Fig. 1.1). Even with a slowing trend it is clear that by 2010, academics and commercial firms were armed with an order of magnitude more computation than their predecessors. This computation allows for the incorporation of greater complexity, and allows a brute force approach to tasks previously thought un-simulatable.

While the opportunities afforded by Moore's Law have diminished, today's scientists and engineers have an unprecedented breadth and depth of tools. The slowing of Moore's Law creates a pessimistic view for the rate of integrated circuit process improvement, but the proliferation of powerful computational tools creates opportunity for the development of theories, and techniques to enable the creation of evermore large-scale and high dimension systems.

Puny computation tools did not stop previous generations of scientists and engineers. They were forced to develop creative solutions not only for the problem they were trying to solve but also for how best to deploy the limited computational tools they have access to. Those veterans may look at the new generation³ as spoiled: lacking the theoretical fundamentals and systematic design approaches that were needed to create systems without massive raw computational power. Regardless of whether that criticism is valid or not, as new scientists and engineers we must capitalize on the advantages and opportunities. First and foremost this means going where our mentors could not. Our goal should be to identify and tackle complex, scalable, high-dimensional problems that were previously impossible without today's tools. The work of this thesis exists in this technological context.

³Including this author.

One Dollar's Worth of Computer Power, 1980–2010

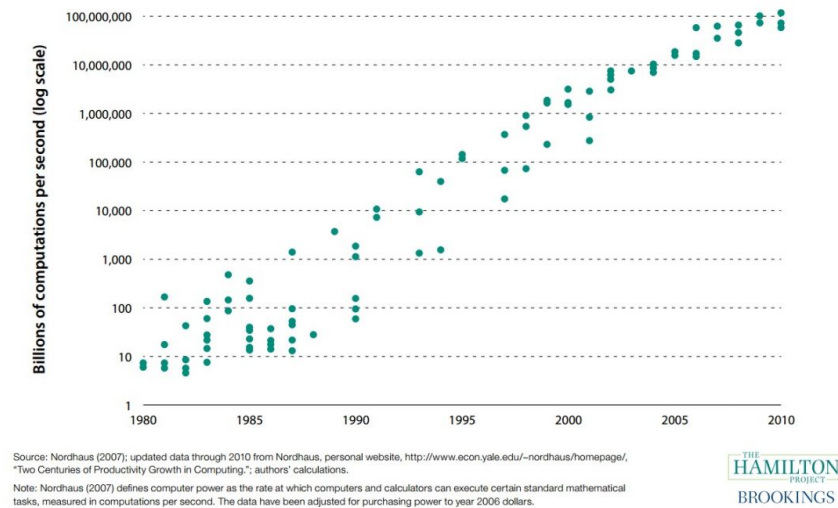


Figure 1.1: Figure from [128] showing the explosion of inexpensive computing from 1980-2010.

1.2 Distributed Microwave Systems

The trend towards distributed systems is not isolated to digital consumer electronics: microwave systems have undergone a similar progression. Microwave systems were first developed as highly centralized broadcast nodes, initially for wireless telegraph, then radio, and commercial television by 1939 [141]. World War II and the space race which followed accelerated wireless system development and began the slow process of decentralization as transceiver radios were deployed in aircraft⁴ for communication and navigation [45] [87] [46]. Phased arrays⁵, a distributed microwave system, were known as early as 1907 ([23]) but limited in their deployment and capabilities. Early arrays, typically deployed in radar systems, were used to create high gain, fixed direction beams [10] [29], or create frequency scanning radiators [136] [74]. While these arrays were an early hint towards a distributed future, they were still largely single port radiators used in a monolithic broadcast paradigm.

⁴From the earliest period of WW2, bombing and interception missions were guided by radio navigation systems. The race to develop countermeasures and counter-countermeasures continued through the Battle of Britain. [141] By mid-war, voice communication systems were used by all major airforces although unevenly, given the material constraints of total war. [40] describes improvised communication systems for flights of 2-5 Shturmovik aircraft and their ground crew using a single, unreliable radio given only to the flight commander, hand-signals, and wing-tip shaking. The radio shortage was later ameliorated by the high losses of Shturmovik planes and pilots.

⁵Phased arrays are synchronized sets of microwave radiators. They are the primary focus of this thesis.

As more complex circuits and systems emerged, arrays for which the phase and amplitude of the excitation of each radiator can be dynamically adjusted, and thereby create electronically steerable beams, became more common. The first of these steerable phased arrays were bulky arrays constructed from discrete components [46] [159] [137]. Eventually monolithic microwave integrated circuits, based on compound semiconductors (e.g., GaAs), began to reduce the size of phased array implementations [35] [126]. Beginning in the 1970s [113], silicon integrated circuits began a march of progress that has led to their complete domination of digital electronics and nearly complete domination of lower-frequency analog electronics. Radio frequency (RF) electronics remained unconquered by silicon until around the turn of the millennium, when silicon low noise amplifiers [18], power amplifiers [7], phase shifters [151] [94], synthesizers [84] [161], and then complete systems [146] [77] [175] emerged. These radio frequency integrated circuits (RFICs) broke the centralized microwave system paragraphs. Previously, the cost, size, and weight of components (constructed from waveguides and vacuum tubes) kept wireless systems from reaching their potential. With RFICs, distributed microwave systems (in particular cell-phones, global position satellites, and wireless internet) define life after the turn of the millennium. These technologies placed transceivers in every room, vehicle, and hand. After several more years of maturation, RF integrated circuit (RFIC) based phased arrays consisting of many transceivers now form the foundation of 5G systems [173].

While the trend towards distributed applications has started for microwave systems it has not completed. Arrays could have more elements and wider distribution, and be used in new applications. We are surrounded by walls, ceilings, and flexible surfaces that could provide the aperture needed for higher bandwidth communication arrays and higher resolution sensing arrays. The primary blocker for these systems is architectural complexity. Phased arrays require a dizzying amount of control to set phase, amplitude, frequency synthesis, and modulation in each transceiver. Fortunately, architectural complexity is the obstacle modern tools best equip us to handle.

The existing array paradigm prioritizes synchronicity — the principle challenge for all arrays. Phased arrays operate using constructive interference between elements. Each element introduces a phase delay to compensate for the difference path lengths that are determined by position. While arrays can be formed by elements arbitrarily

positioned in 3D space⁶, present systems are typically 2D, planar arrays of modest size (4-100 elements). While this design paradigm for phased arrays could be uncharitably characterized as prosaic or “stuck” it emerges from three fundamental challenges in array design and operation:

1. Grating and side lobes in sparse and/or non-uniform arrays.
2. Time delay mismatch across the array elements.
3. Low power and low noise distribution of a phase/frequency reference signal across the elements of the array.

Mitigating these challenges is the critical enabler of new paradigms in array design and application.

1.3 Thesis Outline

This thesis presents unusual architectures that enable new applications for microwave arrays by addressing the fundamental challenges described in the previous subsection. The next chapter provides an overview of the fundamentals of microwave arrays. Chapter 3 describes a relay architecture that allows for arbitrary scaling and the creation of arrays that do not share a timing reference. This allows almost any set of surfaces to be united into an aperture. Chapter 4 describes large scale flexible phased arrays. Flexible arrays can be used in a variety of scenarios that conventional rigid arrays are not suited for. Flexible conformal arrays enable the use of arrays on irregular and dynamically changing surfaces. Flexible deployable arrays allow small form factor systems to utilize large aperture arrays with high gain, electronically-steered beams. Such arrays are especially promising for space systems. Appendix A is a guide for the design and testing of academic electronics payloads based on experiences creating a space-borne demonstration of a flexible phased array.

⁶Microwave arrays can also be formed in time and space, not just space. Synthetic aperture radar (SAR) uses several transmission and reception events from a moving antenna to synthesize a larger array [169].

Chapter 2

MICROWAVE ARRAY FUNDAMENTALS

Given the centrality of microwave arrays to the work described in this thesis, a brief description¹ of the fundamental operating principles of arrays is provided.

Microwave arrays consist of individual elements which radiate or receive electromagnetic waves². In this section we will consider arrays in which the element excitation amplitude and phase can be independently controlled. The most common array functionality, far-field beam-forming, occurs when arrays concentrate power in a certain direction through constructive interference. The location of the constructive interference and accompanying destructive interference are determined by the complex excitations of each array element. For typical, well-behaved, array scenarios, geometric calculations using the element locations and free space wavelength of the frequency of operation can determine the directional pattern of the array.

To quantify the patterns of our arrays we will use directivity, $D(\theta, \phi)$, which is the power density radiated in a given azimuth (θ) and elevation (ϕ) direction divided by the power density of an isotropic antenna radiating the same total power. Directivity has units of dB relative to an isotropic antenna (dBi). The additional effect created combined radiation of the array elements is called Array Factor and is quantified in dB. First, we consider an 8 element array where each element is separated by $d = \lambda/2$. We will use a unitless, frequency independent phasor notation for element excitation. Our first scenario will use an excitation amplitude of 1 and a phase of 0° . This scenario is depicted in Fig. 4.23a.

With this uniform excitation, a beam is created in the broadside direction. To steer the beam of the array, a progressive phase shift is applied to each element. Fig. 4.23b shows how this progressive phase shift is determined for a given steering angle, θ . We arbitrarily define the right most element as our phase reference. Each element in the array has an excitation advanced by $\Delta\alpha$ compared to its rightward neighbor. $\Delta\alpha$ must account for the phase accumulated by the wave travelling the path length difference to the wavefront, $\Delta r = -\frac{\lambda}{2\pi}\Delta\alpha$. We can determine Δr and $\delta\alpha$

¹[104] provides a thorough handling of the intricacies of phased array operations and implementation.

²Our phased array analysis is transmit/receive symmetric but we will use language describing transmission unless otherwise specified.

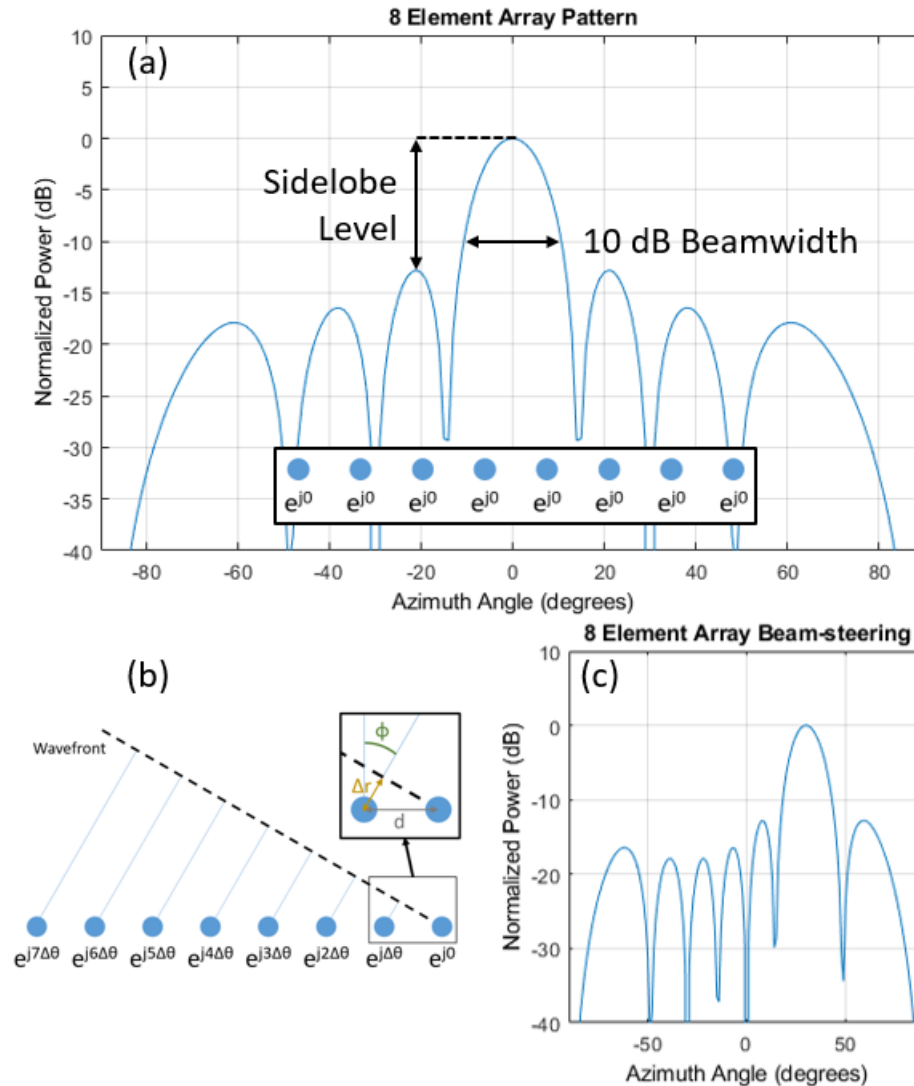


Figure 2.1: (a) Array factor pattern for uniformly excited 8 element array. The pattern is normalized to the peak value. (b) Array beam-steering geometry (c) Array pattern when steered to 30° .

as:

$$\Delta r = d * \sin(\theta). \quad (2.1)$$

Array elements have their own radiation patterns which contribute to the total overall radiation pattern of the array. For a planar array with each element having identical patterns which are identically oriented, the overall array directivity is the product of the array factor and the element pattern. Typical array elements, such as patch antennas have single lobe patterns with 3 dB beamwidth around 120° . These element patterns limit the effective steering range of an array. Fig. 2.2 shows the difference

between the beams steered by an array of isotropic radiators and an array of elements with cosine squared patterns. The steered array beams follow the envelope of the element pattern. Element patterns can offer critical advantages for array operation. All patterns shown thus far are only plotted for $\theta = [0^\circ - 180^\circ]$. For these arrays another beam is created also between $[180^\circ - 360^\circ]$, often referred to as backside radiation. Directional elements such as patch antennas have front to back ratios of > 40 dB, nearly fully preventing the backside lobe.

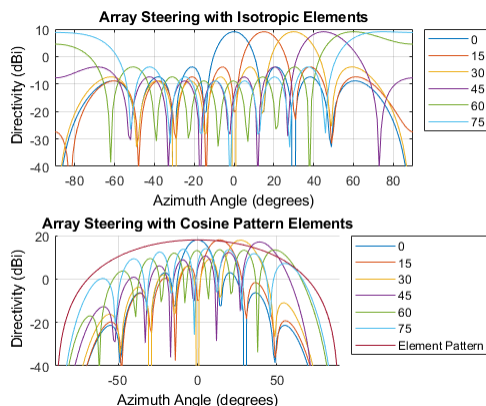


Figure 2.2: 8 element phased array steering with isotropic pattern elements and with cosine squared pattern element. The plotted element pattern has been normalized to the array peak power.

The previous examples use an array with element pitch of $\lambda/2$ which hides a key complication of phased arrays: spread of power outside of the main beam in arrays with lower element density, broadly referred to as sparse arrays. Non-uniform sparse arrays are a complex and well-studied topic but the basic issue is apparent in uniform planar arrays with larger element pitch. Grating lobes are peaks in the pattern that occur in directions other than the primary steering direction due to 2π phase wrapping. In the beam-steering scenario above, the phase difference between waves arriving at the wavefront is 0° . However, any integer multiple of 2π also creates constructive interference. Let the original steering direction be θ_0 . With the beam steered towards θ_0 , peaks occur whenever the following expression is satisfied:

$$\frac{2\pi}{\lambda}d * (\sin(\theta) - \sin(\theta_0)) = 2\pi p (p = 0, \pm 1, \pm 2, \dots). \quad (2.2)$$

Grating lobe free steering is possible when $d \leq \lambda/2^3$. Fig. 2.3 shows how grating lobes emerge for an array of isotropic radiators. This figure also demonstrates how

³When $d = \lambda/2$, it can only be satisfied for $\theta_0 = \pm\pi/2$ and $\theta = -\theta_0$. Since the backside lobe is already present at this location, this effectively means no grating lobe.

the effects of array sparsity may not be entirely negative. While power is spread outside the main beam in sparse arrays, the peak directivity is unchanged. Increasing element pitch increases the array aperture which narrows of the main beam. A more narrow main beam can be useful if the sparse array “curse” can be mitigated by element placement and patter or clever system level design.

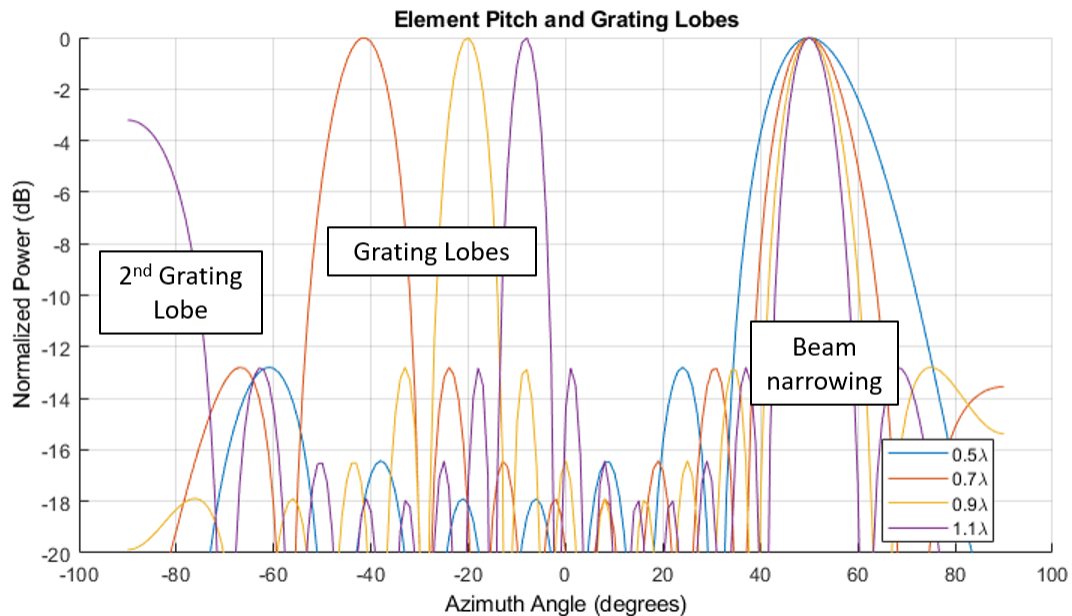


Figure 2.3: 8 Element array with 4 different element pitches steered to 50° . Grating lobes appear on the other side of the field of view.

The array patterns shown so far have used elements excited with uniform amplitudes. This additional degree of freedom can also be used to tune the pattern. The Taylor envelope is commonly used to lower the sidelobes of an array pattern to a constant level. The Taylor amplitude excitations and resulting patterns for an 8 element array are shown in Fig. 2.4. While Taylor weighting is highly effective and widely used, it does widen the main beam and lower its peak⁴. A variety of amplitude envelopes and analytical methods for determining them exist, although Taylor is the most popular.

In addition to directional beam-forming, phased array can perform several other functions. Near-field focusing, shown in Fig. 2.5, maximizes power directed towards a region of space in the near-field of the array⁵. This can be a common

⁴The peak array factor is only lowered if the amplitude weighting of an element cannot be increased beyond the level used in the unweighted pattern which we are comparing to.

⁵When referring to the array near-field, we are not describing the reactive near-field or Fresnel

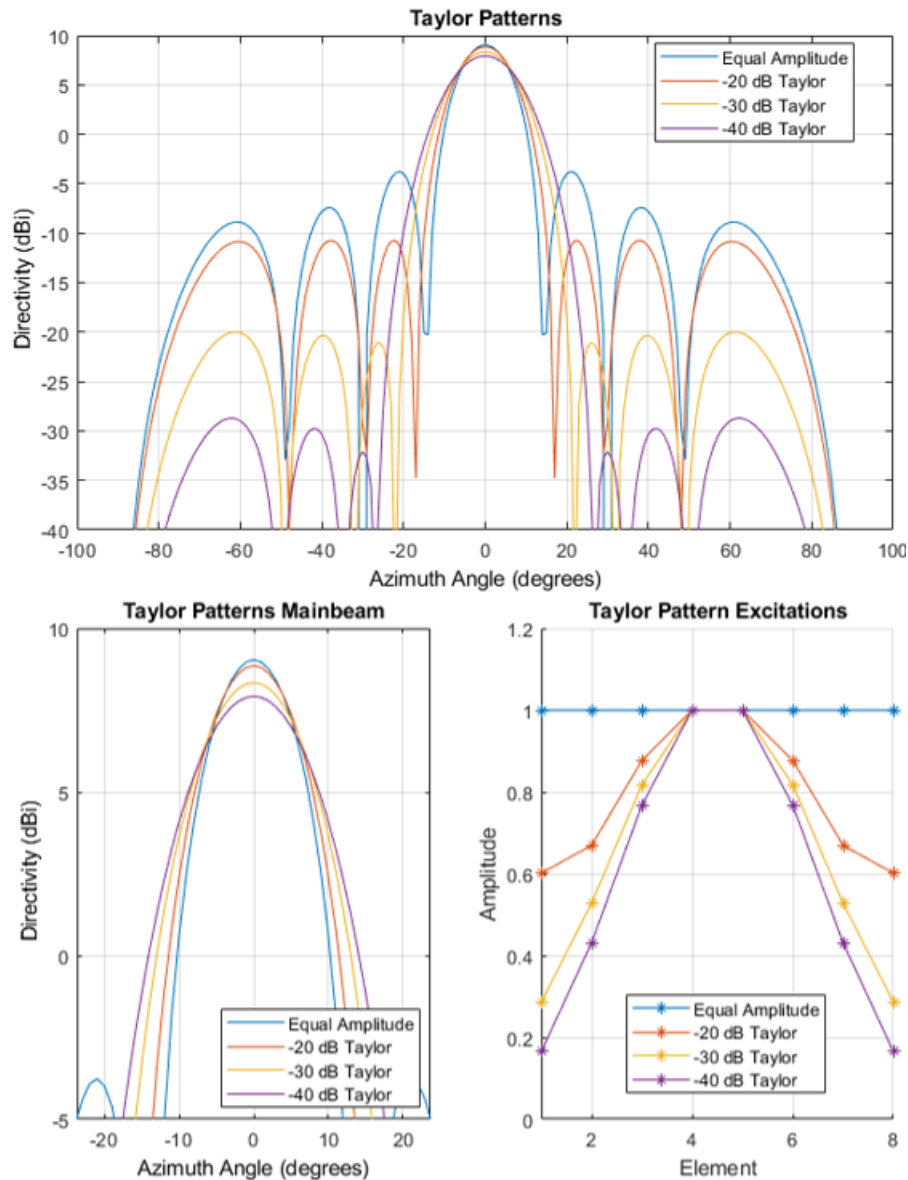


Figure 2.4: 8 element array Taylor patterns and weights for a variety of sidelobe levels.

scenario during array calibration and for large arrays used in wireless power transfer. The excitations needed to maximize power at a point in the array near-field can be determined geometrically. If the target region is sufficiently close to the array, elements may have substantially different view angles to the target. Creating constructive interference at a point in the near-field causes the field to diverge in the far-field. Compared to a far-field beam-steering with a peak in the same direction,

Region of an individual radiator. Instead, we are referring to any location sufficiently close to the array such that the view angle to the location is different for elements in the array.

a near-field focused beam has slightly diminished peak directivity and substantially increased sidelobe levels.⁶

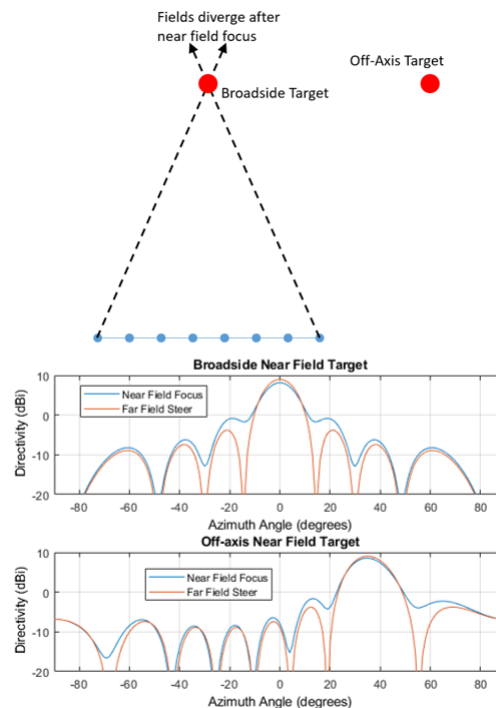


Figure 2.5: Two near-field focusing scenarios for an 8 element array. The broadside focusing location is 8λ away from the center of the array. The off-axis focusing location is 6λ up and 6λ to the right of the array center.

Phased arrays are a powerful multi-purpose tool, but the above examples are ideal use cases. Now we will discuss the non-idealities and additional challenges which must be overcome. An omnipresent concern for phased arrays is unknown or uncontrolled amplitude and phase offset between elements. The causes of these offsets can be constant (often transmission line length offsets) or dynamic (such as transmission line/amplifier temperature coefficients or aging effects). These offsets can be predicted by simulation or analysis, measured, or corrected for through external feedback.

Our analysis thus far has ignored bandwidth of the signal radiated by the array. Radiation patterns, amplifier gain and phase coefficients, and transmission line loss and propagation delay all have frequency behavior which can cause “beam-squint” as the pattern widens. Additionally, microwave arrays have an inherent bandwidth

⁶This effect is relevant when characterizing arrays with a near-field to far-field transformation set-up. Steering the array to the near-field probe prior to measurement will result in a degraded far-field pattern.

limitation when steered using phase rather than time delay. Single frequency phase steering tolerates 2π phase wrapping, creating propagation length offsets in time. When data is transmitted that additional path length means that the signals radiated by elements on the ends of the array will lead/lag each other when the beam is steered at an angle. The effect of this time misalignment is shown in Fig. 2.6. As the symbol rate of the signal transmitted by the array increases, the EVM degrades. While the geometric analysis of beam-steering uses the wavelength of the carrier signal, when considering time delay effects it is useful to consider the wavelength corresponding to the data bandwidth. If this wavelength is on the same order of magnitude as the array's longest dimension, data coherence issues are likely to occur at oblique steering angles.

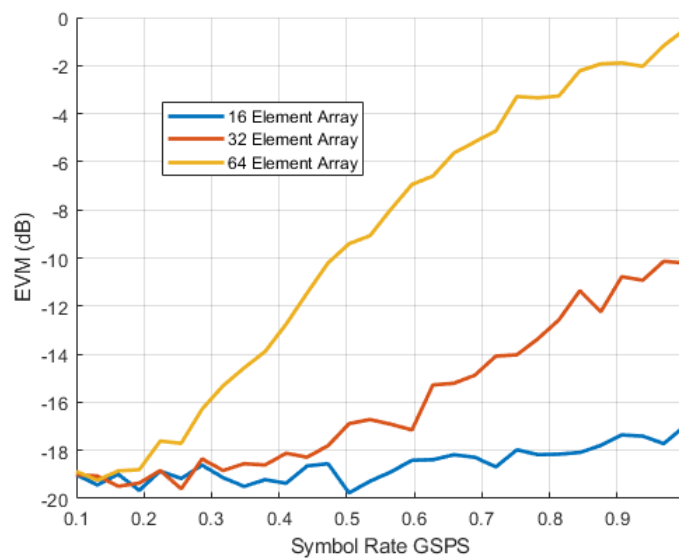


Figure 2.6: Arrays of 16, 32, and 64 elements transmitting a 16-QAM signal steered to 70° . Carrier frequency is 10 GHz, and element pitch is $\lambda/2$. Prior to time delay degradation the SNR at the receiver is 20 dB. EVM degrades as symbol rate increases.

Another non-ideality which must be dealt with by all arrays is mutual coupling. While arrays typically intend to direct energy to a distant target, some of the energy radiated by each antenna is absorbed by the other elements in the array; this energy is called mutual coupling. This coupled power is partially absorbed, lost as heat, and re-radiated which effects the pattern of each element. Critically, mutual coupling causes element drive impedance to have a dependence on steering angle. The element pattern deformation caused by mutual coupling also adds additional complexity to pattern synthesis. In common scenarios, coupling amplitude increases as the

distance between adjacent element coupling decreases. Designers usually try to minimize mutual coupling but for a $\lambda/2$ spaced array -15 dB adjacent element coupling is typical. Mutual coupling also creates a measurable difference in pattern and drive impedance between elements in the middle and edges of the array. These differences can cause many of the simplifying assumptions about element excitations and array patterns to break. To illustrate the effects of mutual coupling, an array model was created in CST [28] and simulated with a time domain solver. The simulation models an 8 element ground plane backed dipole array at a variety of antenna spacing. Fig. 2.7 shows how the element pattern and adjacent element coupling changes as the pitch is swept between 0.5λ and 1.1λ . The pattern changes for both the central and edge elements should not be under-estimated, as the 3 dB beamwidth lobe experiences significant changes in shape and direction.

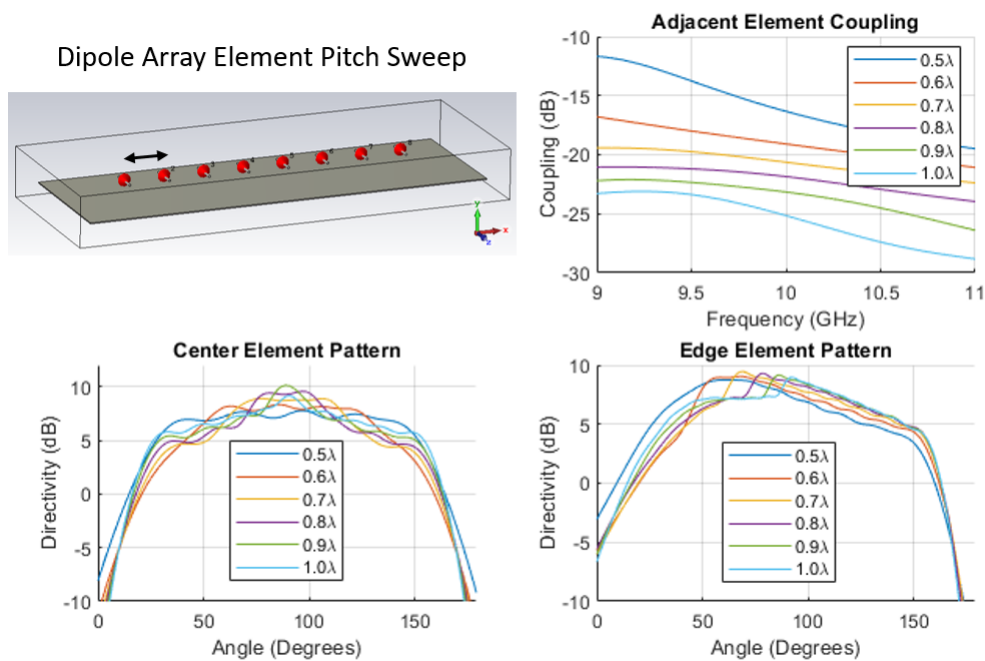


Figure 2.7: Mutual coupling effects on adjacent element coupling and element patterns for center and edge elements.

Excitations for planar, uniformly spaced arrays without mutual coupling can be analytically determined relatively easily. However, irregular element spacing, non-planar array geometry, or the presence of the mutual coupling create sufficient complexity for array pattern synthesis to be a long-running and still active area of scientific inquiry. While pattern synthesis is outside the scope of this thesis, a wide variety of irregular shaped and spaced arrays are presented and thus a brief discussion of synthesis techniques is warranted. The simplest method for

determining element excitations for an irregular array is the aperture projection method [83]. A hypothetical planar antenna aperture is created in front of the curved array. That aperture is excited in a way to create the desired far field pattern. The element locations of the curved array are geometrically projected onto the planar aperture and given excitations corresponding to the excitation at that point on the planar aperture. This, in effect, samples the planar aperture excitation. The projection method generally performs well broadside but its performance degrades when steered to oblique angles.

There also exists a family of iterative methods which use search algorithms and a far-field measurement to reach an optimum. The most common of these is the method of alternating projections. The method defines two sets: the set of all realizable patterns (A) and the set of all patterns which satisfy the requirements (B). Given a starting pattern in A, we project the pattern to set B by adjusting the pattern to meet our requirements. We then project back to set A by using fourier analysis to calculate the excitation coefficients that produce the least-mean-square match to the adjusted pattern.

The method of alternating projections outperformed (converged in less iterations) other iterative pattern synthesis methods in a study in [83]. The downside of this method and other similar iterative methods (such as genetic algorithms) is that a measurement of the array's far-field pattern is required for each iteration. This can be time consuming and logistically challenging, particularly in the field. New techniques for synthesizing complex patterns for irregular arrays with fewer iterations and less measurement complexity are strongly desired.

The array fundamentals described in this section primarily focus on the radiation capabilities and challenges of phased arrays. In order to produce and control this radiation, a variety of electronic components including antennas, phase shifters, frequency synthesizers, power amplifiers, variable gain amplifiers, mixers, summers, and more are required. Additionally, the placement of components and the routing of control, timing synchronization, and data signals must be carefully managed. These architecture and design choices create a staggering space of possible array implementations. The remainder of this thesis describes novel array implementations which provide radiation control in a variety of unique scenarios.

Chapter 3

SCALABLE ROUTER

3.1 Purpose and Principles

The trend towards distributed microwave systems has been accompanied by a demand for higher end user data rates and bandwidth as the information transmitted evolved from morse code (bytes with Hz bandwidth), audio (kilo- bytes/Hz), pictures and low quality video (mega- bytes/Hz), and eventually to high quality video (giga- bytes/Hz).¹ These advances have been hard fought for, as bandwidth is regulated by Shannon's theorem that states the maximum channel capacity is proportional to the available bandwidth and the logarithm of the signal-to-noise ratio (SNR) (plus 1)². System and circuit designers have toiled to improve link budgets and achieve higher data rates and system capacities. On the circuit side, there has been a push to higher frequencies (where more bandwidth is available) by improving critical circuit building block performance, e.g., power amplifier efficiency and linearity or receiver sensitivity. As previously discussed, on the system level, we have moved from single channel static transmitters and receivers to sophisticated programmable massive multiple-input multiple-output (MIMO) systems that can form larger apertures in transmitters and/or receivers to perform a slew of complex functions [70] [148] [121]. These arrays enhance the effective isotropic radiated power (EIRP) in transmitters and sensitivity of receivers to increase the available data rates through the second key parameter in Shannon's theorem, SNR. Also, the spatial directionality and beam confinement provided by arrays enables more effective spatial partitioning of the bandwidth, leading to higher frequency reuse ratios and smaller cell sizes.

Despite these clear advantages, existing phased arrays face aperture scaling limitations inherent to their centralized architecture. The challenge of aggregating every element's signals within the array grows perniciously at higher element numbers and aperture sizes. Furthermore, for high-speed data communication, the difference in data arrival (and departure) times between elements generates dispersion manifested as ISI [60] that must be dealt with through array level delays or complex equaliza-

¹Parham Khial and Samir Nooshabadi were partners in the Scalable Router concept formation, system design, measurements, and documentation. This chapter includes material from [44] and [89].

² $R_B = B \cdot \log_2(SNR + 1)$.

tion schemes in a centralized fashion. Even clever designs rapidly reach practical limitations of signal routing density, interface bandwidth, and data synchronization. Additionally, a centralized approach precludes spatially and/or electrically separated apertures working together.

This chapter presents the scalable router: a decentralized relay array architecture that can selectively receive multiple signals from several desired incident angles and re-transmit them in other arbitrary directions with minimal data distortion. Such scalable routers unite smaller spatially and electrically separated apertures to produce an effective large aperture at high data rates in a decentralized and dynamic fashion. The architecture breaks the scalability constraint and requirement of a physically continuous aperture which limit conventional array designs. While the router re-transmits signals rather than generating its own, it performs the fundamental array function of coherent signal combination with the new capabilities: electronic beam-steering from arbitrarily scaled apertures (greatly enhancing spatial selectivity and array gain) and enables new array form factors by uniting physically and electrically separated apertures.

Intuitively, a scalable router is analogous to a mirror that can be dynamically re-oriented in different directions for different incident signals that will bounce each one of those incoming beams towards different targets in various locations. Unlike a standard passive mirror, this programmable active one amplifies and conditions the signals it reflects. Furthermore this mirror can be constructed out of multiple disconnected elements that could also move in real time.

The ability to operate multiple elements to form a decentralized, non-uniform, and/or dynamically changing array can open a plethora of new opportunities. For instance, locally-powered arrays of elements with no need for timing reference synchronization can be deployed, gradually built-up, and constantly changed across unused walls, ceilings, and buildings surfaces at multiple locations (Fig. 3.1). Furthermore, future infrastructure can allow such systems to be incorporated into various platforms, such as mobile devices, vehicles, building infrastructures, airborne systems, and satellites facilitated by an array architecture decentralized operation and dynamically moving elements.

3.2 Scalable Router Architecture

The scalable router architecture can be seen as evolution and marriage of two existing microwave concepts: the bent pipe relay and the standard centralized phased array.

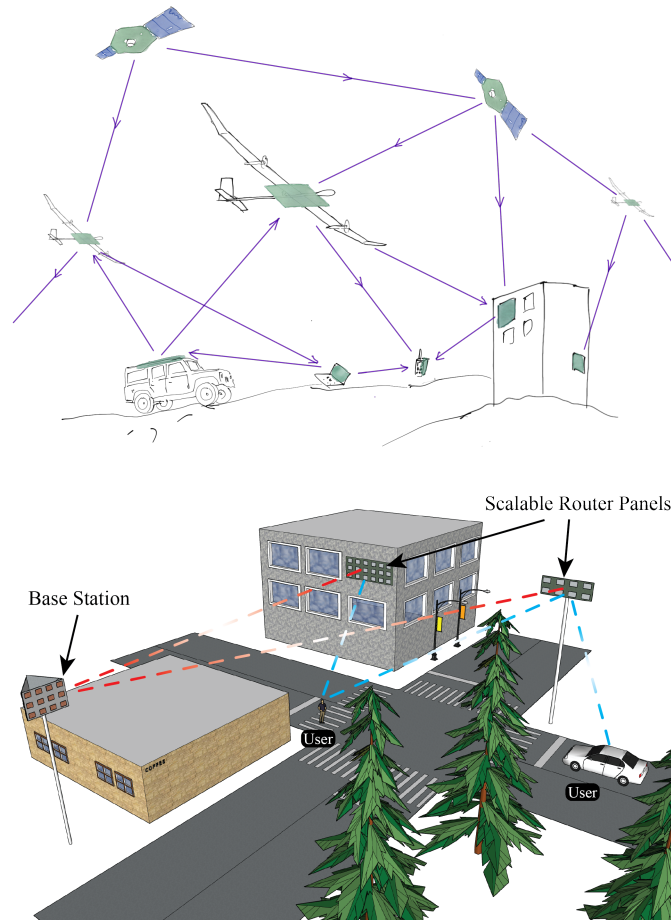


Figure 3.1: The scalable router can be formed by apertures spread across a variety of static and moving surfaces. It can extend the effective reach of basestations to greater distances or areas blocked by obstructions.

The bent pipe relay is essentially a receive antenna, an amplifier, and transmit antenna connected in series (Fig. 3.2a). This simple system re-amplifies incident signals and redirects them with a static, unchanging radiation pattern.

A bent pipe relay can be modified to use two standard M -element phased arrays, one used as a receiver, the other used as a transmitter (Fig. 3.2b). Each phased array creates an electronically steered beam of microwave power by controlling the phase of each element within an antenna array. Now the system can electronically steer the transmit and receive beams.

To create the scalable router, we split the centralized aggregation node that is shared by all elements in the array and add tunable broadband time delays to each branch, as shown in the next step in the progression shown in Fig. 3.2c. For

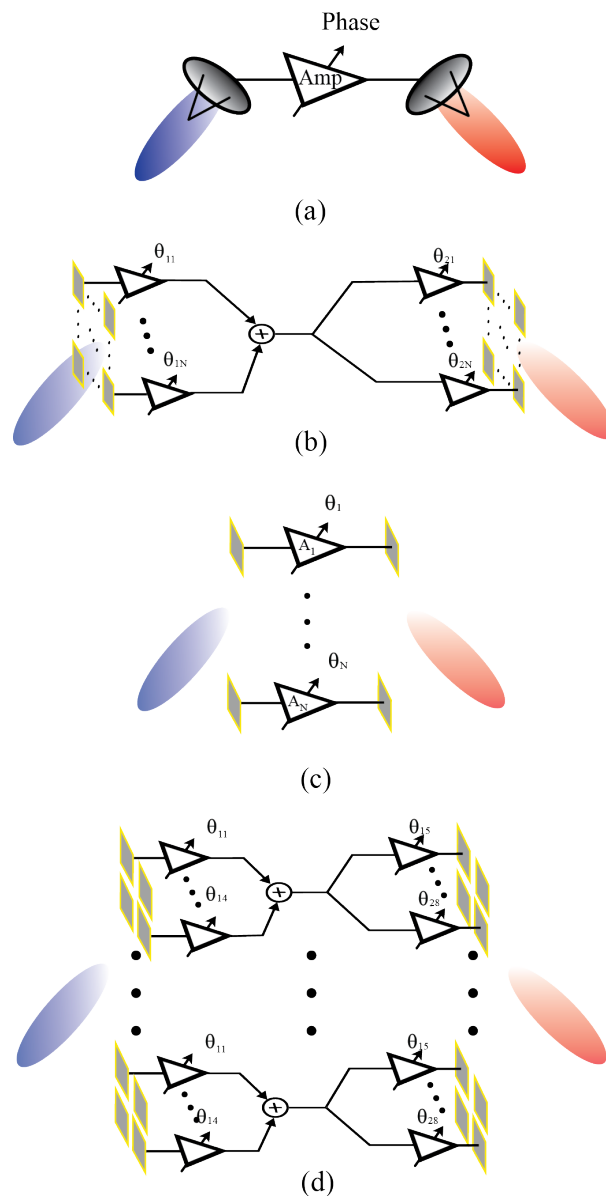


Figure 3.2: (a) Bent pipe relay. (b) Centralized phased array implementation of bent pipe relay. (c) Scalable router system architecture. (d) Hybrid scalable router.

an idealized conceptual model in which amplification, summation, and delay are linear operations, this change is simply an application of the distributive property to a delayed-array. Rather than sum then split the incident signals within the system, signal summation occurs only in the re-radiated beam. The tunable delay elements allow the receive and transmit beams to be steered without centralized signal aggregation occurring within the router³.

³There are some similarities (and differences) between the scalable router architecture and early

While at a highly abstracted level the scalable router can perform all of the functions of a phased array relay, in a real system there are profound implications for noise, linearity, isolation, and other system parameters which we will explore in this work. Fig. 3.2d, described as a hybrid scalable router represents a syncretic state of local centralization and system level decentralization in which the router branches are composed of smaller phased arrays.

A critical feature of the scalable router is that each branch (receive element connected to a transmit element) does not interface with other branches within the array. The transmit and receive beams are steered entirely by setting the delay within each branch (possibly as low frequency digital signals). Not only does this architecture bypass the challenge of centralizing data, but also allows the branches to be implemented without a shared timing reference. The router is fully decentralized: a router may be formed by apertures which are physically separated. The decentralized operation of the scalable router emerges from each branch performing a decentralized function, not reliant on information from any other branch. Fig. 3.3 models idealized operation of a single branch where amplification, delay, and filtering are performed. While these functions can be accomplished by systems at any frequency built with a variety of technologies, Fig. 3.3 shows a down-conversion/up-conversion implementation well suited for integrated circuits at microwave frequencies. Interestingly, the decentralized architecture does not require the local oscillator (LO) signals within a branch to be phase or frequency locked to any other branch. Branch independence enables routers formed by a combination of static arrays, satellites, autonomous aircraft, ground vehicles, or any other surface which can support an aperture.

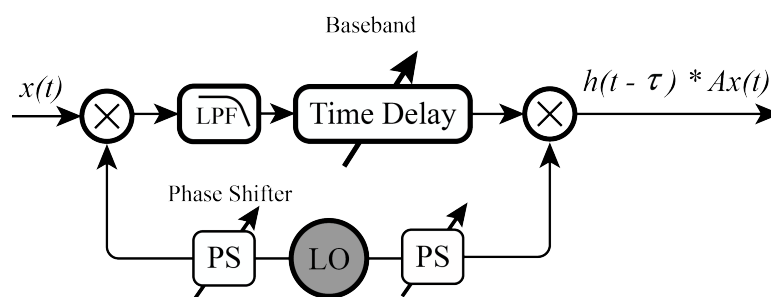


Figure 3.3: Possible integrated circuit branch implementation using baseband time delay. A scalable router branch provides amplification, time delay, and filtering to the signal it receives and transmits.

space fed phased arrays [153]. The scalable router architecture and space fed arrays both have tunable elements with radiative inputs and outputs but differ as the scalable router is decentralized, uses true time delay, and operates in the radiative far-field.

The scalable router architecture is well suited for integration in emerging mm-wave communication infrastructure. Universal adoption of mm-wave systems is hindered by their line-of-sight nature and the high absorption of walls and other obstructions at these frequencies. Attempting to overcome these issues in multi-room indoor settings, dense urban environments, remote areas, and flying systems using traditional phased arrays can lead to unwieldy apertures and power requirements (Fig. 3.1). The scalable router excels in this niche. It can dynamically bounce signals around obstacles or extend and fortify low quality communication links. The scalable decentralized router architecture can enable uninterrupted high-speed connectivity in the presence of large path loss as well as static and/or dynamic obstructions.

Several possible scalable router use-cases are examples of cooperative diversity, which is used as an umbrella term for multi-antenna, relay-reliant, multi-user, or multi-hop schemes intended to increase channel capacity in communication networks [143] [144] [145] [164]. A substantial body of theoretical cooperative diversity research exists, often focusing on optimizing the capacity of a hypothetical network consisting of a base-station and several cellphone users given power constraints and incomplete channel state information [97] [142] [64] [80] [33]. While these analytical works have not explored the challenges, potential, and emergent capabilities of large scale relay array hardware such as the scalable router, their analysis might be fruitfully adapted for specific scalable router use scenarios.

3.3 System Analysis

The scalable router can act as an electronically steerable mirror at microwave frequencies. As the delay within each branch is electronically changed (mirror is rotated), the incident signal is conditioned and re-routed (reflected) to a new direction. Fig. 3.4 models the electronically steerable mirror analogy for a 16 element scalable router. Despite our desire for tidy comparisons, the mirror analogy elides subtle but critical aspects of scalable router beamforming.

The beam patterns of dynamic, spatially decentralized routers can be determined with a geometric derivation. Unlike a conventional centralized phased array, no aggregation occurs within the scalable router, intimately linking the receive and transmit gain beam patterns and deviating from the behavior predicted by our earlier geometric optics analogy.

Fig. 3.5a shows a general, decentralized array structure. The relationship between the intended direction of the received beam pattern, \hat{R}_{rx} , the intended direction of

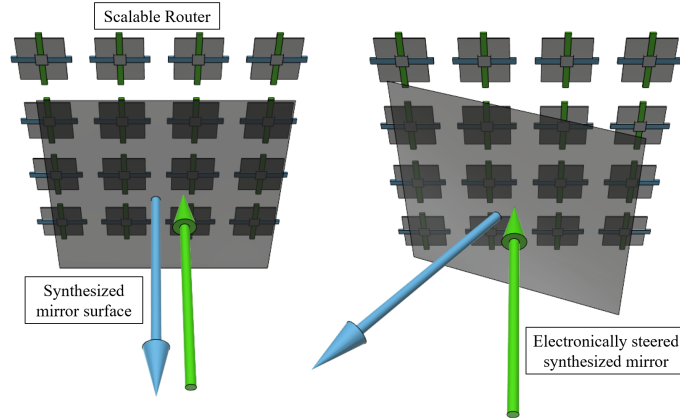


Figure 3.4: A 16 element scalable router synthesizes a microwave mirror (shown as transparent) which can be electronically steered.

the transmit pattern, \hat{R}_{tx} , and the unwrapped phase (a surrogate for the delay), δ_m , of each branch at location \vec{r}_m , can be derived as follows. Considering the origin of our coordinate system as a phase reference, we note that the difference in propagation length to a point \vec{R}_{tx} , between a wave radiated by an emitter at \vec{r}_m and the origin is

$$\begin{aligned} & \left| \vec{R}_{tx} - \vec{r}_m \right| - \left| \vec{R}_{tx} \right| \\ &= \left| \vec{R}_{tx} \right| \sqrt{1 - 2\hat{R}_{tx} \cdot \hat{r}_m \frac{|\vec{r}_m|}{|\vec{R}_{tx}|} + \frac{|\vec{r}_m|^2}{|\vec{R}_{tx}|^2}} - \left| \vec{R}_{tx} \right|. \quad (3.1) \end{aligned}$$

Under the special case $|\vec{r}_m|/|\vec{R}_{tx}| \ll 1$ (which implies that the array aperture is much smaller than the distance to the intended beamforming point), (3.1) can be Taylor-expanded to yield:

$$\left| \vec{R}_{tx} - \vec{r}_m \right| - \left| \vec{R}_{tx} \right| = -\hat{R}_{tx} \cdot \hat{r}_m |\vec{r}_m| + \mathcal{O}\left(\frac{|\vec{r}_m|^2}{|\vec{R}_{tx}|}\right). \quad (3.2)$$

The above propagation length variation manifests itself in the phase propagation term of electromagnetic waves, which under substitution of (3.2) becomes

$$\begin{aligned} & \exp \left[jk \left(-\hat{R}_{tx} \cdot \hat{r}_m |\vec{r}_m| + \mathcal{O}\left(\frac{|\vec{r}_m|^2}{|\vec{R}_{tx}|}\right) \right) \right] \\ & \approx \exp \left[-jk \hat{R}_{tx} \cdot \hat{r}_m |\vec{r}_m| \right], \quad (3.3) \end{aligned}$$

where the above approximation can be made under the far-field condition $|\vec{r}_m|^2 / \lambda \ll |\vec{R}_{tx}|$. We note that (3.3) is the phase difference incurred during transmission of each emitter with respect to the origin. The dual set of phase differentials can be found for the case of an incident wave from a receive direction, \hat{R}_{rx} , in an analogous manner. To keep the notation simpler, we define our new \hat{R}_{rx} to be pointing outward. Combining the two phase terms results in the following phase propagation value:

$$\exp[-jk\hat{R}_{tx} \cdot \hat{r}_m |\vec{r}_m|] \exp[-jk\hat{R}_{rx} \cdot \hat{r}_m |\vec{r}_m|]. \quad (3.4)$$

For coherent beamforming to occur, (3.4) needs to equal 0 for the desired beamforming direction. If a variable unwrapped phase, $e^{-j\delta_m}$, is added to the m th emitter, then coherent beamforming will occur for

$$\delta_m = -k|\vec{r}_m|(\hat{R}_{tx} \cdot \hat{r}_m + \hat{R}_{rx} \cdot \hat{r}_m). \quad (3.5)$$

We note that in (3.5), the required delay for beamforming is given in terms of unwrapped phase δ_m . Noting that $k = \omega/c$, the required phase delay is a frequency dependent term. As noted earlier, for wideband signals a frequency-independent phase delay will result in data decoherence/ISI. Thus, the delay in (3.5) is best implemented via a time-delay, which is given by the recast form of (3.5)

$$t_m = -\frac{|\vec{r}_m|}{c}(\hat{R}_{tx} \cdot \hat{r}_m + \hat{R}_{rx} \cdot \hat{r}_m). \quad (3.6)$$

As a simple and familiar example, the case of a 1D M element array in Fig. 3.5b, with branch pitch d , is studied. For simplicity, we assume that the array coordinates are given by $\vec{r}_m = [0, md, 0]$. This results in (3.6) being evaluated as

$$t_m = -\frac{md}{c}(\sin \theta_{tx} \sin \phi_{tx} + \sin \theta_{rx} \sin \phi_{rx}). \quad (3.7)$$

and since Fig. 3.5b describes the $x - y$ plane, we set $\theta_{rx} = \theta_{tx} = \pi/2$ which results in (3.7) reducing to

$$t_m = -\frac{md}{c}(\sin \phi_{tx} + \sin \phi_{rx}), \quad (3.8)$$

where t_m is the delay of the m th branch with respect to the $m = 0$ branch at the origin. To ensure that all delays are positive, a common delay to all branches may be added. Thus (3.8) can be used to set the internal delay of each emitter to achieve desired reception and transmission angles. Using this expression allows the scalable router to operate as a programmable microwave mirror—the user can set the direction which reflections should be sent. While the above example is for a 1D array, this

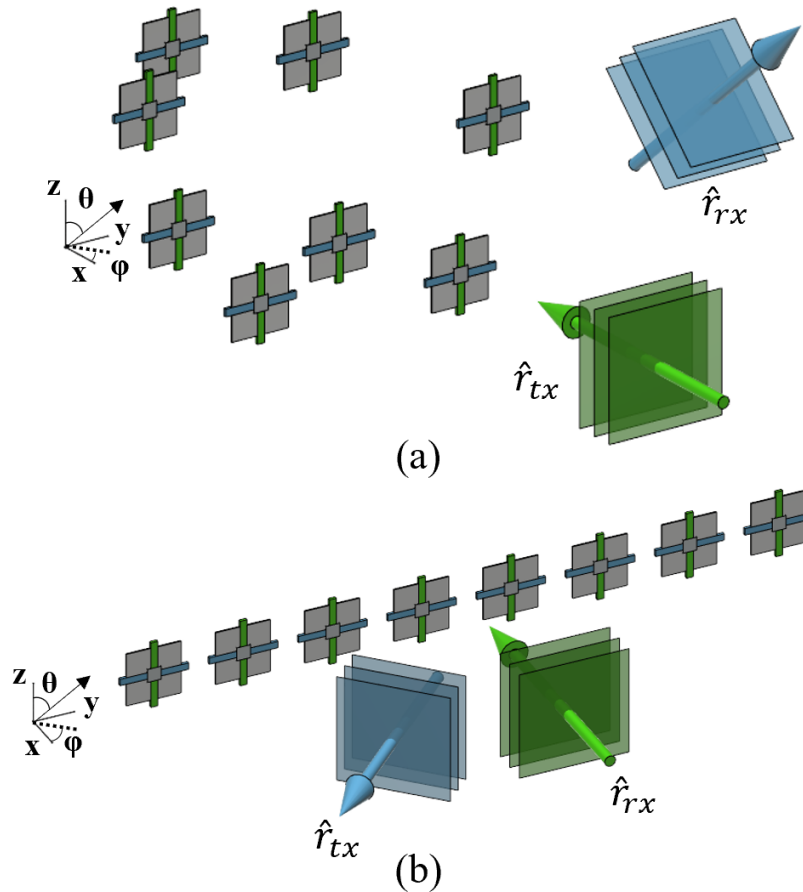


Figure 3.5: (a) An 8 branch router arranged in 3D space (b) A 2D 8 branch router with equidistant branch spacing. That spacing is chosen to be $d = \lambda/2$ for the simulated patterns shown in Fig. 3.6.

derivation can be used for 2D and 3D routers by using the general form found in (3.6).

To produce a conventional beam pattern, we must choose a specific direction for either the receive or the transmit. Consider a 1D 8-branch array with $d = \lambda/2$ branch spacing, such as that shown in Fig. 3.5b, with intended receive direction, $\phi_{rx} = -30^\circ$, and intended transmit direction, $\phi_{tx} = 60^\circ$. The needed branch delays are calculated using (3.8). Fig. 3.6 shows the transmit and receive beam patterns for the programmed array. The transmit beam pattern shows the relative strength of the radiated beam from the router in any given direction when a signal is incident on the router at -30° . The receive beam pattern shows how energy incident on the router from any given direction contributes to the transmitted beam at 60° .

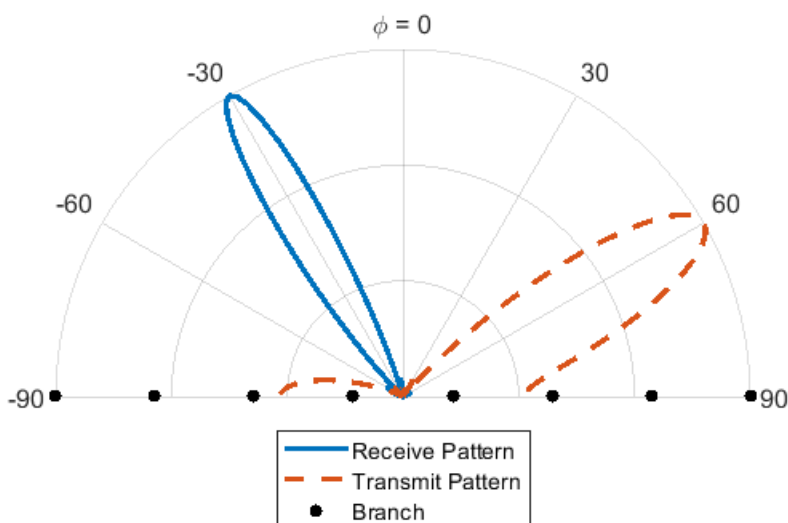


Figure 3.6: Normalized linear magnitude pattern plot for 1D 8-branch linear array with $\lambda/2$ branch spacing, and branch delays programmed for an intended $\phi_{rx} = -30^\circ$ and $\phi_{tx} = 60^\circ$.

Peripheral Vision

While the patterns in Fig. 3.6 describe the intended behavior of the router, attentive readers may note that for a given set of branch delays, signals may be received from, and transmitted to, directions other than intended. We describe this as peripheral vision, since signals incident from outside the directions from which the array is “looking” may be redirected as well. The mathematical justification is apparent from (3.8) as there are many pairs of ϕ_{rx} and ϕ_{tx} that satisfy the equation for a given t_m . While the peripheral vision does not interfere with the primary function of the system, it may be undesirable in certain situations. Fortunately, element position can be used to suppress the router’s peripheral vision.

Router peripheral vision can be quantified for the more general case of a router with steering capability encompassing the entire range of azimuths and elevations. Since the unwanted coherent combination of power is of concern, peripheral vision occurs wherever the carrier signal coherently combines, even though the data signal may be incoherent. Focusing on the carrier signal and assuming far-field conditions, the field at a point in space due to a uniformly excited router is proportional to the

summation of the propagation phases of each branch

$$\left| \vec{E}(\hat{R}_{tx}, \hat{R}_{rx}) \right| \propto \left| \sum_n \exp[-j(k\vec{r}_m \cdot \hat{R}_{tx} + \delta_n + k\vec{r}_m \cdot \hat{R}_{rx})] \right|, \quad (3.9)$$

where \vec{r}_m denotes the location of the m th branch, and \hat{R}_{tx} and \hat{R}_{rx} denote the instantaneous transmit and receive beam directions, respectively. The δ_m term quantifies the added unwrapped phase by each branch that is used to steer the transmitted beam to a desired \hat{R}_{tx} for a given \hat{R}_{rx} , and was defined in (3.5). In this framework, the problem of minimizing peripheral vision reduces to minimizing (3.9) for a given set of \hat{R}_{tx} , \hat{R}_{rx} , \hat{R}_{tx} , \hat{R}_{rx} by varying \vec{r}_m .⁴

As an example of the effect of branch position, \vec{r}_m , on peripheral vision, the maximum transmitted power over all \hat{R}_{tx} as a function of \hat{R}_{rx} is shown in Fig. 3.7 for both a circular and a square router of 9 branches. The branches in the routers were programmed to transmit at $\hat{R}_{tx} = [\phi_{tx} = 45^\circ, \theta_{tx} = 60^\circ]$, and were intending to receive at $\hat{R}_{rx} = [\phi_{rx} = -45^\circ, \theta_{rx} = 30^\circ]$. Contours shown in Fig. 3.7 correspond to the maximum transmitted power in any \hat{R}_{tx} for the given received direction, \hat{R}_{rx} , which is described by a point in the $\phi_{rx} - \theta_{rx}$ plane. Note that the router is programmed to receive a beam in only a desired \hat{R}_{rx} , which corresponds to a single point in the $\phi_{rx} - \theta_{rx}$ plane in Fig. 3.7. Thus, any contours in Fig. 3.7 that lie on points in the $\phi_{rx} - \theta_{rx}$ other than the intended \hat{R}_{rx} represent power that is being received from directions other than \hat{R}_{rx} and subsequently routed to some unintended transmit direction. The higher the amount of this power (contour level in Fig. 3.7), the more peripheral vision is present in the router system. The goal of peripheral vision reduction is to minimize the contours in the Fig. 3.7 so that power is only transmitted when the received beam direction is the intended received beam direction \hat{R}_{rx} .

To normalize the comparison between the square and circle routers in Fig. 3.7, the aperture size of the two arrays are held constant—for a square router with 9

⁴In scenarios where there is a maximum undesired power level that can be transmitted due to the peripheral vision, the minimization can be explicitly stated over all space, for a set \hat{R}_{tx} , \hat{R}_{rx} , as

$$\min_{\vec{r}_m} \iint_S \left| \vec{E}(\hat{R}_{tx}, \hat{R}_{rx}) \right|^2 \mathcal{H} \left(\left| \vec{E}(\hat{R}_{tx}, \hat{R}_{rx}) \right|^2 - P_{max} \right) dS_{rx} dS_{tx} \quad (3.10)$$

where integration over S , the unit sphere, captures different \hat{R}_{tx} , \hat{R}_{rx} directions, and \mathcal{H} is the Heaviside operator and P_{max} the maximum undesired power level.

branches and $\lambda/2$ branch pitch, the circular router has $\lambda/2.25$ branch pitch. Router radiative elements are simulated with a $\cos \theta$ element pattern. As can be seen, the circular router has a better peripheral vision rejection, and highlights the importance of branch placement on minimizing peripheral vision. Note that the actual peak of transmitted power does not occur for the intended receive direction; this is due to the effect of the $\cos \theta$ element pattern. More insight into peripheral vision suppression could be obtained by further analysis of (3.10).

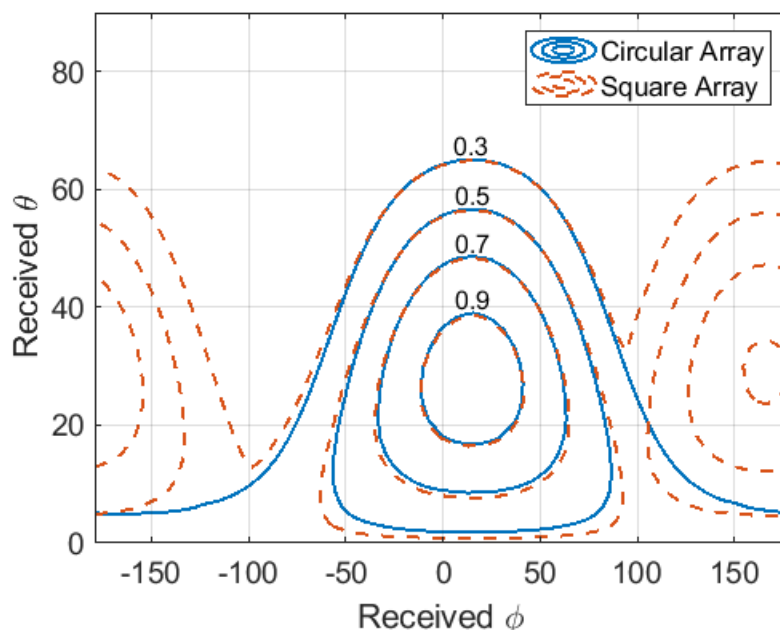


Figure 3.7: Contours showing the normalized maximum transmitted power in any \hat{R}_{tx} as a function of \hat{R}_{rx} for both a circular and square router of 9 branches with a fixed aperture size of λ^2 .

Fig. 3.8 shows a subset of the above analysis, where instead of finding the maximum transmitted power over all \hat{R}_{tx} as a function of \hat{R}_{rx} , the transmitted power in the \hat{R}_{tx} as a function of \hat{R}_{rx} is shown. This is effectively the amount of undesirable power, save for that from the intended receive signal \hat{R}_{rx} , that is transmitted in the desired transmit direction, \hat{R}_{tx} . Once again, to minimize the peripheral vision we want to minimize the contours in Fig. 3.8 so that power is only transmitted when the received beam direction is the intended received beam direction \hat{R}_{rx} .

Scalable router peripheral vision is relevant when blocker signals may be present. While out of band blockers are filtered by the frequency selectivity of the branch antennas and circuits, large in-band blockers could degrade router performance.

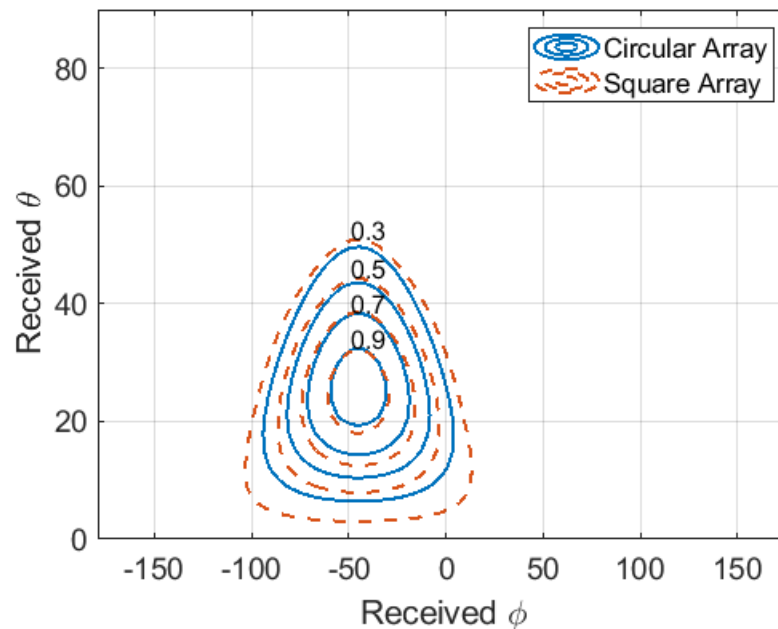


Figure 3.8: Contours showing the normalized transmitted power in \hat{R}_{tx} as a function of \hat{R}_{rx} for both a circular and square router of 9 branches with a fixed aperture size of λ^2 .

The lack of centralization in scalable routers has linearity and blocker tolerance advantages compared to a router constructed from conventional arrays. The greatest amplitude for a blocker signal can occur at the centralized summation node in a conventional array which is avoided in scalable routers. If a blocker signal is high enough power to cause non-linear effects within individual branch circuitry the scalable router will exhibit the same signal intermodulation and gain reduction, which occurs in conventional arrays. In addition to frequency and power, blocker angle of arrival is critical to determining its effect. For the standard, fixed pitch, linear array, a blocker arriving from a direction outside of the intended receive direction will be redirected away from the intended target and will be unlikely to cause any negative effects. For a scalable router with suppressed peripheral vision, a blocker arriving from a direction outside the intended receive direction may not be coherently redirected in any direction. A thorough, probabilistic analysis of blocker suppression and redirection could be performed if router geometry and the likely positions of other relevant transmitters and receivers are known. Unsurprisingly, a high power, in-band blocker arriving at the same orientation as the intended receive direction constitutes a worst case scenario, where the router would rely on branch circuit linearity and the linearity/selectivity of the system it is routing a signal to for

successful operation.

Finally, it should be noted that peripheral vision is only a concern for the router architecture of Fig. 3.2c. For example, in a conventional phased array, such as that shown in Fig. 3.2b, signal aggregation is done before transmit, and peripheral vision is nonexistent. The hybrid architecture of Fig. 3.2d thus results in a lower peripheral vision than Fig. 3.2c for the same number of elements. Additionally, as mentioned before, the peripheral vision described above relates to the unwanted coherent combination of the carrier. Peripheral vision where data coherence is maintained is only a subset of the points in the carrier peripheral vision space and is less of an issue for large, spatially distributed arrays operating in wideband networks.

Data Coherence

The scalable router architecture enables the creation of large aperture arrays (which may be contiguous or physically separated). Data coherence degradation is a natural concern for such systems as ISI and beam-squint occur if within each branch phase delay is used instead of true time delay [60]. These effects are more pronounced when the wavelength of the highest frequency components of an incident signal's modulation is comparable to array aperture size. This makes large aperture arrays steering high bandwidth beams most susceptible.

For a given beam direction, pure phase control maintains perfect coherence only at a single frequency. In order to preserve beam coherence in a band of frequencies and prevent ISI, an additional degree of freedom must be added. This can be achieved by controlling the slope of each branch's phase response with respect to frequency (i.e., adjusting group delay). Programmable time delay within each branch unlocks system scalability—the primary motivation for the scalable router. While true time delay enables high bandwidth arrays, the additional degree of freedom it affords can alternatively be used to simultaneously and independently control two separate full power beams. Dual beam capability is further explained and demonstrated by the first scalable router prototype in section 3.4. However, these two beams do not have true time delay control within their bandwidth as they are using the true time delay control as an additional degree of freedom for beam-steering. The second scalable router prototype (a description of its design and testing can be found in section 3.5) demonstrates multi-beam capabilities with independent true time delay in each beam.

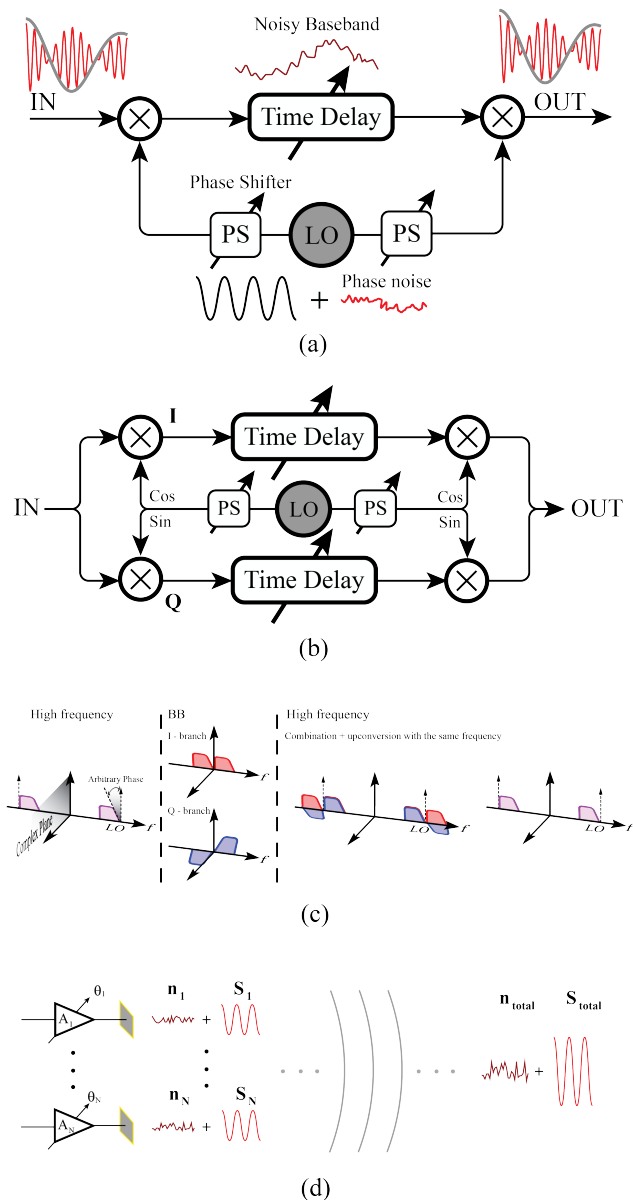


Figure 3.9: (a) A typical branch implementation includes down-conversion and up-conversion of the signal by an LO tone and the application of true time delay. (b) To avoid the image issues associated with single sideband mixing, separate I/Q paths may be used. (c) Visual representation of image rejection by the I/Q architecture. (d) Because the scalable router branches are independent and decentralized, the noise added within each branch is uncorrelated.

Noise

To live up to the scalability potential of the distributed router architecture, the highly complex branch circuits must be manufacturable at a low cost and high volumes. Integrated circuits processes, especially general purpose complementary metal oxide semiconductor (CMOS), can deliver this complexity and volume at an attractive cost. An integrated circuit based scalable router also has the potential to reduce implementation cost and printed circuit board complexity when compared to a conventional two phased array relay. Without a centralization node, the receive and transmit circuitry can be combined within a single integrated circuit die. An integrated circuit based implementation also reduces the marginal cost of additional circuit (such as programmable time delay) needed for a scalable router.

While an integrated circuit implementation has a lot of advantages, it presents a challenge to achieving programmable true time delay with wide range and high resolution at microwave frequencies. Hence, it is preferable to down-convert the received microwave signal and apply true time delay at lower frequencies. This architecture is shown in Fig. 3.9a. To suppress the signal image, the architecture can incorporate an in-phase/quadrature (I/Q) scheme as depicted in Fig. 3.9b-c.

It is noteworthy that the local oscillator (LO) within each branch of the scalable router does not have to be phase or frequency locked to the data carrier frequency or other branches. Also, the down-conversion and up-conversion branch architecture serendipitously suppresses the effect of phase noise in the branch LO. To understand this effect consider an input to the I/Q branch as:

$$X(t) = I(t)\cos(2\pi f_0 t) + Q(t)\sin(2\pi f_0 t), \quad (3.11)$$

where f_0 is the incoming wave frequency. After down-conversion we would have:

$$\begin{aligned} X_I &= \frac{I(t)}{2}\cos[2\pi(f_{LO} - f_0)t + \phi_{LO}(t) + \phi_{PR}] \\ &\quad - \frac{Q(t)}{2}\sin[2\pi(f_{LO} - f_0)t + \phi_{LO}(t) + \phi_{PR}] \\ X_Q &= \frac{I(t)}{2}\sin[2\pi(f_{LO} - f_0)t + \phi_{LO}(t) + \phi_{PR}] \\ &\quad + \frac{Q(t)}{2}\cos[2\pi(f_{LO} - f_0)t + \phi_{LO}(t) + \phi_{PR}], \end{aligned} \quad (3.12)$$

Here f_{LO} is the local oscillator frequency, $\phi_{LO}(t)$ is the associated phase noise, and ϕ_{PR} is the applied phase shift⁵. The output signal after applying true time delay and

⁵It is implicitly assumed in (3.12) that the phase noise of the I and Q are correlated. This is generally a valid assumption if they are generated within the same oscillator core.

up-converting is:

$$\begin{aligned}
 X_{out} = & \frac{I(t - \tau)}{2} \cos[2\pi f_0(t - \tau) - \phi_{PR} \\
 & + \phi_{LO}(t - \tau) - \phi_{LO}(t)] \\
 & + \frac{Q(t - \tau)}{2} \sin[2\pi f_0(t - \tau) - \phi_{PR} \\
 & + \phi_{LO}(t - \tau) - \phi_{LO}(t)].
 \end{aligned} \tag{3.13}$$

As above equation shows the transmitted frequency is exactly at f_0 . This result is independent of each branch local oscillator frequency (f_{LO}). Since the delay, (τ), is on the order of pico-seconds to few nano-seconds, the resultant additional phase noise, due to the term $\phi_{LO}(t - \tau) - \phi_{LO}(t)$, is negligible up to offset frequencies in the giga-hertz range. This near-complete phase noise cancellation bolsters the scalable routers potential for distributed operation as inexpensive reference oscillators with relaxed stability (such as cheap crystal oscillators or on-chip free-running voltage controlled oscillator (VCO) may be used. A measurement of the implemented branch circuit shown in Fig. 3.10 demonstrates this phenomenon clearly. A tone at 25.01 GHz is sent through a branch of the IC (whose details will be discussed in Section 3.4 with a free running VCO around 24.98 GHz. The image at 24.95 GHz exhibits twice the phase noise of the VCO while the re-transmitted tone has a clean spectrum without any of the VCO phase noise.

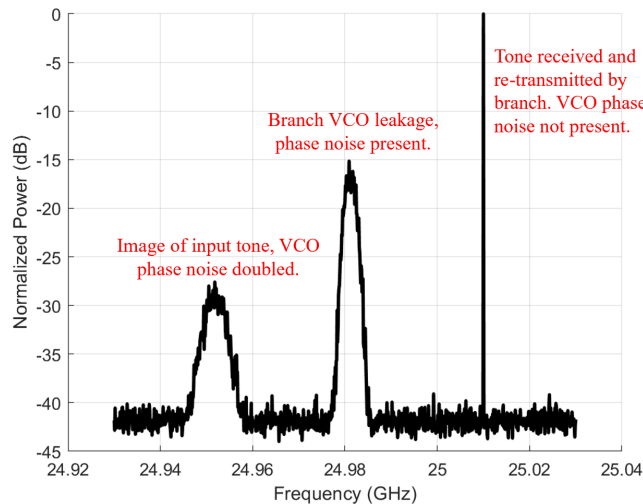


Figure 3.10: Radiative measurement of output spectrum of a branch with free running VCO and excited by an external source. The branch is digitally configured to maximize VCO leakage through up-conversion mixer for better observation of phase noise cancellation.

In addition to phase noise cancellation, the scalable router architecture also provides mitigation of added amplitude noise within each branch. Due to the transceiver branches being fully separate and the absence of any kind of physical summation node within the system, the added noises (antenna noise temperature, noise added by amplifiers, etc...) are uncorrelated. This lack of correlation due to decentralization, shown in Fig. 3.9d, results in higher SNR at the target compared to a relay constructed from traditional, centralized arrays. This noise reduction can be leveraged to trade component level noise performance for other system benefits, for example, reduction of capacitance in a switched capacitor filter to increase bandwidth and reduce on-chip area at the cost of added uncorrelated noise. Decentralization can also help reduce the effect of delay and phase shift quantization noise or setting errors. Uncorrelated stochastic variations or deterministic errors in individual branches are incoherently combined in the transmitted beam of the router, blunting their effect.

Branch Isolation and Self-Interference

Scalable routers are not immune to the self-interference issues that plague many simultaneous transmission/reception (full-duplex) systems. In particular, parasitic feedback from the transmitter output back to the input of the receive chain interferes with system function even if it is far below the levels necessary to cause oscillation. Consider the simplified, frequency independent branch with forward path gain α and parasitic feedback β shown in Fig. 3.11. The delay element within the branch is an ideal constant amplitude phase rotator. The branch's closed loop transfer function phase and normalized amplitude are plotted vs. phase rotator setting for several open loop gains ($\alpha * \beta$) in Fig. 3.11. The parasitic feedback introduces non-idealities to the previously ideal phase rotator. An open loop gain of -20 dB produces nearly ideal behavior but non-ideality quickly emerges as this gain rises. The dependence of these non-idealities on open loop gain can be observed in Fig. 3.12. Fig. 3.12 shows the amplitude and phase error (deviation from the ideal) as open loop gain is changed. Even at an open loop gain of 0.1, the peak phase error exceeds 5° . These non-idealities limit the achievable branch forward path gain, as a gain of 30 dB would require isolation of close to 50 dB for the peak amplitude and phase variations to be rendered unnoticeable. Polarization isolation, isolating radiators on opposite sides of a ground plane, or active feedback cancellation techniques can reduce parasitic feedback to acceptable levels. Provided the branches are implemented by integrated circuits, the additional complexity of active cancellation circuits comes at low marginal cost. While coupling between

adjacent branches may also be a concern, the isolation within a branch is likely to be worse than the isolation between branches of even a dense (0.5λ pitch) array.

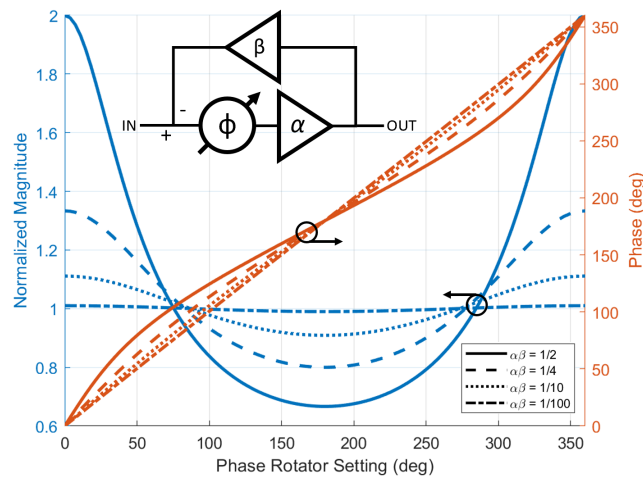


Figure 3.11: Simplified branch transfer function phase and amplitude as ideal, unity gain phase rotation occurs under presence of parasitic feedback.

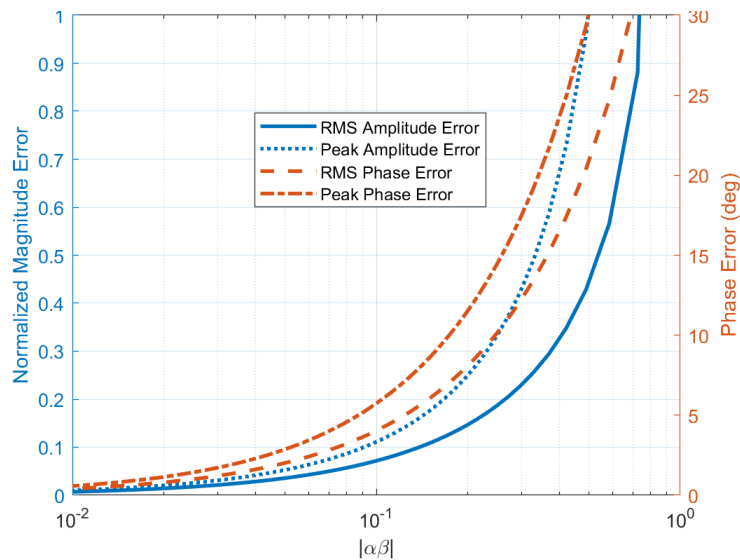


Figure 3.12: Peak and RMS transfer function phase and amplitude error vs the open loop gain of the simplified branch model.

Scalable Routers and Intelligent Reflecting Surfaces

Recent work on the re-routing of mm-Wave signals has not been limited to scalable routers. Another class of relay, called Intelligent Reflecting Surfaces (IRS) or Reconfigurable Intelligent Surfaces (RIS) has been proposed and studied [15] [31] [177] [178]. Similar to scalable routers, these systems are arrays which receive

an incident signal, apply phase delay, apply time delay, or otherwise condition the signal within each element, and then re-radiate incident signals in a new direction by performing beam-forming. Intelligent reflecting surfaces (IRS) typically use tunable reflecting elements based on the DC bias of PIN diodes or varactors. [178] discusses a generic IRS implementation as shown in Fig. 3.13. In IRS metasurfaces, these reflecting elements are significantly smaller than the wavelength [101] [185]. For IRS reflect-arrays, the element density is typically comparable to conventional phased arrays [85] [174] [184]. In contrast, scalable routers use a full transmit and receive chain in each receive and transmit pair in the array. While performing a similar function, these systems differ substantially in key performance metrics and capabilities, each offering a specific set of advantages. This section compares these two systems.

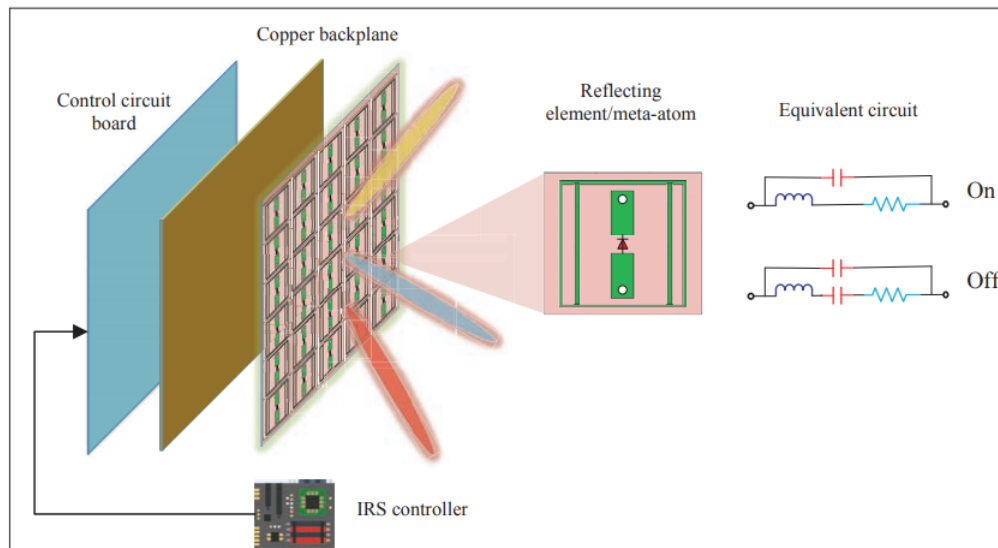


Figure 3.13: Architecture of IRS as presented in [178].

The inherent differences in power consumption and gain between the two relay systems is apparent even from a cursory description. The scalable router uses full analog/digital active integrated circuits, requiring power for amplifiers and phase shifters at a minimum and typically for mixers, buffers, filters, as well. IRS elements are only reverse biased diodes with low current draw, and the circuitry necessary to provide DC bias, likely a digitally controlled IO pin or ADC. This difference in power consumption is a clear advantage for IRS over scalable routers, however the additional power consumption allows scalable routers to have gain (20+ dB in our first prototype described in section 3.4), while even an non-physical ideal IRS

is lossless (0 dB gain). Gain dramatically increases the distance over which high bandwidth communication can be achieved.

We can begin our comparison by analyzing link budgets for several common relaying scenarios. Our simple analysis will consider two separate phenomena: radiative losses during the relaying and loss of data coherence at oblique angles for the relay. The radiative losses determine the minimum size aperture necessary for a relaying task while the coherence losses increase with aperture size, setting an upper limit. Scalable routers do not experience the coherence loss when steering, allowing scaling past the limit set for IRS.

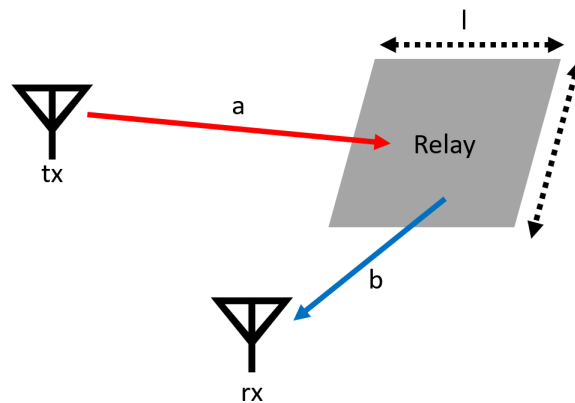


Figure 3.14: Simplified relaying scenario. Square relay of side length l . Transmit antenna is a m away, receive antenna is b m away. Relay could be an IRS or scalable router.

The basic radiative loss scenario is depicted in Fig 3.14. A square relay of side length l relays a signal from a transmitter a distance of a away to a receiver a distance of b . We assume the relay is in the far-field for both the transmit and receive antennas⁶. All distances have units of meters. The relay has a gain of G . $G > 1$ is only possible for scalable routers, not IRS. Let both the receive and transmit antennas be isotropic radiators, with effective aperture $A_{iso} = \frac{\lambda^2}{4\pi}$. Let the power transmitted by the transmit antenna be P_t and the power received by the receive antenna be P_r . We will also define several variables to simplify our later expressions. First is the total distance of the relay path, $d = a + b$. Next is α , which is the ratio of one side of the relay aperture to the total relaying distance, $\alpha = \frac{l}{d}$. Finally we have x , which represents the ratio $\frac{b}{a}$.

⁶When this assumption is broken, the effective aperture of the relay can become large enough to break conservation of energy, capturing more power than is radiated by the transmitter.

The ratio of power received to power transmitted can be written as follows:

$$\frac{P_r}{P_t} = \frac{A_{iso}A_{relay}}{a^2\lambda^2} * \frac{A_{iso}A_{relay}}{b^2\lambda^2} * G. \quad (3.14)$$

We can rewrite this equation using the variables we have defined above as follows:

$$\frac{P_r}{P_t} = \frac{\alpha^4}{16\pi^2} * \frac{(1+x)^4}{x^2} * G. \quad (3.15)$$

These link budgets can be used to analyze both IRS and scalable routers. From this expression we can sweep α , representing the relative size of the array. For this sweep, $G = 1$ and $x = 1$ (relay has unity gain and the transmitter and receiver are equidistant from the relay). This sweep is shown in Fig. 3.15a, and can be used to determine the size of an array needed for a given loss. Fig. 3.15b, shows only the contribution of the $\frac{(1+x)^4}{x^2}$ term.

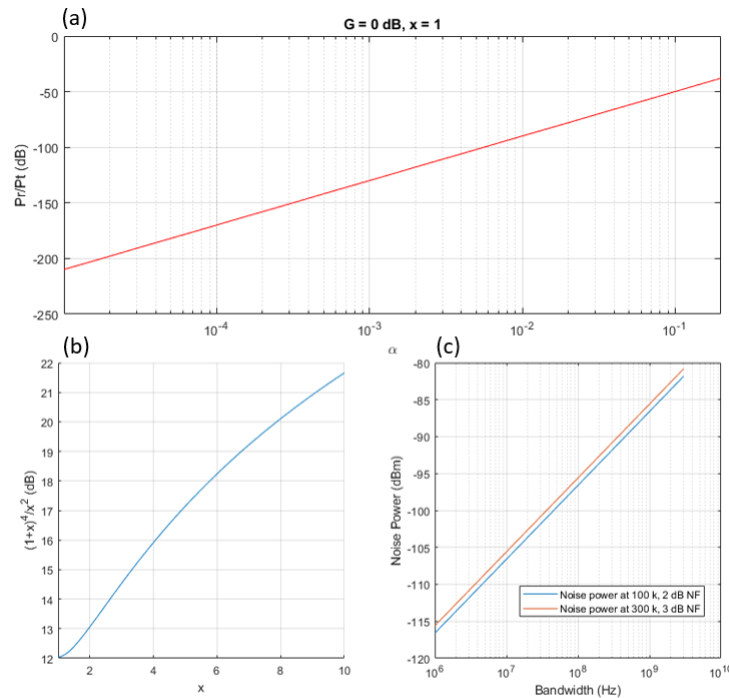


Figure 3.15: (a) Geometric loss from relaying for range of α . α is defined as the ratio of total relaying distance to relay aperture side length. (b) Contribution of position of relay between TX and RX antennas. Equidistant ($x = 1$) is highest loss. (c) Noise power vs bandwidth as calculated by: $P_n = 10 \log_{10} \left(\frac{kBT}{1mW} \right)$. P_n is noise power in dBm. k is Boltzmann's constant. B is bandwidth in Hz. T is temperature in Kelvin.

Fig. 3.15c, shows receiver noise power for a given integration bandwidth and noise figure. While not directly tied to the relay expressions, it does allow us to create

example link scenarios and examine whether IRS (ideal case $G = 0$ dB, more likely $G < -2$ dB) is sufficient or if SCAR's $G > 0$ is needed. The relaying scenarios we will examine are the following: router to user in a small room, router to user in a large room, router to user in an urban environment, a suburban or rural backhaul scenario, and a spacecraft to basestation communication scenario.

$G = 1$ (0 dB) is the ideal, lossless case. Several forms of loss are nearly inevitable for IRS, particularly beam-forming loss due to phase quantization and aperture efficient, η_A less than 100%. The simple diode and varactor based unit cells of IRS implementations typically only have 1-2 bits of phase control. This degrades the peak array factor directivity by up to 3 dB. Our IRS example scenarios will use $G = -3$ dB accounting for both phase quantization and other losses occurring within the unit cell. Both IRS and scalable routers do not capture all power which is incident on their surface, which is reflected in $\eta_A < 1$. For our example scenarios below we will use $\eta_A = 0.7$ for both relay architectures. We will use 20 dB gain for the SCAR. We will have an above noise floor margin of 20 dB with an additional 3 dB to account for other losses such as polarization mismatch, effective aperture decrease at off broad-side, and atmospheric attenuation.

Table 3.1 shows the set-up parameters for each scenario. Table 3.1 shows the resulting link calculations. The maximum achievable bandwidth given a margin above noise margin is shown for both the IRS and SCAR. The green highlighted boxes represent scenarios when the bandwidth is above (in some cases well above) what is practically implementable, meaning thermal noise will not be the limiting factor. For the small room and space-borne reflectarray scenarios, it is likely that the IRS is sufficient. However, for the large room, urban, and suburban/rural backhaul scenarios the achievable bandwidth is smaller than the desired 5G system targets. In these scenarios the SCAR allows for substantially higher bandwidth.

The scenarios discussed above assume broadside reception and transmission for the relays. A real use-case will involve beams steered to angles, likely accompanied by decreases in effective aperture. Oblique beam-steering with large relays has potential for a more insidious issue: data coherence loss from time delay differences between elements. In order to demonstrate this effect we analyze a 1D relay with $\lambda/2$ element pitch, at 28 GHz, relaying a 16-QAM signal. The arrival and departure angles, symbol rate, and number of elements are explored in Fig. 3.16. Error vector magnitude (EVM) is plotted in a variety of scenarios of array size, steering angle, and data symbol rate. Larger arrays, steeper angles, and larger bandwidth all lead to

| Scenario | Routing Distance (m) | Aperture side length (m) | x | Carrier frequency (GHz) | Transmit EIRP (dBm) | Receive antenna gain (dB) | Receive antenna noise temperature (k) | Receive front end noise figure (dB) |
|----------------------------|----------------------|--------------------------|----------------|-------------------------|---------------------|---------------------------|---------------------------------------|-------------------------------------|
| Small room | 8 | 0.2 | 1 | 28 | 30 | 6 | 300 | 3 |
| Large room | 50 | 0.25 | 1 | 28 | 33 | 6 | 300 | 3 |
| Urban | 100 | 0.5 | 1 | 28 | 33 | 6 | 300 | 3 |
| Suburban or rural backhaul | 2000 | 1 | 1 | 24 | 50 | 20 | 300 | 2 |
| Spaceborne reflectarray | 500,000 | 2 | $4 \cdot 10^5$ | 10 | 50 | 20 | 100 | 1 |

Table 3.1: Relaying scenario parameters.

data degradation and limit the use scenarios for IRS. Even the small room scenario whose link budget was previously analyzed demonstrates the importance of true time delay for high bandwidth routing. The small room scenario uses a 0.2 m side length relay, which provides sufficient gain such that thermal noise is not the limiting factor. However, data coherence loss at oblique steering angles could limit the useable channel bandwidth of the relay as shown in Fig.

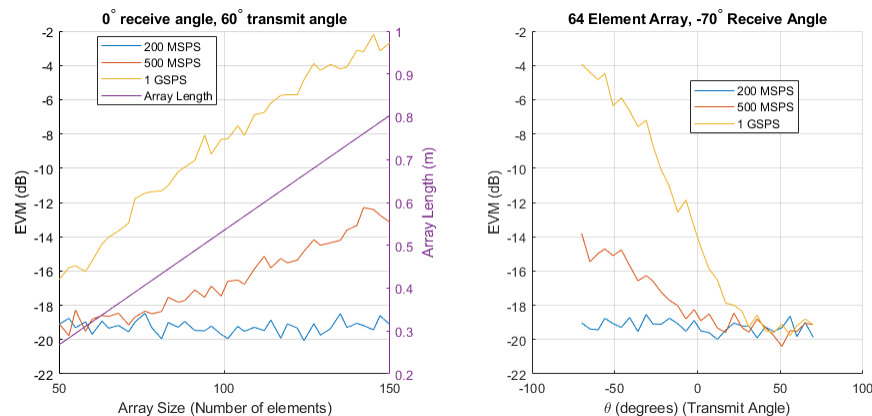


Figure 3.16: EVM degradation due to time offsets for large relays and oblique steering angles. Modulation scheme is 16-QAM. Relays are 1D with $\lambda/2$ pitch at 28 GHz.

While DC power and microwave link budgets likely dominate a system level decision

| Scenario | α | Lossless, Geometric Pr/Pt (dB) | IRS Received Power (dBm) | IRS maximum achievable bandwidth with 23 dB noise margin | SCAR Received Power (dBm) | SCAR maximum achievable bandwidth with 23 dB noise margin |
|----------------------------|-------------------|--------------------------------|--------------------------|--|---------------------------|---|
| Small room | 0.025 | -74 | -42.6 | 33 GHz (Not thermal noise limited) | -19.6 | 6.7 THz (Not thermal noise limited) |
| Large room | 0.005 | -102 | -67.5 | 214 MHz | -44.5 | 21 GHz (Not thermal noise limited) |
| Urban | 0.005 | -102 | -67.5 | 214 MHz | -44.5 | 21 GHz (Not thermal noise limited) |
| Suburban or rural backhaul | $5 \cdot 10^{-4}$ | -142 | -76.5 | 34 MHz | -53.5 | 3.4 GHz (Not thermal noise limited) |
| Space-borne reflectarray | $4 \cdot 10^{-6}$ | -125.9 | -60.4 | 2.6 GHz (Not thermal noise limited) | -37.4 | 523 GHz (Not thermal noise limited) |

Table 3.2: Performance of IRS and scalable router for relaying scenarios.

between an IRS and a scalable router, there are other details worth investigating. The basic function of the systems are identical (re-routing incident microwave signals) but scalable routers can provide additional capabilities. With gain control, scalable routers have far superior null creation ability, which can be an important tool in crowded communication environments. The active gain of the scalable router does come with the potential downside of lower linearity and eventual gain saturation. Scalable routers also have potential for more complex filtering and signal multiplexing as presented in section 3.5. Because scalable routers are made on advanced semiconductor processes, they can potentially incorporate other system functions, generate their own modulation, and function as independent transmitters

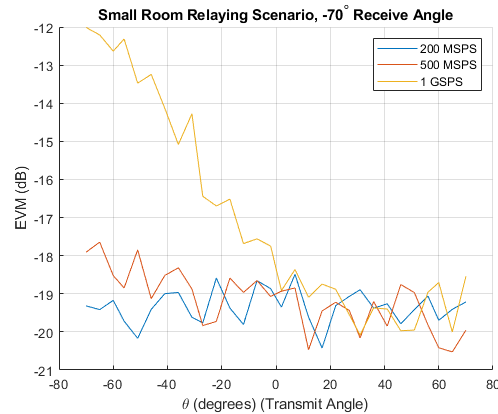


Figure 3.17: EVM of 16-QAM signal at various symbol rates vs steering angle for the small room relaying scenario.

and receivers.

The complexity of control is greater for scalable routers which have additional degrees of freedom for time delay and gain. The additional complexity of the scalable router does not necessarily translate into a substantial difference in cost. While small batch semiconductor production is expensive, advanced processes have excellent cost scaling and there is little difference in the fundamental raw materials needed for production each relay system.

In a practical implementation each system has its own trade-offs. IRS typically use a single antenna or meta-cell for receive and re-transmit, making transmit-arrays (meaning the signal passes through the relay) much more difficult to implement than reflect-arrays (meaning the signal is reflected back towards the direction it originated from). This also limits the polarization diversity which an IRS can take advantage of. Unless a circulator is included with each branch, a scalable router uses separate antennas for receive and transmit. These separate antennas can easily be used to create a transmit-array and perform a polarization transformation between transmission and reception but have a downside of their own. A scalable router reflect-array with densely packed transmit and receive antennas on the same side must consider the coupling between the antennas and the self-interference which could be caused as was discussed in the section 3.3.

Ultimately, each relay system has its own niche in future mm-Wave communication networks. When lack of line-of-sight, rather than low power transmitters or long distances is the limiting factor, an IRS will likely suffice and without adding significant complexity or power consumption. When the data bandwidth of a margin channel

needs to be maximized or multi-channel/null-forming capabilities are needed, the scalable router is the clear favourite.

3.4 Scalable Router Initial Prototype

Our first scalable router is a proof of concept prototype using custom integrated circuit. This prototype is intended to demonstrate basic signal routing and the importance of true time delay for large apertures.

Branch Circuit

The presented router branches are implemented fully on a monolithic CMOS IC with programmable gain and true time delay. CMOS ICs are well suited for scalable router as they not only compactly combine the many digital and analog functions needed for array operation but also offer low cost at high volume. Favorable cost scaling is crucial for the scalable router architecture as cost is as formidable an obstacle as any circuit level performance specification for widespread adoption of arrays of hundreds or thousands of elements. The primary function of the branch circuit is to provide amplification and programmable true time delay to its received signal. The presented branch circuitry uses a baseband hybrid analog/digital time delay unit (HTDU). The branch architecture is shown in Fig. 3.18a. A branch begins with a low noise amplifier (LNA) followed by an I/Q down-conversion mixer. The I/Q mixer's LO is generated on chip. The LO signals pass through vector sum phase rotators that provide 360° phase control. Variable gain amplifiers condition the baseband I/Q signals before they are sent to the HTDU. After the delay unit, the I/Q signals are up-converted using similar LO signals that undergo independently controlled phase rotation. The up-converted I/Q signals are recombined at RF in a vector summer and transmitted by the driver and the PA. Fig. 3.18b-c shows LNA input matching, receiver chain IIP3, and system gain, output power, and compression curves. The die micrograph of the branch IC is shown in Fig. 3.19.

Time delay with fine resolution control and broad variation range is critical to the decentralized router's scalability. Large scale timed arrays are challenging to implement because many existing integrated delays are power hungry, area inefficient, or lacking sufficient range and resolution. Non-IC solutions, such as switchable transmission lines or optical delays, are physically and economically impractical for arrays with hundreds or thousands of elements.

The scalable router HTDU performance requirements are determined by the physical array aperture size and bandwidth requirements of the intended application. For

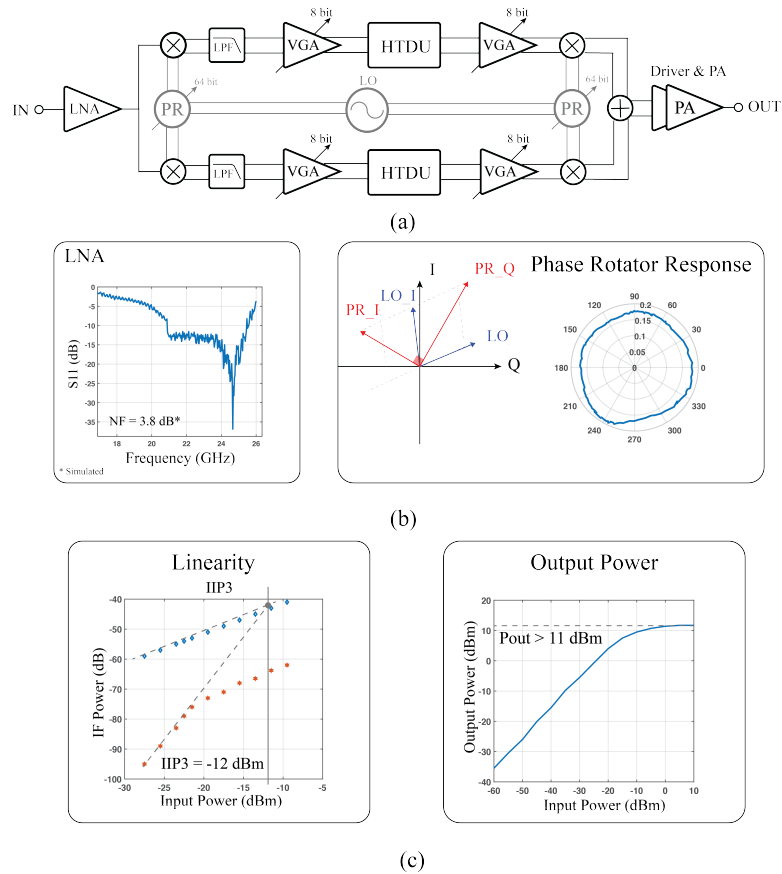


Figure 3.18: (a) Branch integrated circuit architecture (b) LNA matching and Vector sum phase rotator performance (c) System linearity and PA output power.

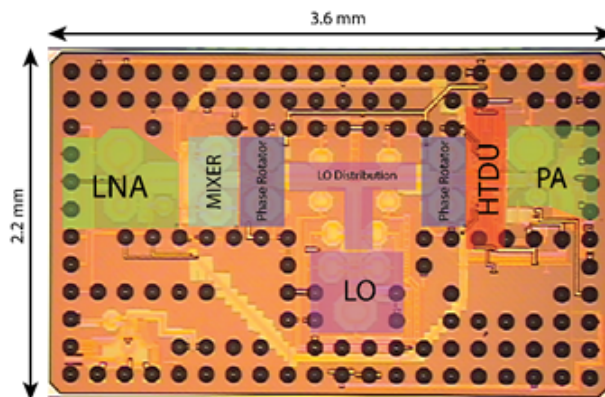


Figure 3.19: Die photo of branch integrated circuit implemented in standard 65nm CMOS process.

instance, in a 1 m aperture span array with 500 MHz baseband bandwidth, two elements on opposite sides of the array may experience time offset of up to 3 ns

while requiring delay adjustment resolution of <20 ps for temporal alignment within 1% of the maximum data frequency content. The 3 ns delay range requirement is larger than existing analog delay solutions [25] [111] [52] while the <20 ps resolution is challenging in purely digital solutions due to unrealistic digital clock requirements [76]. This work uses a hybrid analog/digital switched capacitor delay unit, which fulfils both requirements. A hybrid analog/digital delay unit concept intended for large array applications was recently presented in [55]. Any switched capacitor circuit can be considered as a time delay. The signal is sampled onto the capacitor by a clock edge delivered to the input switch and accessed later by a subsequent clock edge. By controlling the delay between the sample and access clock edges, the delay of the circuit can be changed. To provide sufficient sample rate for the input signal bandwidth, multiple switched capacitors are placed in parallel in an n -path configuration. The input and output switches are controlled by two separate non-overlapping clock generators (NOCs). The time delay is controlled by the relative phase of the two NOCs.

The HTDU (schematic shown in Fig. 3.20) uses 8 switched capacitors in parallel and has fine, medium, and coarse control of the relative phase of the NOCs. The fine and medium control change the phase of the clock driving the output NOC. The fine control uses a DAC to change the bias of a chain of current starved inverters carrying the clock signal. The medium control adds or removes inverters to/from the output clock signal path. The coarse control changes the location of the pulse in the output NOC. The delay element measurements in Fig. 3.21 show 5 ns of range with a minimum step size of 5 ps for the fine step. Minimum step is defined as the smallest step that the non-linear fine delay setting control could be linearized to while still utilizing its full range. The measured delays are determined by fitting a line to the measured phase response and taking its slope (group delay). Digital code “0” for the coarse delay represents a state when the clock pulse for reading from the delay capacitors overlaps the writing clock pulse as such digital code “1” is used for normalization instead. Simulation/analysis curves for coarse, medium, and fine delay are based on extracted delay cell simulations from which the delay range is calculated rather than full system top level simulations. The coarse delay step and range can be increased or decreased by adjusting the NOC clock frequency, with the maximum achievable 10 ns of delay demonstrated in the radiative measurements. In our implementation the input clock can operate in any frequency from 650 MHz to 4 GHz. The clock frequency of 650 MHz (corresponding to 10 ns of delay) is the minimum value for which all the delays in the range can be generated without a

gap.

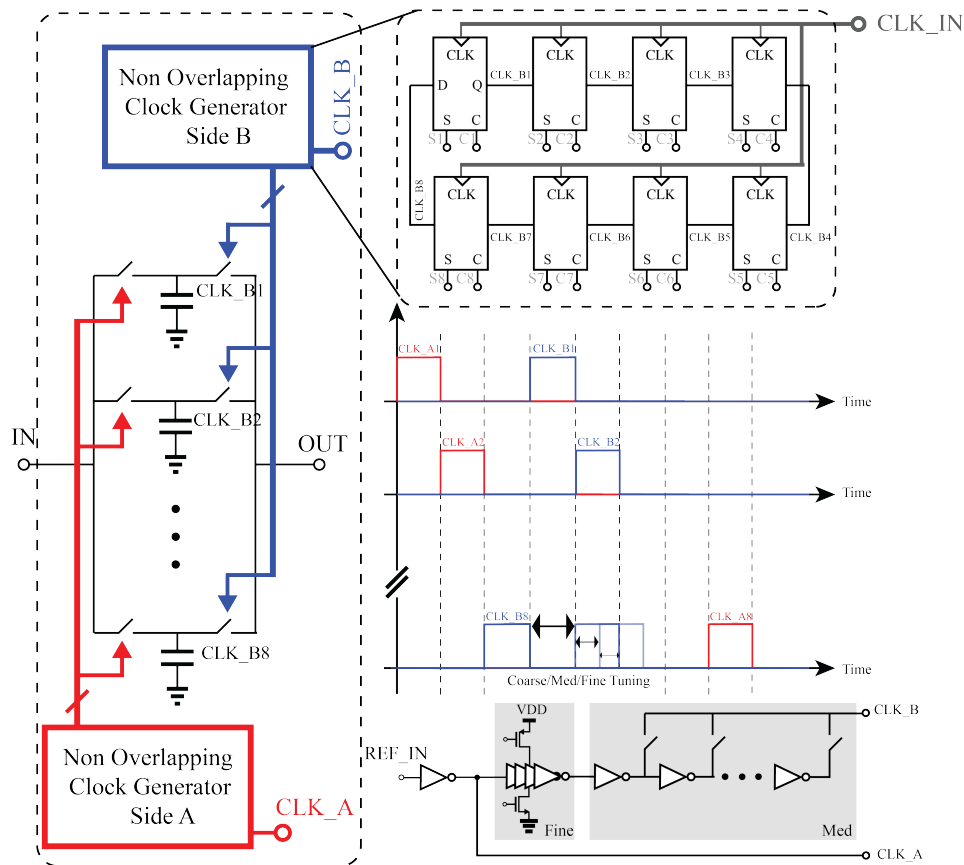


Figure 3.20: Hybrid analog/digital time delay unit (HTDU). Coarse delay is controlled by the initial set/reset state of the NOCs. Medium delay adds or removes inverters and fine delay changes a voltage controlled delay line.

Scalable Router Prototype

A radiative, 4-branch, receive and transmit capable, scalable router prototype was built. Each branch IC is mounted on a printed circuit board (PCB) with orthogonally polarized patch antennas. The scalable router is formed using a number of these branch PCBs arranged in the desired spatial configuration. The branch circuit board, the simulated patch antenna S-parameters (input matching and isolation), and radiation pattern are presented in Fig. 3.22. The simulated isolation between antennas is ~ 50 dB—high enough to not induce significant feedback effects.

The scalable router architecture's potential in large scale array applications where

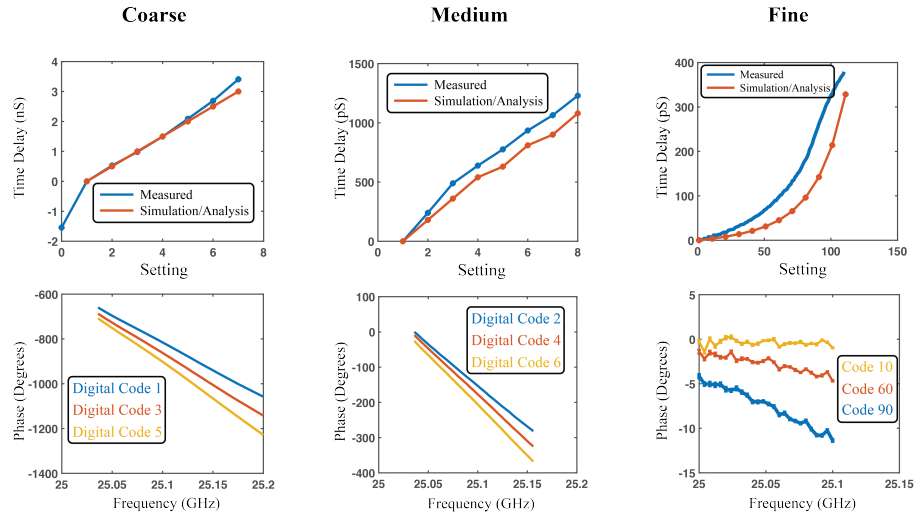


Figure 3.21: Coarse, medium, and fine true time delays and measured phase responses for span of coarse, medium, and fine delay settings. All measurements are referenced to the lowest delay setting.

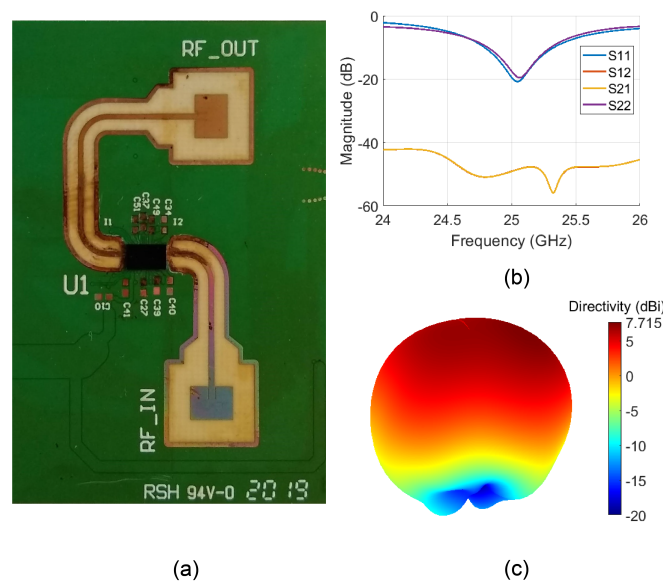


Figure 3.22: (a) Fabricated branch transceiver PCB for radiative measurements of the designed branch integrated circuit. The TX and RX antennas are orthogonally polarized. (b) The simulated S-Parameters of the PCB. (c) The simulated radiation pattern of the designed patch antenna.

there is no shared timing reference between branches is demonstrated in the test set-up depicted in Fig. 3.23. The branches are placed in two pairs separated by 1.5 m. A transmit/receive horn antenna pair is placed 1 m from the leading branch pair.

This transmit and receive horn antenna pair is used to excite the router and measure its re-radiated beam. The total round-trip path length difference between the front pair and back pair is approximately 3 m, which corresponds to 10 ns of delay. The branch circuits share *no* timing information and use internal free running VCOs to provide the LO signal for the circuit.

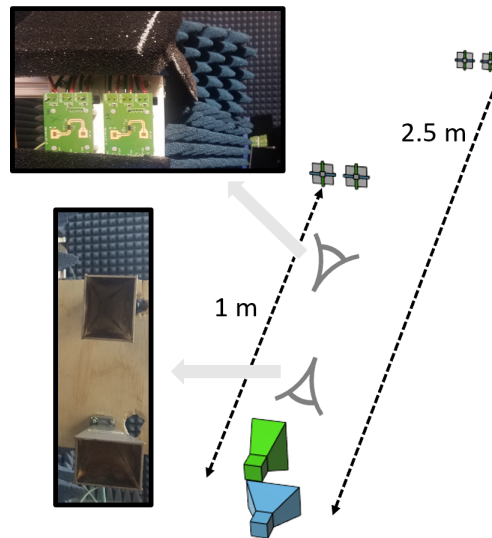


Figure 3.23: Radiative scalable router test set-up. Two pairs of branch circuits are excited by a horn antenna and their re-radiation is measured by the other horn antenna. The branches are not colocated and do not share a timing/phase reference.

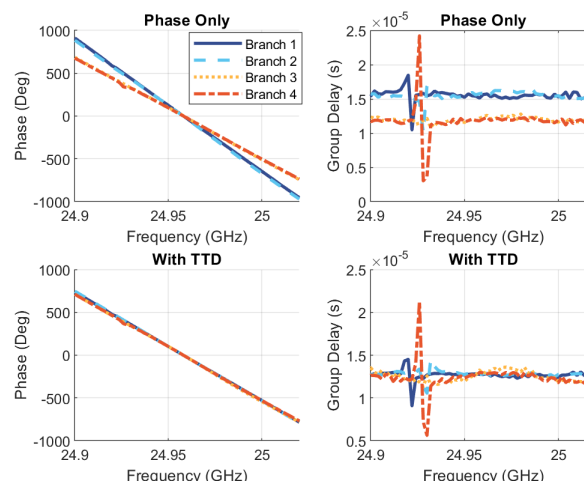


Figure 3.24: Radiatively measured branch phase response and group delays with and without true time delay correction.

To illustrate the routers functionality and the importance of true time delay for the scalable router, two digital configurations of the router were measured. The first

configuration steers the routed beam using only the phase rotators. This matches the elements' phases at only a single frequency point. The 10 ns delay mismatch between the branch pairs causes a difference in group delay (slope of the phase response) and prevents coherent combination of the branches' signals outside of a narrow bandwidth. The second configuration uses true time delay in addition to the phase rotators to match the branch phase responses over a frequency band. By connecting a vector network analyzer (VNA) to the transmit and receive antennas of the set-up, the response of each branch can be measured individually. Fig. 3.24 shows the measured phase response and group delay of each branch with and without true time delay (TTD) correction. The measurements with TTD clearly illustrate matched phase and group delay for all four branches, demonstrating the true time delay adjustment capability of the branch circuit. The peaks in group delay are caused by LO leakage of each branch circuit.

The coherence restored by the branch circuit true time delay is critical for the transmission of data by large arrays. Without this correction, ISI degrades the re-routed data. The same test set-up and branch configurations discussed above were excited by a 24.96 GHz signal modulated with BPSK, 16-QAM and 64-QAM data streams at 45 MSPS. The re-routed signals were measured and demodulated. No equalization was used in the measurement setup. The BPSK eye diagram and 16-QAM and 64-QAM constellations and results of the demodulation are shown in Fig. 3.25. The images on the left hand side correspond to phase-only steering while the images on the right show the results with combined phase and time delay steering. The addition of true time delay noticeably improves the BPSK eye diagram and improves its EVM from 11.4% to 5.2%, while the 16-QAM EVM is improved from 8.6% to 4.4%. The 64-QAM constellation is changed from nearly unrecognizable with phase only steering to an EVM of 4% with phase and time delay steering⁷.

While 45 MSPS is sufficient to observe the importance of true time delay correction, it is even more critical at higher modulation rates. The bandwidth of the presented system is limited by unintentional down-tuning of the branch LOs in the branch integrated circuit.

⁷The 4% EVM may be slightly optimistic as several points at the edges of the constellation may be misidentified as the incorrect symbol. Despite this, the improvement provided by true time delay is undeniable.

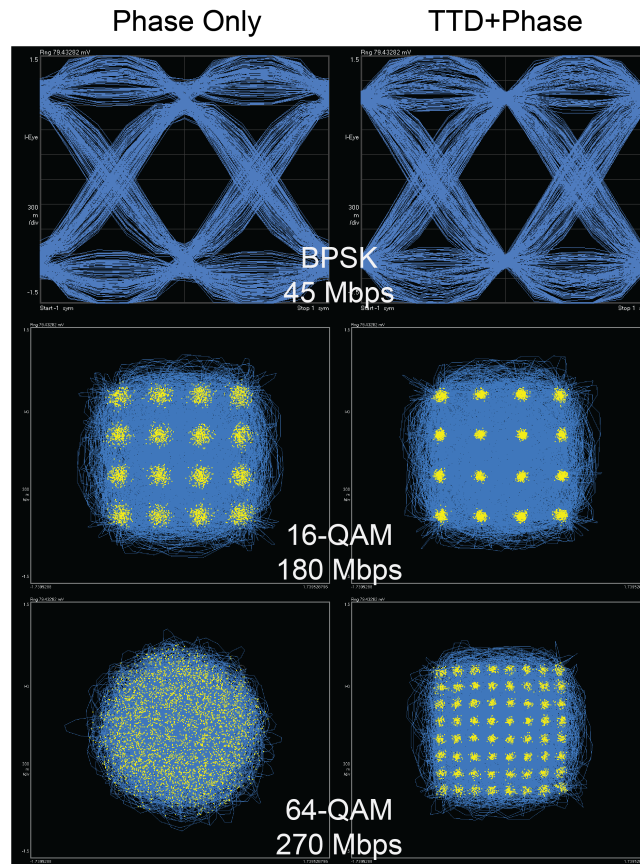


Figure 3.25: Received eye diagrams/constellations for BPSK, 16-QAM and 64-QAM at 45 Msps with beamforming achieved via phase-only steering (left side) or true time delay (TTD) and phase steering (right side).

Dual Beam Demonstration

The true time delay capability within each branch can also be used to independently steer beams at two different frequencies. A phased array forms a beam when the phases of the signals radiated by each element in the array match in the desired direction, creating constructive interference. A dual beam array requires this constructive interference to occur in two desired and potentially arbitrary directions at two different frequencies. Programmable true time delay allows for the phase response slope (group delay) of an element to be changed, while a programmable phase rotator changes the phase response offset or intercept. In the previous measurement, we used these two degrees of freedom to match the offset and slope of multiple branches over a band of frequencies to prevent ISI, but they can also be used to match the phase response of the branches at one frequency in one direction and another frequency in another direction. This in effect creates two independently

controlled full power beams from the array.

To demonstrate the dual beam capability, the test set-up shown in Fig. 3.26 was built. A 4 branch scalable router is radiatively excited by an antenna connected to one port of a VNA, the re-routed signal is measured by an antenna which is connected to the other port of the VNA and mounted on a linear scanning platform. The transmit antenna is 25 cm from the center of the scalable router, slightly offset beneath it. The receive antenna (mounted on the linear scanner) is 55 cm from the center of the router. The dual beam capability of the scalable router is demonstrated by maintaining a broadside beam at 24.9 GHz while simultaneously steering a beam at 25 GHz to three different locations (center, left and right). The steering positions are separated by 5 cm (close to 5° off the broadside direction) and are chosen in order to stay within the grating-lobes caused by the transmit antenna pitch of 5.5 cm.

Fig. 3.27 shows the measured S_{21} phase for all branches for the configuration where the 24.9 GHz beam is steered broadside and the 25 GHz beam is steered left. The phase is measured at two locations: broadside and the position corresponding to the left steered beam. The constructive interference responsible for beamforming is evident by the matched phase for all elements at 24.9 GHz for the center probe position and at 25 GHz for the left probe position. Fig. 3.28 shows successful steering of the beam at 25 GHz while the broadside beam at 24.9 GHz stays constant. The left and right steered traces have been trimmed to prevent grating lobes (at $\sim 15^\circ$ away) from appearing on the opposite side. Static reflections caused by other objects near the set-up were measured separately and subtracted from the presented results.

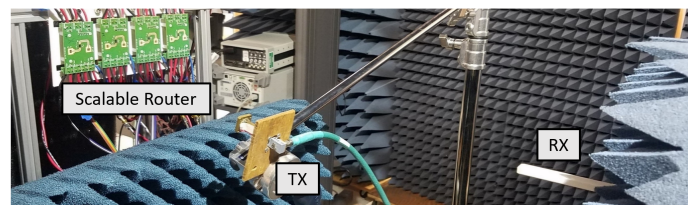


Figure 3.26: Dual beam test set-up. TX and RX antennas connect to VNA. RX antenna is mounted on a linear scanner.

In order to arbitrarily steer beams at two frequencies the branch circuits must be able to change their relative phase to any value from 0 to 360° . Since our system accomplishes this relative change using time delay, the period of the minimum frequency separation of two frequencies that can be fully independently steered is

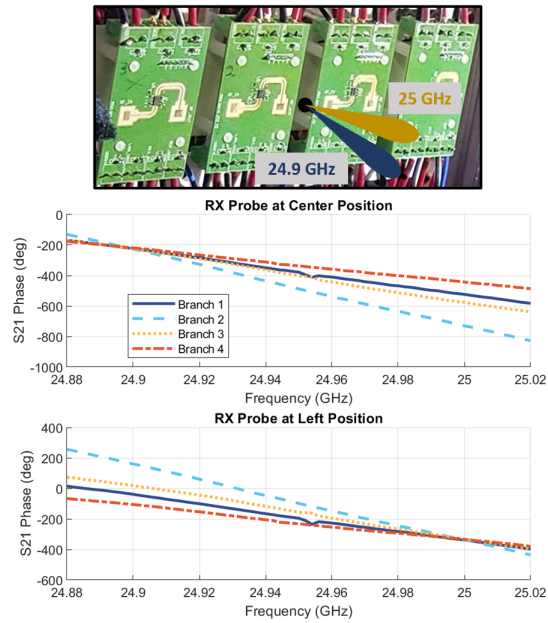


Figure 3.27: Branch phase responses measured at the center and left RX probe positions for the router digital configuration which steers 24.9 GHz to the center and 25 GHz left.

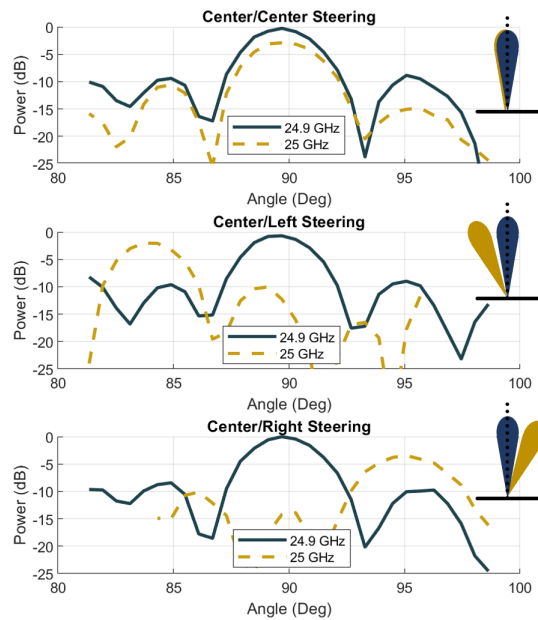


Figure 3.28: Measured patterns at 24.9 and 25 GHz for three different steering configurations. Demonstrates simultaneous, independent control of two receive/transmit beam pairs. The powers are normalized to the same global maximum occurring on the 24.9 GHz beam during center/center steering.

the maximum achievable time delay. Thus 100 MHz separation is the smallest achievable for 10 ns of delay control.

Given the obvious advantages of a single array serving multiple users, multi-beam microwave communication systems have been an active area of research for several decades. An overview of state of the art multi-beam approaches as of 2017 can be found in [68]. When considering the wide variety of approaches and subsequent trade-offs direct comparison between systems is not always apt. Dividing a larger array into independent sub-arrays is a common technique usable with no additional hardware but it divides power and aperture between the beams. The following array hardware paradigms (as well as the scalable router dual beam capability) achieve multiple beams without sacrificing power in the beams.

A well established family of multi-beam systems is multi-port passive (or semi-active) networks used to create a predetermined set of beam patterns. These arrays can be transmit or receive, have been fully integrated [26], and can create a multitude of beams at the cost of design complexity. However, these arrays are not electronically steerable and require separate input drivers to achieve their multi-beam capability.

Another common family of multi-beam arrays are the digital arrays, which process the same received signals in several parallel channels [76] [116]. While these systems can create as many steerable beams as processing power and time are available, the topology has only been shown for receive arrays, not transmit arrays. Furthermore, there can be dynamic range limitations due to the analog-to-digital conversion process.

The scalable router dual-beam capability (enabled by programmable time delay) differs from the previously described paradigms as it derives its two beams by “frequency multiplexing” the array. By tuning the phase response of the element’s at two frequencies, two independent beams are created. It should be noted that transmit dual beam capability is not unique to the scalable router architecture. While programmable true time delay means the router is naturally suited to the task, any transmit array with independent phase and group delay control within each element could achieve it. Because this control is established through analog circuits at baseband it can be used for transmit or receive arrays. Programmable time delay only grants a second beam to control, but additional degrees of freedom for controlling the element phase response could be added.

While each existing approach has distinct disadvantages, the next section presents a filter based approach to provide multiple full-power, electronically steerable, receive and transmit capable beams.

3.5 Multiband Scalable Router

Motivations and Design

This subsection presents a scalable router at 28 GHz, demonstrating for the first time, 3 independently and simultaneously steered receive and transmit channels with independent true time delay control of each channel. Frequency-domain multiplexed (FDM) simultaneous beams allow a scalable router to serve multiple users while utilizing the full potential of the array's gain and aperture size. Critically, with independently controlled FDM beams, a system can provide separate data streams to users who are physically close together without issues that emerge for systems which provide beams that are only spatially multiplexed. While several spatially multiplexed multi-beam integrated phased array receivers have been shown [100] [53] (including with true time delay [76]), the FDM and spatially multiplexed multi-beam transmit capability is unique. Integrated FDM transmit capability without true time delay control was shown in [44] and [186]. Non-integrated solutions such as butler matrices and other fixed beam-location matrices possess transmit multi-beam capability with limitations. The presented fully integrated system demonstrates 3 independently steered FDM receive/transmit beam pairs each with true time delay, enabling array scalability with a total measured data rate of 625 Mb/s, as well as FDM and spatial multiplexing for robust multiple-user access. This capability is enabled by double action N-path filters within each frequency channel. These fully passive N-path filters provide separate time and phase delay control and inductorless higher order filtering, with tunable center frequency and bandwidth.

The system architecture of the presented integrated circuit is shown in Fig. 3.29. The received signal to be re-directed is first amplified by an LNA, and then is down-converted by a 28 GHz LO signal. The down-converted signal is processed by 3 separate baseband channels. The baseband channels filter the signal by frequency and provide programmable amplitude and timing control. The outputs of each channel are summed together then up-converted. At 28 GHz, an IQ summer, driver, and power amplifier (PA) complete the output path. The chip includes two separate branches which share LO generation and reference distribution circuitry. The LO generation circuitry uses a 1.75 GHz reference to generate 28 GHz IQ LO signals and 3.5 GHz IQ signals which are used in the baseband circuitry. Because

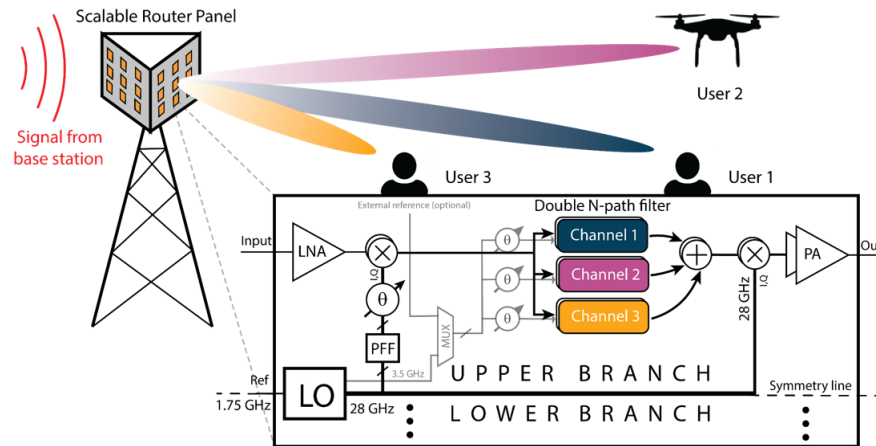


Figure 3.29: Multi-beam scalable router use-cases and integrated circuit architecture. The 3-channel, 2-branch integrated circuit is symmetric about the reference distribution lines.

up-conversion and down-conversion are performed using the same LO, multiple integrated circuits do not need to share a timing reference to perform beamforming. 3.5 GHz differential I and Q signals are tapped from the LO generation circuitry and are used to feed vector sum phase rotators which provide tunable clock signals to the baseband N-path filter circuits. To independently and simultaneously steer multiple receive and transmit beams over a large/spatially separated array aperture, both wideband phase and true time delay control are required, as well as channel discrimination in the frequency domain for single-wire FDM. Minimizing circuit resources via multi-function reconfigurable stages and a passive implementation that is amenable to CMOS scaling is also desirable. In this work, a baseband architecture that uses N-path filters with a combination of both discrete-time (DT) and continuous-time (CT) filter kernels can accomplish the above requirements and is shown in Fig. 3.30.

It has been shown in [132] that a two-port N-path filter with delayed input and output sampling clocks can behave as a BPF with embedded narrowband phase shifting, when the CT LPF kernel is operating in the averaging mode. The phase shift is however a narrowband approximation of a time-delay, and in the presence of wide channel bandwidths does not provide the independent phase and group delay control that multi-channel scalable routers require. To alleviate this issue, if the CT LPF kernel is replaced by a DT equivalent, wideband phase shifting via delayed input and output sampling clocks on the N-path filter can be accomplished. This is because the DT LPF continues to process and filter the signal when the input sampler switch

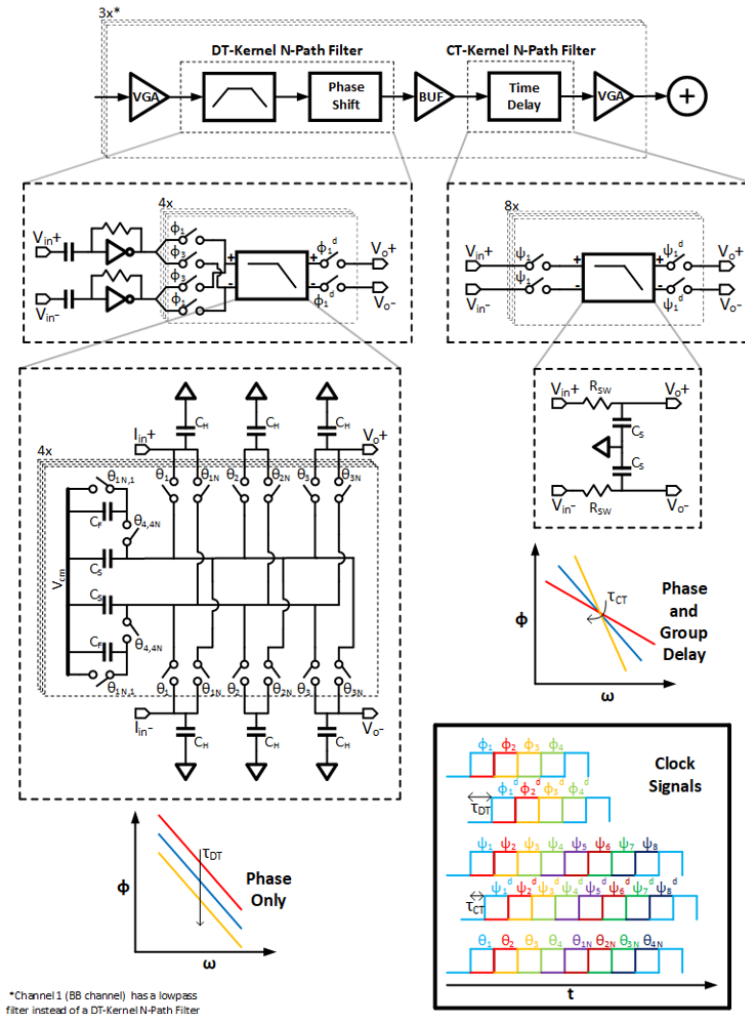


Figure 3.30: Baseband architecture that performs filtering, phase shifting, and true time delay with two different N-path filters.

is open, effectively performing filtering action on a gated signal. The situation is analogous to a block diagram cascade of a LPF in between two gating functions with phase offsets in their gating signals, which provides a wideband phase shift. This is not true for the CT kernel case, since the CT path does not continue to process the signal once the input sampler switch is open—the output is effectively “frozen and waiting” to be sampled by the output sampler switch, resulting in a time delay. To achieve passive, high-order, reconfigurable bandpass filtering with embedded wideband phase shifting, a switched-capacitor LPF is used as the DT LPF kernel. A global feedback is applied around a cascade of real poles via the use of the differential paths [103]. To allow for higher than second order filtering with no peaking, the implemented DT LPF reduces the feedback factor via charge sharing

action in capacitor CF. The implemented third-order filter has close to Butterworth roll-off with no passband peaking. The DT LPF kernel is placed inside a 4-path N-path filter with differential sampling to eliminate the even harmonic response. The filter center frequencies are at 218.75 MHz and 437.5 MHz, and were designed to have 80 MHz of bandwidth. Due to the DT LPF kernel, both the center frequency and channel bandwidth are, in principle, independently tunable by only varying the clock frequency—in this work, however, all clocks are generated from the same source with fixed divider ratios. The true time delay unit consists of a CT kernel N-path filter that is operated in the sampling mode, i.e. $NR_{sw}C \ll T_s$. The sinc-profile magnitude response (ideal sampling) of the time delay unit causes an equilizable roll-off in the third channel, as seen in Fig. 3.31.

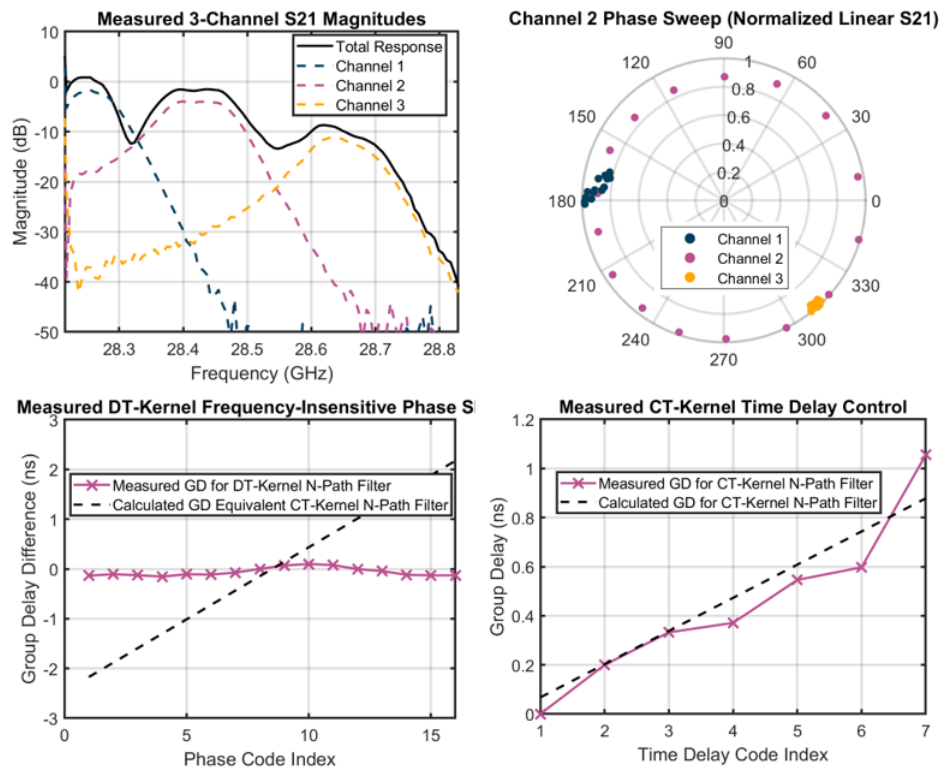


Figure 3.31: The 3-Channel response, individual channel response and channel 2 phase and time delay control are shown for a single branch. Double N-Path filter accomplishes independent phase and time delay control. Channel 2 phase sweep isolation is also shown.

To verify the proposed double N-path filter architecture, Fig. 3.31 shows a coarse phase sweep of the middle channel and its effect on the phase of adjacent channels—the channel isolation is >15 dB. The effect of the phase sweep on the group delay is shown and contrasted with the expected variation for the CT kernel equivalent. The

minimal group delay change supports the proposed architecture, decoupling phase and group delay variation. A coarse sweep of the CT kernel N-path filter also agrees with theory.

Multi-band Scalable Router Prototype

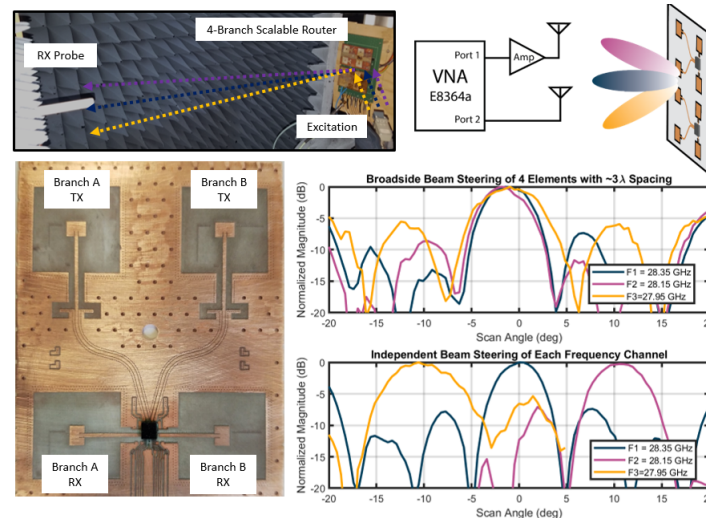


Figure 3.32: Branch scalable router demonstrating simultaneous, independent steering of three beams. Two separate patch antenna circuit boards are used to form the 4-branch router which is excited by a vector network analyzer (VNA). Channels 2 and 3 have had their grating lobes removed in the independent steering to improve readability.

A two chip, four branch radiative scalable router was constructed. The circuit board, measurement set up, and beam-steering demonstration measurements are depicted in Fig. 3.32. Patch antennas are placed at a pitch of 3λ , with the transmit and receive antennas orthogonally polarized. A source antenna illuminates the scalable router which re-radiates the signal towards a probe antenna mounted on a mechanical linear scanning track. The three beams are simultaneously and independently steered: shown steered to broadside and steered to offsets of 12 degrees. The two chips do not share a common frequency/phase reference but still perform coherent far-field combining. This capability, vital for router scalability, is granted by the system architecture which uses the same LO for down-conversion and up-conversion. A data transmission demonstration is shown in Fig. 3.33. The channels are used to transmit 32-QAM at rates of 250 Mb/s, 275 Mb/s, and 100 Mb/s for each of the three channels. These data streams are simultaneously and independently steered by the scalable router and are not post-equalized. The presented integrated circuit uses a novel double N-path filter architecture to enable simultaneous FDM beams within

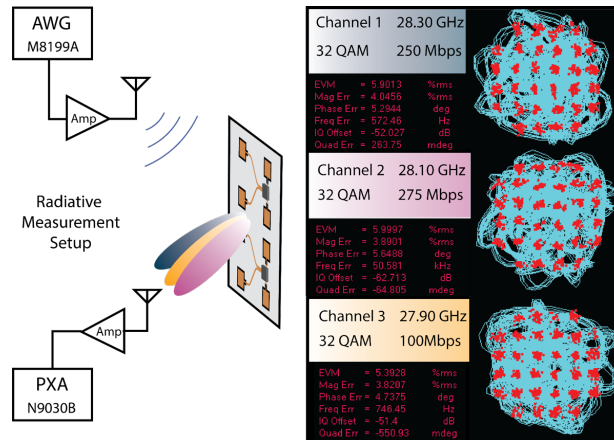


Figure 3.33: Radiative demonstration of simultaneous 3-channel data transmission using 4-branch router.

a scalable router. A 2-chip, 4-branch, scalable router operating without a shared timing reference is used to perform far-field beam-forming and beam-steering and demonstrates wireless data transmission of 600+ Mb/s. The RFIC is shown in Fig. 3.34.

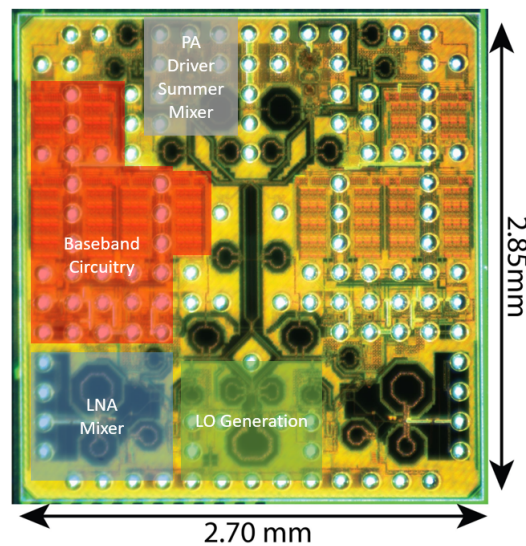


Figure 3.34: Micrograph of multi-beam, two branch integrated circuit.

LARGE SCALE FLEXIBLE ARRAYS

4.1 Introduction

Increased aperture is one of the fundamental advantages of phased arrays over many other antennas.¹ More aperture allows the array to concentrate more power in a narrower area. With sufficient imagination any surface area could potentially be utilized as aperture for an array. Array architectures that unlock new surfaces are a step towards a future which arrays are ubiquitous. Flexible surfaces or surfaces otherwise undergoing mechanical change are a promising area for array development.

Mechanical flexibility introduces considerable challenges for phased array designers. Radio frequency designs involve conductors whose size is comparable to that of the signal wavelength, almost by definition [127]. When these conductors are deformed their field profile deforms as well, causing path length changes, impedance changes, reflections, pattern deformation, and a variety of other potential issues. Given the complexity inherent in phased array systems, it is understandable that RF designers almost always avoid flexibility altogether and opt for flat, rigid profiles with $\lambda/2$ separated radiators. Historically, when low aerodynamic profile, non-planar shapes are needed for aerospace antennas, rigid and statically conformal non-flexible antennas are designed which are suited for a single application and use scenario [11] [39] [82] [51] [86].

While flexible phased arrays are still in their infancy, the broader field of flexible electronics is highly mature. Today's flexible systems use off-the-shelf short-range low-data-rate radio modules (e.g., Bluetooth) and rigid ceramic chip antennas [180] [139] [162] [182] [71] [179]. These RF transceivers lack high gain electronically steerable beams with spatial selectivity, which have become the central feature of

¹Florian Bohn, Behrooz Abiri, Matan Gal-Katziri, Mohammed Reza Hashemi, Ailec Wu, Oren Mizrahi, Alex Ayling, and Mohith Manohara worked on the Caltech Space Solar Power Project and contributed to the concepts, prototypes, and measurements that appear in the Caltech Space Solar Power Project section. System level concepts and prototypes were developed with the Pellegrino Lab and the Atwater Lab. Richard Madonna and Damon Russell also contributed as advisors to the project. The Caltech Space Solar Power section is partially adapted from the material in [54], [88], [62], [105], and [48]. The co-cure fabrication of the pop-up dipole antennas was developed and implemented with Alan Truong, Fabian Wiesemüller, and Eleftherios Gdoutos of the Pellegrino Lab. The material presented in the Flexible Array Shape Reconstruction Section was performed in collaboration with Oren Mizrahi. This chapter is adapted from [42].

emerging communication systems, such as 5G. Future flexible systems could benefit from the orders of magnitude higher data rates and incorporation of microwave ranging, sensing, and power transfer functions. A new design paradigm is needed in order to close the functionality gaps between flexible and rigid RF communication, sensing and ranging systems. Lightweight, dynamically flexible radiating arrays are a promising candidate to answer this challenge. 4.1 presents a variety of flexible phased array concepts and prototypes.

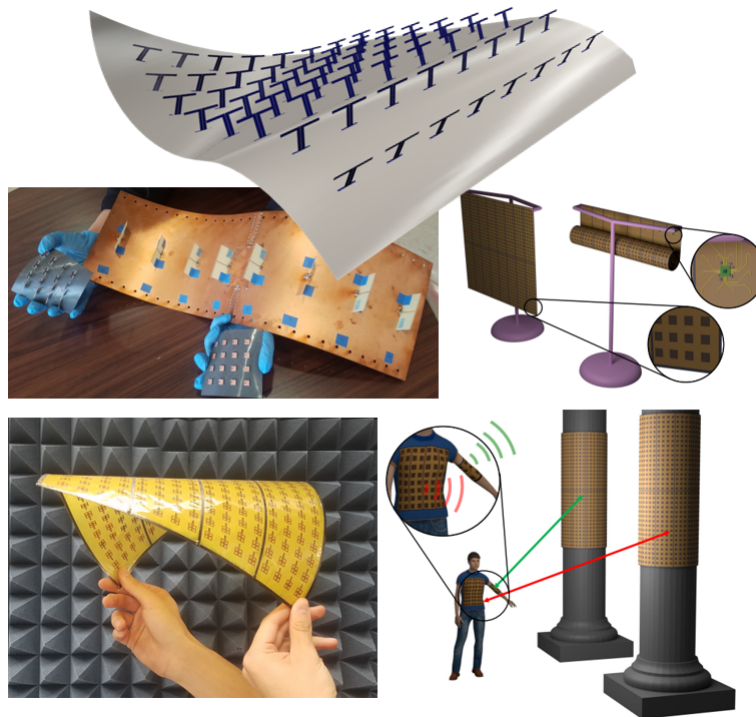


Figure 4.1: Flexible Phased Array Concepts and Prototypes.

Lightweight, dynamically flexible arrays enable significant increases in effective aperture, as they can be used on surfaces and in applications that would not be considered for conventional arrays. Many flexible array applications require deployability and/or conformality. Deployable arrays are sufficiently flexible or jointed such that they can be compactly stored when not in use and then unrolled or unfolded to offer a large aperture when in use. Deployable arrays are under consideration for ultra-large arrays for wireless power transfer in space [62] [134], but could also find use as rapid set-up/take-down communication relays for large events (concerts, conventions, etc) or disaster relief/emergency situations when existing infrastructure is damaged. Alternatively, flexible conformal arrays can create useful apertures on surfaces undergoing constant shape change such as the human body (wearables) or

fit on variously shaped surfaces. A single flexible array design can also be used on several different rigid non-planar surfaces without requiring an additional design cycle to account for specific curvature. For many airborne and space-borne applications, the low mass of flexible arrays is also a boon. Commercial, mechanically steered, low profile antennas for aerospace offer a 30 cm aperture at 5 kg (5.5 g/cm^2) [165], while flexible phased arrays have been reported at 0.1 g/cm^2 [62]. For emerging high altitude platforms [30] [106] such as Airbus Zephyr [75], which aspire to provide internet access during months-long stratospheric flights, even a few kg is a significant fraction of total vehicle weight (75 kg) and any reduction in weight increases flight time and available electrical power.

In this chapter we will discuss the design and operation of flexible phased arrays. First, we will describe the large-scale ultralight, wireless power transfer arrays designed for the Caltech Space Solar Power Project. Second, we present a method for determining the shape of flexible arrays, a critical step in their proper use. Prior to the discussion of our work on large-scale space arrays, we will take a brief moment to discuss typical, existing microwave antennas for space applications.

Existing Space Antennas

Microwaves have long been the go to medium for spacecraft guidance, telemetry, and communication. While optical communication with satellites is receiving increased attention [140], microwaves are unlikely to be unseated as the go-to choice. Low atmospheric absorption, wide availability, low cost, and highly durable generation and reception circuitry, options for both omni-directional and directional radiation, and substantial existing infrastructure in ground stations and flight heritage are compelling reasons for the past, present, and future use of microwaves in space.

Large scale, flexible, deployable arrays represent a significant deviation from previous and existing space microwave antennas. In order to present a complete story, existing systems will be explored in this section.²

The simplest antennas for space systems are low-gain, omni-directional radiators [13] [92]. These antennas allow for transmission and reception without control of the spacecraft's orientation. Some designs achieve omni-directionality using multiple antennas to cover directions blocked by the body of the spacecraft [27] [32]. Higher gain antennas ease requirements on other components in the link and can allow higher

²Several of the example antennas described in this subsection as well as a survey of other existing satellite antennas can be found in [130].

bandwidth channels but must be pointed in the intended direction of radiation. A conventional high-gain antenna requires use of flywheels or other inertial systems to turn the entire spacecraft. Gimballed antennas have been used [50] but also require use of inertial systems to compensate for their angular momentum during steering.

High gain antennas require large apertures. At a point the aperture may exceed what can easily be mounted onto a spacecraft. To overcome this practical limitation, a variety of deployable antennas have been demonstrated [2]. These include mesh dish antennas [24], inflatable arrays [79], and unfolding reflectarrays [66]. These deployable apertures provide high-gain patterns but still require mechanical steering. Electronically steered arrays (ESAs) can rapidly steer beams without effecting satellite pointing. ESAs are also highly desirable for scientific missions as they allow other concerns (such as the primary scientific instrument) to determine spacecraft orientation. They have seen prior use in communication networks but are expected to see a dramatic increase in usage as satellites become integrally tied into planned 5G/6G networks [112] [95] [115]. Published space ESAs are not deployable, meaning they are limited to aperture sizes less than the dimensions of the spacecrafts un-used surfaces.

The flexible phased arrays described in this chapter have the potential to combine the benefits of a deployable aperture and ESAs. An array would be compactly stored in the spacecraft until the payload is delivered to its desired orbit, where it would deploy and begin operation. In space, there is essentially no limit on the volume a flexible or multi-faceted arrays could deploy into. Provided the nuances of reliable mechanical deployment as well as element drive and synchronization are adequately handled, array apertures can be expanded until the beam is too narrow to be properly steered or until time delay correction of data coherence needed. Since arrays are typically single-sided they are also prime candidates for integration with other area intensive subsystems such as photovoltaics or sensing instruments. While large scale flexible phased arrays have a variety of terrestrial uses, the emptiness of space is especially fertile ground.

4.2 Caltech Space Solar Power Project

Introduction to Space Solar Power

“Space solar power” describes a variety of proposed systems for collecting solar power in space and then beaming it to earth for terrestrial use. The need for clean, renewable power on earth requires little explanation. However, the justifications

for generating that power in space are more opaque. Locating photovoltaics in space avoids the major disadvantages of terrestrial solar energy collection such as intermittent availability (i.e. day-night cycle) and influence by changing weather conditions. Clean, renewable power could be continuously available and potentially sent to any location on Earth. Significantly more power can be collected in space than on Earth due to constant direct access to the sun and the absence of losses due to reflection and absorption of solar energy by the Earth's atmosphere.

The vision of orbiting power stations 100s of km wide is straight from science fiction [9]. If completed, a space solar power system would be as or more impressive as any man made wonder of the world. Despite the lofty aspirations of the concept, space solar power systems must bow to economic reality. While it easy to be romantic about this vision, in order to merit the considerable intellectual and financial capital needed for construction, a space solar power system must be able to deliver energy to a location at a power level and price that is competitive with alternatives.

The Caltech Space Solar Power Project is a collaboration between the Caltech Holistic Integrated Circuits Lab (CHIC), the Pellegrino research group, and the Atwater research group. CHIC focuses on the development of the microwave wireless power transfer subsystem, the Pellegrino group focuses on deployable space structures and mission planning, and the Atwater group develops large-scale space-ready photovoltaic technology.

System Architecture

Economic viability is the primary driver of our system architecture. We aim to maximize the power delivered to earth for a given cost. The dominant factor in the project cost of a space solar power system is the cost of launch vehicles for delivering a massive spacecraft array into orbit [47]. While launch costs have fallen considerably in past two decades, another substantial drop would be needed before another cost becomes the leading factor.

Minimizing cost means maximizing the deployed spacecraft area per launch. Given this motivation, our architecture is centered around deployable spacecraft which maximize area for a given stored volume and mass. The goal of a maximizing surface area for volume and mass naturally leads to a flat sheet system. Flat sheets can be compactly stored by folding or rolling. The proposed packaging concept in shown in Fig. 4.2a.

Before we discuss the wireless transfer of power to earth, there is an additional

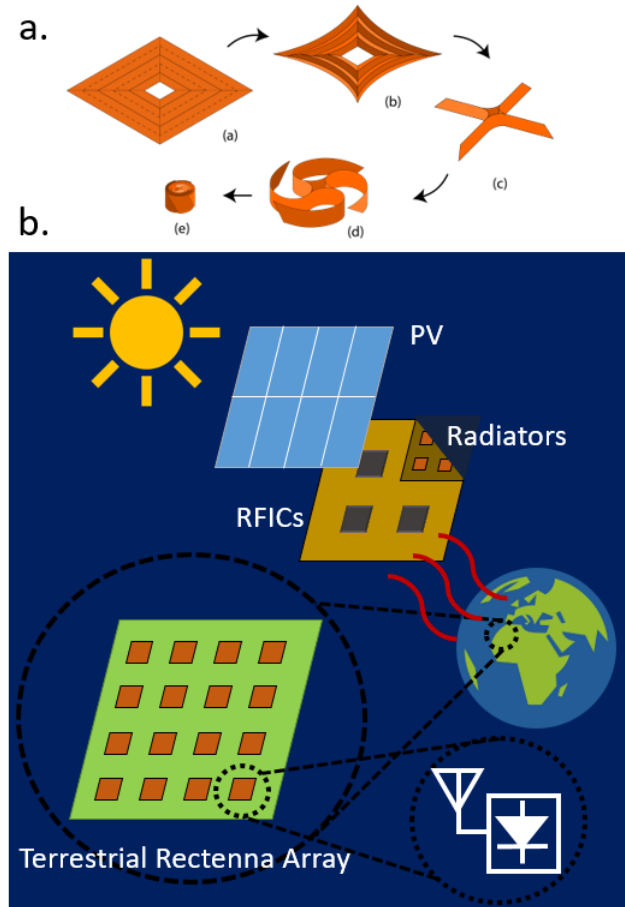


Figure 4.2: (a) Caltech Space Solar Power Project folding concept. (b) System architecture.

power transfer step that must be discussed. The transfer of DC power from the photovoltaics to the subsystem which beams the power to earth may seem mundane but is critical when considering the overall weight and flexibility of the system. DC current carrying lines at lengths of 10s of meters (let alone 100s of meters) are either lossy, heavy, or rigid. As such, our architecture adopts a distributed philosophy that power should be radiated as close as possible to the point where it is collected. A microwave phased array is the natural solution, with the distributed philosophy as the entire solar energy collection aperture can be used to coherently combine the power on earth and provide electronic steering. Microwave phased arrays complex requiring many digital, analog, and RF circuits to perform their functions. The high level of complexity density offered by integrated circuits is absolutely vital maintaining the light weight and flexibility needed for economic viability. The microwave beam of the spacecraft array is steered at power harvesting basestations.

These basestations have large scale rectenna arrays which convert the microwave power to widely useable DC power. Fig. 4.2b illustrates our system architecture and its motivations.

The operating frequency of the architecture is adjustable but intimately tied to size and operation of the array. The upper frequency limit is set by atmospheric propagation loss. Fig. 4.3, reprinted from [134], shows atmospheric loss vs frequency. At 20 GHz propagation loss has risen to around 1 dB, which is an arbitrary but plausible upper limit for atmospheric loss in the system budget and frequency.

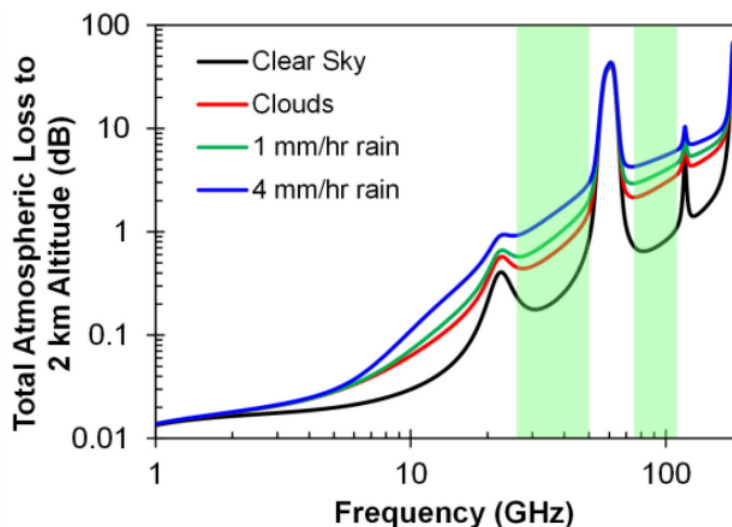


Figure 4.3: Atmospheric loss for 45° line of sight from sea level. Reprinted from [134].

Frequency of operation ties together the collection/transmit area of the spacecraft and the size of the receive area on the ground. To illustrate this point we can construct an exemplary system to analyze. We choose 18% PV efficiency and 33% RF efficiency including incidental losses between the subsystems which are realistic numbers based on our laboratory prototypes. With these efficiencies 6% of the incident solar power reaches the earth as microwave energy. In this scenario we choose a large terrestrial basestation which will be designed to capture all of the power in the first lobe of the radiated beam. The area inside the first null contains close to 84% of the total power which brings our efficiency to 5%. The distance to the first diffraction minimum on the ground, D , is given approximately by:

$$D = 1.22 \frac{R\lambda}{d}. \quad (4.1)$$

R is the distance to the spacecraft, λ is the wavelength of operation, and a rectenna efficiency of 60% brings the final total system efficiency to 3%. The useful power on the ground is given by P , in the equation below:

$$P = I * \eta * \pi * (0.5 * d)^2. \quad (4.2)$$

I is the solar intensity (1.36 kW/m² broadside) and η is the end to end system efficiency (3%). Fig. 4.4 shows the size of the ground segment needed to receive the transmitted power for a range of space system sizes. On the right axis, the useful power after rectification is also plotted. From this plot it is clear that both the space and ground segment would be close to several km in diameter. The parameters we have defined are for capturing and transferring as much power as possible. A space solar power system can also be used to deliver power to remote or other wise challenging locations without the goal of capturing as much radiated power as possible. This partially decouples the ground segment size from the space system size.

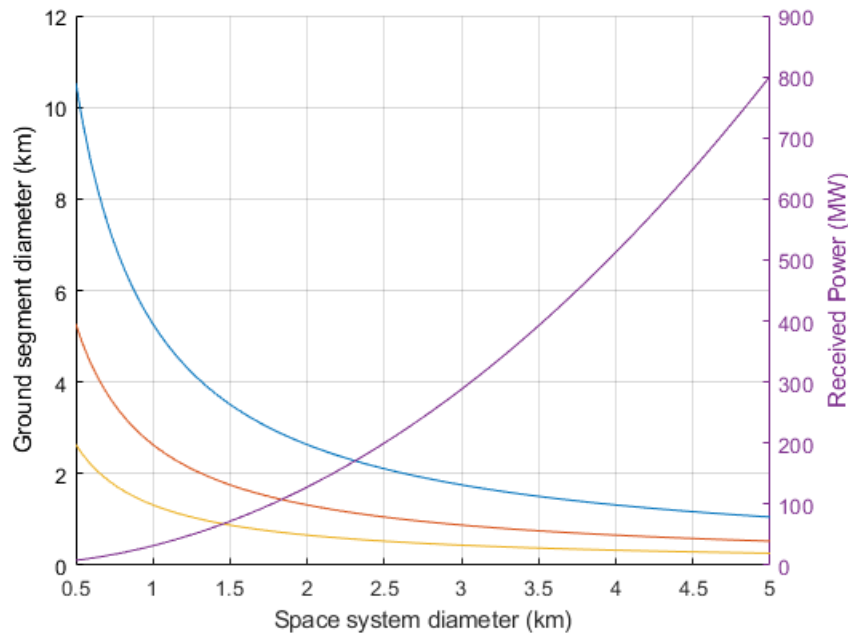


Figure 4.4: Size of ground segment needed to capture 84% of radiated power vs size of space system. The useful power after rectification is plotted on the right axis.

There are other implementation specific frequency concerns. Lower frequency systems require larger element antennas. This extra size is particularly challenging in the “depth” dimension, as the architecture calls for a minimally thick sheet. While

lightweight pop-up radiators are presented in this work, their design becomes more challenging at lower frequencies. Frequency choice also has complex implications for the radio frequency integrated circuit. While the performance of on-chip actives is worse as frequency increases, on-chip passive Q-factor increases. Given a fixed antenna pitch of 0.5λ , the power available to drive each element increases as frequency falls. This increase in power causes trends towards lower numbers of channels per RFIC. Too many channels at a lower frequency reduces the DC power distribution advantages of the distributed architecture and concentrates more waste power in each RFIC, making thermal management more difficult. No matter what frequency is chosen for a complete system, substantial spectrum allocation regulatory challenges will be present. We chose 10 GHz as the operating frequency for our prototypes.

In Fig. 4.4, total size is the independent variable, reflecting a lack of a planned fixed size for the system. Our distributed architecture is intentionally scalable and size agnostic. The collection and emission area can be scaled as needed. While there is a practical limitation on individual spacecraft size, our architecture supposes a formation of space solar power spacecraft which can be added to or replaced as needs and opportunities evolve.

The array prototypes presented in this thesis are intended to collect solar energy on one side and radiate it on the other side. We call this the “single-sided” approach. The single sided approach is simplest system, lowest areal mass, and allows for isolation of the two subsystems. However, our architecture also allows for a “dual-sided” approach in which each side of the space craft can collect solar energy and radiate microwave power. The dual-sided approach increases the total power delivered to earth by avoiding a dead-zone in the orbit when one side of the array faces both the earth and the sun. It should be noted that only one face of “dual-sided” implementation needs to have RF and PV functionality to prevent this dead-zone. This leads to a design decision about which subsystem should be on the unshared side (PV+RF/PV or PV+RF/RF). Initial investigations suggest PV+RF/PV is preferable given the complexity of implementing shared control and timing infrastructure for the RF subsystem.

Our distributed architecture has many advantages but does present considerable implementation challenges. Photovoltaics which are flexible, can survive the radiation and thermal environment of space, and are low cost are challenging to develop. Additionally, the photovoltaic manufacturing process and materials must be scal-

able to the volume needed to produce 100s of km² of area. For the RF subsystem, array synchronization and element phase control is a monumental task. Finally, the proposed formation flying and spacecraft control is significantly more complicated than anything that has yet been demonstrated.

The term “Space Solar Power” almost always refers specifically to systems which exclusively transfer power to earth. However, there are several other space applications for the same technology. A system intending to deliver power to equipment on the moon has been considered as well as systems for missions into deep space. These systems do not have the same economic competition and viability concerns as terrestrial power.

While the three subgroups of the Caltech Space Solar Power Project collaborate closely, the author has worked primarily on the wireless power transfer subsystem, as such that subsystem is the primary focus of the remainder of this chapter.

Wireless Power Transfer Integrated Circuit

The implementation of phased arrays on physically flexible substrates is impossible without a drastic reduction in component count, compared to traditional designs. We utilize custom designed silicon RFIC transmitters as the main building block of our system architecture. Integrated circuits enable high complexity systems in lightweight, low profile form factors. This complexity density is a critical enabler of flexible arrays, as the mass and rigidity of the discrete components necessary for a phased array would be prohibitive. The presented RFIC, weighs 85 mg, and provides 16 channels of phase-locked 10 GHz signals with individually, digitally controlled phase amplitude, allowing the array to synthesize and steer custom beam patterns.

The presented RFIC is implemented in a bulk 65 nm CMOS process and provides independently controlled RF outputs with greater than 360° phase control over a frequency range of 9.4–10.5 GHz. The RFIC uses four identical quadrants to produce 16 outputs. The top-level circuit block diagrams are shown in Fig. 4.5d-e. A low-noise, low-frequency 50 MHz clock is distributed across and on each of the scalable array tiles and used as a reference for the frequency synthesizer (phase-locked loop, PLL). To reduce the PLL reference spurs, a loop filter switch similar to [183] is used with the PLL. The synthesized 2.5 GHz signal is used to further distribute a synchronized reference across the IC to 16 clock multiplier units (CMUs) with an output frequency of 10 GHz, each followed by a power amplifier (PA) with

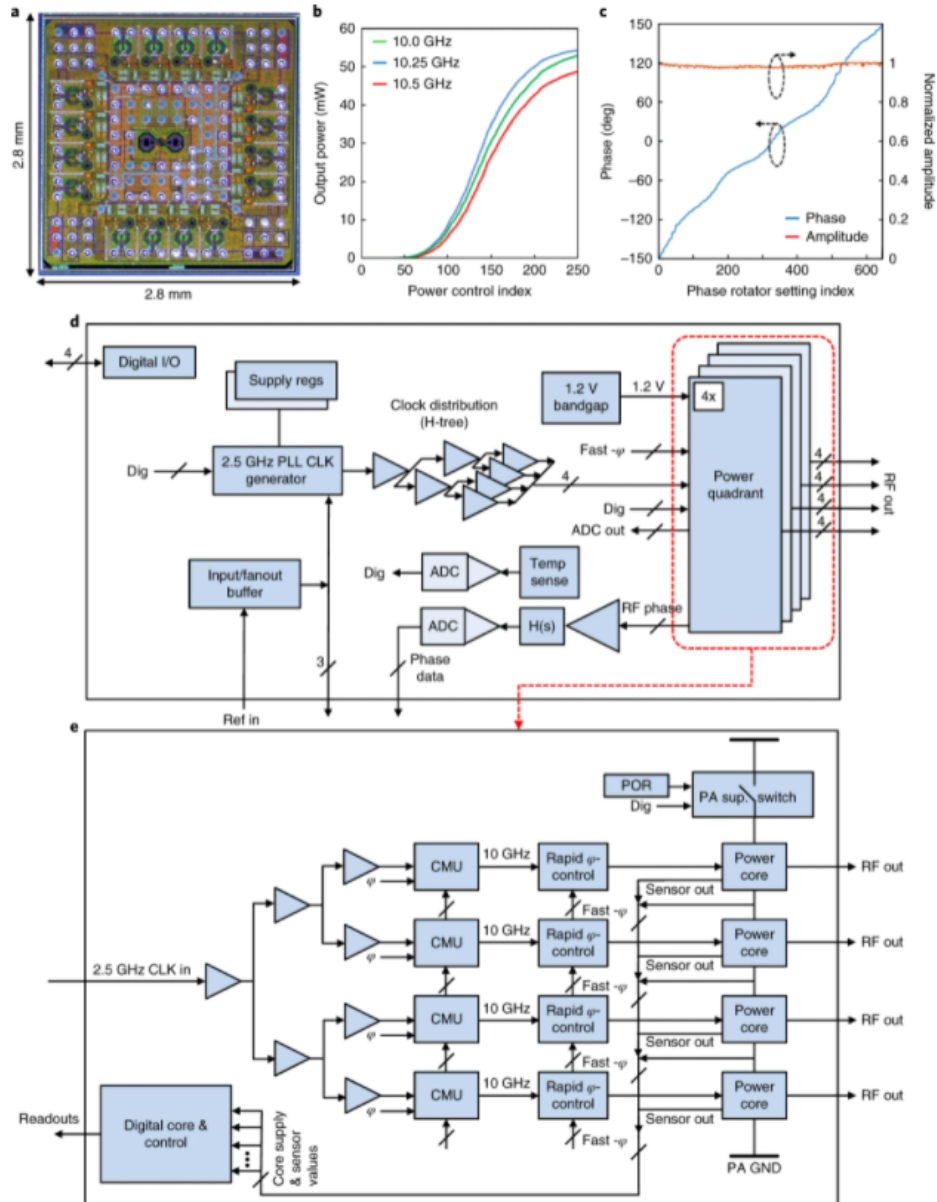


Figure 4.5: (a) Die photograph of the implemented RFIC. (b) Measured output power as a function of power control index. (c) Measured phase and amplitude of a PA versus phase rotator setting. (d) Block diagram of the RFIC architecture. (e) Block diagram of each power quadrant of the RFIC. CLK, clock; ADC, analog-to-digital converter; I/O, input/output; POR, power-on reset; CMU, clock multiplier unit.

peak output power of 17 dBm. This architecture has several advantages. First, the generation and distribution of a system-level clock is easier and consumes less power at lower frequencies. Second, the use of two frequency synthesizers allows for distribution of a 2.5 GHz reference across the RFIC, which reduces pulling between

the channels and lowers the power consumption. Third, the small multiplier of the CMU stage allows implementation of the phase shift inside the PLL. This is achieved by injecting a constant current into the CMU loop filter, which forces its output to have a phase that is offset compared to the reference. Although such a phase shift scheme affects the spurious tone in the output, the effects are insignificant in our case because the spur is located 2.5 GHz away from the carrier and out of the antenna bandwidth. To enable operation from the larger supply voltages, the power supplies of the four quadrant PAs are stacked to share the same current while dividing the supply voltage [20]. Sensors within each PA ensure stable voltage sharing among the PAs of the stack, compensate for temperature variations and monitor the system health during operation. This design allows each PA to generate up to 50 mW of output power at 10 GHz with a power-added efficiency (PAE) of 37%, which is independent of the output phase set by the CMU. A die photograph of the implemented RFIC is shown in Fig. 4.5a.

Several iterations of RFIC have been created throughout the project history. While the version described above uses a 4-stack of current sharing PAs, a 2-stack version was also created and used extensively. Changing the stack allows the RFIC to operate at different supply voltages. This flexibility has been important for the project as a variety of photovoltaic technologies with different operating points have been proposed. While the stacked PAs are decoupled from each other on chip, there are still coupling effects observed which increase for the higher stack count. These effects are minimized with proper thermal management. In later versions of the RFIC, two of the 16 channels possess self-sensing receivers which have been co-designed with the power amplifier, similar to [42] which showed a combined power amplifier and self-sensing receiver circuit that was not integrated into a multi-channel chip. These receivers can be used to perform reflection sensing for phase calibration and shape estimation purposes.

The RFICs are mounted to rigid multilayer interposers, which provide the trace fan-out necessary for interfacing with fine pitch bumps, and are small enough not to limit the bend radius of the larger array. The interposer is shown in Fig. 4.5b.

The thermal performance of the RFIC is critical as high temperatures can lead to PLL/PA instability, lower efficiency, and less responsive phase control. Thermal management is a primary challenge in any spacecraft, especially so in our space solar power architecture. Because our scalable architecture creates an effectively “infinite” two-sided sheet, there is no opportunity for high thermal mass temperature reservoir

and little surface area available for thermal radiation. With all 16 channels running at full power, the presented design sees diminished performance without strong heatsinking. The present chip can be operated with 8 or 12 of the channels active to reduce heat. Future chips could be designed at lower overall power consumption (likely lowering the number of channels) to reduce the thermal burden.

Ultra-light Radiators

Large-scale deployable arrays need a new paradigm in antenna design. Planar antenna arrays are built on continuous sheets of thick, rigid dielectric materials that preclude flexible designs. The use-cases for flat flexible phased arrays typically require radiation from one side of the sheet and electrical isolation from the opposite side which could lay against a variety of conductive, non-conductive, or lossy materials. The presence of back-side objects should not disturb the antenna performance and any power radiated in this direction is wasted, or worse, creates interference with other parts of the system. Hence, directional hemispherical radiators are much preferred. Directional array antennas with modest bandwidth must have depth [91] away from the surface of the carrier printed circuit board.³ Creating this depth is one of the principle challenges of the flexible phased array designer. Mechanically, interfacing a 2D flat flexible circuit board with 3D radiators poses a significant challenge. The radiators must allow flexibility while remaining firmly attached to the flexible circuit board and maintaining their RF performance. In this subsection we present several ultra-light radiator designs which have been successfully built and tested.

Fractal Inspired Modified Patch Antenna

The first ultra-light radiator to be discussed is the fractal inspired modified patch (FIMP) radiator shown in Fig. 4.6. The FIMP is similar to a conventional patch antenna except it uses an air gap dielectric and has Sierpinski carpet inspired cutouts. The air dielectric avoids the mass of a rigid dielectric and allows the antenna sheet to be collapsed into the carrier board. After the gap has been collapsed, the array can be rolled, folded, and compactly stored. The cutout active metal area reduces mass of the antenna and allows for a slight shortening of the antenna dimensions. The radiator still operates based on the fringe fields at its two radiating edges with similar

³Leaky-wave transmission lines and other travelling wave antennas can create directionality without significant depth [102] but are too large to be realistically used in a 2D array with antenna pitch $< \lambda/2$.

performance as a patch. Each radiator consists of an edge-fed square metallic patch fabricated on a single polyimide/conductor layer placed above another conductive layer on polyimide with an air gap distance of $\lambda/10$ chosen. The lower conductor serving as a high-frequency ground plane is part of a multilayer flexible conductor and polyimide board that contains RFIC as well as signal and power distribution lines.

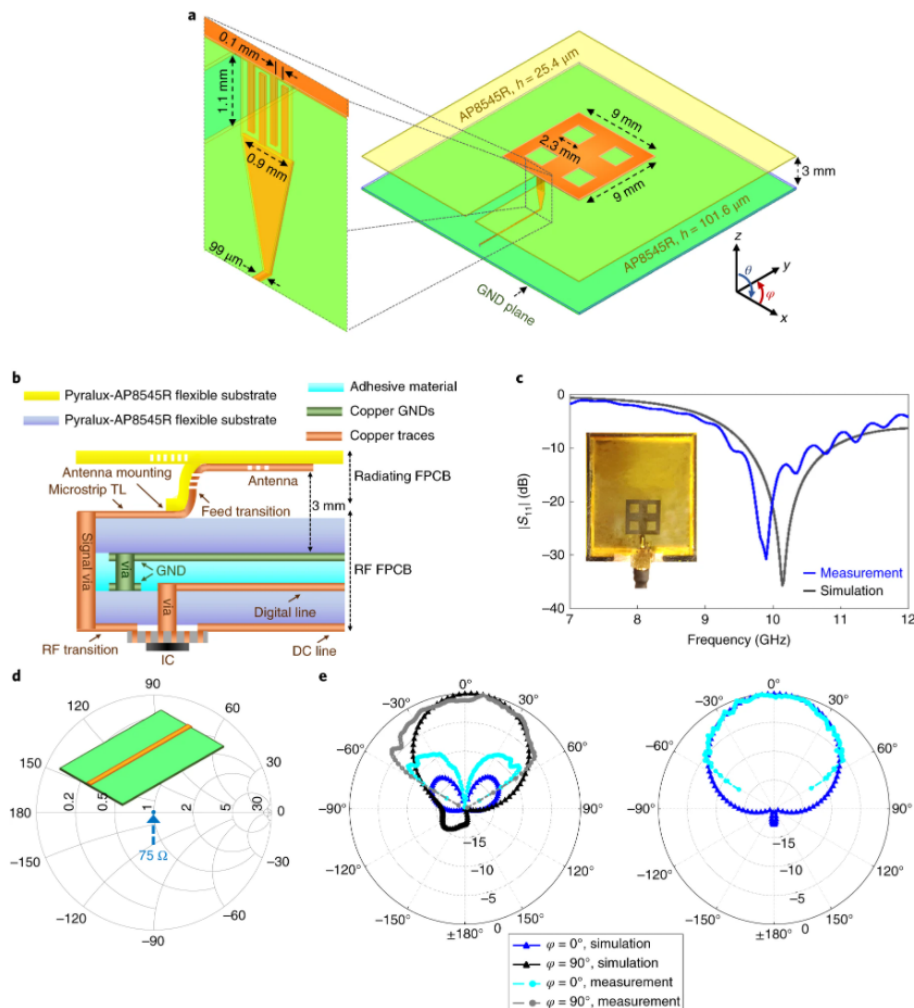


Figure 4.6: (a) Schematic of the radiator. (b) Cross-sectional view of the flexible layers stack. (c) Simulated (black curve) and measured (blue curve) return loss of the flexible radiator. Inset, top view of the working flexible FIMP radiator prototype. (d) Simulated impedance of the designed 75 Ω flexible transmission-line. Inset, the transmission-line configuration. (e) Comparison of simulated and measured radiation patterns along the E plane ($\phi = 90^\circ$) and H plane ($\phi = 0^\circ$) for E_θ (left plot) and E_ϕ (right plot) at the resonance frequency. GND, ground; FPCB, flexible printed circuit board; TL, transmission-line; IC, integrated circuit.

The 10 GHz drive signals are delivered to the FIMP using feed lines connecting the lower flexible board to the radiating sheet across the air dielectric. To achieve and maintain the collapsibility and high performance of the FPA, the collapsible antenna feedline has to be designed properly from both mechanical and electromagnetic perspectives. The direction and collapsibility of the feedlines must be consistent across the entire array for reliable rolling and wrapping. As such, feedlines tapping into the radiators must be oriented in the same direction. The FIMP radiators are therefore edge-fed by a collapsible ‘J’-shaped feeding transitions. The feed transitions connecting the radiator to the high-frequency transmission lines on the lower multilayer board consist of an interdigital capacitor connected to a tapered section. They provide a resonance impedance match between the radiators and the distribution lines. The capacitive loading of this matching approach also results in a smaller radiator (for example, $9 \times 9 \text{mm}^2$ at 10 GHz) at the same resonance frequency compared to a conventional half-wavelength patches. This collapsible radiator configuration results in a higher bandwidth due to larger spacing to the ground plane compared to conventional solid dielectric patch antennas, while significantly lowering the mass and stored volume.

The reflection coefficient of the driving port of a single radiator versus frequency is shown in Fig. 4.6. The simulated and measured results track closely, showing a reflection coefficient better than -30 dB at the frequency of interest with a bandwidth in excess of 12% with a designed port impedance of 75Ω . The simulated and measured radiation patterns of the radiated electric field along the E plane ($\phi = 90^\circ$) and H plane ($\phi = 0^\circ$) are shown in Fig. 4.6e. The FIMP antenna has a radiation efficiency of 97% and maximum total gain of 7.88 dBi at the resonance frequency in simulation. The FIMP antennas are shown in a large scale array in section 4.2.

High Dielectric Patch Antenna

The FIMP patches are well suited for our current space solar power system architecture which must be compactly stored, deploy once, then remain in a planar shape during use. However, many applications call for a system which can readily change shape during operation. To address this need we created discrete high-dielectric patch antennas, shown in Fig. 4.7, which are readily suited for operation on a surface experiencing dynamic shape change. The patches are assembled individually onto the main multilayer board so they do not significantly limit its bend radius. The use of high dielectric materials confines the patch’s fields and allows for the minia-

turization needed for overall array flexibility. As the substrate's dielectric constant increases, the fields that are contained in it, as well as the radiating fringing fields become more dense. This increased density leads to additional loss and decreased bandwidth [120] [123]. To overcome this issue, several approaches exist to increase the bandwidth of patch antennas [114] [90] and to reduce the size of low-dielectric radiators [138] [176]. In our work we use a traditional design as a proof-of-concept (Fig. 4.17b-c), where the feed and landing-pad form an equivalent LC impedance conversion circuit to match the antenna impedance to the one of the feeding transmission line. The high dielectric patch antennas are shown in a large scale array in section 4.2.

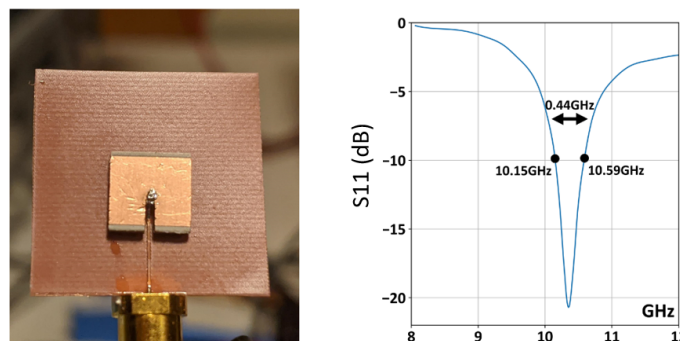


Figure 4.7: High dielectric patch single element test board and matching.

Fully Collapsible Lightweight Dipole Antenna

The FIMP sheet based design stows compactly but cannot readily flex once deployed. The high dielectric patches can be part of a highly flexible array but cannot be stored compactly. Our deployable dipole radiator design was motivated by a desire to improve mechanical reliability, simplify fabrication, and better navigate the trade-off between deployability and flexibility shown in the previously discussed patch designs.

The antenna is shown in Fig. 4.8. Collapsibility and compatibility with large-scale, lightweight arrays drive the shape, materials, and manufacturing process. The antenna is made from a single $25\mu\text{m}$ -sheet of polyimide with etched copper on both sides. Polyimide, rather than traditional rigid substrates, allows for the flexibility needed for collapsibility and self-deployment. To provide the desired shape after deployment, the polyimide sheet is combined with a glass fiber composite frame that has been cured into the “J” shape seen in Fig. 4.9a. The composite is a 3-ply

stack of JPS Composites 1067 glass fiber impregnated with Patz-F4 resin, layered in a $45^\circ/90^\circ/45^\circ$ configuration.

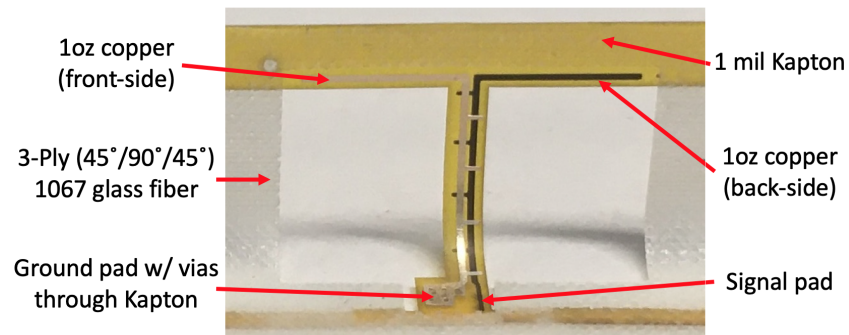


Figure 4.8: A collapsible dipole antenna in its operational configuration with its components labelled.

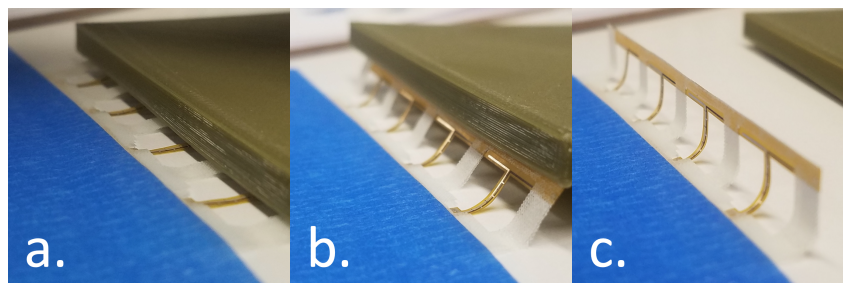


Figure 4.9: Antenna collapsibility: (a) Collapsed, flat configuration, (b) Intermediate state during redeployment. (c) Operational configuration.

To ensure a robust mechanical connection between the polyimide circuit sheet and the glass fiber frame, these sub-components are co-cured. To do this, we place the flexible polyimide circuit sheet on top of the un-cured composite layers, place the entire stack into a silicone mold, and cure⁴ in an autoclave. Co-curing offers a number of advantages. Aligning the antenna sheet and fiber when flat, and then placing it into the shaped silicone mold for co-curing, is simpler and more accurate than attempting to align the flexible sheet after curing the glass fiber into a non-planar shape. Co-curing also eliminates the need for additional adhesive and an application step, as the fiber is already impregnated with epoxy. Moreover, this process is highly scalable and lends itself to bulk manufacturing of antennas from large sheets of glass fiber and polyimide circuit sheets. Cutouts in the glass fiber

⁴Curing is done at 120°C and 80 psi for 2 hours.

and polyimide reduce weight and increase collapsibility, as demonstrated in the sequence of images in Fig. 4.9.

The presented antenna can be split into three sub-components: circuit board contact, a feed transmission line, and the radiating arms. The antenna is driven by a single-ended transmission line from a PCB, with one pad connecting to the transmission line ground (also the radiator ground plane) and the other pad connecting to the transmission line signal trace. The feed transmission line, which rises in a “J” shape from the board, is critical to proper functioning of the antenna as it must accomplish single-ended to differential conversion (balun) and impedance matching between the 50Ω transmission line on the PCB and the dipole arms. To achieve a near 50Ω impedance on the thin and narrow polyimide substrate of the feed, the design relies on distributed capacitance formed by overlapping copper on opposite sides of the polyimide. The simplest way to achieve this capacitance is using a “edge overlapping sandwich” design as depicted in Fig. 4.10a. However, the relative position of etched copper on either side of the polyimide is subject to significant manufacturing variation and, thus, capacitance variation. High manufacturing sensitivity is undesirable, thus motivating use of the finger overlapping design we developed for this work. Fig. 4.10 illustrates the difference between the sandwich and finger overlap transmission lines. By using fingers to achieve the necessary distributed capacitance for the feed transmission lines, the effect of $\pm 50\mu m$ alignment errors from manufacturing on $|S_{21}|$ is reduced from >1.2 dB to <0.2 dB.

To evaluate the performance of the pop-up dipole, a prototype 1-by-8 antenna array was created and characterized. Measurements are compared to FDTD simulations of the antenna array. Input matching for the 4th antenna, while the other antennas are terminated to 50Ω , is presented in Fig. 4.11. The simulated and measured gain patterns are presented in Fig. 4.12. The measured and simulated broadside gain is 5.3 dBi. Both measured and simulated patterns exhibit slight lobe splitting along the array axis. The antenna demonstrates a -10 dB bandwidth of approximately 1.5 GHz and a half-power beam width close to 110° in both the $\phi = 0^\circ$ and $\phi = 90^\circ$ cuts.

The pop-up dipoles radiate efficiently and have been extensively environmentally tested⁵.

⁵The pop-up dipoles were environmentally tested with the process discussed in Appendix A.

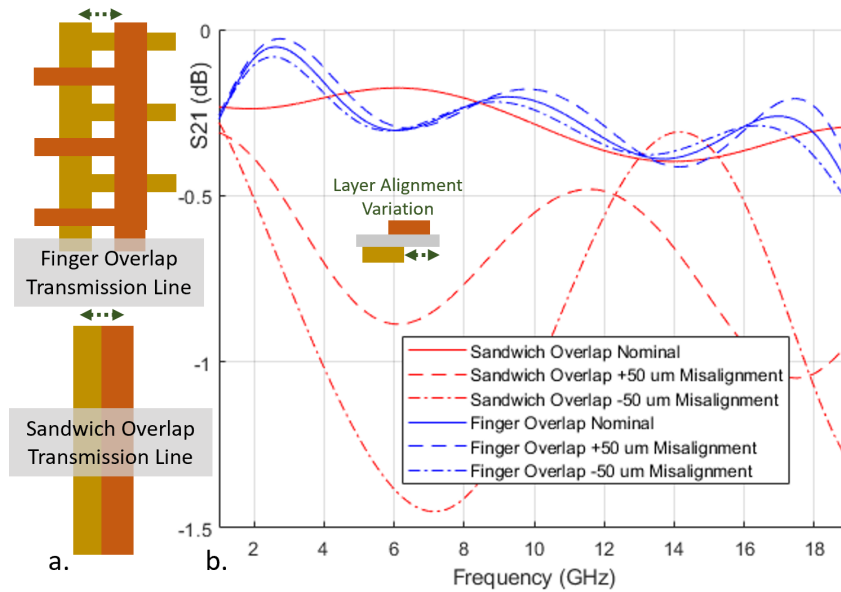


Figure 4.10: (a) Sandwich and finger overlap feed transmission line designs (b) FDTD simulation of s-parameters of the two transmission line designs. $\pm 50 \mu\text{m}$ alignment error is added from the nominal design dimensions.

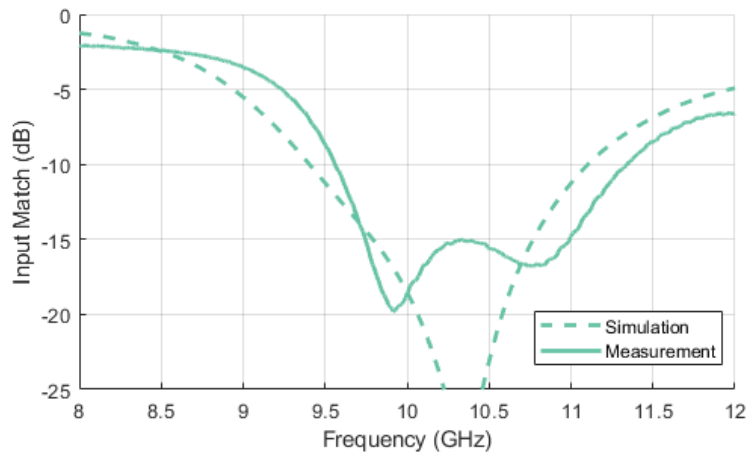


Figure 4.11: Simulated and measured antenna input match.

Future Radiator Development

An area of future development for the project is radiators designed specifically for dual-sided systems. The co-existence of photovoltaics and RF radiators on the same side implies optically transparent RF radiators and/or photovoltaics that are transparent or otherwise benign to the RF structures. Barring a new paradigm, the co-existence of the photovoltaics and RF will cause a loss in efficiency in one or

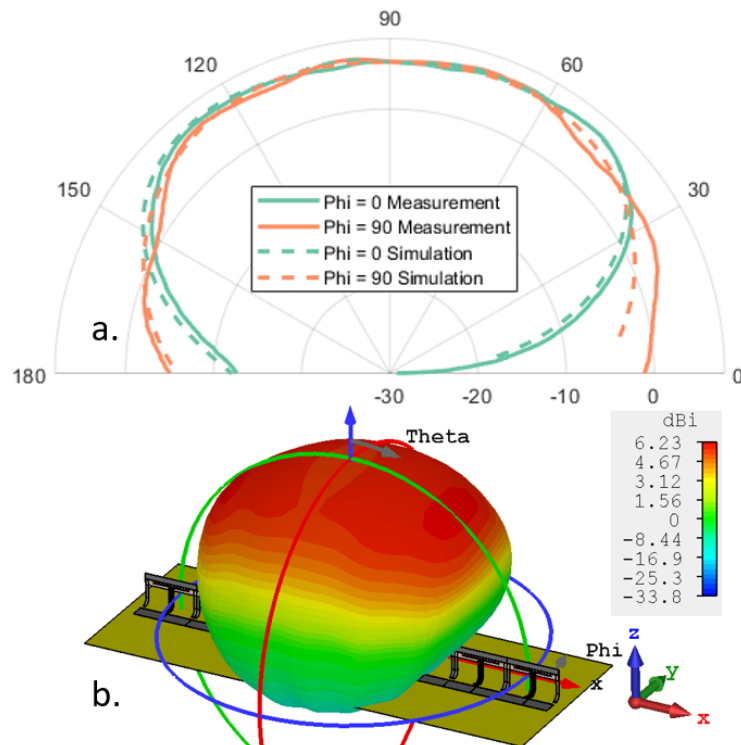


Figure 4.12: (a) Simulated and measured collapsible pop-up dipole element patterns. (b) Simulated 3D pattern with scale and axis.

the other as light is blocked by the radiators and RF currents fields interact with thinner conductors and lossy material. Optically transparent RF radiators have been explored in [163] [150] [129]. A target of 80% optical efficiency and 80% represents an achievable target. However, the additional requirements of lightweight, flexibility, and mass-producibility create a considerable challenge for the next generation of space solar power radiator development.

Carrier Flex Board and Infrastructure

While RFICs provide the electrical functionality for flexible arrays, they must be accompanied with mechanical infrastructure. The increased popularity of flexible circuit boards in consumer electronics and RFID systems has led to improvements in flexible printed circuit manufacturing in terms of resolution, layer count, cost, and availability. Fortunately, flexible materials with favorable behavior at microwave frequencies exist. An example is polyimide⁶, one of the most common flexible substrates. Its dielectric constant (~ 3.4) and loss are well characterized and fairly stable at RF. The loss tangent of ~ 0.005 at 19 GHz is comparable to rigid commercial

⁶Commonly known as Kapton[®], manufactured by DuPont[™].

high-frequency materials [37]. These characteristics allow the design of microwave structures on thin substrates with reasonable transmission line dimensions⁷. If lower loss tangent and thinner sheets are required, there exist commercial Teflon infused polyimide substrates [38].

Both our large scale and small scale prototypes are built on 4-layer flexible boards. Typically one layer is used for microstrip transmission line routing, one layer used for a ground plane, and the final two layers are used for digital and power routing. In some implementations the ground plane is meshed to decrease mass and increase flexibility. While not yet implemented, it is also possible that the polyimide substrate could also be meshed in areas without conductors.

Excluding DC power and the RF signals driving the radiators, the digital control signals and timing synchronization signal are the only other traces present on the flexible PCB. The existing prototypes use an Atmel SAMD21 microcontroller to program the volatile memory cells on the RFIC which configure its various subcircuits. These microcontrollers can eventually be integrated onto the RFIC to save material cost and simplify assembly. This integration step is unlikely to be taken until the space solar power project has matured beyond prototypes and is close to its final functional form. For now, each RFIC and has a microcontroller nearby. For the prototype arrays, a central controller interfaces with these microcontrollers to provide array level control.

Photovoltaic Integrated Tile Prototype

In this section we describe a 16 element array build with the 4-stack RFIC driving the FIMP antennas described above. This array was combined with a concentrator based photovoltaic subsystem to form a fully functional, small scale demonstrator of the Caltech Space Solar Power architecture.

The wireless power transfer portion of the prototype is formed by a single RFIC driving 16 FIMP radiators arranged in a 4x4 formation with an 18mm (0.6λ) spacing. The active area, defined as the fraction of the prototype containing functional elements, is $72 \times 72 \text{ mm}^2$. The mass of this active area is 5.5 g, corresponding to an areal mass density of slightly more than 0.1 g/cm^{-2} , which is one of the major achievements of the presented foldable and collapsible phased array architecture. Thin carbon fiber frames and a carbon fiber collapsible S-spring are used to stabilize

⁷A 50Ω transmission line on a $75 \mu\text{m}$ kapton substrate is roughly 0.2 mm wide. This is wide enough to be easily and reliably manufactured and narrow enough to allow stubs, curves, and impedance transformation.

and separate the 4-layer board and radiator flexible sheets when deployed. Fig. 4.13 shows the RF performance of the prototype.

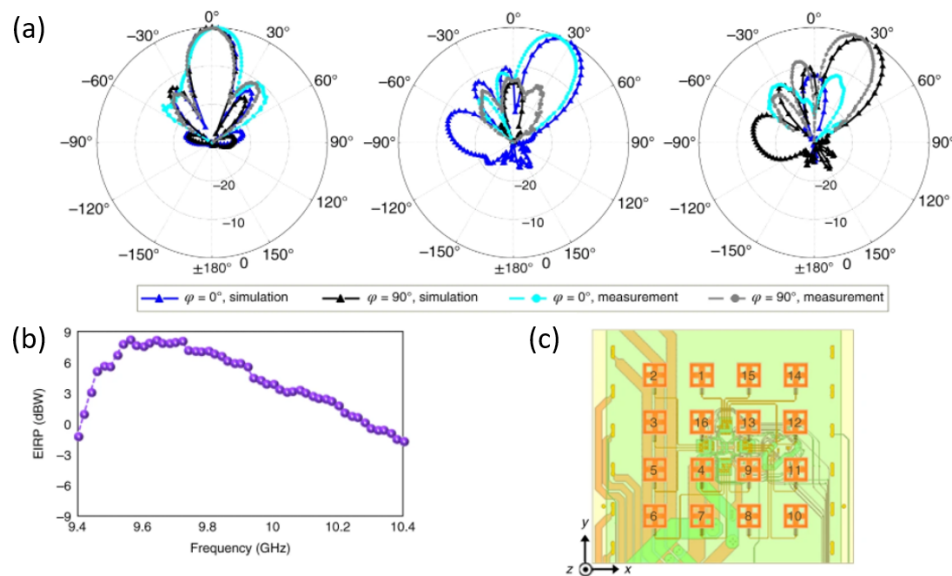


Figure 4.13: (a) Simulated and measured radiation patterns of the total radiated E fields along the E plane ($\phi = 90^\circ$) and H plane ($\phi = 0^\circ$) for three scan angles, ($\phi = 0^\circ, \theta = 90^\circ$), ($\phi = 0^\circ, \theta = 30^\circ$) and ($\phi = 90^\circ, \theta = 30^\circ$), shown from left to right. (b) Measured EIRP. (c) Radiating element referencing. The near-fields, far-fields, and hologram plots are measured at $f= 9.8$ GHz. Each PA draws nearly 180 mA at 1.1 V.

Co-located photovoltaics and RF antenna apertures are attractive for many applications because both the collected solar power and the antenna gain are proportional to the shared aperture area. Optically transparent antennas and partially shared apertures [152] [69] have been proposed for collecting solar power and radiating RF power from the same side of a single aperture, which leads to a reduction of the effective aperture for both PV and RF subsystems. Alternatively, collecting solar power from one side of an aperture and reflecting RF from a passive reflectenna on the other side has been demonstrated in [67] as a way to achieve full aperture utilization for both subsystems. Our work demonstrates a shared PV–RF aperture with electronic beam-steering, without a fundamental aperture loss. The RF tile is combined with a concentrator-based PV array, demonstrating a self-contained power transfer system. The concentrator-based solar power generation used in our architecture is similar to the system found in [168] [88]. The radiator side and the RFIC side of the tile are shown in Fig. 4.14a-b, respectively. The combined PV tile is intended for use in a large-scale space solar power transfer array but could also

be used as a self-powered terrestrial RF beacon. PV power is well suited for this scalable tile architecture because each tile features self-contained power collection and transmission. The distributed power transfer architecture avoids high-mass DC power lines within the array and is robust to failure of individual photovoltaics, integrated circuits or radiators. The solar cell design uses concentrator blinds mounted on the RFIC side of the multilayer flexible board, as shown in Fig. 4.14c. Thin carbon fiber concentrator blinds are a low-mass alternative to conventional flat-panel solar cells. Each blind concentrates incident light onto a small strip of PV material mounted across the back of the blind directly in front of it. The concentrator and PV design are described in [168] [88]. Electrical and physical integration of the photovoltaics and concentrators occur only on the RFIC side of the flexible board. This maintains the collapsibility of the air gap and feeds shown in Fig. 4.14d and does not change the radiation characteristics of the antennas as the flexible board ground layer provides shielding. Figure 4.14e shows the unmodified radiators on the bottom side of the tile. Figure 4.14f shows the tile illuminated by an AM0 solar simulator (simulating the sunlight spectrum outside the Earth's atmosphere), demonstrating solar power collection and RF wireless power transfer to illuminate a light-emitting diode (LED) on a handheld rectenna board.

Large Scale Array Prototypes

While the previously discussed tile prototype provided validation for our basic system architecture, it does not demonstrate array scaling. In order to show array scaling with multiple RFICs, we created two different 16 RFIC, 256 element arrays. These implementations, we use the 2-stack version of the RFIC. One array uses the FIMP radiators described in section 4.2. This array is closer to the space solar power vision of a system which is stored and deployed only once. The other 256 element array is built using the high-dielectric patch antennas. This array is suited for applications that need dynamic flexibility.

256 Element FIMP Array

Fig. 4.15 depicts the 256 element FIMP array. While the constitute components of the system are similar to the prototype tile, the task of scaling is still challenging. This challenge is especially prominent in assembly. The antenna sheet is assembled on the main board by first soldering the feeds to the carrier board transmission lines (Fig. 4.15c) and then lifting the radiator sheet such that the antenna feeds rise from the transmission lines on the carrier board. Small glass fiber springs or supports

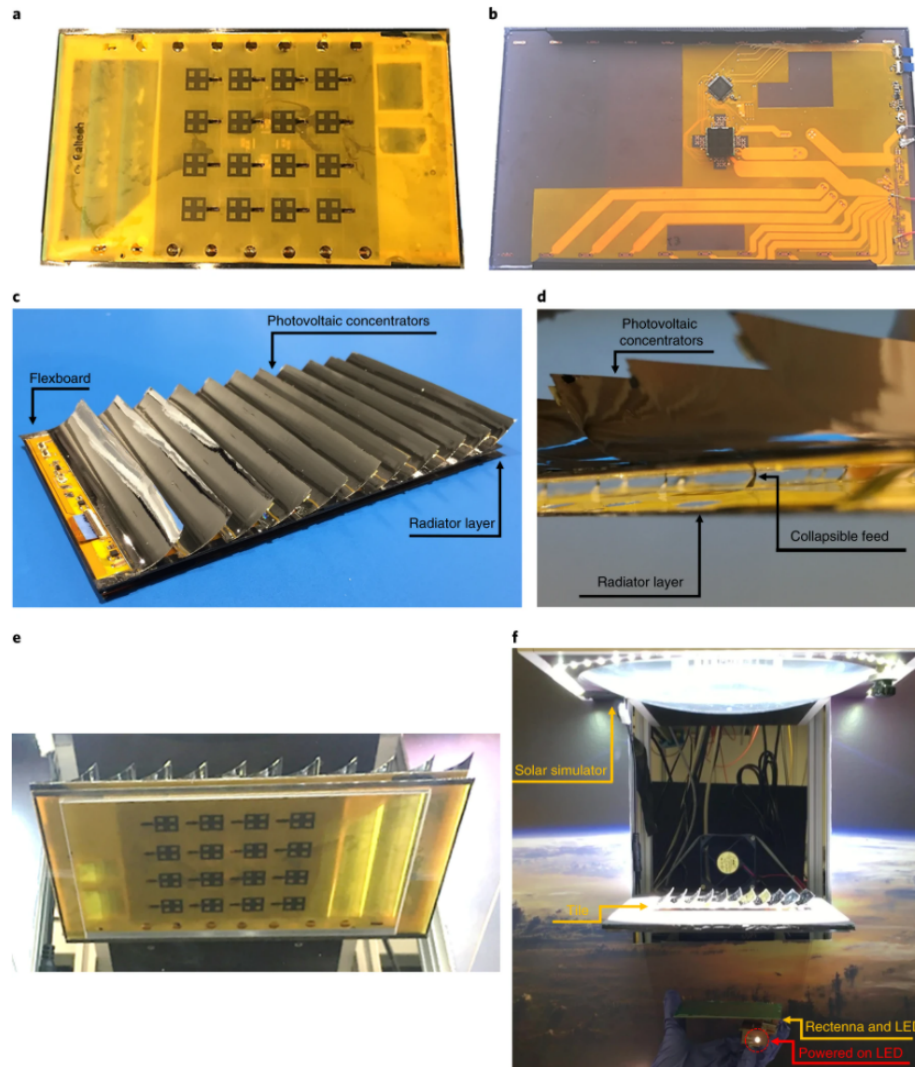


Figure 4.14: (a) View of the radiator side of the tile. (b) View of the RFIC side of the tile. (c) PV concentrators of the integrated tile. Concentrators are mounted on the same side of the four-layer RF flexible board as the RFIC. (d) Side view of the integrated tile. RF feedlines and the antenna layer are isolated from the photovoltaics and concentrators. Collapsibility is maintained in the integrated tile. e, Radiator side of the integrated tile. (f) Demonstration of power collection and transmission. A solar simulator illuminates the tile, which radiates RF power to the rectenna, lighting an LED.

then hold the antenna sheet deployed while providing some movement flexibility that relieves structural stress. A “sandwich” fixture aligns the sheet and carrier board for batch soldering.

The design is intended for use with a distributed DC power supply (photovoltaics in a space solar power system). A distributed power source avoids the ohmic

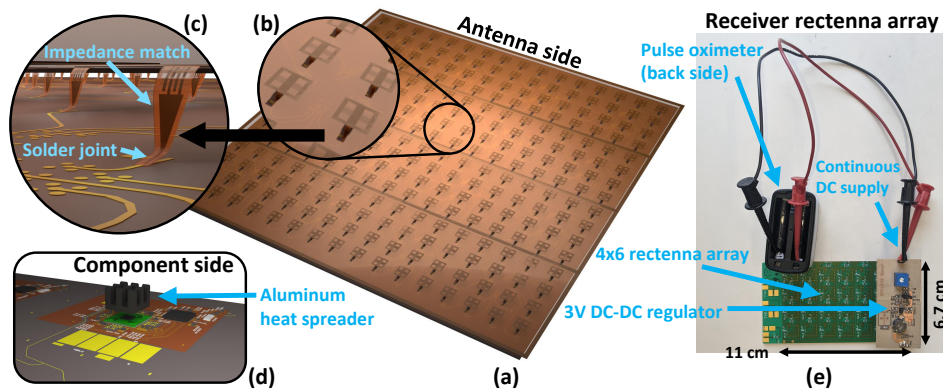


Figure 4.15: Antenna sheet structure. (a) This antenna sheet assembled on the back side of the base-design main board. (b) Printed antenna patterns and (c) antenna feed assembly. (d) Aluminum heat-spreaders. (e) Power receiver board with an example consumer device (a commercial pulse-oximeter) attached to it.

losses and extra mass of long power distribution lines, simplifying the component-side design of the main board. However, distributed photovoltaic supplies are poorly suited to laboratory characterization of the array. As such, we use a low resistance flexible board strap as a surrogate to local power generation. A nominal DC voltage of 1.8V is supplied to each of the RFIC's four PA quadrants. The 1.8V DC supply is also converted to 1.2 V supply by a linear regulator, for the rest of the IC circuitry, and to 3.3 V by a voltage doubler to power the off-chip micro controllers. These additional regulators are miniature (about 2 mm \times 2 mm) and do not contribute much to the overall area and power consumption of the system. The system performance is characterized in a terrestrial lab rather in the intended, much colder space environment. To handle the higher temperatures of testing conditions we attach a commercial aluminum heat-sinks with a thermal resistance of 32°C/W on top of each IC, which can typically dissipate 3.7W from a 14 mm² area of 0.3 mm thick silicon die (Fig. 4.15d). The result is a high power and low mass radiating array, with a 2D phase steering and deformation correction capability, which can radiate up to 0.8 W at a distance of 2 m away from the antenna surface. A small array of 4 \times 6 10 GHz tuned rectennas is used as a receiver to focus the beam pattern using our closed-loop procedure [16]. In other measurements, the receiver feeds a 3.3 V DC-DC module converter continuously powering electrical instruments and demonstrating wireless power transfer, as shown in Fig. 4.15e. As illustrated in Fig. 4.16a-b, the measured radiation pattern does not precisely follow the expected analytical far-field curve that is commonly used as a reference in such measurements.

The reasons are reflections from the antenna ground, fabrication imperfections and the fact that at 10 GHz the far-field limit of a 30 cm \times 30 cm aperture is actually at 6 m. Despite these differences, a comparison of the measured main lobe shape, and the one calculated from

$$AF[\theta] = \frac{\sin \left[N \left(\frac{\pi d}{\lambda} \sin \theta \right) \right]}{N \sin \left(\frac{\pi d}{\lambda} \sin \theta \right)} \quad (4.3)$$

results in a very good match. The first null from broadside in the analytical equation is when $N(\pi d/\lambda) \cdot \sin \theta = \pi$. For radiators at a distance $d = 0.6\lambda$ from each other this is an angle of $\sin \theta = 1/9.6$ radians or 6° . This result agrees well with the measured size of the main lobe and proves that the field from the individual radiators is combined coherently.

One potential use of our system is to wirelessly power vital sign monitors of isolated patients in a dynamic environment. This use case is especially relevant and important in the event of a world-wide, airborne, viral pandemic which requires medical crews to be completely isolated from the treated patients while performing continuous treatment and monitoring. In this work we use our 6.7 cm \times 11 cm receiver array to power a commercial 60 mW pulse oximeter in *real time*, as shown in Fig. 4.16c, without the need for additional batteries. The analytical pattern and measured power distribution in the main lobe are used to predict the maximum distance at which the oximeter will be powered. A rectenna array with peak efficiency of 45% at 10 GHz [16], followed by a DC-DC converter with efficiency of 60%-80%⁸ that boosts the output to the required voltage levels, projects a usable range of 1.22 m - 1.45 m away from the transmitter. In practice, we achieved a maximum operating range of 1 m with an RF to DC power transfer of about 80 mW. This is likely due to imperfect focusing and high startup power draw that prevents the oximeter from turning on at a larger distance.

The high power smart array is lightweight and efficient, but limited in its bend radius due to its dual sheet structure. That in conjunction with a low-voltage supply makes it more suitable for single deployment scenarios with a distributed local DC power supply. It can be stored with the antenna sheet flattened against the main board, creating a more flexible single sheet, then later deployed for use. It is flexible up to the radial mismatch between the antenna sheet and the main board, and the physical strength of the thin antenna leads that connect between the two.

⁸Efficiency is input power dependent.

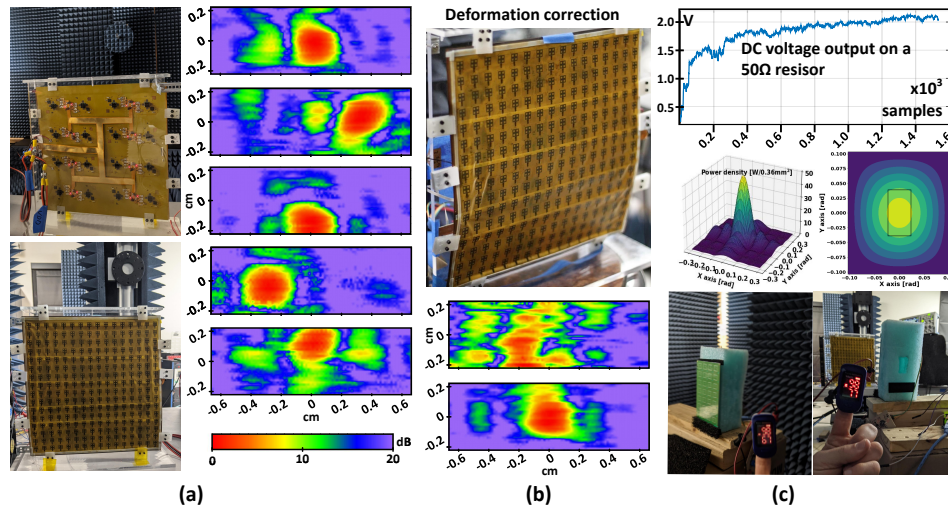


Figure 4.16: Antenna sheet array measurements. (a) Beam-steering, (b) deformation correction, (c) wireless power transfer of about 80 mW at 1 m away from the transmitter (top), expected power delivery distribution to the remote receiver at ~ 1.4 m away (center), and real-time powering of a pulse-oximeter (bottom).

256 Element High Dielectric Patch Array

The flexibility limitations of the FIMP array motivated the design of another 256 element array better suited to dynamically flexible applications. In addition to improving flexibility, we also desired to improve the operation of the array from a single, non-distributed supply. To accomplish this we expanded the power strap board to two layers, reducing ohmic loss and allowing for additional components to be mounted to it. We chose to distribute higher voltage, lower current power to further reduce losses. In our implementation we distribute up to 6 V along the array (Fig. 4.17d), and use a commercially available switching regulator that has the required inductors integrated onto its chip package for the conversion to the local 1.8 V domain. As a result, the resistive loss of the DC supply lines is reduced by a factor of 3 compared to the high power array that was presented previously. The supply line remains thin enough to not limit the array conformability. The local 1.8 V regulators are powered from an external, high voltage, 125 W, 75 V input commercial miniature which allows the system to operate from a standard bench supply or from a laptop power brick.

The last addition to this second enhanced-flexibility design is a replacement of the tall aluminum heatsinks with a low profile solution. Here we assembled flat ceramic heat spreaders on top of the RFICs and placed 165 μm thick, 40 mm \times 15 mm

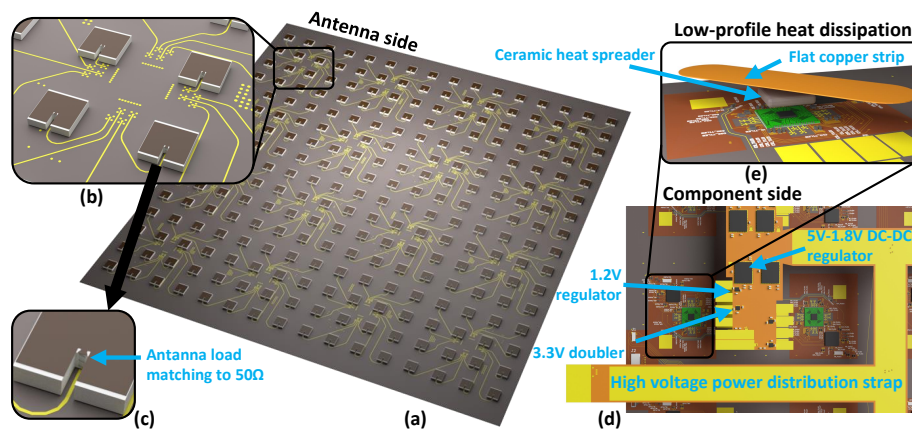


Figure 4.17: Flexible and robust smart antenna design. (a) Main boards with (b) Discrete patch antennas. (c) The antenna feed via is used for impedance matching. (d) High voltage (up to 6 V) power delivery strap with local voltage regulator. (e) Low-profile heat spreaders.

copper strips on top of them to conduct heat away from the RFIC (Fig. 4.17e). The use of flat and bendable heat conductors enables the array to conform to curved surfaces such as airplane bodies, where the carrier surface itself participates in the heat conduction away from the chips, and closer to the flat back-surfaces required for wearable devices.

The structural and functional flexibility is first demonstrated in a laboratory context. Fig. 4.18a shows that the array can be bent in the horizontal and vertical dimensions, with concave and convex radii smaller than 23 cm. After the array is conformed to the desired surface, it is fully functional and programmable, and is able to demonstrate 2D beam focusing, pattern recovery, and steering to all directions (Fig. 4.18b). While concave focusing is functional, the quality of the resulting pattern is lower than convex bends because surface reflections effect the array element coupling. Increased coupling may manifest as EM reflections which can be accounted for in the focusing process, or as PA load coupling and signal pulling in the RFIC integrated PLLs, which are large-signal effects and are in general not restored in a linear calibration process. In addition to the focusing of bent and deformed arrays, our array is used to demonstrate the ability to correct the antenna pattern in the event of damage to several RFICs in the array. Fig. 4.18c shows a focused array with 16 working ICs. If four of them are damaged (turned-off), the pattern is changed, but can be nearly recovered after re-focusing. A similar result is obtained for a mixed-experiment (Fig. 4.18d) where the flexible array is bent and directed at an

angle from the receiver, and two of its chips shut down. In another demonstration of the functional flexibility of the array, we use two receivers and a modified focusing goal; by optimizing the power at both receivers simultaneously we show a splitting of the beam in two directions simultaneously. Like the high power implementation, this array is also capable of powering a remote pulse oximeter (Fig. 4.18e), but at a reduced distance of 40 cm away from the radiator. The reduced range is a result of the design choice to optimize flexibility and robustness at the expense of raw transmission power. Lastly, the array was deployed outdoors and its beam was focused at a building entrance about 1.5 m away from the antenna surface. With the deployed array, we were able to deliver enough power to our receiver to light a high-power indicator LED, as illustrated in Fig. 4.18f. This demonstration shows that the dynamic array is robust enough to be carried, deployed, operated, and measured in the field.

Space Demonstrator

In 2022, the Caltech Space Solar Power Project will launch low earth orbit (LEO) demonstrations of the wireless power transfer, photovoltaic, and deployable structure subsystems. The wireless power transfer demo is MAPLE (**M**icrowave **A**rray for **P**ower Transfer, **L**EO **E**xperiment). MAPLE depicted in Fig. 4.19, is a 2 chip, 32 element array, which will demonstrate the essential functions of the power transfer subsystem, providing a critical verification of the space-readiness of our approach. It uses the pop-up dipole antennas described in section 4.2. Appendix A describes the MAPLE project at length in the context of a general guide to academic space payload design.

Asymptotic Projections for Power Transfer Subsystem

Given the forward-looking ambition and substantial time scales needed for complete scaling and deployment of the proposed space solar power project, projections of the minimum achievable areal mass of future space solar power systems are useful tools for understanding the viability of the architecture. The Caltech SSPP team calls these “asymptotic” projections, as they represent the upper limit of what is achievable with existing materials. Our projections have assumed a baseline level of performance which should not be significantly degraded by the design changes chosen to reduce mass. This subsection describes the asymptotic mass projection of the wireless power transfer subsystem. The photovoltaic subsystem and mechanical infrastructure have made similar projections.

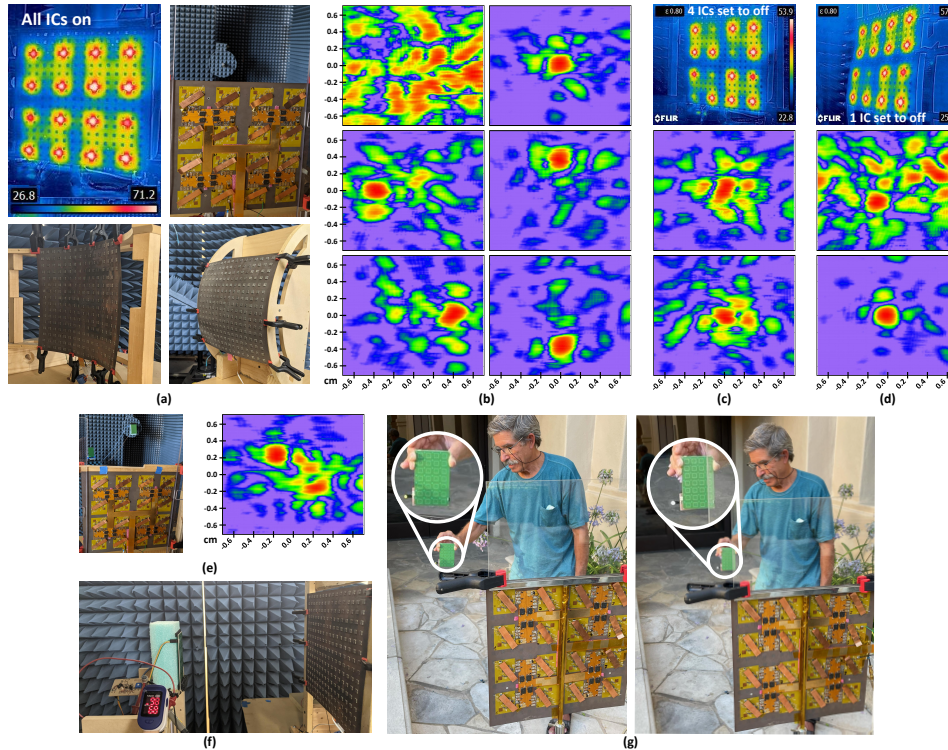


Figure 4.18: Flexible array measurements. (a) horizontal and vertical convex and concave flex capability to bend radii smaller than 23 cm. (b) Representative focusing and steering capabilities. (c) Compensation in software for damaged RFIC. At the top shown an array with four non-functional. Below, the resulting pattern of broadside phase settings. At the bottom, pattern after re-focusing. (d) Focusing of a wavy surface with non-working ICs. (e) Lobe-splitting by focusing to two different targets. Note the side-lobe combining between the two peaks.(f) Wireless power transfer to real-time power a pulse oximeter 40 cm away from the antenna. (g) Outdoor deployment and focusing to power an LED indicator. The LED is on when the receiver is at the focus point (right) and of when moved away from it (left).

The first mass reducing assumption made is the incorporation of the digital control microcontroller into the RFIC die. This dramatically reduces the complexity of the flexible circuit board, removing up to 12 traces used as digital interface lines. The IC expands from its current dimensions of 2.8 mm by 2.8 mm to 3 mm by 3 mm to accommodate the additional digital circuitry. It is conceivable that the IC could be made smaller by switching to a process node smaller than 65 nm, but given that additional circuitry and interfaces may need to be incorporated, we will keep the 9 mm² dimension. The thickness can be reduced to 100 um after fabrication. We treat the RFIC as if it was made entirely of pure silicon although other materials

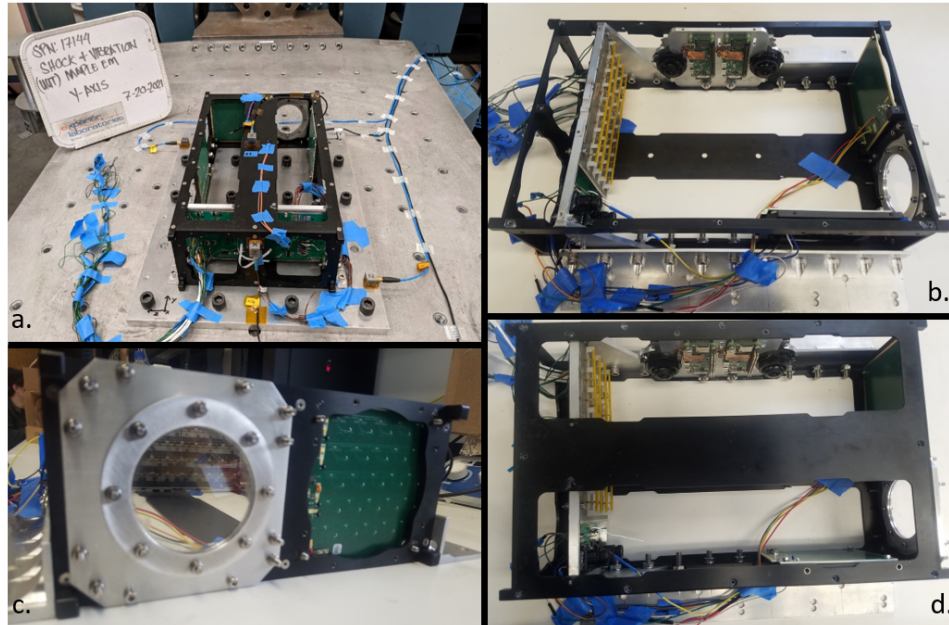


Figure 4.19: MAPLE Engineering Model. (a) At mechanical testing facility. (b) Image of MAPLE with top removed. (c) MAPLE flexible array seen through sapphire window. (d) Image of MAPLE.

are present⁹. We also assume that the IC attaches to the flexible circuit board without use of a rigid interposer board. This change assumes future improvements in flexible circuit board manufacturing capabilities to match the current capabilities of a typical high-quality rigid circuit board manufacturer. The incorporation of the digital controller into the RFIC removes interface bumps, slightly easing the requirements on the interface between the flex board and the IC. We also assume that an underfill epoxy similar to 3M DP2216 epoxy [1] is used to provide mechanical strength to the IC/flex board interface. The underfill is assumed to be up to 1/5 of the IC volume. The IC will also need an additional aluminum sheet to act as a radiation shield and heat spreader. We account for the mass of a 100 μm thick sheet of aluminum that is double the area of the IC. Note the majority of the thickness is likely to be concentrated over the IC itself. Our projections assume that in continuity with the existing prototypes, each chip drives 16 radiators that are separated by 0.6λ pitch at 10 GHz.

We now describe the asymptotic flexible circuit board. The flex board consists of a

⁹These other materials include silicon dioxide and aluminum which are close enough to bulk silicon in mass to ignore the difference. There are also thin layers of polyimide or other similar polymers which are lower mass than silicon but not present in sufficient quantities to merit inclusion in our analysis.

substrate (polyimide) and a conductor (presently copper but possibly aluminum in the future). To minimize mass we choose as thin polyimide as possible (10 μm) and only place conductor when explicitly needed. The polyimide can likely be meshed or cheesed to reduce its weight by an additional 10-25%. We only assume one layer of polyimide which supports two layers of conductors. This reduction from the four conductor layers in the current design is justified by the removal of the digital routing lines and re-designed radiators. Additionally one side of the board will have coated with a high emissivity coating weighing $0.5 \frac{\text{g}}{\text{m}^2}$.

The first conductor to be added is the DC current carrying lines. We assume 1.5 A of current¹⁰ from the photovoltaics for each IC. On average this current is expected to travel roughly 1 tile's length when accounting for the path to chip in the center of the tile and the return path. We chose sufficient conductor cross section such that <2% power is lost. All conductors are chosen to be 10 μm , which is the same thickness as 1/3 oz copper and much thicker than the skin depth at 10 GHz of 0.652 μm .

The next conductor group to be considered is the transmission lines which connect to each antenna. To minimize mass we are not including a ground plane in the design. This requires a differential design such as an edge-coupled transmission line. Our projection assumes 0.2 mm width traces that run a distance of $1.8 \cdot \text{pitch}$ on average.

The projection includes two radiator designs. The first is a "no ground-plane" Yagi-Uda antenna design. The design aims for 90% mainlobe efficiency using 3 or 4 arms that are 0.2 mm wide and $\lambda/2$ long. $\lambda/4$ pitch between reflectors is assumed. It is supported by a pop-up frame similar to the deployable antennas described in [43].

The other radiator design is a dipole with minimal ground plane. Our existing designs have used ground planes with 50% fill factor without deleterious effects. A non-uniform fill factor of 20%, concentrated in the high field region of the ground plane could be achieved without substantial reduction to radiation efficiency.

A comparison between the two antenna designs starts with mass. Our current glass fiber frame material is $31 \frac{\text{g}}{\text{m}^2}$. We can assume reduction in that areal mass to at least $25 \frac{\text{g}}{\text{m}^2}$. The Yagi-Uda antenna design has a greater fractional mass contribution from the frame material than the dipole. If the support material areal mass can

¹⁰Even at 1 V this current implies a highly optimistic estimate of PV efficiency (over 20%) and sun angle (exactly broadside). This optimistic estimate leads to a more conservative mass projection as more conductor is needed to carry the current without much loss.

be reduced to $10 \frac{g}{m^2}$ or lower than the Yagi-Uda implementation is projected to be lower mass than the dipole design. Electrically there are several aspects which the dipole is likely superior. When accounting for front to back ratio it is likely the dipole has superior mainlobe efficiency. The dipole ground lines could also be re-used as DC conductors, allowing further mass reduction. Because of the complete lack of ground plane, the Yagi-Uda implementation is more promising for dual-side photovoltaic system architectures. Fig. 4.20a-b show models of each proposed radiator.

Compared to the radiators or integrated circuits, the reference distribution system is at lower level of technological readiness, making it more difficult to project accurately. Our projection anticipates three levels of reference distribution. First a wireless reference, likely at microwave frequency, is transmitted from earth to each spacecraft. At a central node on each spacecraft, the wireless reference is modulated on to an optical signal which is distributed across the spacecraft through optical fiber. Optical synchronization of microwave arrays over long fiber distances was shown in [49]. The optical reference drives j wired distribution nodes. j is chosen to be 100 for the asymptotic projection but can be adjusted as the spacecraft size scales up or down. The wired reference nodes demodulate the optical signal and distribute the reference at microwave frequencies through transmission lines to a number of RFICs. For the asymptotic projection this fanout (k) was also chosen to be 100. Fig. 4.20c shows a block diagram of the reference distribution system. The reference distribution and digital control require synthesizer and amplifier tiles at each level of hierarchy. Each spacecraft will have a single wireless to optical reference conversion tile which also handles digital signals that weighs 50 times the mass of a standard tile. The optical to microwave conversion will be handled by a tile that weighs 5 times the mass of a standard tile and is also used for digital signals.

The digital control system is equally difficult to project given the lack of ultra-large scale prototypes or even comparable systems. Given that the digital control system must also convey information over the same distances and environment as the reference network, we assume that the control mass contribution will be close to the reference's contribution. To account for the digital control system we duplicate the reference network mass while acknowledging the limitations of this assumption.

The first integrated tile prototypes presented in section 4.2 illustrate a clear issue that must be addressed in a large scale system: area mismatch between the PV and RF subsystems. In a real system the RF circuits must operate only using the power

captured by the photovoltaics corresponding to their area. This power is limited and depends on angle with the sun. Maximally efficient DC power to radiated RF power conversion requires dual optimization of the PV and RFIC operating points and be maintained over the range of expected operating powers. Adaptive schemes for mutual power optimization have been proposed and should be incorporated into any fully functional systems.

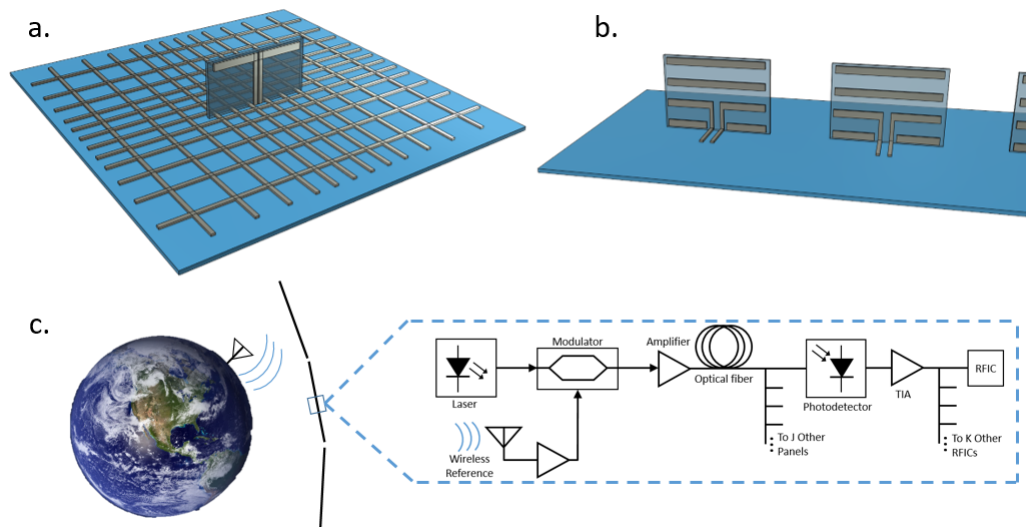


Figure 4.20: (a) Model of non-uniform grid ground plane backed dipole. (b) Model of Yagi-Uda antenna without ground plane. (c) Reference distribution diagram.

The result of the asymptotic mass projection is shown in Fig. 4.21¹¹. Fig. 4.21a calculates the active area mass (mass without counting the reference distribution networks) for a single RFIC and its constituent radiator. 0.174 g is a factor of 30 lower than the demonstrated active area mass of 5.5 g shown in our integrated demo tiles. Fig. 4.21b-c present the total areal mass of the wireless power transfer system with $j = k = 100$ and $j = k = 256$ respectively. The dominate masses are the circuit board, the DC current carrying lines, and the RF radiators. While the circuit board is unlikely to significantly decrease in mass, the other two dominate mass contributors could hypothetically be lowered. The DC current carrying lines are conservatively designed for the projected current and could be shared with the antenna ground plane. While we fully count the DC current carrying lines in our

¹¹This footnote describes several specific choices made in the mass projection model. The circuit board is cheesed by a factor of 0.1 meaning that 90% of the board remains. The dipole radiator design was chosen assuming a support material areal mass density of 25 g/m². The optical fiber is assumed to run row/column instead of an h-tree.

wireless power transfer subsystem projection, they could be partially or fully counted towards the photovoltaic mass instead. The projected RF radiator topologies are unlikely to significantly decrease in mass without material improvements (such as to the support frame materials). However, it is conceivable that new ultra-lightweight radiator topologies could meaningfully lower the mass. The opportunities to lower these areal mass values are limited but implementing a real system which is close to these values would be an incredible achievement. Both of these projected areal masses are well below the areal mass of a single sheet of printer paper, $80 \frac{g}{m^2}$.

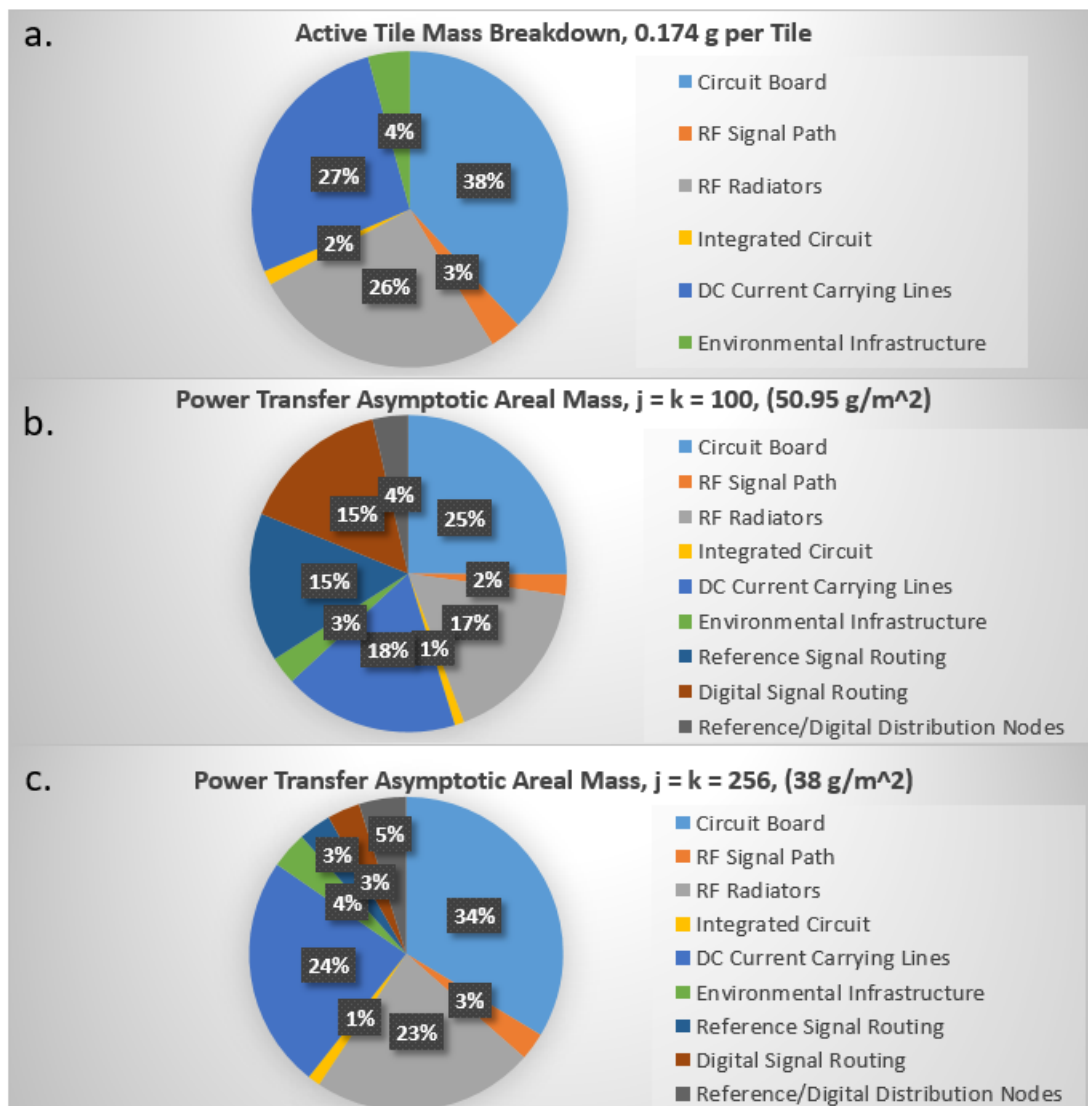


Figure 4.21: (a) Active tile mass projection. (b) Area mass projection for $j = k = 100$. (c) Area mass projection for $j = k = 256$.

With these asymptotic results, we now ask how close to the asymptotic projection a

realized system must achieve in order to be economically viable. [47] thoroughly describes the economic competitiveness of the Caltech Space Solar Power Architecture compared to existing terrestrial power generation systems. The chosen comparison metric is levelized cost of electricity (LCOE). LCOE measures the average net cost of power production for a generating system over its lifetime. Fig. 4.22 shows an estimate of the Caltech Space Solar Power System LCOE for a given spacecraft specific power. This spacecraft specific power is calculated with not just the wireless power transfer subsystem mass, but the photovoltaic and deployable structure masses as well. For the asymptotic point on Fig. 4.22 the other subsystem masses are projected to experience the same fractional reduction in mass as the wireless power transfer system. This assumption is consistent with internal studies by the Caltech SSPP team through which we have seen that the system mass is roughly split evenly between the subsystems for both demonstrated prototypes and forward-looking projections. The other three points on the curve are “Demonstrated”, “Goal”, and “Competitive”. “Demonstrated” is an extrapolation of the mass of the single tile integrated prototype. “Goal” is a target value set as an achievable but challenging goal for the project. “Competitive” is the spacecraft specific power that would allow space solar power to compete with terrestrial, local, power sources almost anywhere on earth. To be clear, a realized system will still be useful and economically viable without reaching the “Competitive” marker. Space solar power is intended to power areas where traditional power sources are difficult or impossible to deploy (remote areas, natural disaster sites, etc.). In these areas non-space solar power systems’ LCOE is substantially higher than the generic scenario represented by “Competitive”. The asymptotic projection sits close enough to “Competitive” to allow systems that fall well short of the projected mass target to be useful and viable.

4.3 Flexible Array Shape Calibration

Introduction

The ultra-thin, ultralight large-scale arrays proposed for the Caltech Space Solar Power Program will inevitably experience shape deformation. The momentum of orbital adjustment and possibly even solar pressure will be enough to bend sheets of polyimide reinforced with composite fibers more than enough to effect beam-steering. For a relatively modest 10-m array, a 0.15% deformation will change the relative position of the edge elements by $\lambda/2$ compromising the beam-focusing capabilities of the array. This deformation can be corrected by the feedback loop with an external receiver described in [61] but for a large enough array it may be

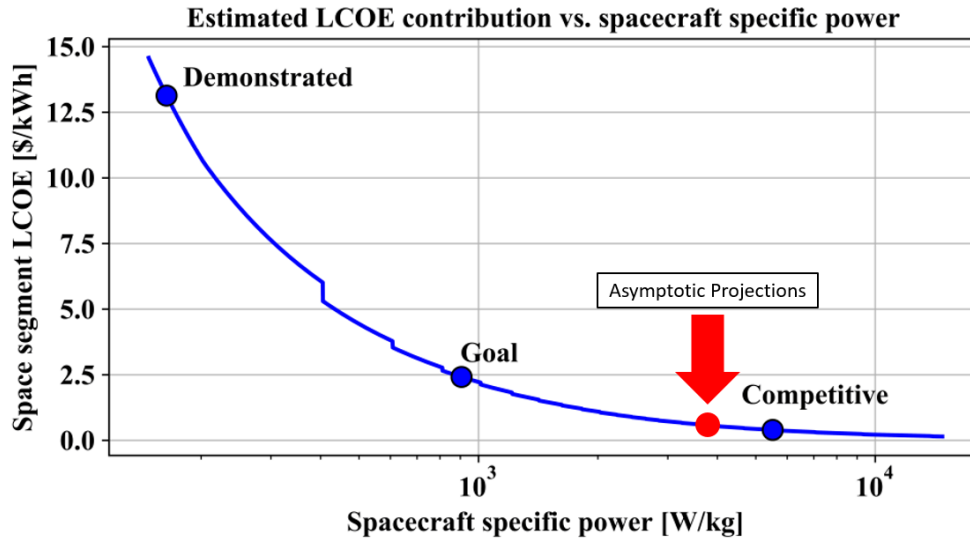


Figure 4.22: LCOE plot from [47] with asymptotic projection from this work added to curve.

necessary to measure and correct for deformation across the surface of the array without external feedback.

The flexibility of the Space Solar Power Array is a consequence of its massive size and ultralight construction. However, there is a growing interest intentionally flexible arrays for human body wearable arrays, deployable systems, and sensing systems which conform to the material under test. These applications, as well as the space solar power array need a suite of tools capable of compensating for shape change during operation.

While flexible arrays are an emerging paradigm, non-planar array shapes have been in use since almost as long as arrays themselves. Rigidly conformal arrays, which are fixed to a nonplanar surfaces, have been and are still used in low profile (aerodynamically and/or visually) radio frequency (RF) systems [11] [39] [82], mostly for streamlining purposes. For these mechanically static arrays, unusual shape and orientation of array elements is analyzed and accounted for during the design phase as these systems are used for a single, rigid shape. The task of pattern synthesis with these arrays is well-studied and has been accomplished using techniques such as geometric analysis [93] [133] and various optimization algorithms [170], including genetic algorithms [147] [4] [63]. While these techniques are effective, flexible array shape may not be known or static.

Flexible phased arrays, which can constantly change shape during deployment and

operation, also suffer from irregular element position and orientation. However, their antenna positions may not be known in advance and accounted for during design. As such, flexible phased arrays must be able to determine their shape and dynamically update phases to control beam coherence and direction during operation. An example of a flexible phased array is shown in Fig. 4.23. Flexible arrays could operate while curling with biological and mechanical joints or while fluttering in the wind if fast and accurate array shape reconstruction can be achieved. Shape calibration



Figure 4.23: A 2D flexible phased array antenna sheet with 256 10 GHz patch antennas.

refers to adjustments of element excitation phases to account for changes in relative element position and orientation within the array. Without shape calibration, the beam-forming, beam-steering, beam-focusing, arbitrary wavefront generation, and interference suppression capabilities of a flexible phased array quickly disappear. Shape calibration of flexible arrays using ancillary resistive strain sensors was shown in [22]. These additional sensors increase system complexity by incorporating a new sensing domain and utilizing hardware not already present in phased array systems. Additionally, each resistive strain sensor only offers a single measurement value. For an array with complex bending geometry (having high sinuosity or lacking bilateral symmetry), a single, localized measurement will not accurately capture array shape. Designing a flexible phased array with a limited number of ancillary sensors requires knowledge of the expected space of curvatures the array surface will experience during design, limiting the applications of such an array.

Superseding prior calibration approaches, shape reconstruction describes a more complete and more difficult task: full determination of the shape of the array and the surface to which it is conformed. We propose a framework for performing shape reconstruction only from local measurements of mutual coupling between elements

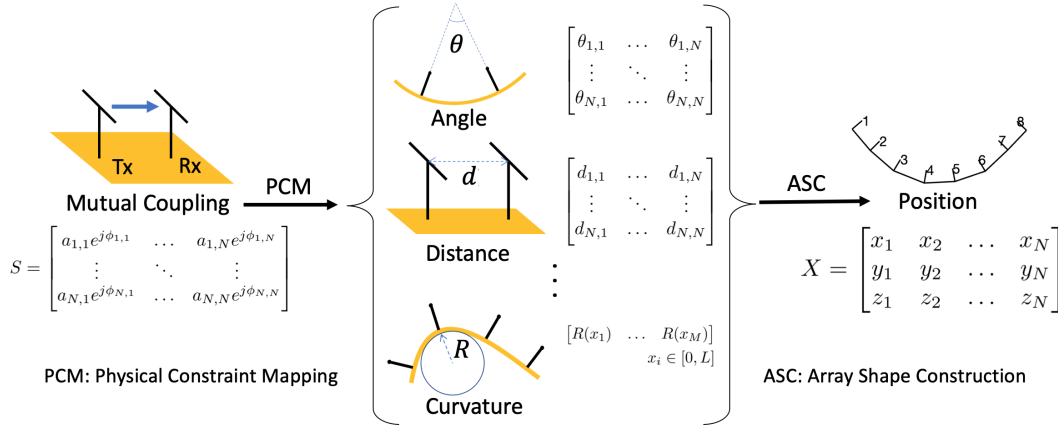


Figure 4.24: A block diagram of our framework for mutual coupling-based shape reconstruction.

in a flexible phased array. While phased arrays are typically designed to direct an electronically steerable beam of microwave power towards a far-field target, some fraction of the power radiated by one element in the array is absorbed by the other elements. This incidental power transmission is called mutual coupling. While in extreme cases it may be detrimental to array performance, mutual coupling provides information about the state of elements within the array. [149] [17] use mutual coupling measurements in an array with known shape and symmetry to determine the phase offset of elements within the array. Mutual coupling shape reconstruction transposes the problem: using mutual coupling measurements to determine relative position of elements in the array.

In most practical cases, mutual coupling measurements contain sufficient information for array shape reconstruction but an analytical and algorithmic framework is required to turn an inter-element coupling matrix into element positions. We propose a two-step, modular framework which is adaptable to different algorithmic approaches accounting for different sets of antenna properties and physical constraints.

The framework, using our proposed algorithms, is successfully demonstrated on two different passive arrays with different radiators. To demonstrate a realistic system-level implementation of such algorithms, we designed and built a flexible, active 10 GHz array using monolithic radio frequency integrated circuits (RFICs). RFICs provide timing synchronization, frequency synthesis, signal amplification, digitization, and a multitude of digital control functions with a millimeter-scale footprint. With this density of complex functions, discrete components can be

removed, avoiding their bulk and rigidity which would be prohibitive for a truly flexible design. The integrated circuit-based flexible phased array presented in Section 4.3 represents a new paradigm in array design, only recently enabled by the proliferation of RFICs. Before discussing the RFIC array, we describe the framework and the motivations guiding our implementation.

Framework

Overview

Fig. 4.24 illustrates the modular framework for mutual coupling-based shape reconstruction. The framework begins with mutual coupling data represented as a matrix. The first step of the framework, called physical constraint mapping (PCM), processes the mutual coupling information to produce physical constraints of the array shape, such as element distances, mutual angles, or local curvatures. These physical constraints can be represented in different formats (matrix, etc.), but all contain the necessary information to reconstruct the shape. The second step, called array shape construction (ASC), utilizes the physical constraints to generate the actual positions of all elements and, thus the array shape. This is, of course, the goal and purpose of this framework.

In the following sections, we present the framework and specific examples of PCM and ASC algorithms. We define the following terms: a mutual coupling matrix $S \in \mathbb{C}^{N \times N}$, a physical constraint matrix $B \in \mathbb{R}^{N \times N}$, and a position matrix $X \in \mathbb{R}^{d \times N}$, where N denotes the number of array elements and d denotes the number of physical dimensions we expect our array to live in¹². While the framework is general, in this paper we present results for flexible phased arrays with a single row of $N = 8$ elements that we will assume can only live in $d = 2$ dimensions. We will demonstrate that the flexibility of this framework allows for the reconstruction of planar phased arrays with arbitrary N that can potentially live in $d = 3$ dimensions.

The choice of algorithm for PCM and ASC is almost entirely dependent on the primary physical constraint we choose to use (e.g., relative distances or curvatures). The freedom to choose B gives this framework much of its modularity; different physical constraints will be better suited for different antenna systems. For our work, we use Euclidean distance matrices (EDMs) as candidates for the physical constraint matrix [34].

¹² $d \in \{1, 2, 3\}$.

A Euclidean distance matrix, $E \in \mathbb{R}^{N \times N}$ is defined as:

$$E_{mn} = |\vec{r}_m - \vec{r}_n|^2 \quad (4.4)$$

where \vec{r}_n ($n \in \{1, 2, \dots, N\}$) is the position vector associated with point n . The matrix describes the squared distance between points in a d -dimensional point cloud. EDMs are apt candidates for B because we can use known relationships between coupling and distance to devise the PCM algorithm and use existing algorithms for determining position from relative distance.

As we will discuss below, distance impacts both the phase and power of mutual coupling measurements. We propose an algorithm, called Spiral Match, as a candidate for PCM. Moreover, the problem of solving for the relative positions of an arbitrary number of points in an arbitrary number of dimensions given an EDM, E , is critical to a number of applications and, thus, is well-studied [34]. We have a wealth of options for ASC that each account for different types of EDMs; for this system, we use a semi-definite optimization to solve for the relative position.

Mutual Coupling Model

Accurate mapping of coupling measurements to physical parameters of the array (PCM in Fig. 4.24) is critical for proper shape reconstruction. The PCM algorithm presented is called Spiral Match (discussed in detail in Section 4.3) and maps the measured complex-valued coupling to a distance between the phase centers of the elements. Near- and far-field electromagnetic interactions among the elements and with the environment can lead to a rich and sometimes non-trivial behavior for the mutual coupling. Reactive fields, occlusion (blocked line of sight), surface waves, and multi-path reflections off the ground plane, other elements, and nearby objects, could affect the observed coupling between elements. Exact modeling of these effects is challenging in simple, ideal scenarios and is impractical if not impossible in the continuously changing context of a flexible phased array. Fortunately, these effects are second order in many intra-array coupling scenarios, where a far-field-like propagation mode dominates. Instead of an electromagnetically complete coupling model, we aim to create a simplified model with sufficient accuracy for shape reconstruction and adaptability for use with a variety of element radiator types.

The underlying philosophy behind Spiral Match is to match the measured coupling to distance using far-field properties of the element antennas as the individual antenna properties can be easily measured and are relatively insensitive to array shape. We

start by approximating the coupling between antennas i and j in terms of the electric field of a far-field propagating plane wave, i.e.,

$$S(|l_{mn}|) \approx \frac{A}{|l_{mn}|} e^{-j(\omega t + k|l_{mn}|)} \quad (4.5)$$

where $|l_{mn}|$ is the linear distance between antennas m and n , k is the wave number, ω is the angular frequency, and A is an arbitrary amplitude scaling factor. It is assumed that phase grows linearly with distance between antennas ($|l_{mn}|$) and the coupled power falls off as $\frac{1}{|l_{mn}|^2}$.

To evaluate this approximation, a simple study is performed with two 2.5 GHz ground plane backed folded dipole antennas (described in detail in Section 4.3). The coupling between dipole antennas was measured vs. their distance, as shown in Fig. 4.25a. Note that the ground plane is modified to maintain continuity at all distances. The coupling power and phase are plotted in Fig. 4.25b-c. The measured coupling power is accompanied by two trendlines: the first follows the Friis $\frac{1}{|l_{mn}|^2}$ trend, the second following a $\frac{1}{|l_{mn}|^4}$ trend¹³.

The coupling phase measurements roughly follow the linear trend predicted by the expression for a far-field propagating wave. Fig. 4.26 compares the pair measurement results to the coupling measurements between elements in a flat, 8 element 1D array of the same folded dipoles with pitch of 72 mm. Since the element pitch is fixed, in-array phase measurements only exist at multiples of 72 mm. These measurements also follow the linear model suggesting that the presence of other elements in the array does not significantly disturb the phase of the propagation. While the measured phases in the study do not match the linear model precisely, they do suggest that the trend holds.

While a more accurate and complex phase model *could* be developed, there is a fundamental trade-off between the specificity of the antenna models and the generality of the algorithm; we have taken the position of keeping the model more general.

¹³This $\frac{1}{|l_{mn}|^4}$ trend is commonly observed for communications systems with signals travelling long distances over an infinite conductive or lossy surface (usually the earth) [65]. For close distances, the measured coupling follows the $\frac{1}{|l_{mn}|^4}$ as the ground plane approximates an infinite conductive surface. However, as the distance between antennas increases the infinite surface approximation no longer holds as the ground plane becomes relatively narrow and the measured coupling returns to the $\frac{1}{|l_{mn}|^2}$ trend. This change in the distance exponent has a relatively small effect on the final shape reconstruction accuracy but emerges from a known, measurable phenomenon and can be incorporated into Spiral Match for a given array without much added modelling complexity.

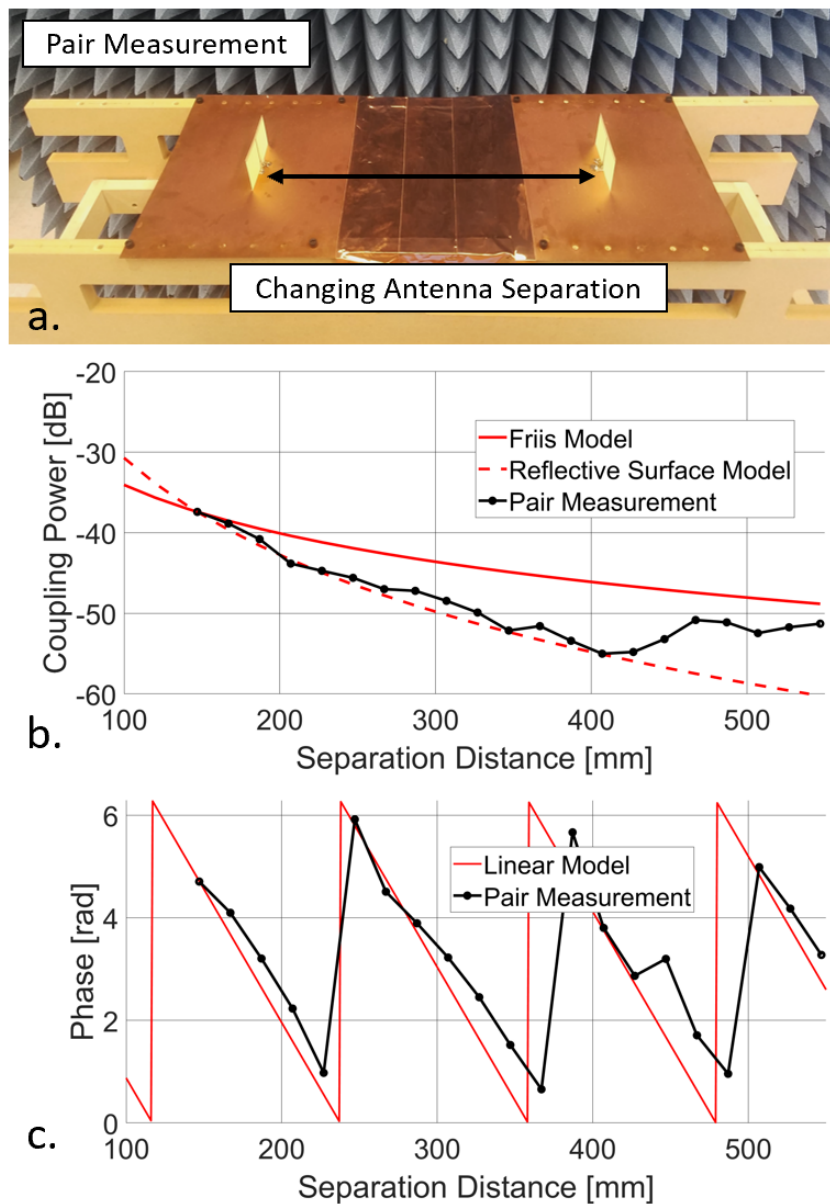


Figure 4.25: (a) Antenna pair coupling study test set-up. Continuous ground plane is maintained for all antenna distances. (b) Coupling power measurement compared with two different propagation models. Measurement averaged over the bandwidth from 2.3 to 2.7 GHz. (c) Coupling phase measurement plot. Antenna pair measurements compared with far-field linear phase propagation model. Measurement is at 2.48 GHz. In both the power and phase plots linear model traces are normalized to the first measured distance.

Under the coupling scenarios of Fig. 4.25, the elements experience relative position changes but no relative rotation. However, when a flexible phased array is bent, its elements experience changes in both position and orientation. To account for

the change in coupling due to this rotation we employ the far-field radiation pattern of the element antennas. Element radiation patterns can be determined through analysis, simulation, or measurement.

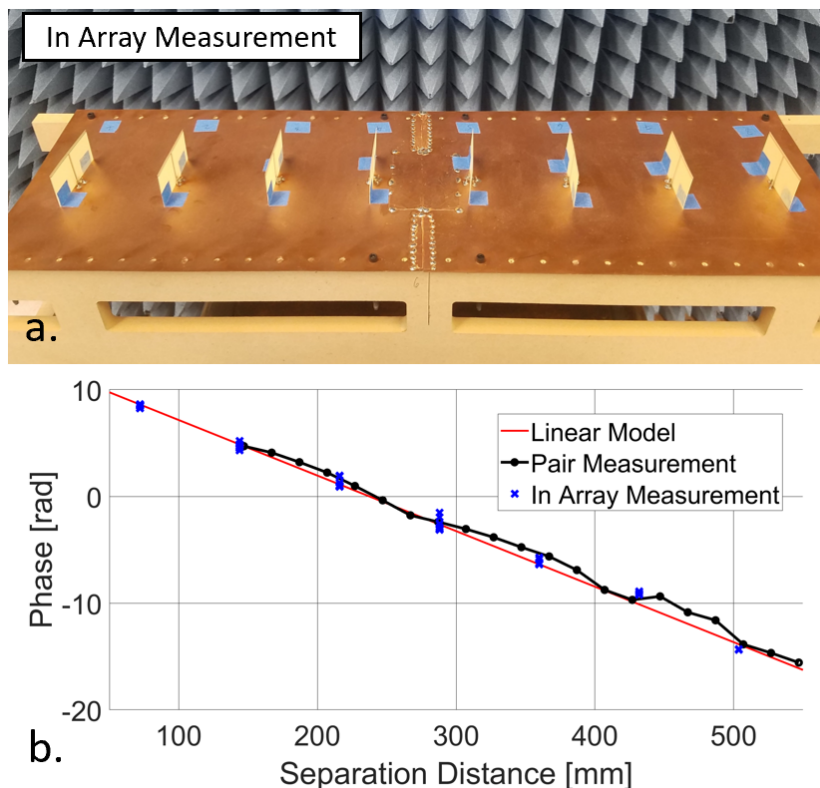


Figure 4.26: (a) Ground plane backed dipole array. (b) Unwrapped coupling phase measurement plot. In array measured phased is compared to antenna pair measurements and far-field linear phase propagation model. Measurement is at 2.48 GHz. Traces are normalized to the first pair measurement distance.

We will demonstrate that although far-field phase propagation and radiation pattern are imperfect models of the coupling between elements within a phased array, they can be used to produce accurate shape reconstructions.

With the motivation for and justifications of the Spiral Match clarified, the following section details its implementation and the nuances which emerge.

Spiral Match

In this section, we will discuss the details of Spiral Match, which is a candidate for PCM. The name Spiral Match is inspired by the spiral shape generated in a polar plot of the decaying amplitude and rotating phase vs. distance of propagating waves.

Definitions and Assumptions

Our overall goal is to generate a bijection (i.e., a one-to-one correspondence) between mutual coupling and distance. We begin by modeling the raw mutual coupling matrix $S \in \mathbb{C}^{N \times N}$ for a 1-dimensional phased array¹⁴ as

$$S_{mn} = \frac{a_m D_m(\theta_{mn}) a_n D_n(\theta_{nm})}{|l_{mn}^{\vec{}}|} e^{-j(\phi_m + \phi_n + k|l_{mn}^{\vec{}}|)} \quad (4.6)$$

$$\theta_{mn} = \cos^{-1} \left(\frac{\hat{r}_m \cdot l_{mn}^{\vec{}}}{|l_{mn}^{\vec{}}|} \right) \quad (4.7)$$

where a_m is the total fixed amplitude offset (due to line attenuation, mismatch, gain, etc.) in antenna m , $D_m(\theta)$ is the directivity of antenna m for an angle θ relative to broadside, $l_{mn}^{\vec{}}$ is the vector pointing from the phase center of antenna i to the phase center of antenna n , ϕ_m is the total fixed phase offset in antenna m , and \hat{r}_m is the unit vector normal to the surface of the array, that describes the orientation of antenna m . We take $D_m(\theta = 0) = 1$ for all m s. We assume no significant angle-dependence for the phase response of the antenna.

As is evident, there are amplitude and phase offset terms that can prevent us from drawing a bijection between coupling and distance. To isolate the distance terms, we perform a one-time calibration of the array in the completely flat configuration. The information gathered during this measurement is another coupling matrix, S^{flat} :

$$S_{mn}^{\text{flat}} = \frac{a_m D_m(\theta_{mn}^{\text{flat}}) a_n D_n(\theta_{nm}^{\text{flat}})}{|l_{mn}^{\text{flat}}|} e^{-j(\phi_m + \phi_n + k|l_{mn}^{\text{flat}}|)} \quad (4.8)$$

Because the geometry of the flat configuration is fixed and known, we can make some basic assumptions to simplify the model for flat coupling. First, in a flat array $\theta_{mn}^{\text{flat}} = \frac{\pi}{2}$, when $m \neq n$. Moreover, assuming our array is composed of identical antennas, $D_n(\theta) = D_m(\theta) = D(\theta)$ for all m 's and n 's. Thus, we can simplify our flat coupling model to:

$$S_{mn}^{\text{flat}} \cong \frac{a_m a_n D \left(\frac{\pi}{2} \right)^2}{|l_{mn}^{\text{flat}}|} e^{-j(\phi_m + \phi_n + k|l_{mn}^{\text{flat}}|)} \quad (4.9)$$

¹⁴The model for a 2D phased array is very similar, and involves only changing the directivity function to a function of two variables (i.e., $D_i(\theta_{mn}, \varphi_{mn})$), the azimuth and elevation angles between elements m and n .

Moreover, $|\vec{l}_{mn}^{\text{flat}}|$ is known in advance. To eliminate the fixed power and phase offsets, we define the normalized transfer function, H :

$$H_{mn} \equiv \frac{S_{mn}}{S_{mn}^{\text{flat}}} \quad (4.10)$$

$$= \frac{D(\theta_{mn})D(\theta_{nm})}{D\left(\frac{\pi}{2}\right)^2} \frac{|\vec{l}_{mn}^{\text{flat}}|}{|\vec{l}_{mn}|} e^{-jk(|l_{mn}| - |\vec{l}_{mn}^{\text{flat}}|)} \quad (4.11)$$

$$\{Q, \Lambda\} = \text{evd}\left(-\frac{1}{2}JEJ\right)$$

$$x = \text{diag}\left(\sqrt{\lambda_1}, \dots, \sqrt{\lambda_d}, \mathbf{0}_{(n-d)}\right) Q^T$$

Constant Curvature Assumption

The dependence of the transfer function, H , on the angle matrix, θ presents a complication. Angles θ_{mn} and θ_{nm} are two *additional* degrees of freedom, theoretically independent of $|\vec{l}_{mn}|$, that present a challenge to finding a bijection between coupling and distance. In the case of two mechanically detached radiators, each of the three variables $|\vec{l}_{mn}|$, θ_{mn} , and θ_{nm} can induce changes in the coupling independently.

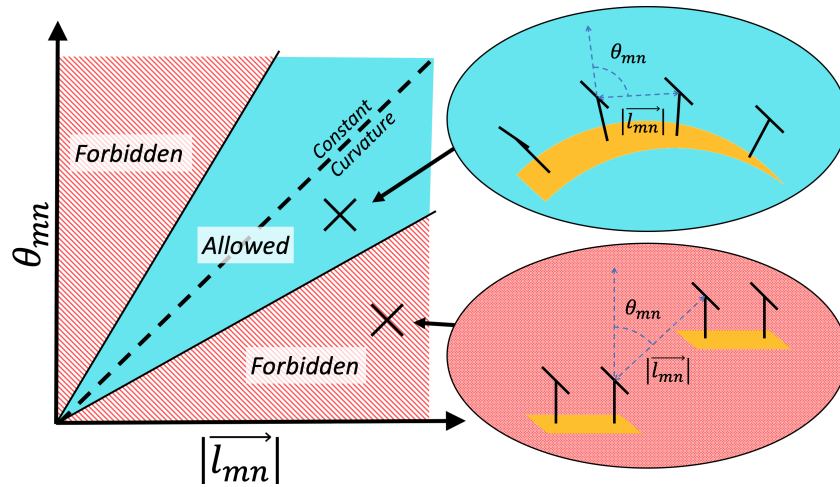


Figure 4.27: A visualization of forbidden and allowed regions of the $\theta_{mn} \otimes |\vec{l}_{mn}|$ vector space for physically restricted phase arrays. The “constant curvature” line is shown in dashed blue in the center of the allowed region. We also illustrate an example of a shape that generates an allowed $\{\theta_{mn}, |\vec{l}_{mn}|\}$ pair (top right) and a forbidden $\{\theta_{mn}, |\vec{l}_{mn}|\}$ pair (bottom right). As we can see, the forbidden $\{\theta_{mn}, |\vec{l}_{mn}|\}$ pair can only be generated if the array is cut in half.

However, because our radiators are fixed to a non-stretchable ground plane¹⁵, mechanical constraints in this system reduce the allowable space of parameters from all of \mathbb{R}^3 to a smaller subspace in \mathbb{R}^3 . To illustrate this, let us consider the special two dimensional case of only $|\vec{l}_{mn}|$ and θ_{mn} ; the mechanical constraint has the effect of partitioning \mathbb{R}^2 into “forbidden” and “allowed” subspaces, where pairs of $\{|\vec{l}_{mn}|, \theta_{mn}\}$ in the “forbidden” subspace are incompatible with the mechanical constraint, as illustrated in Figure 4.27. The “allowed” pairs occupies a subspace in the shape of a triangular wedge: for some distances, the angular freedom is highly restricted and for other distances the angular freedom is large¹⁶.

There are multiple methods of dealing with the problem of optimizing over a high dimensional space while respecting the mechanical constraints at play. One is to computationally simulate the array and generate the $\{|\vec{l}_{mn}|, \theta_{mn}, \theta_{nm}\}$ triplets through brute force. Another is to attempt to characterize this subspace analytically. Finally, we have the option of assuming this subspace is very thin, and treating it as a line. This third option is equivalent to assuming the array ground plane only takes on shapes of constant curvature and this is the option we elect to use for the purposes of this paper¹⁷. This is reasonable, as in most practical case where the surface bends smoothly without sharp kinks, the local curvature in a small neighborhood of several adjacent antennas can be considered constant. This allows our approach to be applied locally even for non constant curvature cases.

Furthermore, the signal-to-noise ratio (SNR) of measurements between elements that are far apart, with many intervening elements, is lower than elements within a smaller neighborhood (due to occlusion, reflections, attenuation, etc.) and do not contribute a great deal to the overall quality of the shape reconstruction¹⁸. As

¹⁵Even a stretchable ground plane places restrictions on antenna mobility and introduces a mechanical constraint that reduces the allowable space of independent variables, though to a lesser degree.

¹⁶Two caveats about the exact visualization presented:

1. This plot looks different for different antenna pairs and is characterized by $|\vec{l}_{mn}^{\text{flat}}|$.
2. The exact appearance presented here is inaccurate: The allowed region may not grow positively with increasing distance. The constant curvature assumption is not guaranteed to be a line. The space may not be symmetric.

¹⁷It should be noted that the general framework presented so far does not depend on this assumption and implementations of the first two options are certainly possible.

¹⁸This assumption does not preclude an ability to reconstruct the shape of phased array systems with large numbers of elements. We can instruct our algorithm to only measure and model local measurements which can each have a different curvature. Although for each small neighborhood of antennas a constant local curvature is assumed, the curvature for an adjacent (and possibly overlapping

we will see in Section 4, coupling measurements between far apart elements have a diminishing impact on shape reconstruction, and thus it is not necessarily important how we model them.

Using the constant local curvature assumption, we have reduced the space of independent variables to \mathbb{R}^1 and have thus found a bijection between θ_{mn} and $|l_{mn}^{\vec{}}|$. This implies we can replace our angle-dependent directivity, $D(\theta_{mn}(|l_{mn}^{\vec{}}|))$, with a distance-dependent directivity, $D(|l_{mn}^{\vec{}}|)$. This simplifies our transfer function model to:

$$H_{mn} = \frac{D(|l_{mn}^{\vec{}}|)^2 |l_{mn}^{\text{flat}}|}{D(|l_{mn}^{\text{flat}}|)^2 |l_{mn}^{\vec{}}|} e^{-jk(|l_{mn}^{\vec{}}| - |l_{mn}^{\text{flat}}|)} \quad (4.12)$$

We choose to determine the relationship between θ_{mn} and $|l_{mn}^{\vec{}}|$ computationally; we begin by geometric modeling of the array. An example of the array model with a constant radius of curvature is shown in Figure 4.28, where a 2.5 GHz flexible phased array with 0.6λ antenna spacing and dipole antennas that extend 0.25λ normal to the local ground plane is shown.

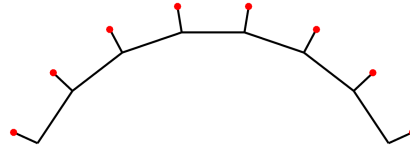


Figure 4.28: A side view of a flexible phased array ($f = 2.5$ GHz, 0.6λ antenna spacing, quarter-wave dipole antennas) with constant curvature, $R = -0.222m$. Ground plane and dipole feed in black, antennas in red.

We iterate over a large number of radii of curvature¹⁹, where $R < 0$ correspond to convex array orientation and $R > 0$ to concave array orientation. At each iteration, we generate one-to-one mappings $R \xrightarrow{\mathfrak{N}} |l_{mn}^{\vec{}}|$ and $R \xrightarrow{\mathfrak{I}} \theta_{mn}$. To generate our bijection, we simply invert \mathfrak{N} :

$$\theta_{mn}(|l_{mn}^{\vec{}}|) = \mathfrak{I}(\mathfrak{N}^{-1}(|l_{mn}^{\vec{}}|)) \quad (4.13)$$

Practically, this is implemented simply as a vector of θ_{mn} and a vector $|l_{mn}^{\vec{}}|$, which are paired, and correspond to a vector of curvature radii.

set) can be different, leaving open the possibility for a shape with varying curvature.

¹⁹In this example, $R \in \pm[0.025, 1]$ m

We now have a bijection between distance and angle, pushing us one step closer to incorporating directivity in our model. To quantify directivity, there are a number of options: analytical antenna model, simulated directivity pattern, and direct measured results. Any of these options yields a function $D(\theta)$, which completes our model for the transfer function, H .

Iterative Spiral Match

Armed with a model that draws a bijection between mutual coupling and distance, we can theoretically execute Spiral Match. The Euclidean distance between the elements m and n , as defined by (4.4), can be estimated by minimizing the magnitude of the difference between the measured transfer function, $H_{mn}^{\text{meas}} = S_{mn}^{\text{meas, bent}} / S_{mn}^{\text{meas, flat}}$, and the estimate of (4.12):

$$E_{mn} = \left(\arg \min_{|\vec{l}_{mn}| \in [d_{mn}^{\min}, d_{mn}^{\max}]} \left| H_{mn}^{\text{meas}} - H_{mn}(|\vec{l}_{mn}|) \right| \right)^2 \quad (4.14)$$

where d_{mn}^{\min} , d_{mn}^{\max} are the minimum and maximum physically possible distances for the antenna pair. This can be envisioned as the projection of the measurement H_{mn}^{meas} onto the closest location on a spiral generated by H_{mn} , shown in Fig. 4.29, and is the essence of Spiral Match. This location corresponds to the predicted distance, $|\vec{l}_{mn}|$. Unfortunately, because of measurement noise and imperfection, solving for the Euclidean distance in a single step led to errors, which can result in potentially non-physical solutions.

Single step Spiral Match projection is prone to issues in the presence of non-line-of-sight (NLOS) element coupling for convex configuration, where NLOS and surface-mode coupling can dominate. In this case, power changes do not follow the simple directivity model. Additionally, amplitude ambiguity at a given phase for an imperfect measurement can lead to erroneous projection of the measurement onto an incorrect segment of the spiral (introducing distance error on the order of λ).

Small distance error is acceptable and can potentially be fixed in the second step of our framework SDR (semi-definite relation); large distance error, however, often makes SDR unworkable and results in a completely erroneous shape prediction. Mitigating large distance error is the intention of the iteration process discussed below.

To mitigate these issues, we invoke Spiral Match in a number of iterations, each time adding more constraints to the system to help ensure the accuracy of the predicted

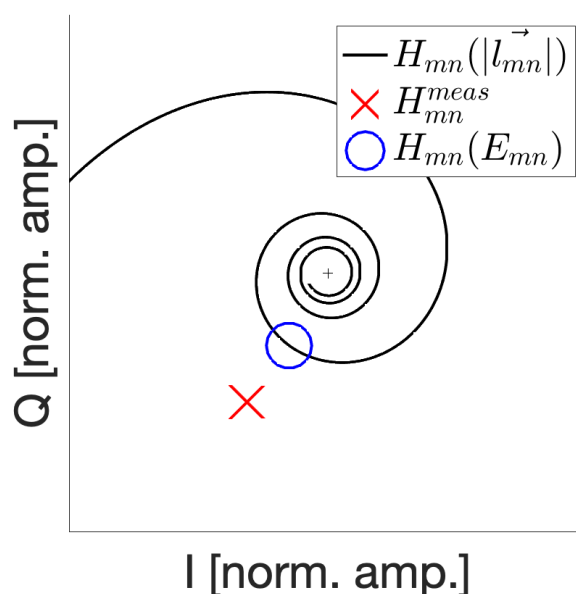


Figure 4.29: A visualization of the Spiral Match algorithm. In black, the coupling transfer function model, $H_{mn}(|\vec{l}_{mn}|)$, for variable distance is given. The red “X” is our measured coupling, H_{mn}^{meas} . It is “projected” onto the model via the argmin function to give us the blue circle, which is the position on the model that corresponds to our predicted distance, E_{mn} .

| Iteration # | Constraint(s) | Action | Result | Calculation | Output |
|-------------|-----------------------------|--------------------------------|--------|--------------------|-------------------|
| 1 | - | - | E^1 | Calculate polarity | Polarity |
| 2 | Polarity | Add directivity if concave | E^2 | Run RWC | Phase wrap matrix |
| 3 | Polarity, Phase wrap matrix | Restrict distance search space | E^3 | - | - |

Table 4.1: Iterations of Spiral Match

Euclidean distance. These iterations and the associated constraints are shown in 4.1. In the first iteration, we assume no curvature polarity (concave/convex) to minimize constraints on the problem. Without a polarity, we make no assumption of the geometry, and, thus, *do not* include directivity in the model. For the first pass, we assume $D(|\vec{l}_{mn}|) = 1, \forall i, |\vec{l}_{mn}|$ and use the optimization function in Eq. 4.14 to compute the first prediction of the EDM, E^1 . The result of this first iteration is a very crude prediction of Euclidean distance that is sufficiently accurate to determine

the polarity of the shape. The polarity $p \in \{-1, +1\}$ (-1 being convex and $+1$ being concave) is decided using a voting scheme²⁰:

$$p = \text{sign} \left(\sum_{i \neq j} \text{sign} \left(|l_{mn}^{\vec{\text{flat}}}| - E_{mn}^1 \right) \right) \quad (4.15)$$

In the second iteration, we use p to inform whether or not to include directivity in the coupling model. The second prediction of the EDM, E^2 is computed using the optimization function in (4.14). Having eliminated ambiguity about polarity and including the directivity for concave shapes, we can turn our attention to the problem of phase wrapping-induced distance error. These errors are on the order of λ , which is often large enough to violate physical constraints, and so it becomes germane to develop such a solution that will intelligently identify violations. We call it ‘‘Recursive Wrap Correction’’ (RWC).

RWC is an algorithm that converts a matrix of integers, $R \in \mathbb{Z}^2$, representing the number of complete phase wraps associated with the distances in E^2 , to a ‘‘corrected’’ phase wrap matrix, R' . It can also correct for outlier measurements not caused by phase-wrapping that may carry large distance error. The details of RWC can be found in the appendix of [42].

In the third iteration of the Spiral Match algorithm, the search space for distance is truncated to a single one-wavelength range as follows:

$$|l_{mn}^{\vec{}}| \in [R'_{mn}\lambda, (R'_{mn} + 1)\lambda] \quad (4.16)$$

to ensure that all predicted distances have the same number of wraps as RWC predicted. If R' is correct, this has the effect of ensuring there are no phase wrapping-induced distance errors, which improves Spiral Match’s accuracy. Spiral Match culminates with a final minimization, using the reduced search space:

$$E_{mn}^3 = \left(\arg \min_{|l_{mn}^{\vec{}}| \in [R'_{mn}\lambda, (R'_{mn} + 1)\lambda]} \left| H_{mn}^{\text{meas}} - H_{mn}(|l_{mn}^{\vec{}}|) \right| \right)^2 \quad (4.17)$$

At this point, it’s unlikely E^3 is perfectly symmetric. This is acceptable for the purposes of the next step (ASC) but it can be advantageous because we have two

²⁰ $N^2 - N$ pairs is an even number and it’s possible that $p = 0$. If this happens, it’s likely because $|l_{mn}^{\vec{\text{flat}}}| - E_{mn}^1 \approx 0$ and a small degree of error in E_{mn}^1 is pushing the difference above and below zero for different (i, j) . In this case, the array is likely in a flat or an approximately flat shape and the choice of polarity is almost irrelevant. In the algorithm, we overwrite $p = 0$ cases to have $p = +1$ for these incredibly rare circumstances.

candidates for distance for each element pair. We can leverage this advantage by finding some metric to compare these two, and opting to use the better one. An obvious candidate for this metric is the “projection error”, ΔH , defined as:

$$\Delta H_{mn} = \min_{|\vec{l}_{mn}| \in [R'_{mn}\lambda, (R'_{mn}+1)\lambda)} \left| H_{mn}^{\text{meas}} - H_{mn}(|\vec{l}_{mn}|) \right| \quad (4.18)$$

which corresponds to the distance in the complex plane between the measurement and the model at the predicted point, E_{mn}^3 . A large projection error is an indication that the model does not possess a complex value close to the measurement, implying large measurement error. However, this implication only holds some of the time; we have observed that this correlation between prediction error and projection error occurs for the patch antennas discussed below, but not for the dipole antennas. Because this is another “switch”, we can elect to turn flip it or not. To “flip it”, we force the EDM to be symmetric using the projection error as the deciding metric:

$$E_{mn}^{3'} = \begin{cases} E_{mn}^3 & \Delta H_{mn} \leq \Delta H_{nm} \\ E_{nm}^3 & \Delta H_{mn} > \Delta H_{nm} \end{cases} \quad (4.19)$$

where $E^{3'}$ is the symmetricized version of E^3 . E^3 (or $E^{3'}$) is the input to the second phase of the shape reconstruction framework algorithm, discussed below.

A Candidate for ASC: Semi-Definite Relaxation

Using a prediction of the EDM corresponding to antenna phase centers on a flexible phased array, E^3 , we can solve the problem of reconstructing relative position, or shape. Like many other high-dimensional problems, this can be solved with a single eigenvalue decomposition [34]. Solving the position problem with an EDM in this way is called “Classical Multi-Dimensional Scaling” (MDS), which involves few matrix operations. MDS, simple as it is, typically fails for imperfect EDMs. If, for example, $E_{mn} = |r_i - r_j|^2 + \alpha_{mn}$, where α_{mn} is some noise-adding term, our eigenvalue decomposition may yield complex (i.e. non-physical) eigenvalues. Additionally, sparse or mislabeled EDMs cannot be used with MDS. A number of algorithms have been written and studied for different purposes and qualify as candidates for the second transformation, ASC [34].

In this system, we do not suffer from sparse or mislabeled EDMs and choose to use semi-definite relaxation (SDR)²¹ as the candidate for ASC, for the following reasons:

²¹We implemented SDR as recommended in [34], written in MATLAB using “cvx”, a framework for performing convex optimization in MATLAB [56].

1. SDR offers the option to use a mask matrix W to weight elements in the EDM individually. This allows us to control how much each EDM entry “matters”. Because local coupling measurements have higher quality than distant measurements, we want to be able to weight local measurements more.
2. SDR searches a much smaller, convex vector space and, thus, guarantees a physical result while also decreasing runtime.
3. SDR showed the best performance along multiple metrics in [34].

The option to use a mask matrix W to window entries that have not been collected (i.e. in mic/speaker localization in a large theatre) is an option that allows us to use this method for large array systems, or ones where some elements have only either a receiver or a transmitter. In this work, we collect a completely dense EDM, and we use a mask matrix to weight entries based on SNR.

Recognizing that $\text{SNR}(S_{mn}) \propto \frac{1}{|l_{mn}|^2}$, it is likely that EDM error, δE , defined as:

$$\delta E_{mn} = \left| |l_{mn}^{\vec{}}| - E_{mn}^3 \right| \quad (4.20)$$

follows the general trend:

$$\delta E_{mn} \propto |l_{mn}^{\text{flat}}|^k \quad (4.21)$$

where k is some unknown exponent. We can leverage this known relationship by weighting higher quality EDM entries more than lower quality ones. The intuitive approach to implement this is to have entries in matrix W decrease as we move away from the diagonal.

We have the freedom to design W as we choose, based on the system, to minimize shape reconstruction error. We have explored a number of structures for W , some of which are presented in Table 4.3. In most of these structures, we have a design “knob” that can be turned to adjust for different systems and optimized to minimize shape reconstruction error. We have found the best performance with a mask matrix where entries are uniform for close pairs and exponential for far pairs.

Passive Flexible Phased Arrays

Test Apparatus

In order to validate the proposed shape reconstruction method, we built several connectorized flexible phased arrays. While lacking the dynamic, multi-purpose

Table 4.2: EDM Mask Matrix Structure Candidates

| Type | Equation | Knob(s) |
|-------------|--|-----------|
| Uniform | $W_{mn} = 1$ | - |
| Binary | $W_{mn} = \begin{cases} 1 & m - n < a \\ 0 & m - n \geq a \end{cases}$ | a |
| Linear | $W_{mn} = a m - n + b$ | a, b |
| Quadratic | $W_{mn} = a m - n ^2 + b m - n + c$ | a, b, c |
| Exponential | $W_{mn} = a^{-b m-n } + c$ | a, b, c |

capabilities of an integrated flexible phased array, connectorized arrays allow for quick measurements of mutual coupling (e.g., by a standard vector network analyzer). The connectorized array elements are designed to have center frequencies close to 2.5 GHz with element pitch of 0.6λ . Results from eight-element, 1D arrays with folded dipole and patch antennas are presented in the following subsections.

A block diagram of the measurement setup of a connectorized array on the rigid frame is depicted in Fig. 4.30. In order to measure the full coupling matrix of the array without changing connectors, each element connects to an RF splitter then two digitally controlled 8-to-1 RF multiplexers, which are then connected to the ports of a vector network analyzer. A computer and script controls the multiplexers, triggers the VNA, and logs the coupling measurements. To flex the connectorized arrays into known shapes in a quick and repeatable fashion, rigid wooden frames of known convex and concave bend radii were designed and built. These frames are shown in the first column of Fig. 4.34.

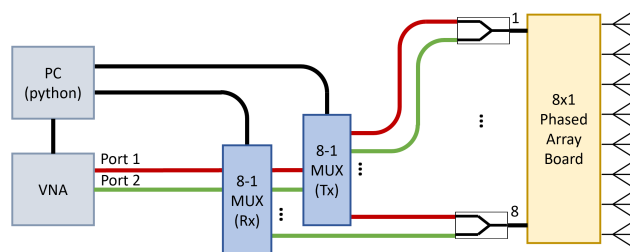


Figure 4.30: Test set-up for coupling measurements of connectorized arrays.

Folded Dipole Array Results

The folded dipole used in the measurements is shown in Fig. 4.31. Ground plane backed dipoles (folded or unfolded) are well suited to mutual coupling shape reconstruction. Radiation from a dipole originates from the current distribution on the arms and is initially omni-directional (except for the direction along the arms themselves) prior to reflection off of the ground plane. Because this omni-directional radiation originates well above the ground-plane, the coupling is less sensitive to occlusion and has propagation properties close to the ideal far-field assumed by our simplified propagation model. The folded dipole presents an input impedance of 275Ω at its arms. A high impedance edge-coupled quarter-wave transmission line extends to ground plane, transforming the antenna input impedance and connecting to a 50Ω SMA connector.

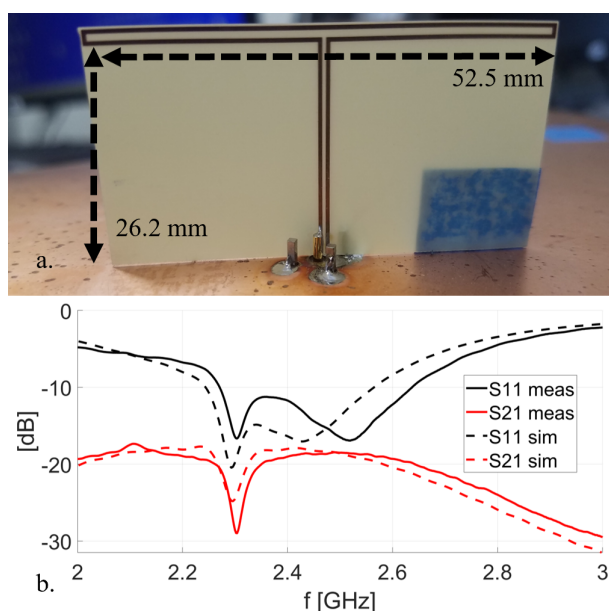


Figure 4.31: (a) Folded dipole antenna design dimensions. (b) Measured and simulated folded dipole input matching and adjacent element coupling.

The folded dipole array shape reconstruction results are shown in Fig 4.32. The far-field radiation pattern used in the algorithm was determined using a finite difference time domain (FDTD) simulator. The accuracy of Spiral Match is measured by ΔE , the mean element pair distance error. ΔE is the mean difference between the predicted distances and the “truth” distance predicted by the known physical design dimensions of the frames. The accuracy of the shape reconstruction is measured by Δx , which is the mean difference between the reconstructed element position and the

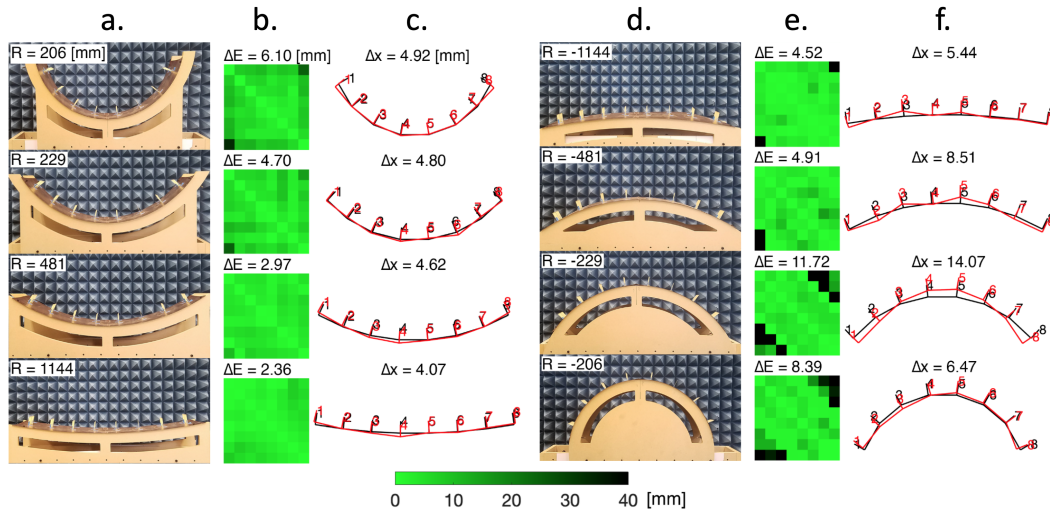


Figure 4.32: Shape reconstruction results for passive 2.5 GHz folded dipole phased arrays. a. Concave wooden frames with dipole antennas and curvature radii. b. EDM error heatmaps and mean EDM error (ΔE) for concave shapes. c. Reconstructed antenna shapes (red), true antenna shapes (black), and mean shape error (Δx) for concave shapes. d. Convex wooden frames with dipole antennas and curvature radii. e. EDM error heatmaps and mean EDM error (ΔE) for convex shapes. f. Reconstructed antenna shapes (red), true antenna shapes (black), and mean shape error (Δx) for convex shapes.

position of the elements according to the frame design dimensions. An exponential weighting matrix was used within the semidefinite relaxation algorithm.

Patch Antenna Array Results

The next array used for testing the shape reconstruction algorithm is an eight element linearly polarized patch antenna array. While the folded dipole antennas are near ideal candidates for shape reconstruction, patch antennas present a greater challenge. The challenges offered by patch antennas are a bellwether for if shape reconstruction could be a ubiquitous tool for a wide variety of flexible arrays or is limited to a narrow subset of ideal systems. Typical patch antennas are low profile, highly resonant, and inherently directional with radiation emerging from fields located at both ends of the patch along its excitation axis (E-field line). In a flexible array, their low profile means they are more susceptible to occlusion and do not share the pseudo-omnidirectionality of the ground plane backed dipoles. The highly resonate nature (particularly when built on thin substrates) leads to low matching bandwidth. Low matching bandwidth can effect the quality of coupling measurements as a pair of

patches could de-tune from each other as the array changes shape.

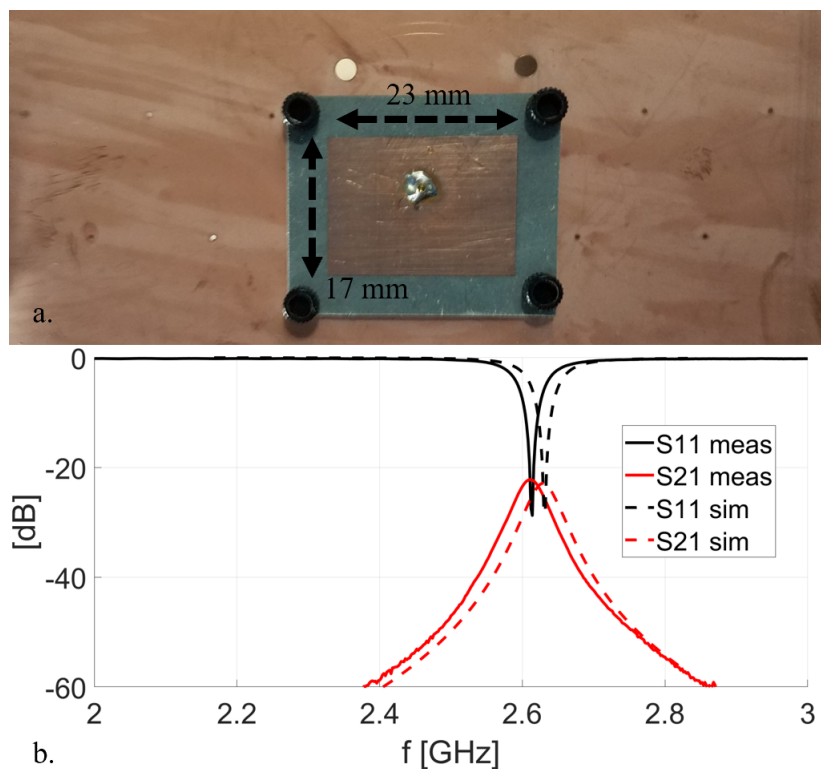


Figure 4.33: (a) Patch antenna design dimensions. The substrate extends 5 mm around the copper patch. (b) Measured and simulated patch antenna input matching and adjacent element coupling.

The presented patch antenna, depicted in Fig. 4.33, is made with 1.27 mm thick high dielectric substrate (ϵ_r 11.2) in order to reduce their size and better facilitate bending. The feed is inset by 6.35 mm in order to match to 50 ohms. The far-field radiation pattern used in the algorithm was determined using an FDTD simulator. The results of the patch antenna shape reconstruction is shown in Fig. 4.34. The patch antennas shape reconstruction is as accurate as the dipole reconstruction with the exception of the most convex shape. The final matrix in Fig. 4.34 shows higher error in the off diagonal element pair distances which would indicate that occlusion caused by the extreme bend is the culprit. Despite this, the results show the viability of the shape reconstruction algorithm for radiator with tightly confined near-field profile.

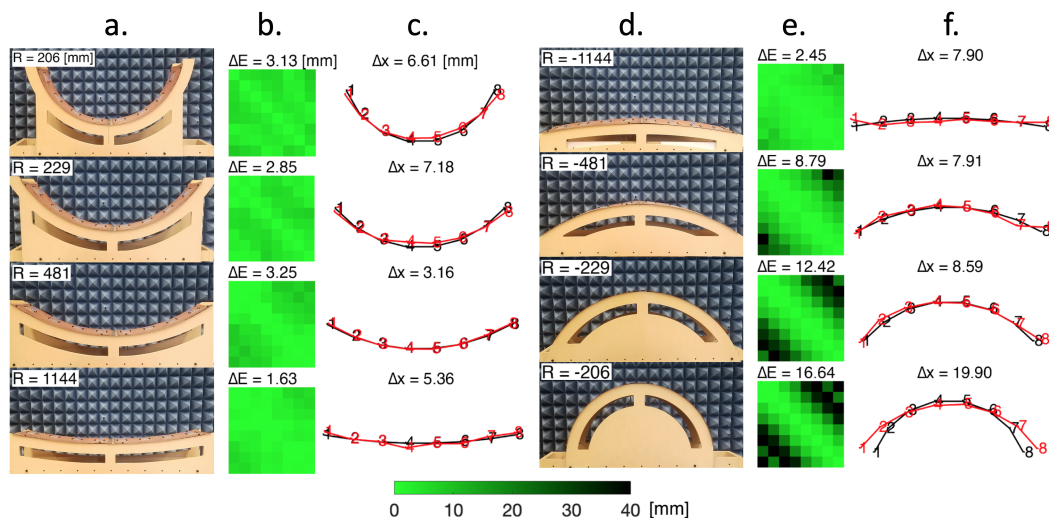


Figure 4.34: Shape reconstruction results for passive 2.5 GHz patch antenna phased arrays. (a) Concave wooden frames with patch antennas and curvature radii. (b) EDM error heatmaps and mean EDM error (ΔE) for concave shapes. (c) Reconstructed antenna shapes (red), true antenna shapes (black), and mean shape error (Δx) for concave shapes. (d) Convex wooden frames with patch antennas and curvature radii. (e) EDM error heatmaps and mean EDM error (ΔE) for convex shapes. (f) Reconstructed antenna shapes (red), true antenna shapes (black), and mean shape error (Δx) for convex shapes.

Active Integrated Flexible Phased Array Array Design

While the passive, connectorized arrays presented above are useful tools for understanding mutual coupling shape reconstruction, they do not provide the utility of a fully integrated flexible phased array. A truly self-contained flexible phased array is enabled by RFICs, which combine array element functions (frequency synthesis, phase shifting, power amplification, etc.) in a compact and low-profile package. Conventional silicon ICs are rigid, but are sufficiently small as to not significantly change flexibility of a larger flexible phased array. An integrated circuit flexible phased array prototype was created to demonstrate mutual coupling shape calibration and reconstruction. The implemented array is a 1D, eight-element transmit and receive capable array operating at 10 GHz built on a 4-layer flexible printed circuit board (PCB), as presented in [41] and shown in Fig. 4.35. The following subsections briefly describe the subcomponents of the array.

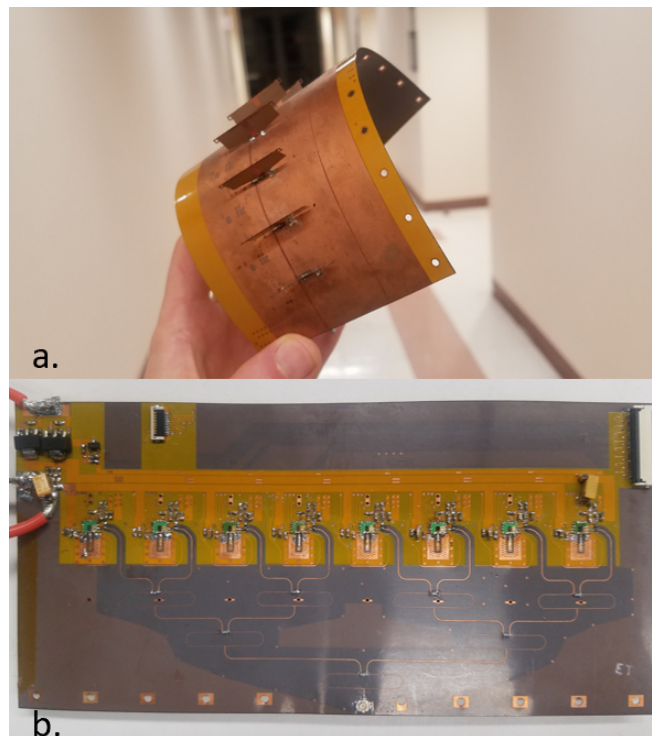


Figure 4.35: (a) Integrated circuit-based flexible phased array with 8 elements bent in hand with front shown. (b) Array back with feed network, chips, interposers, and circuitry shown.

Element Circuit

Each element circuit consists of a custom single channel transmitter/receiver integrated circuit which is implemented in a standard 65nm CMOS process. While the space solar power tile and 256 array prototypes use a 16 channel RFIC, the shape calibration array is formed by single channel chips with similar subcircuit blocks. The block diagram is shown in Fig. 4.36 and RFIC die photo and interposer are shown in Fig. 4.37.

The RF path of the RFIC starts with a 2.5 GHz phase reference signal, which is shared by all elements in the array. The phase reference is used by the phase-locked loop (PLL) to synthesize 10 GHz IQ signals. The PLL uses programmable divider current injection to provide $360^\circ+$ phase control to its output which is fed to both the transmit and receive paths. An SPI digital interface controls all programmable sub-circuits. In the transmit path, the signal passes through a programmable IQ summation phase shifter which provides another independent 360° phase control. The phase shifter is controlled by a programmable SRAM, allowing for rapid phase-

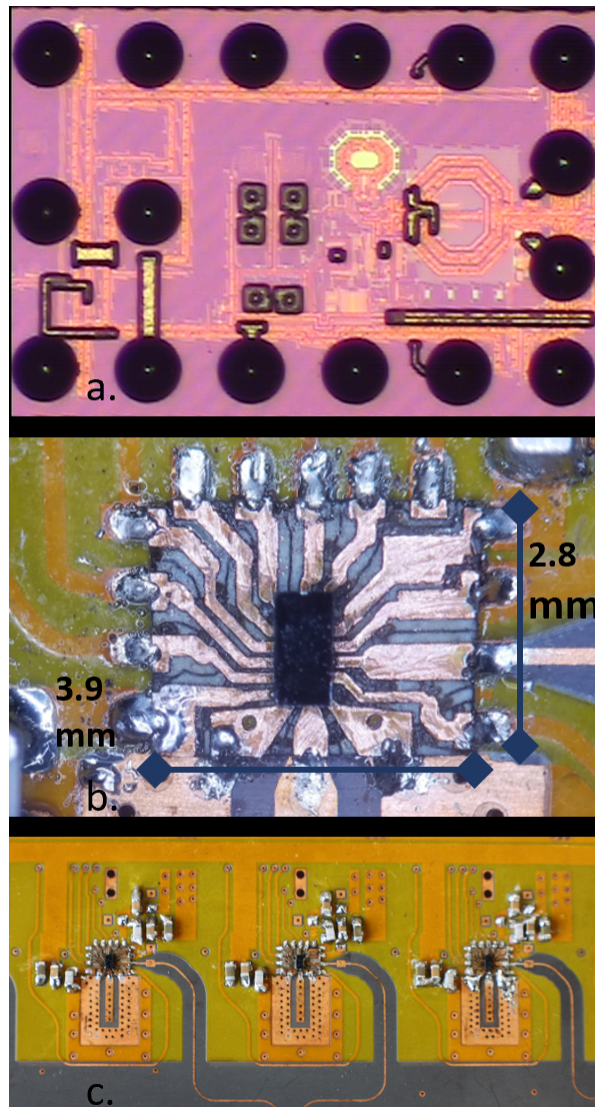


Figure 4.37: (a) RFIC die photo. (b) Interposer with RFIC. (c) 3 interposers mounted on flexible printed circuit board.

capacitors are aligned with the axis of bending to minimize their effect on overall stiffness, ensuring that bend radius is limited by plastic deformation of the flexible PCB.

Radiator

The radiator, built from a single sheet of copper on polyimide, is a ground plane backed dipole. By aligning the dipole arms with the axis of bending, the array can be flexed significantly without strongly affecting radiator performance. In addition to having favorable properties for shape reconstruction, ground plane backed dipoles

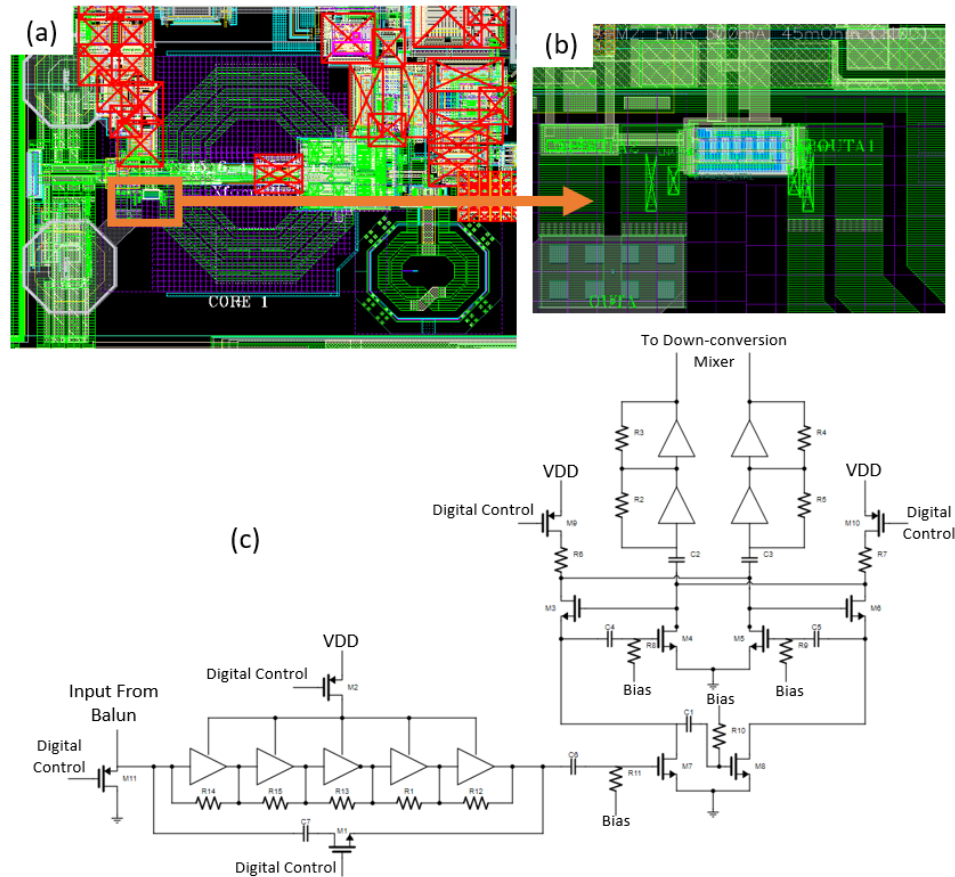


Figure 4.38: (a) Image of RFIC layout CAD file. PA output balun is shown in the center. The output leg which feeds receiver is boxed in orange. (b) Balun output leg is cut and large transistor switch is added. (c) Schematic of receiver circuit. Amplifier symbol represents an inverter.

provide the wide, single lobe pattern that is desirable for beam-steering applications. The radiator, shown in Fig. 4.39a, is mounted perpendicular to the surface of the ground plane which avoids the need for a thick, likely rigid, layer of substrate. Element pitch is 0.6λ . The measured and simulated far-field patterns with and without bending is shown in Fig. 4.39b-c. One leg of the radiator connects to a single-ended transmission line while the other is grounded. The vertical feed acts as a balun to convert the input to a differential drive for the radiating arms. Residual asymmetry is observed in Fig. 4.39b as the pattern tilts slightly towards the grounded leg. Overall, the simulated, flat, and bent results match closely. Deviation between bent and flat performance is present in the $\phi = 90^\circ$ cut where the bent result experiences slightly less lobe splitting than the flat simulated and measured results. This is consistent with the expectation that a convex bend increases element

spacing, decreasing the inter-element coupling which contributes to lobe splitting. This pattern change with array shape is small and does not meaningfully affect the quality of the shape reconstruction results.

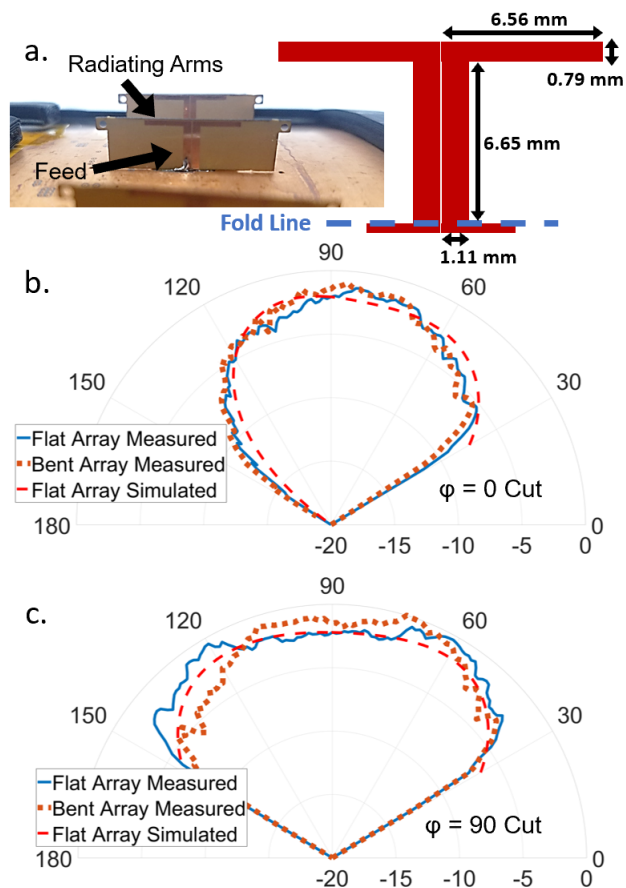


Figure 4.39: Element Radiator. (a) Radiators mounted on flexible printed circuit board and radiator dimensions. The feet beneath the fold line are soldered to the circuit board. (b) Measured and simulated in-array element pattern for $\varphi = 0^\circ$ cut. Pattern is measured flat and when array is conformed to a 120 mm convex bend radius. (c) Measured and simulated in-array element pattern for $\varphi = 90^\circ$ cut. All measurements are normalized to their global maximum.

Active Integrated Flexible Phased Array Shape Reconstruction

Shape reconstruction using the flexible integrated circuit-based phased array is demonstrated in Fig. 4.40. Eight rigid frames ($R = \pm 100, 150, 220, 400$ mm) were used to provide repeatable reference dimensions. The on-chip power amplifiers and receivers were used to collect the coupling measurements. When adjusted by a factor of four to account for wavelength difference between 2.5 GHz and 10 GHz,

the final shape error, Δx , outperforms the connectorized 2.5 GHz dipole array. The minimum, maximum, and average Δx is lower. While some of this performance increase can be contributed to a smaller ratio of bend radii to array length, it shows the viability of shape reconstruction in integrated circuit arrays. The shape reconstruction framework is shown to be frequency agnostic by these results. While the framework itself is agnostic, there are practical concerns for which frequency is involved. The 10 GHz array is smaller, as such nearby objects and reflectors relatively farther away and less likely to effect local coupling measurements through reflections. As such the higher frequency may be responsible for the more accurate results. Improved quality of coupling measurements does come with a mechanical trade-off. As the operation frequency of the array rises, its flexibility could decrease as the density of rigid or semi-rigid components and the complexity and thickness of signal routing increases with finer antenna pitch.

Generalizing For Other Systems

The framework presented in this work is multi-staged and multi-faceted, offering many opportunities for modification and expansion. In this section we will revisit how this framework can easily be implemented when other antennas, sizes, or array constraints are in use.

Our choice of EDMs as a physical constraint is a convenient (perhaps obvious) one but by no means the only one. A system that has other sensors or capabilities can easily accommodate an algorithm relying on angle or curvature as the constraint. Choosing another physical constraint necessitates modifications to or alternatives for PCM and ASC as well.

Spiral Match (the PCM algorithm in our implementation) is rooted in a model for the coupling—this model can easily be changed to include other constraints or known EM phenomenon to improve its versatility and our accuracy. We used our simplified model to predict the Euclidean distance in three iterations but, again, these iterations and the constraints they leveraged were system-dependent. Additional iterations can be added if a system is more or less constrained. Moreover, the parameters of our iterations can be easily changed for new systems. For example, the constraints used in the Recursive Wrap Correction algorithm can be easily changed.

New candidates for PCM could leverage frequency diversity if the system included broadband antennas. While broadband systems *could* use the single frequency approach presented in this work, frequency diversity would alleviate phase wrapping

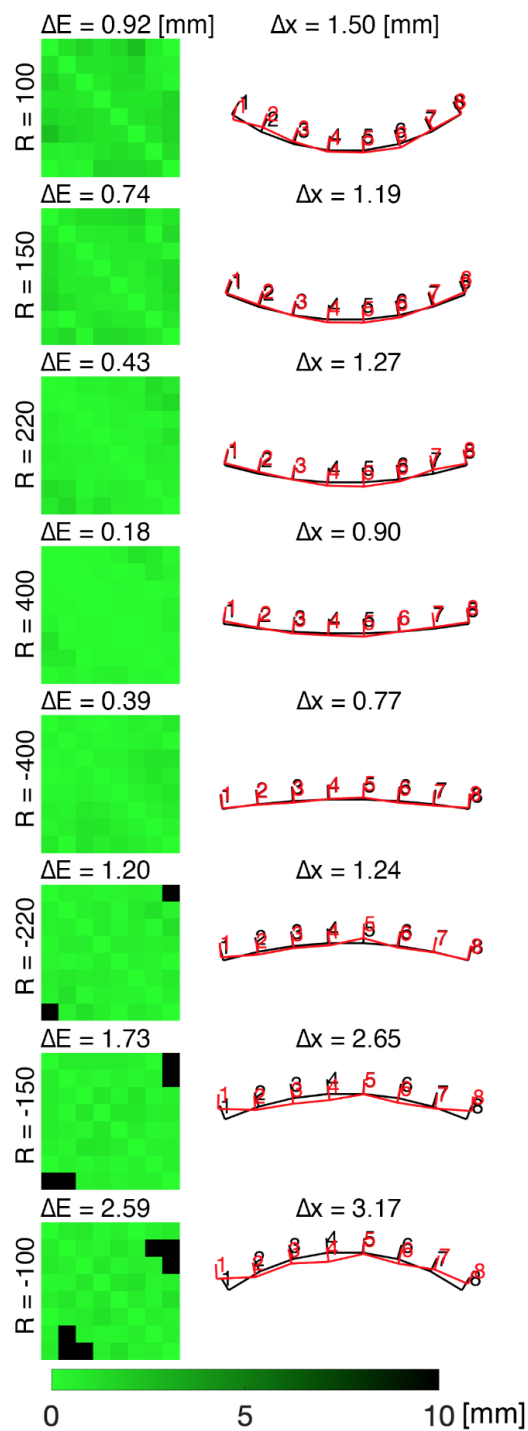


Figure 4.40: Shape reconstruction results for integrated 10 GHz phased arrays with dipole antennas for various radii of curvature. Left: EDM error heatmaps and error mean (ΔE). Right: Reconstructed antenna shapes (red), true antenna shapes (black), and shape error mean (Δx).

ambiguity when determining distance. Mutual coupling could be measured at multiple frequencies or using a chirp similar to frequency modulated continuous wave (FMCW) radar from which a distance matrix would then be constructed.

EDM (the ASC algorithm in our implementation) algorithms are well-researched, each meant to solve a different type of problem. If we choose to implement this framework in a massive 2D array (say 100x100), we might choose to only investigate coupling locally, leaving us with a sparse EDM. This system might demand a different method to deal with highly sparse EDMs. The freedom to choose the ASC algorithm makes the framework highly modular to any number of non-idealities in the EDM. Many EDM applications, especially those discussed in [34], include a mask matrix as a design parameter. We had success with banded mask matrices that decay exponentially, but perhaps another system will demand a different structure.

This work can serve as the beginning of a broad study into shape reconstruction algorithms and the diverse applications they makes possible. This is included but not limited to high-element arrays, strongly asymmetric shapes, stretchable arrays, 2D arrays, and large distributed systems. We believe mutual coupling measurements are sufficient for reconstructing array shape in all of these circumstances and offering exciting possibilities in the future.

*Appendix A***ELECTRONICS DESIGN FOR ACADEMIC SPACE PAYLOADS****A.1 Introduction**

In 2020, the Caltech Space Solar Power Project began work on the first space demonstration of the wireless power transfer, photovoltaic, and deployable structures technology which had been developed through the program. **Microwave Array for Power Transfer, Low Earth Orbit Experiment (MAPLE)** is the wireless power transfer experiment. MAPLE represents a new frontier for the Caltech Holistic Integrated Circuits Lab, as the previous 20 years of lab work had mostly been on lab-bench systems intended for brief measurement and demonstration purposes. The challenge of taking a system from a tangle of cables and circuit boards on a lab-bench to a space ready form-factor is immense. This document, intended for students working on space projects without prior space experience, will explain in detail the approach, techniques, and lessons needed for a successful academic space mission, as learned through the MAPLE project.

While the challenge was considerable, the MAPLE team was fortunate to have access to veteran advisors¹ with decades of experience on a variety of space missions. Those advisors helped fill in critical gaps in knowledge and with experience and intuition that is difficult to develop in a class room. Having someone with experience who can be consulted is strongly recommended for any space project, hopefully this document can convey at least part of their wisdom. While there are resources documenting space missions², these resources have too much ground to cover to fully explain the minutiae of implementation. Seemingly mundane details, such as epoxy choice and application process, can quickly become a blocking issue for an academic project without prior experience. Given this reality, this document contains particular and highly specific details.

All space missions balance trade-offs in risk, cost, and time. Flight heritage (the successful use of a part or process in prior mission) offers the chance to inherit knowledge and experience from someone else. The document uses MAPLE as

¹Dr. Richard Madonna acted as mission manager for the combined 3-payload space solar power project. Dr. Damon Russell served as an advisor on MAPLE offering guidance both at the project planning level and the technical detail level.

²Space Mission Analysis and Design [98] is the consensus recommended starting point.

a lens to examine problems and solutions that will be commonly encountered by academic space payloads. The author hopes that the flight heritage of parts and processes from MAPLE will save time and provide peace of mind to readers.

A.2 Mission Opportunity

Many academic projects develop technology that is eventually intended to operate in space. However, cost and time constraints mean that relatively few project teams will have the opportunity to actually demonstrate their technology in space. The opportunities that do exist come in a variety of forms, each with its own set of trade-offs.

Space-like Missions

There are several space-like environments which provide compelling, albeit incomplete, verification of space technology. While lacking the sex appeal of a conventional space mission, these environments can provide some verification at a substantially lower cost point with greater schedule flexibility. Space-like environments offer the advantages of retesting a failed experiment within weeks and give the opportunity to recover the payload after testing. They allow for troubleshooting, measurements, and observations that would be impossible for a conventional mission.

The most accessible space-like environment is a high altitude balloon flight. Balloon flights are typically performed using helium filled mylar balloons which can reach near space altitudes of 40 km. There are extensive online resources on how to conduct balloon flights [155]. The limitations on mass, maximum altitude, and duration as well as challenges orienting the payload mean that such flights are not suitable for in all cases. Fig. A.1 shows images from a high altitude balloon payload launched by a class at California Institute of Technology. Many universities have a similar program and may have resources which can be used.

Space simulation testing facilities offer an alternative method to demonstrate the space readiness of a payload. Typically using a thermal vacuum chamber to model the cold vacuum of space and an infrared source to model the suns energy, these facilities replicate the conditions experienced by payloads travelling outside the earths atmosphere. While not presenting the full radiation environment of space or the months long duration of a standard mission, they do provide an accurate thermal and vacuum environment and can be combined with mechanical testing (often at the same facility) to simulate the effects of launch [117].

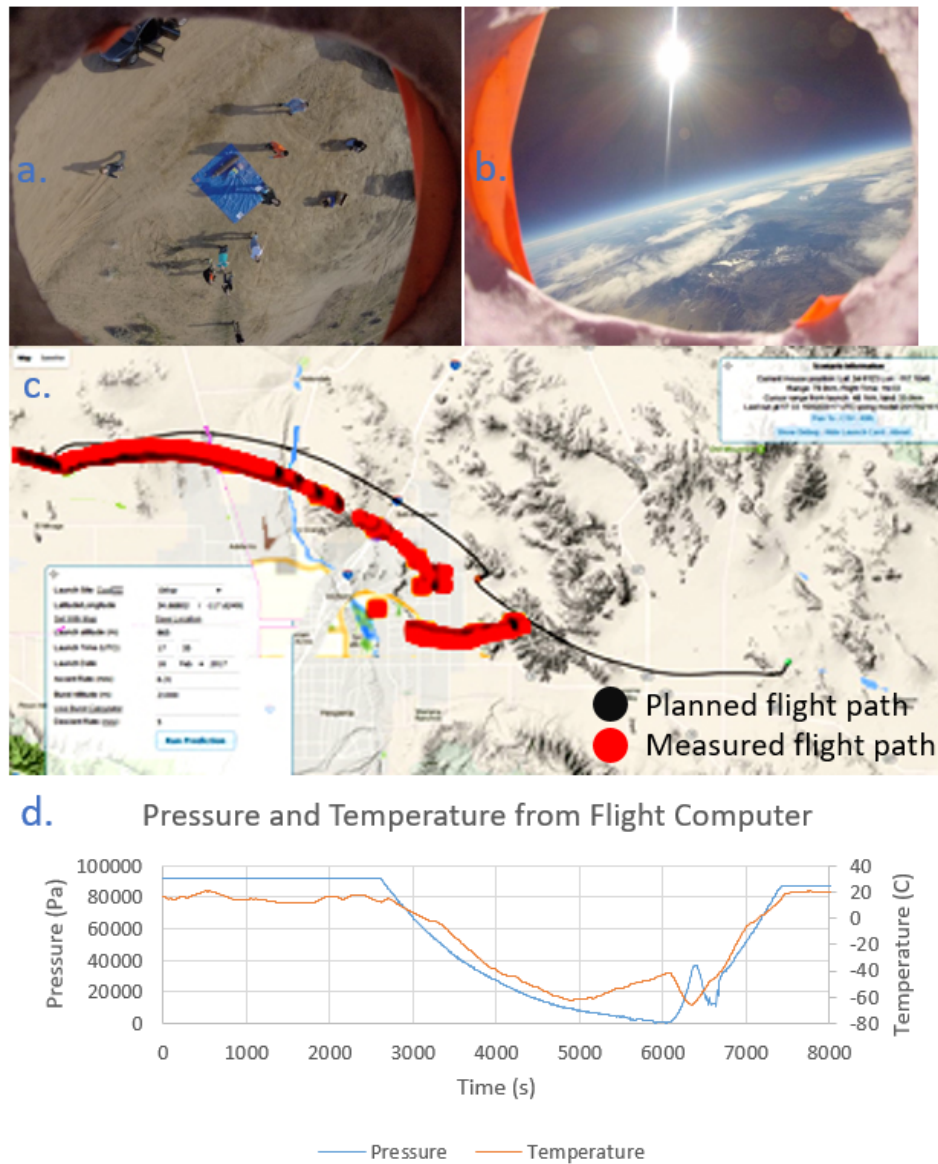


Figure A.1: (a) Image of the high altitude balloon launch site taken from the payload. (b) Image taken by the payload during flight. (c) Comparison of the planned flight path and the flight path measured by the onboard GPS. (d) External pressure and temperature data from the payload.

High altitude aircraft offer another road to a space-like environment, albeit a more expensive and less traveled one than that of balloons or space simulation facilities. At the high-end of high altitude vehicles is the X-37B, a re-usable orbital test vehicle. In early 2021, a space solar power tile was demonstrated using the X-37B, a reusable robotic orbital test vehicle [134]. While the X-37B likely presents prohibitive cost and accessibility barriers for most academic researchers, high altitude aircraft

payload hosting could become more available at a lower cost as development of high altitude platforms (HAPs) progresses [58].

Space Missions

The boom of “New Space” and the blossoming of small satellites provide a variety and quantity of academic space opportunities that would have been inconceivable two decades ago. The most common academic payload are CubeSats. CubeSats are miniature satellites made from standardized 10 cm x 10 cm x 10 cm modules. CubeSats have exploded in popularity and lead the charge on a broader nanosat trend. As a consequence of their proliferation, CubeSat design and test resources are plentiful [96] [181]. Many launch vehicles and larger satellites have CubeSat storage and launch infrastructure, allowing multiple CubeSat projects to hitch a cheap ride onto each primary mission. For the academic payload designer, CubeSat infrastructure and interchangeability is a strong advantage as many off-the-shelf modules and CubeSat specific products are available.

An alternative to CubeSats and other nanosats are hosted payloads. Hosted payloads attach to larger satellites and are not deployed mid-flight. The host can offer power, uplink/downlink, and orientation control to the hosted payload, removing significant responsibilities from the hosted payload designer. However there is a trade-off in cost and hosted payloads requires greater interplay between academic and host teams for thermal and electrical interfaces and mission planning. The efficiency of host and customer interplay should improve as hosted payloads mature. Hosted payloads allow larger form factors than typical nanosat platforms. MAPLE is a hosted payload on Momentus’ Vigoride platform.

Regardless of deployment method, a passing familiarity with the basic terms used to describe spacecraft orbits will serve electronics designers well. Circular earth orbits can be split into three broad categories: low earth orbit (LEO), medium earth orbit (MEO), and geostationary orbit (GEO). Fig. A.2 shows a visualization of each orbit and describes some of the conditions payloads will experience at those orbits. Non-circular (i.e. elliptical) orbits such as Molniya orbits are also used on occasion. While a variety of orbits are available, the majority of academic payloads are flown at LEO, where launch opportunities are more plentiful and less expensive. MAPLE will be placed in a sun-synchronous low earth orbit with a local time of the ascending node³ and an altitude of roughly 500 km. The total mission duration is

³Abbreviated as LTAN, this term means the time that the equator is crossed during the satellite’s orbit.

6 month but MAPLE's active period will likely only be a few weeks. For a ground station at Caltech in southern California, a pass from MAPLE will last between 5 and 10 minutes. This ground station will observe the 10 GHz signal emitted from MAPLE with +/- 200 KHz doppler shift.

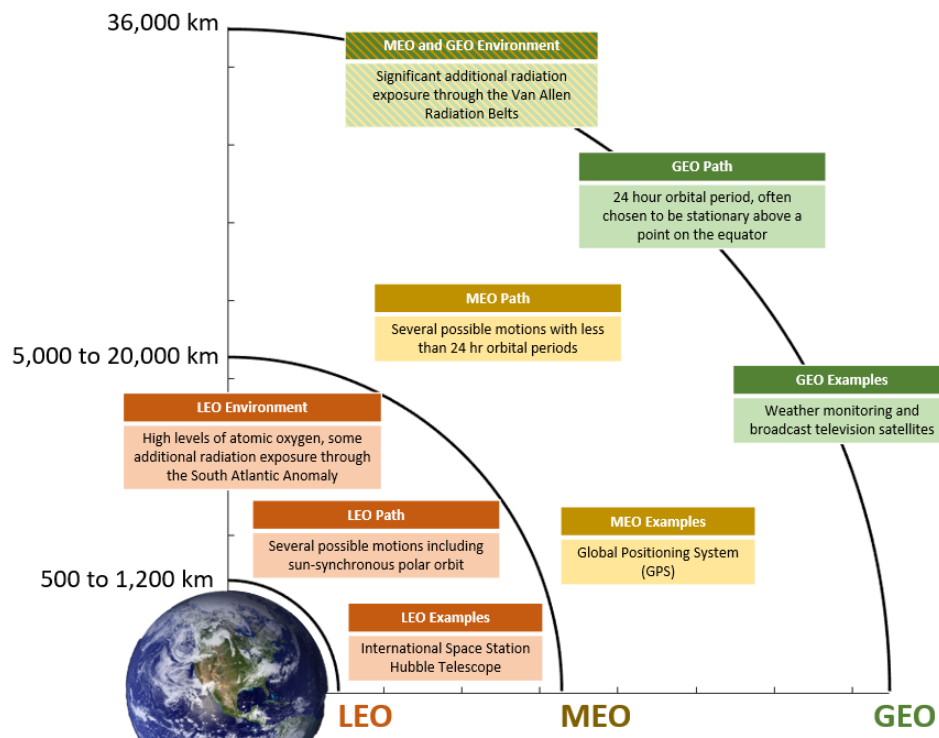


Figure A.2: Details of LEO, MEO, and GEO orbits. The altitude ranges listed on the vertical axis represent approximate bounds as no strict boundaries are universally defined. The LEO, MEO, and GEO altitude lines are at 700 km, 15,000 km, and 36,000 km above the surface of the earth, respectively.

The International Space Station (ISS) provides a unique alternative to the previously mentioned satellites. A service is offered for space station crew members to attach the payload to the exterior of the station while providing power, uplink, and downlink [131]. Notably this is one of few space missions that offers an opportunity for recovery of the payload. There are a variety of funding sources, but these opportunities are in high demand. Prospective experimenters should expect to face significant bureaucracy and oversight prior to accessing one of the greatest triumphs of human technological development.

Any of these space environments require a launch vehicle to place the payload in its desired orbit. In the decade from 2010 to 2020 many private launch companies emerged including SpaceX, Blue Origin, Rocket labs, Virgin Orbit, United Launch

Alliance, ABL Space Systems, and others. Innovation and competition among these firms and government endeavors has continually driven launch costs lower, enabling the proliferation of small satellite payloads. While the availability of launches for academic payloads has increased, the fundamental similarities between satellite launch vehicles and inter-continental ballistic missiles remain. As such, launches are subject to strict government oversight, rigid schedules, and safety procedures, and are continually at risk of delay and failure. The launch provider will require the payload to pass a battery of tests to ensure that it will not interfere with the mechanical, thermal, or electrical operation of the vehicle and other payloads present. Academic payloads should not expect any significant accommodation or attention from the launch vehicle provider and if the schedule or safety standards cannot be met then an mass stand-in will fly instead⁴. The Momentus Vigoride host vehicle for MAPLE will be launched by a SpaceX Falcon 9. Vigoride and the Falcon 9 fairing are shown in Fig. A.3.

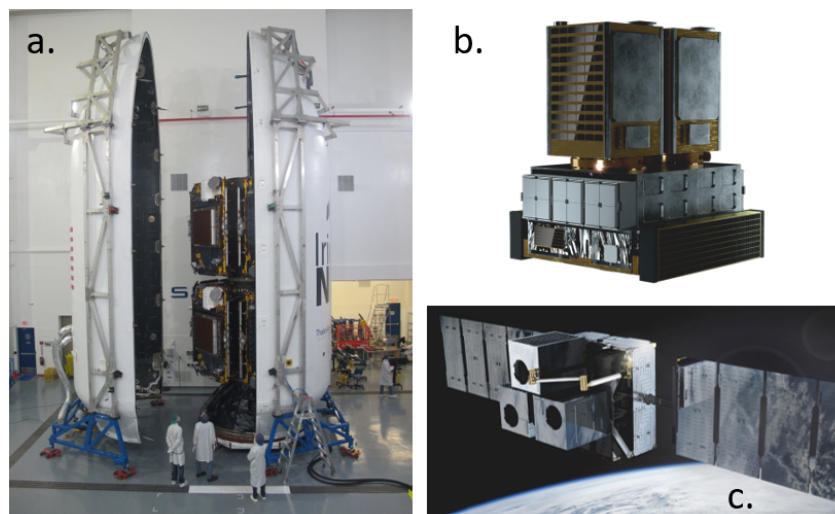


Figure A.3: (a) SpaceX Falcon 9 fairing from [158] (b) Rendering of Momentus Vigoride in stowed configuration from [156] (c) Rendering of Momentus Vigoride in flight configuration with solar panels deployed from [156]. Three hosted payloads sit on the payload deck.

Once the payload is in space it will need to convey the results of its experiments to earth, likely communicating with a ground station. Conveniently for hosted payloads and ISS experiments, uplink/downlink is handled by existing infrastructure rather than the academic payload. For satellites such as Vigoride, a network of ground stations around the world are contracted to ensure connection for as much of the

⁴In this event you are highly unlucky to get refunded for your mission, caveat emptor.

orbit as possible. The downlink available to MAPLE is <20 MBs a day shared with the other two co-hosted payloads of the Space Solar Power Project. Pictures, video, high resolution multi-channel sensors, and other data intensive applications can easily exceed this limit. Many academic satellites have similar or more stringent budgets, and questions about how much data is generated, where it will be stored, and what will be prioritized for download should be considered early in the mission planning process.

CubeSats, unlike hosted payloads and space station experiments, need to develop their own uplink/downlink channels and organize the appropriate base station infrastructure. In addition to downlink through the Vigoride host vehicle, MAPLE plans to intermittently beam a signal to earth where it will be detected by a ground station constructed by the MAPLE team at Caltech. The link budget for this communication channel is shown in table A.1 and highlights the challenge building reliable uplink/downlink infrastructure in-house and the convenience of host vehicle capabilities. The expected receiver noise power for a variety of noise temperature and receiver bandwidth scenarios are shown in table A.2. With an expected received signal power of around -120 dBm and a front end noise figure of 5 dB, there is not significant margin in the link budget. For high bandwidth data transfer this link budget becomes even more challenging. Note that doppler shift must be accounted for as the receive bandwidths in the noise power tables are less than the expected doppler shift.

| Quantity | Value | Note |
|----------------------------------|----------|---|
| MAPLE Transmit EIRP | 35 dBm | 32 Element Phased Array |
| Free Space Path Loss | 169.3 dB | 700 km at 10 GHz |
| Attenuation and Alignment Losses | 1.5 dB | Losses from atmosphere and polarization mismatch |
| Receive Antenna Gain | 20 dB | Highly directional antenna with mechanical tracking |
| Front End Noise Figure | 5 dB | Conservative estimate |

Table A.1: MAPLE Estimated Link Budget Quantities

| Noise Temperature | 5 KHz | 10 KHz | 100 KHz |
|-------------------|------------|------------|------------|
| 10 °K | -151.6 dBm | -148.6 dBm | -138.6 dBm |
| 50 °K | -148.6 dBm | -141.6 dBm | -131.6 dBm |
| 100 °K | -141.6 dBm | -138.6 dBm | -128.6 dBm |

Table A.2: Noise powers for given receive antenna noise temperature and bandwidth.

A.3 Project Planning

Successful engineering project management requires experience and expertise in a wide range fields and has been analyzed, debated, and discussed at considerable length. Rather than attempt to re-invent the field, this document will provide notes and lessons learned specific to academic space payloads. It is worth re-iterating that the experienced project consultants, provided for MAPLE by Dr. Damon Russell and Dr. Richard Madonna, are invaluable to project planning and identifying when plans have moved past optimistic and become unrealistic.

Prior to planning the budget and schedule for a project, the team members and funding source must be in accord about the technology readiness level (TRL) of experimental components and the class of the mission. TRL measure the maturity of a system or subsystem. The NASA TRL table is shown in Fig. A.4. MAPLE, and many other academic space missions aspire to take a technology near TRL 4 and take it to TRL 7. If the core technology of an proposed academic space mission starts below TRL 4 it will be difficult (and un-advised) to complete the mission within 1-2 years. A mission's class (NASA definition shown in Fig A.5.) determines the amount of risk that is willing to be tolerated for the mission. Additional time, money, and people are used to drive risk down. High class missions (A and B) are tested to higher standards and reduce risk by using almost exclusively flight proven components. Academic space missions are at their heart Class D but likely carry greater personal significance than that would imply for those providing their time and money for the mission.

The needed budget for a space project can be shocking for a student coming from a bench-top academic experiment background. Space-grade hardware is often specially designed for the environment and has strict standards of manufacturing and quality control and many components may be sold by companies with near monopolies in the market. As such, expect "Flight Ready" parts to be sold at a premium (100x standard pricing in extreme cases). Table A.3 shows the price of several parts purchased by MAPLE and their lower grade equivalents. At a fundamental level cost increase accompanies risk reduction. Using non-flight grade and commercial off the shelf (COTS) parts can dramatically reduce costs but add risk which must be understood by the stakeholders of the project. That risk can be mitigated with further component level testing (again adding cost). Choosing which components to get expensive space-grade versions of is a core challenge for academic electronic payload design.

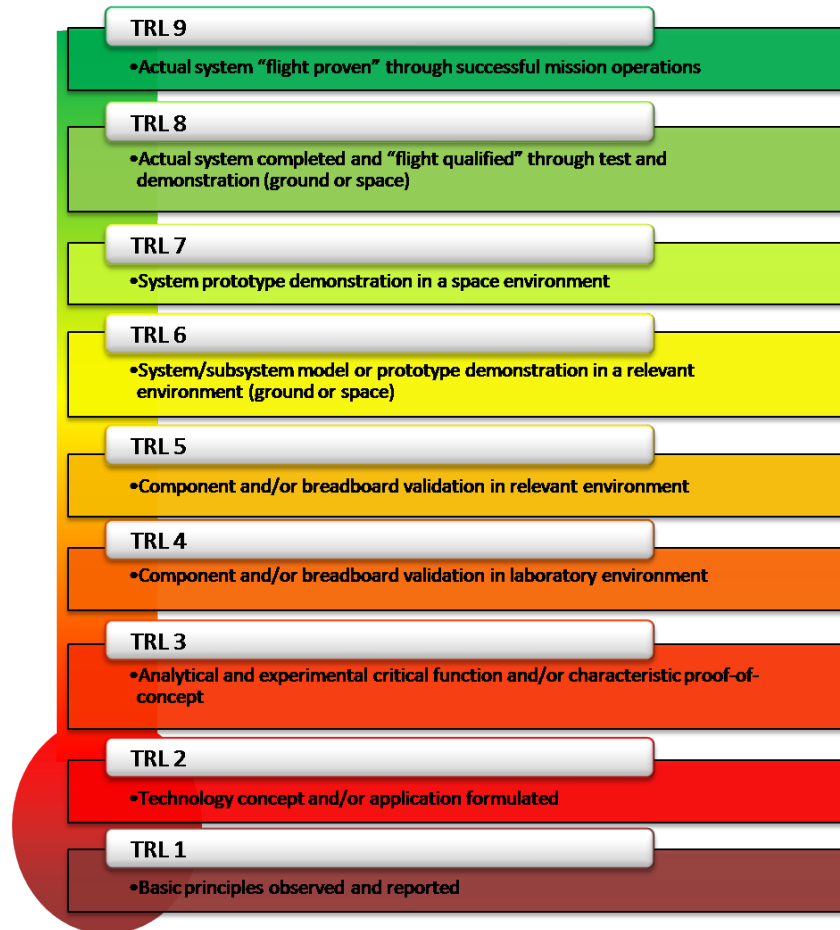


Figure A.4: NASA Technology Readiness Level Table [166]

| Type of Component | COTS | Space-grade |
|-----------------------------|-----------------------|-----------------------------|
| White LED[99] [72] | (\$0.50) | (\$15) |
| Voltage Regulator[73] [109] | (\$3) | (\$500) |
| Microcontroller[107] [108] | (\$5) | (\$1000) |
| 4-Layer Circuit Board[122] | FR4 substrate (\$100) | Polyimide substrate (\$500) |

Table A.3: Price comparison for several COTS and space grade components.

The most costly mistake (in both money and time) for the MAPLE project came when selecting a camera to photograph the payload in space. While not critical to the scientific objectives of the mission, photographs provide information about the condition of the core systems and allow the work to be presented in compelling way. The MAPLE team first selected a camera with flight heritage but limited documentation (Gumstix Ironstorm [59]). After investing significant time trying

| Characterization | Class A | Class B | Class C | Class D |
|---|---|--|--|--|
| Priority (Criticality to Agency Strategic Plan) | High priority | High priority | Medium priority | Low priority |
| National significance | Very high | High | Medium | Low to medium |
| Complexity | Very high to high | High to medium | Medium to low | Medium to low |
| Mission Lifetime (Primary Baseline Mission) | Long, > 5 years | Medium, 2-5 years | Short, < 2 years | Short, < 2 years |
| Cost | High | High to medium | Medium to low | Low |
| Launch Constraints | | Medium | Few | Few to none |
| In-Flight Maintenance | N/A | Not feasible or difficult | Maybe feasible | May be feasible and planned |
| Alternative Research Opportunities or Re-flight Opportunities | No alternative or re-flight opportunities | Few or no alternative or re-flight opportunities | Some or few alternative or re-flight opportunities | Significant alternative or re-flight opportunities |

Figure A.5: NASA Mission Classes from [81]

and failing to develop working software⁵ the MAPLE team switched a more simple Arducam Camera [8]. While lacking flight heritage, the Arducam were compatible with available voltages and digital interfaces of the SAMD21 motherboards. The Arducam's were intended to work with Arduino and as such the MAPLE team had to completely re-write drivers to work from scratch with our motherboard. This tied up significant work-hours on a project with limited personnel. While the Arducam functioned well enough to survive thermal tests, multiple Arducams could not be made to reliably run from shared I2C and SPI lines.

After months of development and testing with Arducam, we decided that these issues could not be resolved. We then switched to Raspberry Pi High quality Camera [125] and Camera Module V2 [124]. The Raspberry Pi and its camera have flight heritage and as much or more documentation than any electronic component⁶. In retrospect this seems like an obvious choice but at the time we considered the Raspberry Pi a non-starter because it could not be powered by the 3.3V regulator on the aggregation panel. Additionally, the Raspberry Pi boards were substantially larger than we wanted to fit into MAPLE. The DC power issue was solved by feeding the Raspberry with 5V directly from same line powering the aggregation panel. A few more mechanical holder components needed to be designed and tested to

⁵The Gumstix Ironstorm reached end-of-life at almost the exact same time it was chosen for use in MAPLE. Available software resources were removed the internet mid-project.

⁶Raspberry Pi is the go-to hobbyist low level computer platform, meaning a multitude of tutorials and examples are easily accessible.

accommodate the new boards and cameras, including a revision of the aggregation panel. Fortunately, the digital interfacing and control (which had taken weeks to establish unreliably with the Arducam and Gumstix cameras) was accomplished in a single afternoon. This mistake cost \$8000+ and 100s of hours of effort, required another round of mechanical and thermal testing, and delayed the Flight Model by almost 3 months.

While the MAPLE camera saga is long and winding, we can reduce it to a few fundamental lessons learned about selecting digital components. Do not underestimate the importance of your team's prior experience and infrastructure with certain hardware. Even a small amount of experience can help get over the "activation energy" that often derails digital systems. Our camera experience also demonstrates the importance of picking well documented components that are in the proper portion of their product life cycle.

The parts, processes, assembly firms, and testing firms needed for the project should be identified as early as possible. If aspects of the exploratory phase are left until later in the project the budget will creep up as undercounted costs rise and the schedule will inevitably slip as the team waits for quotes and external firms slowly complete their tasks. Doing work in-house and using lab and university facilities instead of contracting an external firm will save time and money. In general, the MAPLE team completed as much testing as possible in-house but paid for professional external manufacturing and assembly. Appendix *Budget* documents the expenses of the MAPLE project. Tests by external firms account for 24% of the total budget and could have accounted for 50% if not for use of Caltech resources. External facilities often have a per hour or per day cost and it is important to come fully prepared and ready to maximize value of the time.

The above discussion and the later budget breakdown omit what is likely the greatest expense: launch costs. While launch costs have decreased substantially, booking passage to space for a small/medium payload will likely cost 10s or 100s of thousands dollars. While there are exclusive opportunities at lower costs, the launch method and price should be determined at the beginning of a project in the event they become prohibitive in cost or lead time.

MAPLE used three versions of the electronic hardware: first a benchtop model for testing functionality, then an engineering model (EM) used for environmental testing, and finally a flight model (FM). The benchtop and EM models are shown in Fig. A.6. The three model approach is adaptable to most projects. As the benchtop

provides the first opportunity for verification of components and performance and allows software development to begin, it should be completed as early in the schedule as is feasible. If the core technology is starting at 4+ TRL, previously constructed subsystems may be able to be re-used as part of the bench top model. Even if it differs partially in form and functionality from the later models, early warning of incorrect footprints, misread datasheets, or more serious issues are critical. Once a prospective component is confirmed, a quantity sufficient for the EM, FM, and back-ups should be purchased. This avoids delays from long lead times and the unfortunate scenario of a forced switch of components because the part used for the benchtop or EM is out of stock. The EM which follows the benchtop must be similar enough in form and function to the FM such the environmental testing results are compelling. The schedule should have sufficient slack such that if the EM fails during testing there is sufficient time for revision and re-testing. The board designer should purchase components and boards for at least one “extra” copy of the EM. If the EM passes all environmental testing than the copy becomes the FM. If the EM fails environmental testing than the copy can be modified and used as the new EM. The FM delivery date to the launch provider provides the point around which the schedule should be anchored.

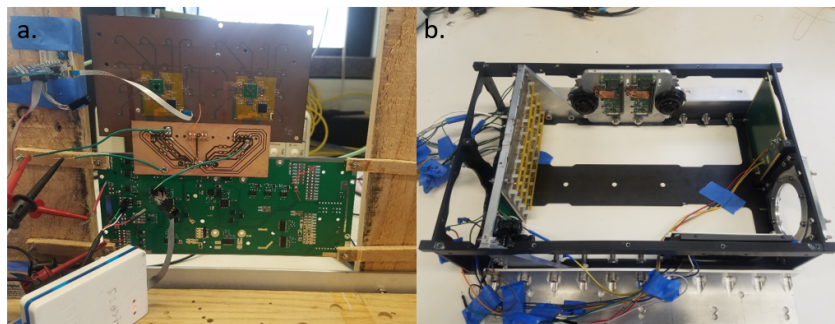


Figure A.6: (a) MAPLE bench top model. Electrically functional but not ready for environmental testing. (b) Electrically functional MAPLE engineering model which has been successfully environmentally tested. FM assembly is in progress as this document is being prepared.

A.4 Electrical Design

Board level design provides many opportunities for risk reduction in space payloads. The most important decisions are in component selection. Identifying components with flight heritage saves time and money while adding confidence to the mission. While not guaranteed to work, components with heritage have been used at the

temperature ranges and radiation environment of space. Heritage components can be identified by a patchwork of individual publications, published databases, and word of mouth. While it is difficult to construct an academic payload entirely from components with heritage, identifying digital or mixed mode components with successful flight or radiation testing histories will significantly reduce risk. After components are selected there are several design principles and techniques which should be employed.

1. **Redundancy**

Properly implemented redundancy at either the component or subsystem level significantly reduces risk of component failure. While systematic design issues are not solved by redundancy, radiation events and thermal/mechanical failures can be survived if appropriate redundancy is present. Redundancy does add complexity to board designs and adds time to development and testing, which should be taken into account as a trade-off.

2. **Modularity**

Initial circuit board designs should allow for components to be swapped and or added/removed based on needs emerging from testing or evolving requirements. The cost and time saved by not having design, fabricate, and populate a new board can save a project with a tight schedule. The follow list is MAPLE specific but is likely relevant to other systems.

- Pi or T networks instead of resistive dividers, in the event a filter is needed later.
- Additional heater location and heater lines.
- Unused digital IO lines from microcontroller taken to headers or wire mounting locations.
- Hardware designed to keep software programmable as late into the assembly process as possible.

3. **Plentiful Health Sensing**

While temperature and supply voltage/current sensing may not be part of the primary scientific mission, they provide critical information for fault assessment and testing. Once the payload is deployed, these sensors may provide the only information that can be used to assess and alleviate issues that arise.

On a more practical note, integrated temperature, current, and voltage sensing save significant time and complexity during radiation, thermal, and vacuum testing by avoiding additional external sensing hardware.

4. Upset/Fault Tolerance

When possible, components and subsystems should be designed to fail gracefully. Several examples of such are listed below

- If digital communication to a subcomponent fails it should place itself into a non-destructive configuration. Additionally, other subcomponents attempting to communicate with it should not hang. If necessary a component may need to be able to be un-powered by the flight computer or other processor.
- Digital control lines should have the appropriate pull-up or pull-down resistors to minimize loss of functionality in the event of digital controller failure.
- Regulators and components with over current protection or shutdown should be used when possible. A component failing as a short should not be able to pull a shared supply low enough to effect other components.
- When using linear regulators, placing two in series can prevent upsets from radiation events from being fatal to components down stream.
- Ensure that redundancy does not add additional failure modes. MAPLE uses 4 digitally enabled redundant reference oscillators for the phased array. As shown in Fig. A.7, the oscillators are AC coupled together in the event that one fails and does not exhibit high-Z DC behavior.

5. Conservative Design

Secondary circuitry which supports the primary experiment of the mission should be designed conservatively as there is little to gain for use low margin, complicated, or unproven techniques to push performance outside of the purview of scientific interest. While this philosophical approach is situational, it should be consistently applied when de-rating components. While a general rule of 0.5 de-rating factor for peak currents and voltages likely safe, NASA's de-rating guide [171] provides more specific guidelines. Voltage regulators used for MAPLE's RFIC power amplifier supplies were not sufficiently de-

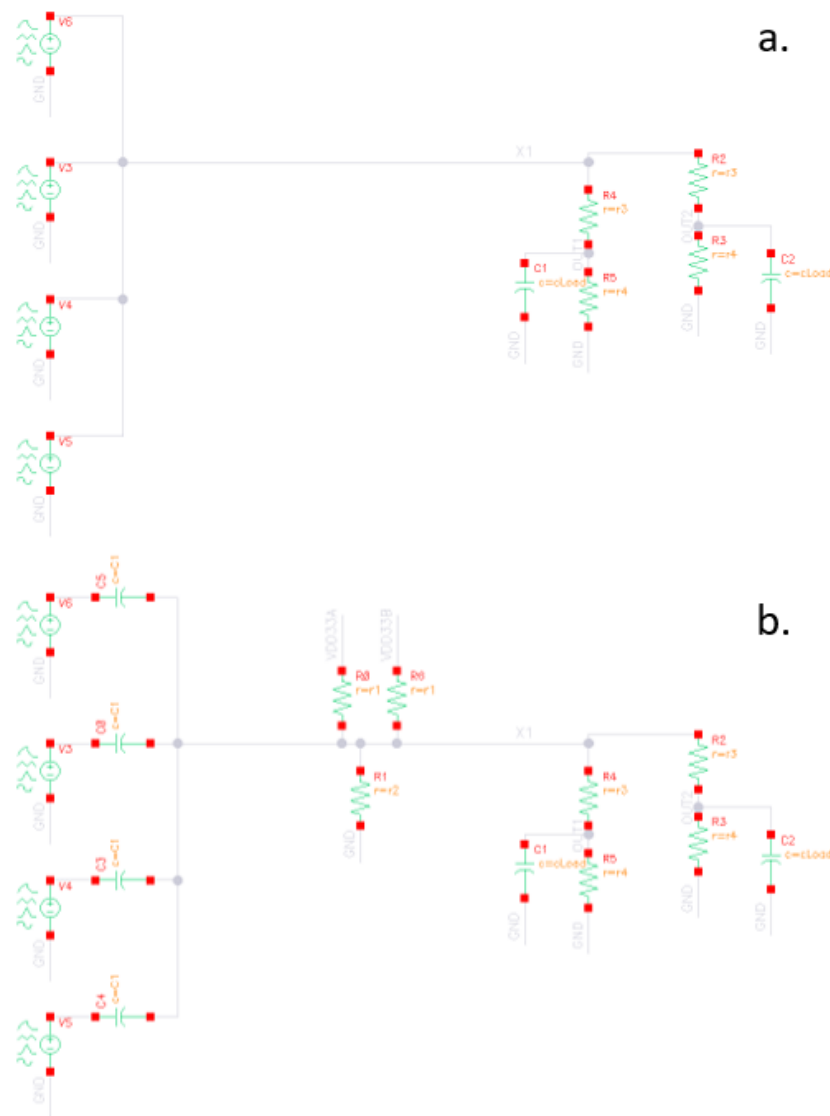


Figure A.7: (a) Sources representing MAPLE reference oscillators are DC-coupled, risking complete system failure if one fails such that its enable/disable digital pin no longer works. (b) Sources representing MAPLE reference oscillators are AC-coupled, allowing individual oscillators to fail as shorts to VDD or GND without effecting the other oscillators.

rated from their current limit, creating concern and a time-sink that could have been avoided.

A.5 Mechanical and Thermal Design of Circuit Boards

After electrical functionality is established with the benchtop model, mechanical or thermal issues are the most significant obstacles for electronic systems. Thermal and

mechanical design choices are often intertwined. The chassis thermal connection to the custom RFICs of MAPLE's flex array was a substantial concern during EM design and was the only part to experience failure in preliminary environmental testing. While the custom part and custom heatsink proved challenging, there are several conventional approaches which should be employed in most designs.

1. Wires that interface with a circuit board should have strain relief designed into the PCB. The strain relief ensures that solder joints do not bear mechanical loads. Fig A.8 shows the strain relief used in MAPLE.
2. Circuit components which dissipate power should have clear thermal paths to the thermal sink. Staking, use of small amounts of epoxy to fix components to PCBs, and potting, complete coverage of components with epoxy, bolster mechanical and thermal connections. While potting can cause thermal issues by insulating components from convection in terrestrial applications, no such concern exists in the vacuum of space. A thick ground plane (2+ oz copper) and exposed conductor around the perimeter of the PCB help get heat out of the board. Thermal epoxy can then be used to connect the PCB to the chassis frame, creating a wide, low thermal resistance path. The epoxies used in MAPLE are documented later in this subsection.
3. Circuit board substrates with superior thermomechanical properties should be used when possible. Low coefficient of thermal expansion (CTE) and strong mechanical adhesion of traces even after many temperature cycles is desired. Polyimide is the go-to space grade substrate, selected over woven fiber glass composites such as FR4. For multi-layer PCBs consisting of different substrate materials, CTE should be matched to prevent warping or delamination of traces at temperature extremes.
4. Ensure that the minimal width traces and vias on a board are mechanically viable. MAPLE's polyimide boards used 8 mil minimum trace width rather than 4 mil (which is within the capability of the board house manufacturing equipment) to guarantee robustness.
5. A polymer coating, typically parylene, should be applied to populated circuit boards when possible. The polymer coating provides electrical insulation in the event of loose conductors or debris and prevents moisture damage or

corrosion. The MAPLE team elected not to coat areas with 10 GHz radio frequency signals as the parylene was not present in simulation or testing.

6. For bare die integrated circuits or BGA parts, underfill epoxy should be used.

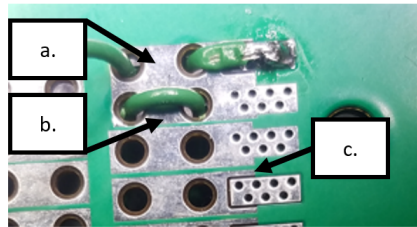


Figure A.8: (a) Strain relief consisting of two holes and a solder pad. Wire emerges for use on the camera side of the board. Thermal damage is evident in the stranded wire insulation. In later assemblies, insulation with better thermal property was used. (b) Wire strain relief seen from the opposite side of the board. (c) In later versions of the board the solder was enlarged and moved further from the holes. Additionally the ground pour around the wire holes was covered with mask to reduce risk of shorting.

While not strictly thermal or mechanical in nature, there are several general design principles which be followed. Vented screws should be used for blind-tapped holes to prevent failure in vacuum. All stand-alone conductors should have a DC current bleed path to chassis ground. In MAPLE, all circuit boards share “PCB ground” which connects to chassis ground at a single point through a mega-ohms sized resistor. The bleed path prevents large potential difference build-up and its accompanying plasma/arcing issues; use of a single resistor to connect to chassis ground avoids unintentional current loops.

Payloads require a variety of epoxies during assembly. Spacegrade epoxies with proper outgassing and temperature behavior are necessary. Below is a list of epoxy’s used in the MAPLE payload.

1. For mechanical purposes, 3M DP2216 Gray, was used. DP2216 has a 90 minute work life, cures over several days at room temperature, and has no special application requirements.
2. For the critical thermal connection between the custom RFIC and the aluminum PCB frame which acts as a heat sink, Loctite Stycast 2850 and CAT 9 were combined at a ratio of 100:3.5 by weight. Boldline control beads

were also added to the mixture. The mixture was vacuum de-gassed prior to application.

3. For creating thermal bonds between PCBs and the aluminum components they are mounted on, a mixture of Solithane 113 and Catalyst 300 at a weight ratio of 100/65 was used. For potting and encapsulation of components on circuit boards a mixture of Solithane 113, Catalyst 300, and CAB-O-SIL at a weight ratio of 100/74/10 was used.
4. For the custom RFIC underfill, NAMICS KT11276-1-54 was used. The epoxy must be stored below -40°C . Prior to application, the parts must be pre-baked, and after application the underfill must be cured at temperature. Improper application can lead to voids forming. For the FM parts the MAPLE relied on Palomar Technologies for application.

A.6 Space Environment

While thermal and mechanical stresses are typically the dominant concerns during the design of space-ready hardware, there are other conditions which must be accounted for. The first of these concerns is outgassing, which is the release of trapped gas from materials undergoing pressure or temperature changes. These released gasses can condense onto lenses, optical sensors, photovoltaics, or thermal coatings and interfere with their function. The launch provider will likely provide outgassing standards (typically measured in percentage of mass loss or volume loss) which must be met. Outgassing is avoided primarily through the use of low-outgassing materials [172] for the construction of the payload. It is also reduced by maintaining clean surfaces and performing a bake-out (high temperature and vacuum environment to accelerate outgassing) of the payload prior to flight. The polymer coating mentioned above also helps reduce outgassing

The second of these concerns is atomic oxygen. Mono-atomic oxygen outside the earth's atmosphere will cause erosion and oxidation of exposed surfaces. Oxidation is particularly hazardous for optical sensors and lens which could become opaque. Expected fluence is highly dependent on altitude, solar activity, and orientation relative to spacecraft ram. SPENVIS (SPace ENVironment Information System [157]) can be used to determine expected atomic oxygen levels given orbit information. The expected atomic oxygen fluence for the MAPLE mission is 8.5×10^{16} particles per day in the ram direction of the spacecraft. For a 180 day mission this would be 1.53×10^{19} total particles. The erosion yield of Kapton H polyimide and copper are

3×10^{-24} [14] and 8.7×10^{-27} [36], respectively. For the expected MAPLE fluence, this would be a thickness decrease of 45 μm for polyimide and 135 nm for copper. Considering that most of MAPLE is covered by MLI and MAPLE will not be in the RAM direction, it is unlikely that erosion from atomic oxygen will pose a significant risk in MAPLE.

Tin whiskers are the final space environment concern discussed in this section. Whiskers (usually from high purity tin or zinc surfaces) are thin, crystalline strands which form over time. Whisker propensity is increased by oxidation, temperature stress, and mechanical stress. Use of leaded solder prevents tin whiskers in nearly all cases. Conformal coat, potting, or other encapsulation techniques further reduce risk. Leaded solder was used for all MAPLE components except for the custom radio frequency integrated circuits (RFICs). The RFICs were factory bumped with non-leaded solder bumps. To reduce the risk of tin whiskers the previously described underfill was used.

A.7 MAPLE Qualification Testing

Mechanical Testing

During launch payloads will undergo significant mechanical stress including acceleration, vibration, and shocks. These stresses can cause catastrophic failures as well as subtle failures such as broken solder joints, loose wires, and unfocused cameras. Taking an experiment from a loose collection of boards and wires to a secure payload which can survive these stresses is one of the fundamental tasks an academic space project will have to overcome. There is a wide array of mechanical tests a payload could be subjected to. It is likely that the launch provider and payload host will provide a list of tests and test levels which a payload must reach. If no other guidance exist NASA General Environmental Verification Standard (GEVS) [57] can be consulted.

In most scenarios, the needed tests can be accomplished using a standard shake table. MAPLE shake testing took place in three progressive stages, shown in Fig. A.9. MAPLE relied on a small shake table overseen by the Graduate Aerospace Laboratory of Caltech (GALCIT) for initial testing⁷. This initial testing discovered issues with the RFIC heatsink which were addressed prior to testing at Exporior Labs. This initial testing saved \$10k+ and created schedule flexibility. Even if an in-house shake table is unavailable, simply shaking a payload as hard as possible by

⁷In-house mechanical testing was facilitated by Alex Wen and Alan Truong of the Pellegrino Lab at Caltech.

hand is a passable workmanship test. When a shake table is available, a variety of tests can be run. The tests run with MAPLE's EM at Experior Labs are described below.



Figure A.9: (a) Component level mechanical testing at Caltech. (b) Preliminary EM mechanical testing at Caltech. (c) EM mechanical testing at Experior Labs.

1. Sine Vibration

In sine vibration, the shake table is excited with a sinusoidal waveform. While sine vibration can be used to stress test the payload, it is often used at low amplitude to identify the vibrational modes of the system. Design fidelity can be assessed by comparing the measured mode frequencies to predictions from analysis or simulation. Low amplitude sweeps can also be used to determine mechanical changes, such as damage caused by high stress tests.

2. Random Vibration

Random vibration excites the payload with a waveform that has a specific power spectral density envelope, often specified by the launch provider. Because the phase of the excitation frequency components are randomized, the time domain waveform peak amplitude can vary for the same excitation.

3. Sine Burst

For a sine burst test a low frequency, high amplitude waveform is applied to the payload simulation a quasi-static load. For MAPLE the sine burst waveform was 15 cycles of a 15 Hz sine with rising then falling amplitude.

4. Shock

Shock testing simulates the rapid acceleration cause by explosion, collision, or detachment of objects from the spacecraft. A variety of situational shock tests (all of which are high stress, low duration) can be performed. A shake table can be used provided it has sufficient actuation power and bandwidth.

The amplitude levels at which tests should be conducted is situational. Once the expected levels to be experienced during flight are determined, it is typical to test the engineering model to +3 or +6 dB above those levels to establish margin. The test plan executed at Experior used low amplitude sign sweeps to check for structural damage to the payload between each of the other tests. Random vibration, sine burst, and shock tests are conducted in several steps with amplitude increasing from low to high. Fig A.10 shows waveforms representing each test type and the measured sensor output for the testing performed on the MAPLE EM at Experior Labs.

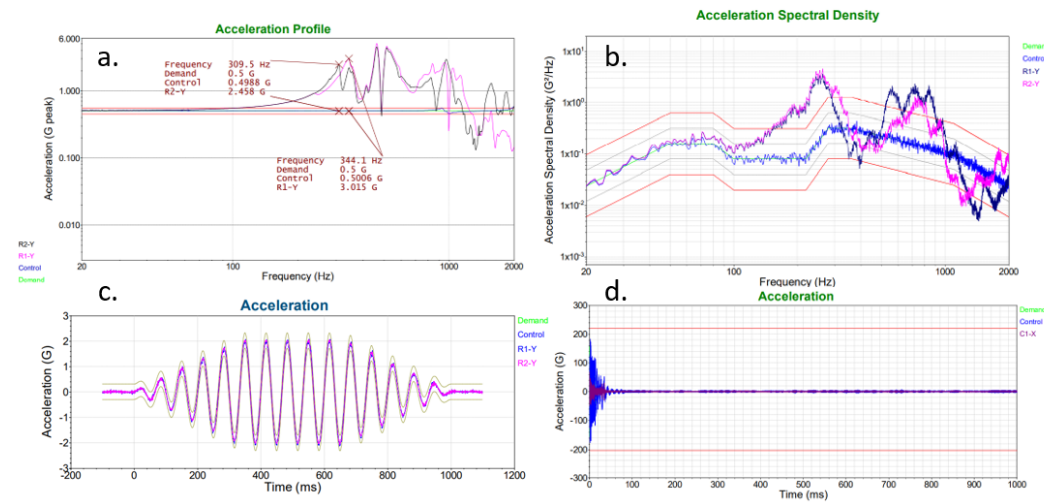


Figure A.10: MAPLE EM Y-axis mechanical testing excitation and response. (a) Sine Vibration (b) Random Vibration (c) Sine Burst (d) Shock.

Thermal Testing

The thermal environment of space is uniquely challenging. With no atmosphere for convective heat exchange, radiation provides the only mechanism for heat exchange in space. When a payload is shaded and un-powered it can easily cool to -40°C or lower. When powered or in view of the sun, payloads can heat beyond the failure point of conventional electronics if the heat cannot escape through conduction or radiation. While fully replicating the strong vacuum of space and radiation spectrum of the sun is challenging, testing payloads over the range of expected temperatures is feasible using standard compressive cooling, resistive heating thermal chambers.

Before thermal testing can be performed, the mission thermal environment must be determined. CubeSats and other standalone payloads primarily concern themselves with their orbit and own operations. Hosted payloads must thermally interface with the host spacecraft. The negotiation of this thermal interface can be a time consuming, iterative process. A common approach is for subsystems to be thermally isolated from the spacecraft, radiate their peak power usage, and rely on heaters to maintain a minimum threshold in cold scenarios. An example of this approach can be as follows: first identify the maximum and minimum acceptable temperatures for the payload (with margin). Next, calculate the needed surface emissivity of the payload ⁸ such that an acceptable cold temperature can be maintained with the available heater power. Finally, use that emissivity and the maximum sustained power consumption to determine the maximum temperature the payload will reach during operation. If the calculated maximum temperature is unacceptable than the operation plan can be changed (allowing for duty-cycled operation), or the heater budget can be increased.

After discussions with the host vehicle provider, it was decided that MAPLE would be thermally coupled to the host vehicle chassis, and covered with multi-layer insulation (MLI) blankets, which are low emissivity and reduce heat exchange with space. This decision was made considering MAPLE's relatively low peak power and duty cycle, MAPLE's insensitivity to mid-experiment shut down due to thermal concerns, and the favorable expected temperature range of the payload deck on which MAPLE is mounted.

After the thermal environment has been established, thermal tests should be performed that accurately model the expected scenarios. Thermal chambers are relatively inexpensive and will serve most needs for standard academic payload. Unfortunately these thermal chambers cannot accurately test the emissivity/absorptivity of surfaces. Testing firms such as NTS [117] may be able to successfully model radiative thermal behavior but are likely outside the scope of academic project budgets and schedules. The following list describes several tests which can be performed without access to a full space environment simulator.

1. A **stepped temperature sweep** is the most basic thermal test which can be run on an electronic payload. Electronic functionality is tested at several temperatures within the range. The sweep range is typically defined to be

⁸The Stefan-Boltzmann law [98] can be used. $j = \epsilon\sigma T^4$ where j is the energy radiated per unit surface area, ϵ is the surface emissivity, σ is a constant, and T is the thermodynamic temperature.

the expected flight environment with margin. The testers should ensure the electronics reach thermal equilibrium at each temperature before continuing to the next step.

2. **Thermal cycling** emulates the light/shadow cycles of a standard orbit by repeatedly heating and cooling the payload to the edges of the expected temperature range. This cycling places stress on mechanical interfaces between materials with different CTE and cause failures in electronics which are not rated to survive the range. Whether the payload should be powered or un-powered during these cycles is determined by the mission plan.
3. **Cold soak** emulates a long period where the payload operates at low power or is un-powered all together by dropping the payload temperature to the lower limit of the expected range and maintaining that temperature for up to several days.
4. **Thermal shock** is rapid temperature change which places mechanical stress on the payload. Thermal shock may be experienced during launch. While hot/cold chambers for shock exist, dunking sub-components in liquid nitrogen provides an adequate test.

Fig. A.11 depicts the thermal chamber used for MAPLEs stepped sweep, cycling, and cold soak testing. Even if components are rated for the temperature range of the mission it is still important to check their performance. While the core functions of MAPLE were constant with temperature, both the Arducam and Raspberry Pi cameras experienced noticeable white balance changes over the tested temperature range. Fig. A.12 shows how artifacts and white balance change with temperature for the camera used within MAPLE.

Thermal Vacuum Testing

Ideally thermal tests are performed at vacuum to avoid convective heat transfer. The previously mentioned tests were performed at ambient pressure due to the limitations of the thermal chamber available to the MAPLE team. A small, inexpensive vacuum chamber with integrated resistive heater was acquired. While the MAPLE frame could not fit inside, several of the payload PCBs were placed inside and configured for testing. Wires had previously been inserted through the lid of the chamber such that the contents could be powered. While sealant was placed around the wire holes,

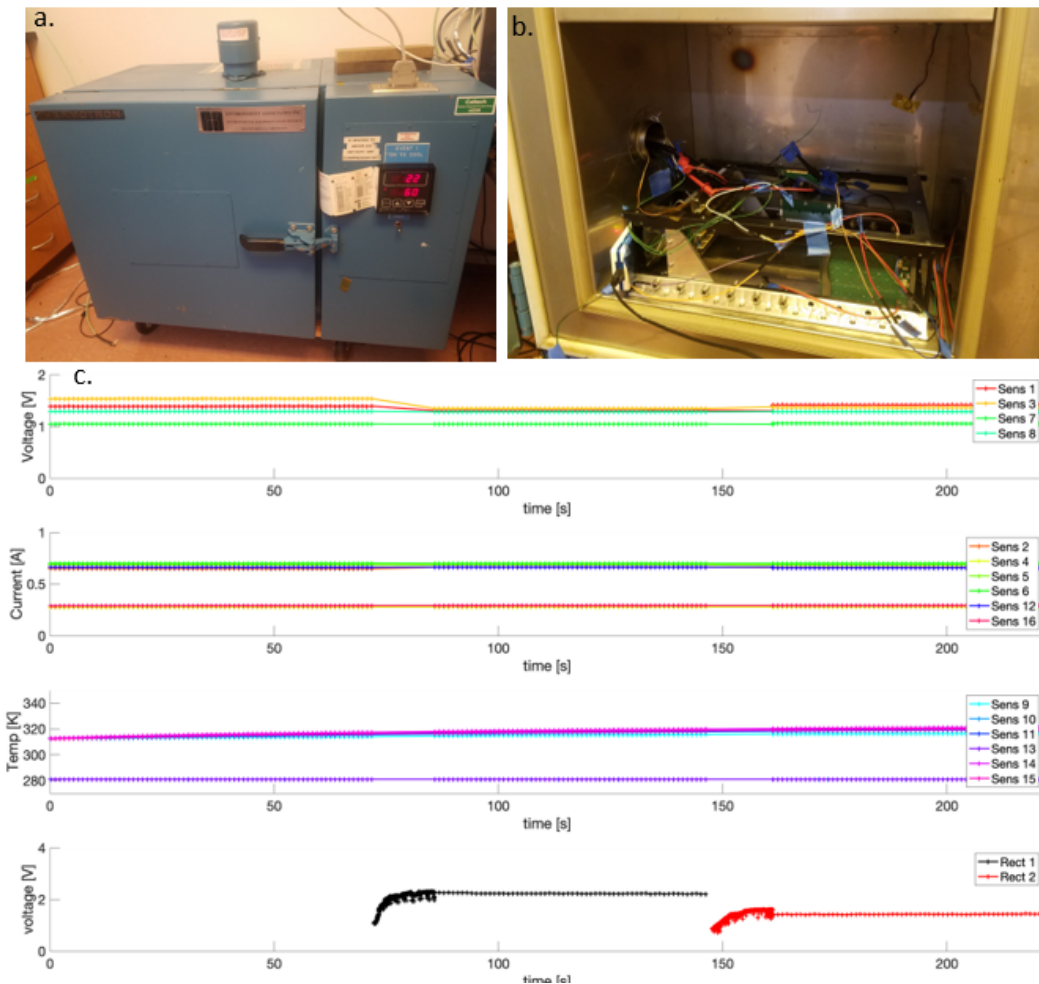


Figure A.11: (a) Thermal chamber. (b) MAPLE EM inside thermal chamber. (c) Voltage sensing, current sensing, temperature sensing, and wireless power transfer experiment logged measurements (from top to bottom). The thermistor of sensor 13 was disconnected during this experiment.

there was a leak, which limited the pressure in the tank to 0.1 atm. This is well below the vacuum strength of space or a properly sealed chamber, but does prevent most convective heat transfer. With proper wire-hole seal it is likely a significantly stronger vacuum can be pulled using the same chamber. The resistive heater was used to raise the temperature of the electronics to 50°C and dry ice placed around the exterior was used to lower the temperature to -5°C . The MAPLE electronics functioned without issue over this range. Fig. A.13 shows a simple thermal vacuum chamber and the MAPLE vacuum test set-up. The Raspberry Pi cameras were later

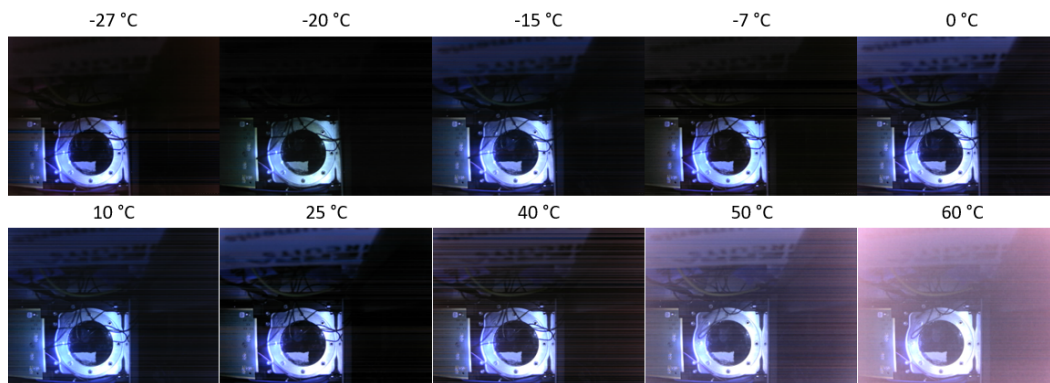


Figure A.12: Arducam images at a range of temperatures. White balance changes and artifacts appear.

tested successfully in a true TVAC chamber⁹. The inexpensive, in-house approach is sufficient for most academic payloads if it is properly conducted.

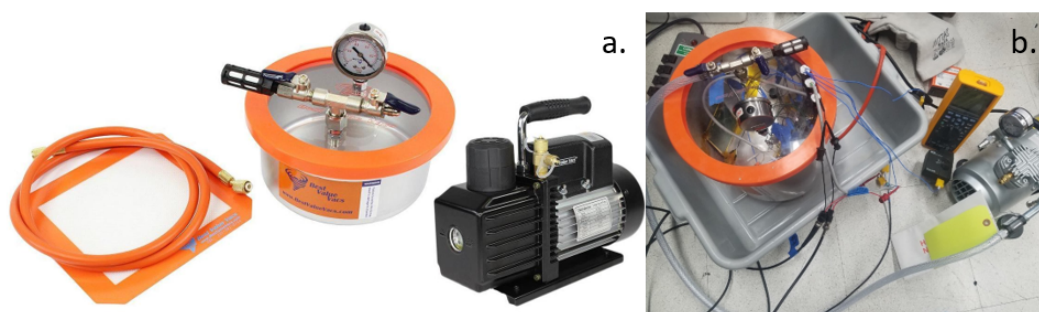


Figure A.13: (a) In-house TVAC chamber components from [167]. (b) MAPLE aggregation panel and flex array TVAC testing.

Radiation Testing

Radiation effects on electronics can manifest in a variety of ways but this document will focus on total ionizing dose (TID) and single event effects (SEE). TID is cumulative damage often from excess charge in the dielectric layers of integrated circuits. Over time these charges can change threshold voltages, increase leakage, and cause device failures. SEE are caused by individual particles that strike sensitive nodes in an integrated circuit. These strikes can cause destructive or nondestructive latchup, voltage transients, bit flips, or other damage.

Particle fluence is strongly orbit dependent. SPENVIS was used to determine the expected radiation environment for MAPLE's orbit, to which other LEO orbits

⁹Our TVAC testing was performed in Atwater Lab at Caltech by Michael Kelzenberg and Samuel Loke.

should be similar. The expected dose for the entire 6 month MAPLE mission is shown in Fig. A.14. The plot shows that shielding beyond a few mm of aluminum has diminishing effects. The custom RFIC at the heart of the MAPLE experiment is fabricated in a 65nm process. [78] indicates that a 500 krad dose will cause substantially increased leakage in the 65nm process, a dose of <100 krad will not have a measureable effect. As such the MAPLE team did not elect to TID test the custom RFIC.

The MAPLE team did elect to perform limited SEE proton testing at Texas A and M University's (TAMU) radiation effects facility. MAPLE mission predicted proton flux for two different shielding thicknesses is shown in Fig. A.15. At TAMU, the components were tested with 48 MeV protons, which is short of conservative NASA mission standards and short of the maximum energy particles that will be experienced during the MAPLE mission. Higher energy heavy ion testing was available at additional expense and logistical effort but the MAPLE team's budget and schedule lead to the decision to limit component tests to protons. While proton testing comes short of more thorough radiation tests, it provides simple go/no go decisions for components that would have no testing otherwise. This go/no go status was critical for the custom RFIC at the heart of MAPLE's mission. If this component had proved highly susceptible to SEE, MAPLE likely would have been significantly delayed, re-imagined, or cancelled all together. Fig. A.16 shows the MAPLE radiation testing set-up at TAMU. Academic missions without custom integrated circuits may opt to skip radiation testing. As mentioned in the electronics design section, use of existing radiation tested components is strongly advised. Many tested components can be found in published compendiums from JPL [119] [118] [5] [6]. These published component lists are tested to a higher standard than that of MAPLE.

A.8 Regulatory

There are several regulatory processes that academic space payloads must comply with. Payloads with any kind of radio transmission must coordinate with the FCC to legally operate. There are several types of licenses which be applicable. CubeSats and other stand-alone academic payloads will likely file an experimental license. MAPLE is jointly filing for a commercial license with the host vehicle, a somewhat unusual configuration, but in compliance with requests from the FCC.

An academic payload team is expected to provide a link budget, expected radiation patterns, operating schedule, operating locations, and a contingency plan for turning

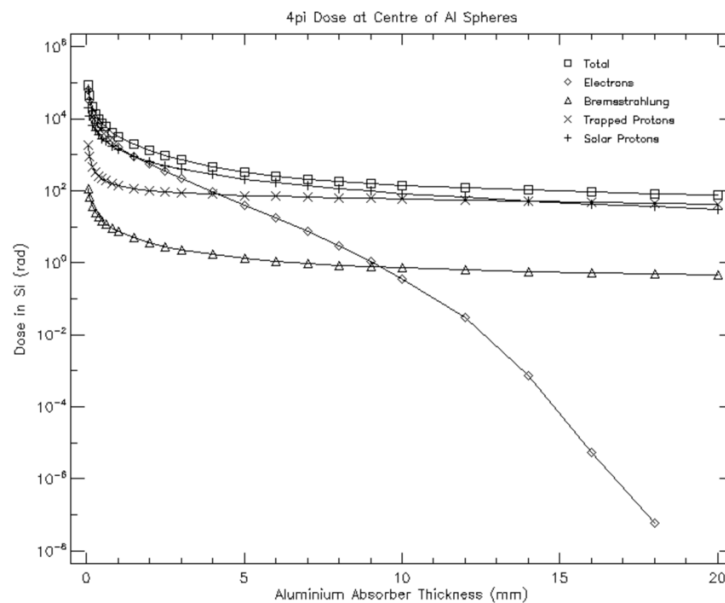


Figure A.14: Expected TID for given shielding thickness for MAPLE mission as predicted by SPENVIS.

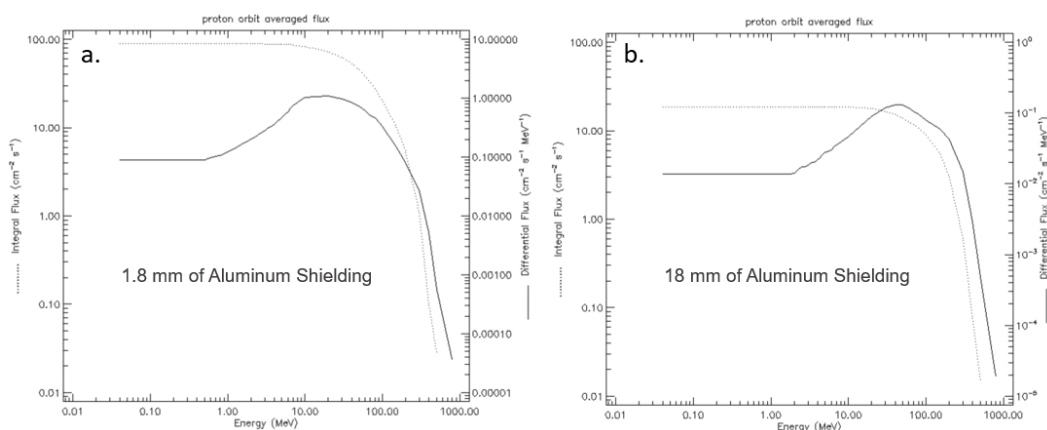


Figure A.15: Expected proton flux for MAPLE mission as predicted by SPENVIS. Integrated flux shows expected flux of particles at higher energy levels than shown on the x-axis. Differential flux is the derivative of integral flux. (a) Result with 1.8 mm of shielding. (b) Result with 18 mm of shielding.

off transmission if requested. The FCC also requires a debris mitigation plan. Successful applications to the FCC will also secure permission from the International Telecommunication Union (ITU). The MAPLE team contracted a lawyer to organize and submit our application to the FCC and assist in coordination with the host vehicle legal team. It is likely this prevented critical mistakes and is strongly recommended. The FCC licensing process should be expected to take several months and should

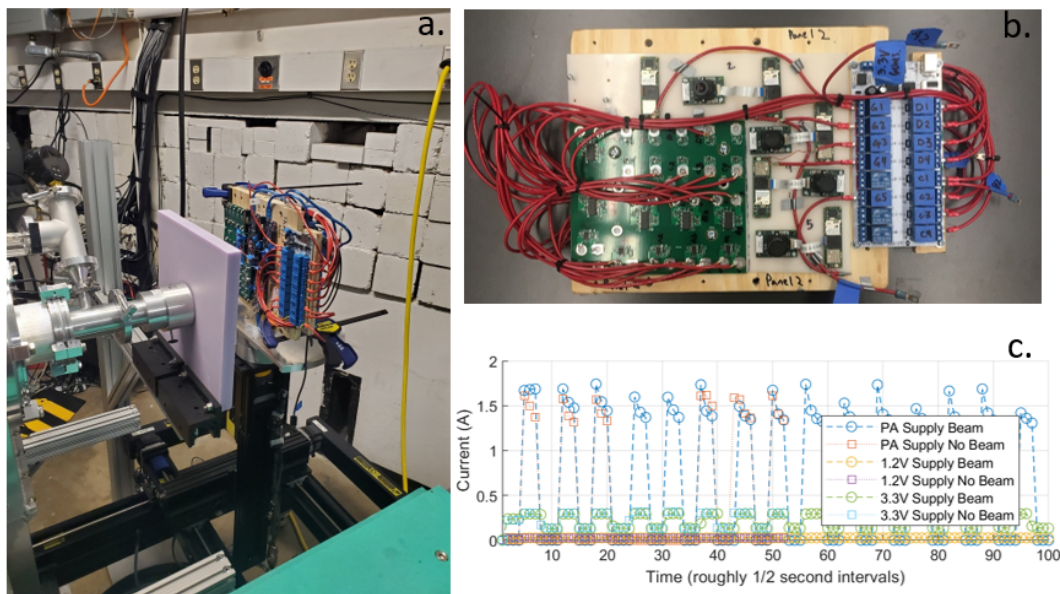


Figure A.16: (a) One of the MAPLE component panels mounted on the proton beam set-up at TAMU. (b) MAPLE component test panel. Digitally controlled switches allow each component under test to be powered separately. This prevents a single failed component from pulling the entire panel's supply to ground. (c) Measured current for RFIC before and during proton testing.

be started as early as possible.

In addition to EM spectral licensing payloads with remote sensing capability (including cameras) must contact the National Oceanic and Atmospheric Administration (NOAA) to determine if a license is required. MAPLE's cameras were included in an inquiry to NOAA and do not require a license.

A.9 Results and Conclusions

Several breakdowns of the spending in the MAPLE project are shown in Fig. A.17. We performed extensive testing and used space grade materials. Without radiation testing, testing costs could be significantly reduced. Additionally, the MAPLE team developed almost all circuits and circuit boards in-house, requiring more iterations than a project that uses more off-the-shelf CubeSat circuit boards. A key cost driver of the electrical components was the fact that MAPLE is a microwave project. Our microwave circuits required low loss substrates and fine feature size which rapidly inflates board production costs. The cost breakdown by prototype shows cost increasing with functionality and verification level as we progressed from benchtop model to EM then FM. The cost of switching to the Raspberry Pi cameras late in

the project was separated into the “Camera Fix” category. In retrospect, the camera switch and other MAPLE purchases could have been avoided with better planning or more careful design. The final cost break splits all costs into two categories: unavoidable costs and avoidable costs. While the avoidable costs do represent unfortunate mistakes, they account for less than 1/4 of the total project cost.

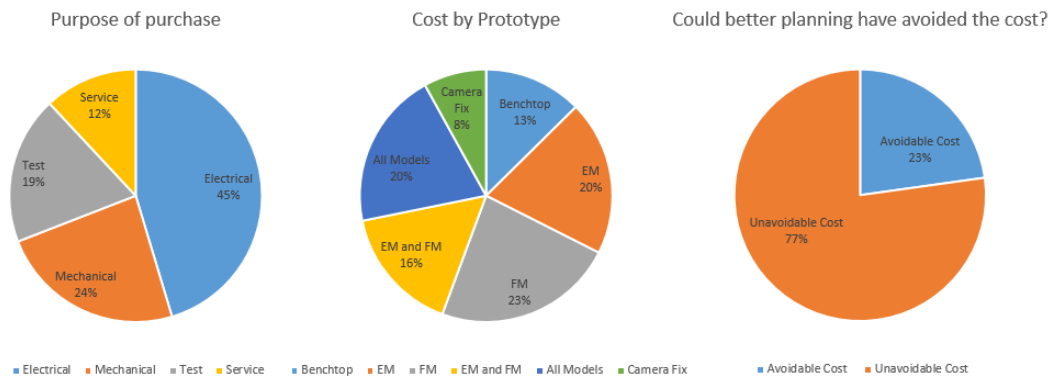


Figure A.17: Several categorical breakdowns of the spending in the MAPLE project.

MAPLE’s launch date is well after the publication of this thesis. While the success or failure of the mission will color a reader’s opinion of this document, it is important to remember that the guidance given here is intended to reduce risk. Risk cannot be reduced to zero and this information is best used in concert with other resources.

BIBLIOGRAPHY

- [1] 3M. “3M Scotch-Weld Epoxy Adhesive 2216”. In: (Nov. 30, 2021). URL: https://www.3m.com/3M/en_US/p/d/b40066446/ (visited on 11/30/2021).
- [2] Suhila Abulgasem et al. “Antenna Designs for CubeSats: A Review”. In: *IEEE Access* 9 (2021), pp. 45289–45324. DOI: 10.1109/ACCESS.2021.3066632.
- [3] Chris Albrecht. “Do You Really Need a Smart Olive Oil Bottle? You may Actually Want Oliverys”. In: (Aug. 29, 2019). URL: <https://thespoon.tech/do-you-really-need-a-smart-olive-oil-bottle-you-may-actually-want-oliverys/> (visited on 11/08/2021).
- [4] Rene J. Allard, Douglas H. Werner, and Pingjuan L. Werner. “Radiation Pattern Synthesis for Arrays of Conformal Antennas Mounted on Arbitrarily-Shaped Three-Dimensional Platforms Using Genetic Algorithms”. In: *IEEE Transactions on Antennas and Propagation* 51.5 (May 2003), pp. 1054–1062. DOI: 10.1109/TAP.2003.811510. URL: <https://ieeexplore.ieee.org/stamp/stamp.jsp?tp=&arnumber=1208512>.
- [5] Gregory R. Allen et al. “2015 Compendium of Recent Test Results of Single Event Effects Conducted by the Jet Propulsion Laboratory’s Radiation Effects Group”. In: *2015 IEEE Radiation Effects Data Workshop (REDW)*. 2015, pp. 1–14. DOI: 10.1109/REDW.2015.7336703.
- [6] Gregory R. Allen et al. “2017 Compendium of Recent Test Results of Single Event Effects Conducted by the Jet Propulsion Laboratory’s Radiation Effects Group”. In: *2017 IEEE Radiation Effects Data Workshop (REDW)*. 2017, pp. 1–9. DOI: 10.1109/NSREC.2017.8115429.
- [7] I. Aoki et al. “Fully integrated CMOS power amplifier design using the distributed active-transformer architecture”. In: *IEEE Journal of Solid-State Circuits* 37.3 (2002), pp. 371–383. DOI: 10.1109/4.987090.
- [8] Arducam. *SPI Camera Series*. 2022. URL: <https://www.arducam.com/spi-microcontroller-cameras/#wp-block-themeisle-blocks-advanced-columns-e3e4da1d> (visited on 01/02/2022).
- [9] Isaac Asimov. “Reason”. In: *Astounding Science Fiction* (1941).
- [10] M. Bailey, F. Beck, and W. Crosswell. “Vertically polarized stacked arrays of omnidirectional antennas”. In: *IEEE Transactions on Antennas and Propagation* 18.2 (1970), pp. 285–290. DOI: 10.1109/TAP.1970.1139667.
- [11] L. Bailin. “The radiation field produced by a slot in a large circular cylinder”. In: *IRE Transactions on Antennas and Propagation* 3.3 (1955), pp. 128–137.

- [12] Roberto Baldwin. “Amazon Made a \$55 Soap Dispenser that Reminds You to Wash for 20 Seconds”. In: (Aug. 2, 2021). URL: <https://www.engadget.com/amazon-smart-soap-dispenser-200025903.html> (visited on 11/08/2021).
- [13] Satish kumar Bandlamudi et al. “Compact ultra wide band sinuous antenna”. In: *2017 IEEE International Conference on Antenna Innovations Modern Technologies for Ground, Aircraft and Satellite Applications (iAIM)*. 2017, pp. 1–6. DOI: 10.1109/IAIM.2017.8402529.
- [14] Bruce A. Banks et al. “Prediction of Atomic Oxygen Erosion Yield for Spacecraft Polymers”. In: *Journal of Spacecraft and Rockets* 48.1 (2011), pp. 14–22. DOI: 10.2514/1.48849.
- [15] Ertugrul Basar et al. “Wireless Communications Through Reconfigurable Intelligent Surfaces”. In: *IEEE Access* 7 (2019), pp. 116753–116773. DOI: 10.1109/ACCESS.2019.2935192.
- [16] Behrooz Abiri. “Precision at Scale: System Design from Tiny Biosensors to Giant Arrays”. PhD thesis. Pasadena, CA, USA: California Institute of Technology, 2020. DOI: 10.7907/t3cz-c785. URL: <https://thesis.library.caltech.edu/13857/>.
- [17] D. Bekers, R. van Dijk, and F. van Vliet. “Mutual-coupling based phased-array calibration: A robust and versatile approach”. In: *2013 IEEE International Symposium on Phased Array Systems and Technology*. 2013, pp. 630–637.
- [18] A. Bevilacqua and A.M. Niknejad. “An ultrawideband CMOS low-noise amplifier for 3.1-10.6-GHz wireless receivers”. In: *IEEE Journal of Solid-State Circuits* 39.12 (2004), pp. 2259–2268. DOI: 10.1109/JSSC.2004.836338.
- [19] Steve Blank. “What GlobalFoundries’ Retreat Really Means > Things Will Never be the Same for Consumer Devices”. In: (Sept. 10, 2018). URL: <https://spectrum.ieee.org/what-globalfoundries-retreat-really-means> (visited on 11/08/2021).
- [20] Florian Bohn, Behrooz Abiri, and Ali Hajimiri. “Fully integrated CMOS X-Band power amplifier quad with current reuse and dynamic digital feedback (DDF) capabilities”. In: *2017 IEEE Radio Frequency Integrated Circuits Symposium (RFIC)*. 2017, pp. 208–211. DOI: 10.1109/RFIC.2017.7969054.
- [21] Igor Bonifacic. “Amazon Made a \$55 Soap Dispenser that Reminds You to Wash for 20 Seconds”. In: (Aug. 2, 2021). URL: <https://www.engadget.com/amazon-smart-soap-dispenser-200025903.html> (visited on 11/08/2021).

- [22] B. D. Braaten et al. “A Self-Adapting Flexible (SELFLEX) Antenna Array for Changing Conformal Surface Applications”. In: *IEEE Transactions on Antennas and Propagation* 61.2 (2013), pp. 655–665.
- [23] Karl Ferdinand Braun. *Electrical Oscillators and Wireless Telegraphy, Nobel Lecture*. Dec. 1909. URL: <https://www.nobelprize.org/prizes/physics/1909/braun/lecture/>.
- [24] Nacer Chahat et al. “CubeSat Deployable Ka-Band Mesh Reflector Antenna Development for Earth Science Missions”. In: *IEEE Transactions on Antennas and Propagation* 64.6 (2016), pp. 2083–2093. DOI: 10.1109/TAP.2016.2546306.
- [25] M. Cho, I. Song, and J. D. Cressler. “A True Time Delay-based SiGe Bidirectional T/R Chipset for Large-Scale Wideband Timed Array Antennas”. In: *2018 IEEE Radio Frequency Integrated Circuits Symposium (RFIC)*. 2018, pp. 272–275.
- [26] T. Chu and H. Hashemi. “True-Time-Delay-Based Multi-Beam Arrays”. In: *IEEE Transactions on Microwave Theory and Techniques* 61.8 (2013), pp. 3072–3082.
- [27] J. Costantine et al. “Deployable antennas for CubeSat and space communications”. In: *2012 6th European Conference on Antennas and Propagation (EuCAP)*. 2012, pp. 837–840. DOI: 10.1109/EuCAP.2012.6206124.
- [28] CST. *CST Studio Suite 3D EM Simulation Software*. 2022. URL: <https://www.3ds.com/products-services/simulia/products/cst-studio-suite/> (visited on 01/03/2022).
- [29] W. Cumming. “A nonresonant endfire array for VHF and UHF”. In: *IRE Transactions on Antennas and Propagation* 3.2 (1955), pp. 52–58. DOI: 10.1109/TAP.1955.1144291.
- [30] Flavio A. d’Oliveira, Francisco C. Lourenco de Melo, and Tessaleno C. Devezas. “High Altitude Platforms - Present Situation and Technology Trends”. In: *Journal of Aerospace Technology and Management* 8.3 (2016). DOI: <https://doi.org/10.5028/jatm.v8i3.699>.
- [31] Linglong Dai et al. “Reconfigurable Intelligent Surface-Based Wireless Communications: Antenna Design, Prototyping, and Experimental Results”. In: *IEEE Access* 8 (2020), pp. 45913–45923. DOI: 10.1109/ACCESS.2020.2977772.
- [32] M. Deshpande and J. Peipmeier. “Design and Development of VHF Antennas for Space Borne Signal of Opportunity Receivers for Cubesat Platforms”. In: *2016 IEEE International Symposium on Antennas and Propagation and North American Radio Science meeting*. 2016. URL: <https://ntrs.nasa.gov/citations/20160000216>.

- [33] A. Dimas, D. S. Kalogierias, and A. P. Petropulu. “Cooperative Beamforming With Predictive Relay Selection for Urban mmWave Communications”. In: *IEEE Access* 7 (2019), pp. 157057–157071.
- [34] Ivan Dokmanic et al. “Euclidean Distance Matrices: Essential theory, algorithms, and applications”. In: *IEEE Signal Processing Magazine* 32.6 (Nov. 2015), pp. 12–30. ISSN: 1053-5888. DOI: 10.1109/msp.2015.2398954. URL: <http://dx.doi.org/10.1109/MSP.2015.2398954>.
- [35] C. Donn and A.E. Bollesen. “A 16-element, K-band monolithic active receive phased array antenna”. In: *1988 IEEE AP-S. International Symposium, Antennas and Propagation*. 1988, 188–191 vol.1. DOI: 10.1109/APS.1988.94024.
- [36] D. Dooling and M. M. Finckenor. *Material Selection Guidelines to Limit Atomic Oxygen Effects on Spacecraft Surfaces*. 1999. URL: <https://ntrs.nasa.gov/api/citations/19990064119/downloads/19990064119.pdf> (visited on 08/27/2021).
- [37] DuPont™. *Pyralux-AP, technical information*. URL: https://www.pragoboard.cz/download/pyralux_ap.pdf.
- [38] DuPont™. *Pyralux-TK, technical information*. URL: https://sepcu.ru/wp-content/uploads/2018/01/Pyralux_TK_DataSheet.pdf.
- [39] J. Eberle, C. Levis, and D. McCoy. “The flared slot: A moderately directive flush-mounted broad-band antenna”. In: *IRE Transactions on Antennas and Propagation* 8.5 (1960), pp. 461–468.
- [40] Vasily B. Emelianenko. *Red Star Against the Swastika: The Story of a Soviet Pilot over the Eastern Front*. Greenhill Books/Lionel Leventhal Limited Park House, 2005. ISBN: 1-85367-649-7.
- [41] A. C. Fikes et al. “Flexible, Conformal Phased Arrays with Dynamic Array Shape Self-Calibration”. In: *2019 IEEE IMS*. 2019, pp. 1458–1461.
- [42] Austin Fikes, Oren S. Mizrahi, and Ali Hajimiri. “A Framework for Array Shape Reconstruction Through Mutual Coupling”. In: *IEEE Transactions on Microwave Theory and Techniques* 69.10 (2021), pp. 4422–4436. DOI: 10.1109/TMTT.2021.3097729.
- [43] Austin Fikes et al. “Fully Collapsible Lightweight Dipole Antennas”. In: *Presented at IEEE International Symposium on Antennas and Propagation* (2021).
- [44] Austin Fikes et al. “Programmable Active Mirror: A Scalable Decentralized Router”. In: *IEEE Transactions on Microwave Theory and Techniques* 69.3 (2021), pp. 1860–1874. DOI: 10.1109/TMTT.2020.3042516.
- [45] Ronald M. Foster. “Directive diagrams of antenna arrays”. In: *The Bell System Technical Journal* 5.2 (1926), pp. 292–307. DOI: 10.1002/j.1538-7305.1926.tb04302.x.

- [46] H.T. Friis and C.B. Feldman. “A Multiple Unit Steerable Antenna for Short-Wave Reception”. In: *Proceedings of the Institute of Radio Engineers* 25.7 (1937), pp. 841–917. DOI: 10.1109/JRPROC.1937.228354.
- [47] Matan Gal-Katziri. “Precision at Scale: System Design from Tiny Biosensors to Giant Arrays”. In: *Thesis at California Institute of Technology* (2020). DOI: 10.7907/t3cz-c785.
- [48] Matan Gal-Katziri, Austin Fikes, and Ali Hajimiri. “Flexible Smart Antenna Arrays”. In: *Submitted to Nature Partner Journal Flexible Electronics* (2022).
- [49] Matan Gal-Katziri et al. “A 28 GHz Optically Synchronized CMOS Phased Array with an Integrated Photodetector”. In: *2021 IEEE Radio Frequency Integrated Circuits Symposium (RFIC)*. 2021, pp. 111–114. DOI: 10.1109/RFIC51843.2021.9490452.
- [50] S. Gao et al. “Antennas for Modern Small Satellites”. In: *IEEE Antennas and Propagation Magazine* 51.4 (2009), pp. 40–56. DOI: 10.1109/MAP.2009.5338683.
- [51] Yuchen Gao et al. “A High-gain Conical Conformal Antenna with Circularly Polarization and Axial Radiation in X-band”. In: *2019 13th European Conference on Antennas and Propagation (EuCAP)*. 2019, pp. 1–4.
- [52] S. K. Garakoui et al. “Compact Cascadable gm-C All-Pass True Time Delay Cell With Reduced Delay Variation Over Frequency”. In: *IEEE Journal of Solid-State Circuits* 50.3 (2015), pp. 693–703.
- [53] Robin Garg et al. “4.3 A 28GHz 4-Element MIMO Beam-Space Array in 65nm CMOS with Simultaneous Spatial Filtering and Single-Wire Frequency-Domain Multiplexing”. In: *2020 IEEE International Solid-State Circuits Conference - (ISSCC)*. 2020, pp. 80–82. DOI: 10.1109/ISSCC19947.2020.9063120.
- [54] Eleftherios Gdoutos et al. “A lightweight tile structure integrating photovoltaic conversion and RF power transfer for space solar power applications”. In: *2018 AIAA Spacecraft Structures Conference*. DOI: 10.2514/6.2018-2202. eprint: <https://arc.aiaa.org/doi/pdf/10.2514/6.2018-2202>. URL: <https://arc.aiaa.org/doi/abs/10.2514/6.2018-2202>.
- [55] E. Ghaderi et al. “An Integrated Discrete-Time Delay-Compensating Technique for Large-Array Beamformers”. In: *IEEE Transactions on Circuits and Systems I: Regular Papers* 66.9 (2019), pp. 3296–3306.
- [56] Michael Grant and Stephen Boyd. *CVX: Matlab Software for Disciplined Convex Programming, version 2.1*. <http://cvxr.com/cvx>. Mar. 2014.

- [57] GSFC. *General Environmental Verification Stand (GEVS) for GSFC Flight Programs and Projects*. 2021. URL: https://nepp.nasa.gov/docuploads/FFB52B88-36AE-4378-A05B2C084B5EE2CC/EEE-INST-002_add1.pdf (visited on 07/23/2021).
- [58] GSMA. *High Altitude Platform Systems*. 2021. URL: <https://www.gsma.com/futurenetworks/wp-content/uploads/2021/06/GSMA-HAPS-Towers-in-the-skies-Whitepaper-2021.pdf> (visited on 07/23/2021).
- [59] Gumstix. *Overo Ironstorm BY COM*. 2022. URL: <https://www.gumstix.com/legacy/overo-ironstorm-by-com.html> (visited on 01/02/2022).
- [60] A. Hajimiri et al. "Phased array systems in silicon". In: *IEEE Communications Magazine* 42.8 (2004), pp. 122–130.
- [61] Ali Hajimiri et al. "Dynamic Focusing of Large Arrays for Wireless Power Transfer and Beyond". In: *IEEE Journal of Solid-State Circuits* 56.7 (2021), pp. 2077–2101. DOI: 10.1109/JSSC.2020.3036895.
- [62] Mohammed Reza M. Hashemi et al. "A flexible phased array system with low areal mass density". In: *Nature Electronics* 2.5 (May 2019), pp. 195–205. ISSN: 2520-1131. DOI: 10.1038/s41928-019-0247-9. URL: <https://doi.org/10.1038/s41928-019-0247-9>.
- [63] Randy L. Haupt. "Genetic Algorithm Applications for Phased Arrays". In: *Applied Computational Electromagnetics Society (ACES) Journal* 21.3 (Nov. 2006), pp. 325–336.
- [64] V. Havary-Nassab et al. "Distributed Beamforming for Relay Networks Based on Second-Order Statistics of the Channel State Information". In: *IEEE Transactions on Signal Processing* 56.9 (2008), pp. 4306–4316.
- [65] Simon Haykin and Michael Moher. *Modern Wireless Communication*. 1st ed. New Jersey: Prentice Hall, 2004.
- [66] Richard E. Hodges et al. "ISARA - Integrated Solar Array and Reflectarray CubeSat deployable Ka-band antenna". In: *2015 IEEE International Symposium on Antennas and Propagation USNC/URSI National Radio Science Meeting*. 2015, pp. 2141–2142. DOI: 10.1109/APS.2015.7305460.
- [67] Richard E. Hodges et al. "ISARA - Integrated Solar Array and Reflectarray CubeSat deployable Ka-band antenna". In: *2015 IEEE International Symposium on Antennas and Propagation USNC/URSI National Radio Science Meeting*. 2015, pp. 2141–2142. DOI: 10.1109/APS.2015.7305460.
- [68] W. Hong et al. "Multibeam Antenna Technologies for 5G Wireless Communications". In: *IEEE Transactions on Antennas and Propagation* 65.12 (2017), pp. 6231–6249.

- [69] J. Huang and M. Zawadzki. “Antennas integrated with solar arrays for space vehicle applications”. In: *2000 5th International Symposium on Antennas, Propagation, and EM Theory. ISAPE 2000 (IEEE Cat. No.00EX417)*. 2000, pp. 86–89. DOI: 10.1109/ISAPE.2000.894730.
- [70] M. Huang and H. Wang. “A Mm-Wave Wideband MIMO RX With Instinctual Array-Based Blocker/Signal Management for Ultralow-Latency Communication”. In: *IEEE Journal of Solid-State Circuits* 54.12 (2019), pp. 3553–3564.
- [71] I. Wicaksono et al. “A tailored, electronic textile conformable suit for large-scale spatiotemporal physiological sensing in vivo”. In: *npj Flex Electron*. 4.5 (Apr. 2020). DOI: <https://doi.org/10.1038/s41528-020-0068-y>.
- [72] MCD Electronics Inc. *MCDE-539 High Power GaN White LED Dome Lens Can, Hermetically Sealed*. 2022. URL: <http://mcdelectronics.com/userfiles/1185/files/LED%5C%20Products/MCDE539.pdf> (visited on 01/03/2022).
- [73] Texas Instruments. *TPS767*. 2022. URL: <https://www.ti.com/product/TPS767> (visited on 01/03/2022).
- [74] A. Ishimaru and Hang-Sheng Tuan. “Frequency scanning antennas”. In: *1958 IRE International Convention Record*. Vol. 9. 1961, pp. 101–109. DOI: 10.1109/IRECON.1961.1151012.
- [75] Jack Loughran. *Solar-powered aircraft flown for nearly three weeks without landing*. Accessed: 2021-10-12. 2021. URL: <https://eandt.theiet.org/content/articles/2021/10/solar-powered-aircraft-flown-for-nearly-three-weeks-without-landing/>.
- [76] S. Jang et al. “A 1-GHz 16-Element Four-Beam True-Time-Delay Digital Beamformer”. In: *IEEE Journal of Solid-State Circuits* 54.5 (2019), pp. 1304–1314.
- [77] J. C. Jensen et al. “Single-chip WiFi b/g/n 1×2 SoC with fully integrated front-end amp; PMU in 90nm digital CMOS technology”. In: *2010 IEEE Radio Frequency Integrated Circuits Symposium*. 2010, pp. 447–450. DOI: 10.1109/RFIC.2010.5477372.
- [78] Jize Jiang et al. “Total Ionizing Dose (TID) effects on finger transistors in a 65nm CMOS process”. In: *2016 IEEE International Symposium on Circuits and Systems (ISCAS)*. 2016, pp. 5–8. DOI: 10.1109/ISCAS.2016.7527156.
- [79] Zhang Yi Jiang and Chen Jun. “Membrane Patch Antenna Array with Inflatable Cavity”. In: *2019 International Symposium on Antennas and Propagation (ISAP)*. 2019, pp. 1–3.

- [80] Y. Jing and H. Jafarkhani. “Network Beamforming Using Relays With Perfect Channel Information”. In: *IEEE Transactions on Information Theory* 55.6 (2009), pp. 2499–2517.
- [81] Mike DiNicola Joe Mrozinski and Hamid Habib-Agahi. *Nasa Instrument Cost Model, Impact of Mission Class on Cost*. 2016. URL: https://www.nasa.gov/sites/default/files/atoms/files/13_nicm_missionclass_2016nasacost_symposiumfinal_rev3_tagged.pdf (visited on 07/23/2021).
- [82] E. Jones and J. Shimizu. “A wide-band transverse-slot flush-mounted array”. In: *IRE Transactions on Antennas and Propagation* 8.4 (1960), pp. 401–407.
- [83] L. Josefsson and P. Persson. *Conformal Array Antenna Theory and Design*. Piscataway, NJ: IEEE Press, 2006. ISBN: 978-0-471-46584-3.
- [84] V. von Kaenel et al. “A 320 MHz, 1.5 mW@1.35 V CMOS PLL for micro-processor clock generation”. In: *IEEE Journal of Solid-State Circuits* 31.11 (1996), pp. 1715–1722. DOI: 10.1109/JSSC.1996.542316.
- [85] Hirokazu Kamoda et al. “60-GHz electrically reconfigurable reflectarray using p-i-n diode”. In: *2009 IEEE MTT-S International Microwave Symposium Digest*. 2009, pp. 1177–1180. DOI: 10.1109/MWSYM.2009.5165912.
- [86] G. S. Karthikeya et al. “A conformal UHF antenna for cargo helicopter belly”. In: *2016 IEEE 5th Asia-Pacific Conference on Antennas and Propagation (APCAP)*. 2016, pp. 285–286. DOI: 10.1109/APCAP.2016.7843207.
- [87] F.G. Kear. “Maintaining the Directivity of Antenna Arrays”. In: *Proceedings of the Institute of Radio Engineers* 22.7 (1934), pp. 847–869. DOI: 10.1109/JRPROC.1934.226737.
- [88] Michael D. Kelzenberg et al. “Ultralight Energy Converter Tile for the Space Solar Power Initiative”. In: *2018 IEEE 7th World Conference on Photovoltaic Energy Conversion (WCPEC) (A Joint Conference of 45th IEEE PVSC, 28th PVSEC 34th EU PVSEC)*. 2018, pp. 3357–3359. DOI: 10.1109/PVSC.2018.8547403.
- [89] Parham P. Khial et al. “Multi-beam, Scalable 28 GHz Relay Array with Frequency and Spatial Division Multiple Access Using Passive, High-Order N-Path Filters”. In: *Submitted to Radio Frequency Integrated Circuits Symposium (2022)*.
- [90] Ahmed Khidre et al. “Wide Band Dual-Beam U-Slot Microstrip Antenna”. In: *IEEE Transactions on Antennas and Propagation* 61.3 (2013), pp. 1415–1418. DOI: 10.1109/TAP.2012.2228617.

- [91] Per-Simon Kildal, Enrica Martini, and Stefano Maci. “Degrees of Freedom and Maximum Directivity of Antennas: A bound on maximum directivity of nonsuperreactive antennas.” In: *IEEE Antennas and Propagation Magazine* 59.4 (2017), pp. 16–25. DOI: 10.1109/MAP.2017.2706659.
- [92] Orcun Kiris. “A Vibration Resistant GNSS Antenna with Reduced Size and Weight for Wideband Satellite Applications”. In: *2020 IEEE International Symposium on Antennas and Propagation and North American Radio Science Meeting*. 2020, pp. 1841–1842. DOI: 10.1109/IEEECONF35879.2020.9330099.
- [93] Hirokazu Kobayashi. “Simple Calculation Method for Conformal Beam-Scanning Array Pattern”. In: *2019 13th European Conference on Antennas and Propagation (EuCAP)*. 2019, pp. 1–5.
- [94] Kwang-Jin Koh and Gabriel M. Rebeiz. “0.13 μ m CMOS Phase Shifters for X-, Ku-, and K-Band Phased Arrays”. In: *IEEE Journal of Solid-State Circuits* 42.11 (2007), pp. 2535–2546. DOI: 10.1109/JSSC.2007.907225.
- [95] B. Pavan Kumar et al. “A spherical phased array antenna with unequal amplitude excitation for satellite application”. In: *2017 IEEE International Conference on Antenna Innovations Modern Technologies for Ground, Aircraft and Satellite Applications (iAIM)*. 2017, pp. 1–4. DOI: 10.1109/IAIM.2017.8402564.
- [96] Cal Poly CubeSat Systems Engineering Lab. *CubeSat 101*. 2017. URL: https://www.nasa.gov/sites/default/files/atoms/files/nasa_cslc_cubesat_101_508.pdf (visited on 07/23/2021).
- [97] J. N. Laneman, G. W. Wornell, and D. N. C. Tse. “An efficient protocol for realizing cooperative diversity in wireless networks”. In: *Proceedings. 2001 IEEE International Symposium on Information Theory (IEEE Cat. No.01CH37252)*. 2001, p. 294.
- [98] Wiley J. Larson and James Richard Wertz. *Space Mission Analysis and Design*. 2nd. Microcosm, 1991.
- [99] CREE LED. *C512A-WNS/WNN: 5-mm Round White LEDs*. 2022. URL: <https://cree-led.com/media/documents/C512A-WNS-WNN-942.pdf> (visited on 01/03/2022).
- [100] Nayu Li et al. “A 4-Element 7.5-9 GHz Phased Array Receiver with 8 Simultaneously Reconfigurable Beams in 65 nm CMOS Technology”. In: *2020 IEEE Radio Frequency Integrated Circuits Symposium (RFIC)*. 2020, pp. 83–86. DOI: 10.1109/RFIC49505.2020.9218299.
- [101] Christos Liaskos et al. “A New Wireless Communication Paradigm through Software-Controlled Metasurfaces”. In: *IEEE Communications Magazine* 56.9 (2018), pp. 162–169. DOI: 10.1109/MCOM.2018.1700659.

- [102] Sungjoon Lim, C. Caloz, and T. Itoh. “Metamaterial-based electronically controlled transmission-line structure as a novel leaky-wave antenna with tunable radiation angle and beamwidth”. In: *IEEE Transactions on Microwave Theory and Techniques* 53.1 (2005), pp. 161–173. DOI: 10.1109/TMTT.2004.839927.
- [103] Sevil Zeynep Lüleş, David A. Johns, and Antonio Liscidini. “A Third-Order Integrated Passive Switched-Capacitor Filter Obtained With a Continuous-Time Design Approach”. In: *IEEE Transactions on Circuits and Systems I: Regular Papers* 66.10 (2019), pp. 3643–3652. DOI: 10.1109/TCSI.2019.2914638.
- [104] Robert J. Mailloux. *Phased Array Antenna Handbook, 2nd Ed.* Norwood, MA: Artech House, Inc., 2005. ISBN: 1-58053-689-1.
- [105] Gal-Katziri Matan et al. “Scalable, Deployable, Flexible Phased Array Sheets”. In: *2020 IEEE MTT-S International Microwave Symposium (IMS)*. 2020.
- [106] Khaleel Mershad et al. “Cloud-Enabled High-Altitude Platform Systems: Challenges and Opportunities”. In: *Frontiers in Communications and Networks* 2 (2021). DOI: 10.3389/frcmn.2021.716265.
- [107] Microchip. *ATmega128*. 2022. URL: <https://www.microchip.com/en-us/product/ATmega128> (visited on 01/03/2022).
- [108] Microchip. *ATmegaS128 Radiation Tolerant AVR8 MCU*. 2022. URL: <https://www.microchip.com/en-us/product/ATmegaS128> (visited on 01/03/2022).
- [109] Microsemi. *Space-grade Linear Regulators and LDOs*. 2022. URL: <https://www.microsemi.com/product-directory/rad-hard-hybrid-regulators/679-ultra-low-dropout> (visited on 01/03/2022).
- [110] Roberto Minerva, Abyi Biru, and Domenico Rotondi. “Towards a Definition of The Internet of Things (IoT)”. In: *IEEE Internet of Things* (May 27, 2015). URL: https://iot.ieee.org/images/files/pdf/IEEE_IoT_Towards_Definition_Internet_of_Things_Revision1_27MAY15.pdf (visited on 11/08/2021).
- [111] I. Mondal and N. Krishnapura. “A 2-GHz Bandwidth, 0.25–1.7 ns True-Time-Delay Element Using a Variable-Order All-Pass Filter Architecture in 0.13 μm CMOS”. In: *IEEE Journal of Solid-State Circuits* 52.8 (2017), pp. 2180–2193.
- [112] Seong-Mo Moon et al. “Phased Array Shaped-Beam Satellite Antenna With Boosted-Beam Control”. In: *IEEE Transactions on Antennas and Propagation* 67.12 (2019), pp. 7633–7636. DOI: 10.1109/TAP.2019.2930129.

- [113] Gordon E. Moore. “Cramming more components onto integrated circuits, Reprinted from Electronics, volume 38, number 8, April 19, 1965, pp.114 ff.” In: *IEEE Solid-State Circuits Society Newsletter* 11.3 (2006), pp. 33–35. DOI: 10.1109/N-SSC.2006.4785860.
- [114] Muhammad Imran Nawaz et al. “A review on wideband microstrip patch antenna design techniques”. In: *2013 International Conference on Aerospace Science Engineering (ICASE)*. 2013, pp. 1–8. DOI: 10.1109/ICASE.2013.6785554.
- [115] James A. Nessel et al. “Potential Applications of Active Antenna Technologies for Emerging NASA Space Communications Scenarios”. In: *2020 14th European Conference on Antennas and Propagation (EuCAP)*. 2020, pp. 1–5. DOI: 10.23919/EuCAP48036.2020.9135544.
- [116] T. Nishio et al. “A high-speed adaptive antenna array with simultaneous multibeam-forming capability”. In: *IEEE Transactions on Microwave Theory and Techniques* 51.12 (2003), pp. 2483–2494.
- [117] NTS. *Space Simulation*. 2021. URL: <https://www.nts.com/services/testing/environmental/space-simulation/> (visited on 07/23/2021).
- [118] Martha V. O’Bryan et al. “Compendium of Single Event Effects for Candidate Spacecraft Electronics for NASA”. In: *2012 IEEE Radiation Effects Data Workshop*. 2012, pp. 1–9. DOI: 10.1109/REDW.2012.6353739.
- [119] Martha V. O’Bryan et al. “Single Event Effects Compendium of Candidate Spacecraft Electronics for NASA”. In: *2009 IEEE Radiation Effects Data Workshop*. 2009, pp. 15–24. DOI: 10.1109/REDW.2009.5336321.
- [120] Bhartia P. et al. *Microstrip antenna design handbook*. Boston, MA: Artech House, 2001. ISBN: 978-0890065136.
- [121] J. Pang et al. “A 28-GHz CMOS Phased-Array Beamformer Utilizing Neutralized Bi-Directional Technique Supporting Dual-Polarized MIMO for 5G NR”. In: *IEEE Journal of Solid-State Circuits* (2020), pp. 1–1.
- [122] Rush PCB. *Printed Circuit Board and Assembly*. 2022. URL: <https://rushpcb.com/> (visited on 01/03/2022).
- [123] P. Perlmutter, S. Shtrikman, and D. Treves. “Electric surface current model for the analysis of microstrip antennas with application to rectangular elements”. In: *IEEE Transactions on Antennas and Propagation* 33.3 (1985), pp. 301–311. DOI: 10.1109/TAP.1985.1143581.
- [124] Raspberry Pi. *Raspberry Pi Camera Module V2*. 2022. URL: <https://www.raspberrypi.com/products/camera-module-v2/> (visited on 01/02/2022).
- [125] Raspberry Pi. *Raspberry Pi High Quality Camera*. 2022. URL: <https://www.raspberrypi.com/products/raspberry-pi-high-quality-camera/> (visited on 01/02/2022).

- [126] J.R. Potukuchi et al. “MMICs insertion in a Ku-band active phased array for communications satellites”. In: *IEEE International Digest on Microwave Symposium*. 1990, 881–884 vol.2. DOI: 10.1109/MWSYM.1990.99719.
- [127] David M. Pozar. *Microwave Engineering*. John Wiley and Sons Inc., Hoboken New Jersey, 2012. ISBN: 9788126541904.
- [128] The Hamilton Project. *One Dollar’s Worth of Computer Power, 1980-2010*. URL: https://www.hamiltonproject.org/charts/one_dollars_worth_of_computer_power_1980_2010.
- [129] Haochuan Qiu et al. “Compact, Flexible, and Transparent Antennas Based on Embedded Metallic Mesh for Wearable Devices in 5G Wireless Network”. In: *IEEE Transactions on Antennas and Propagation* 69.4 (2021), pp. 1864–1873. DOI: 10.1109/TAP.2020.3035911.
- [130] Yahya Rahmat-Samii, Vignesh Manohar, and Joshua Michael Kovitz. “For Satellites, Think Small, Dream Big: A review of recent antenna developments for CubeSats.” In: *IEEE Antennas and Propagation Magazine* 59.2 (2017), pp. 22–30. DOI: 10.1109/MAP.2017.2655582.
- [131] Kristine Rainey. *Space Station Research and Technology*. 2020. URL: https://www.nasa.gov/mission_pages/station/research/news/organization (visited on 08/24/2021).
- [132] Negar Reiskarimian et al. “Analysis and Design of Two-Port N-Path Bandpass Filters With Embedded Phase Shifting”. In: *IEEE Transactions on Circuits and Systems II: Express Briefs* 63.8 (2016), pp. 728–732. DOI: 10.1109/TCSII.2016.2530338.
- [133] Francesco Rigobello et al. “Pattern recovering of conformal antenna array for strongly deformed surfaces”. In: *2017 11th European Conference on Antennas and Propagation (EUCAP)*. 2017, pp. 869–871. DOI: 10.23919/EuCAP.2017.7928769.
- [134] Christopher T. Rodenbeck et al. “Microwave and Millimeter Wave Power Beaming”. In: *IEEE Journal of Microwaves* 1.1 (2021), pp. 229–259. DOI: 10.1109/JMW.2020.3033992.
- [135] David Rotman. “We’re not Prepared for the End of Moore’s Law”. In: (Feb. 24, 2020). URL: <https://www.technologyreview.com/2020/02/24/905789/were-not-prepared-for-the-end-of-moores-law/> (visited on 11/08/2021).
- [136] W. Rotman and A.A. Oliner. “Periodic Structures in Trough Waveguide”. In: *IRE Transactions on Microwave Theory and Techniques* 7.1 (1959), pp. 134–142. DOI: 10.1109/TMTT.1959.1124637.
- [137] R. Roush and J. Wiltse. “Electronically steerable S-band array”. In: *IRE Transactions on Antennas and Propagation* 9.1 (1961), pp. 107–109. DOI: 10.1109/TAP.1961.1144934.

- [138] C.R. Rowell and R.D. Murch. “A capacitively loaded PIFA for compact mobile telephone handsets”. In: *IEEE Transactions on Antennas and Propagation* 45.5 (1997), pp. 837–842. DOI: [10.1109/8.575634](https://doi.org/10.1109/8.575634).
- [139] S. Heinrich et al. “Three-dimensional integrated stretchable electronics”. In: *Nat Electron* 1 (Aug. 2018), pp. 473–480. DOI: <https://doi.org/10.1038/s41928-018-0116-y>.
- [140] Rudolf Saathof et al. “Optical satellite communication space terminal technology at TNO”. In: *International Conference on Space Optics — ICSSO 2018*. Ed. by Zoran Sodnik, Nikos Karafolas, and Bruno Cugny. Vol. 11180. International Society for Optics and Photonics. SPIE, 2019, pp. 213–222. DOI: [10.1117/12.2535939](https://doi.org/10.1117/12.2535939). URL: <https://doi.org/10.1117/12.2535939>.
- [141] Tapan Sarkar K. et al. *History of Wireless*. John Wiley & Sons Inc., 2006. ISBN: 9780471718147.
- [142] A. Scaglione and Yao-Win Hong. “Opportunistic large arrays: cooperative transmission in wireless multihop ad hoc networks to reach far distances”. In: *IEEE Transactions on Signal Processing* 51.8 (2003), pp. 2082–2092.
- [143] A. Sendonaris, E. Erkip, and B. Aazhang. “Increasing uplink capacity via user cooperation diversity”. In: *Proceedings. 1998 IEEE International Symposium on Information Theory (Cat. No.98CH36252)*. 1998, p. 156.
- [144] A. Sendonaris, E. Erkip, and B. Aazhang. “User cooperation diversity. Part I. System description”. In: *IEEE Transactions on Communications* 51.11 (2003), pp. 1927–1938.
- [145] A. Sendonaris, E. Erkip, and B. Aazhang. “User cooperation diversity. Part II. Implementation aspects and performance analysis”. In: *IEEE Transactions on Communications* 51.11 (2003), pp. 1939–1948.
- [146] Hae-Moon Seo et al. “A Low Power Fully CMOS Integrated RF Transceiver IC for Wireless Sensor Networks”. In: *IEEE Transactions on Very Large Scale Integration (VLSI) Systems* 15.2 (2007), pp. 227–231. DOI: [10.1109/TVLSI.2007.893586](https://doi.org/10.1109/TVLSI.2007.893586).
- [147] Cheol-Min Seong et al. “Conformal Array Pattern Synthesis on a Curved Surface with Quadratic Function using Adaptive Genetic Algorithm”. In: *2013 Asia-Pacific Microwave Conference (APMC)*. 2013.
- [148] S. Shahramian et al. “A Fully Integrated 384-Element, 16-Tile, W-Band Phased Array With Self-Alignment and Self-Test”. In: *IEEE Journal of Solid-State Circuits* 54.9 (2019), pp. 2419–2434.
- [149] C. Shipley and D. Woods. “Mutual coupling-based calibration of phased array antennas”. In: *Proceedings 2000 IEEE International Conference on Phased Array Systems and Technology (Cat. No.00TH8510)*. 2000, pp. 529–532.

- [150] Zachary J. Silva and Christopher R. Valenta. “Evaluating Optically Transparent Conductors at RF and Microwave Frequencies: A New Figure of Merit”. In: *IEEE Microwave and Wireless Components Letters* 31.4 (2021), pp. 349–352. DOI: 10.1109/LMWC.2021.3057669.
- [151] K.M. Simon et al. “A production ready, 6-18-GHz, 5-b phase shifter with integrated CMOS compatible digital interface circuitry”. In: *IEEE Journal of Solid-State Circuits* 27.10 (1992), pp. 1452–1456. DOI: 10.1109/4.156453.
- [152] R.N. Simons and R.Q. Lee. “Feasibility study of optically transparent microstrip patch antenna”. In: *IEEE Antennas and Propagation Society International Symposium 1997. Digest. Vol. 4. 1997*, 2100–2103 vol.4. DOI: 10.1109/APS.1997.625381.
- [153] Merrill I. Skolnik. *Radar Handbook, 2nd Ed.* New York, NY: McGraw-Hill, 1990. ISBN: 0-07-057913-X.
- [154] Tony Smith. “Megahertz Myth”. In: *The Guardian* (Feb. 27, 2002). URL: <https://www.theguardian.com/technology/2002/feb/28/onlinesupplement3> (visited on 11/08/2021).
- [155] UK High Altitude Society. *A Beginners Guide to High Altitude Ballooning*. 2008. URL: https://ukhas.org.uk/general:beginners_guide_to_high_altitude_ballooning (visited on 05/28/2021).
- [156] Momentus Space. *Satellite as a Service*. 2021. URL: <https://momentus.space/services/> (visited on 07/23/2021).
- [157] Royal Belgian Institute for Space Aeronomy. *SPENVIS*. Version 4.6.10. May 27, 2021. URL: <https://www.spennis.oma.be/>.
- [158] SpaceX. *Falcon User’s Guide*. 2020. URL: https://www.spacex.com/media/falcon_users_guide_042020.pdf (visited on 01/03/2022).
- [159] J. Spradley. “A volumetric electrically scanned two-dimensional microwave antenna array”. In: *1958 IRE International Convention Record*. Vol. 6. 1958, pp. 204–212. DOI: 10.1109/IRECON.1958.1150684.
- [160] Scientific American Editorial Staff. “End of Moore’s Law: It’s Not Just About Physics”. In: (Aug. 28, 2013). URL: <https://www.scientificamerican.com/article/end-of-moores-law-its-not-just-about-physics/> (visited on 11/08/2021).
- [161] R.B. Staszewski et al. “All-digital PLL and transmitter for mobile phones”. In: *IEEE Journal of Solid-State Circuits* 40.12 (2005), pp. 2469–2482. DOI: 10.1109/JSSC.2005.857417.
- [162] T. Terse-Thakoor et al. “Thread-based multiplexed sensor patch for real-time sweat monitoring”. In: *npj Flex Electron*. 4.18 (July 2020). DOI: <https://doi.org/10.1038/s41528-020-00081-w>.

- [163] H. Takhedmit et al. “Transparent rectenna and rectenna array for RF energy harvesting at 2.45 GHz”. In: *The 8th European Conference on Antennas and Propagation (EuCAP 2014)*. 2014, pp. 2970–2972. DOI: 10.1109/EuCAP.2014.6902451.
- [164] X. Tao, X. Xu, and Q. Cui. “An overview of cooperative communications”. In: *IEEE Communications Magazine* 50.6 (2012), pp. 65–71.
- [165] Thinkom. *What to Consider When Evaluating Phased Arrays*. Accessed: 2021-10-12. 2021. URL: <https://www.thinkom.com/phased-array-specs/>.
- [166] Irene Tzinis. *Technology Readiness Level*. 2012. URL: https://www.nasa.gov/directorates/heo/scan/engineering/technology/technology_readiness_level (visited on 07/23/2021).
- [167] Best Value Vacs. *Vacuum Chambers and Ovens*. 2022. URL: <https://shopbv.com/> (visited on 01/03/2022).
- [168] Nina Vaidya et al. “Lightweight Carbon Fiber Mirrors for Solar Concentrator Applications”. In: *2017 IEEE 44th Photovoltaic Specialist Conference (PVSC)*. 2017, pp. 572–577. DOI: 10.1109/PVSC.2017.8366046.
- [169] Jakob Van Zyl and Yunjin Kim. *Synthetic Aperture Radar Polarimetry*. John Wiley & Sons Inc., 2010. ISBN: 978-1118115114.
- [170] L.I. Vaskelainen. “Iterative least-squares synthesis methods for conformal array antennas with optimized polarization and frequency properties”. In: *IEEE Transactions on Antennas and Propagation* 45.7 (1997), pp. 1179–1185. DOI: 10.1109/8.596912.
- [171] Michael J. Viens. *EEE-INST-002*. 2008. URL: <https://nepp.nasa.gov/index.cfm/12821> (visited on 01/02/2022).
- [172] Michael J. Viens. *Outgassing Data for Selecting Spacecraft Materials*. 2008. URL: <https://outgassing.nasa.gov/> (visited on 07/23/2021).
- [173] Yun Wang et al. “A 39-GHz 64-Element Phased-Array Transceiver With Built-In Phase and Amplitude Calibrations for Large-Array 5G NR in 65-nm CMOS”. In: *IEEE Journal of Solid-State Circuits* 55.5 (2020), pp. 1249–1269. DOI: 10.1109/JSSC.2020.2980509.
- [174] Zhenglong Wang et al. “1 Bit Electronically Reconfigurable Folded Reflectarray Antenna Based on p-i-n Diodes for Wide-Angle Beam-Scanning Applications”. In: *IEEE Transactions on Antennas and Propagation* 68.9 (2020), pp. 6806–6810. DOI: 10.1109/TAP.2020.2975265.
- [175] Renaldi Winoto et al. “A WLAN and bluetooth combo transceiver with integrated WLAN power amplifier, transmit-receive switch and WLAN/bluetooth shared low noise amplifier”. In: *2012 IEEE Radio Frequency Integrated Circuits Symposium*. 2012, pp. 395–398. DOI: 10.1109/RFIC.2012.6242307.

- [176] Hang Wong et al. “Small Antennas in Wireless Communications”. In: *Proceedings of the IEEE* 100.7 (2012), pp. 2109–2121. DOI: 10.1109/JPROC.2012.2188089.
- [177] Qingqing Wu and Rui Zhang. “Intelligent Reflecting Surface Enhanced Wireless Network via Joint Active and Passive Beamforming”. In: *IEEE Transactions on Wireless Communications* 18.11 (2019), pp. 5394–5409. DOI: 10.1109/TWC.2019.2936025.
- [178] Qingqing Wu and Rui Zhang. “Towards Smart and Reconfigurable Environment: Intelligent Reflecting Surface Aided Wireless Network”. In: *IEEE Communications Magazine* 58.1 (2020), pp. 106–112. DOI: 10.1109/MCOM.001.1900107.
- [179] Y. Jin et al. “Identifying human body states by using a flexible integrated sensor”. In: *npj Flex Electron.* 4.28 (Oct. 2020). DOI: <https://doi.org/10.1038/s41528-020-00090-9>.
- [180] Y. Wang et al. “All-weather, natural silent speech recognition via machine-learning-assisted tattoo-like electronics”. In: *npj Flex Electron.* 5.20 (Aug. 2021). DOI: <https://doi.org/10.1038/s41528-021-00119-7>.
- [181] Bruce D. Yost. *Small Satellite Reliability Initiative Knowledge Base*. 2020. URL: <https://s3vi.ndc.nasa.gov/ssri-kb> (visited on 08/20/2021).
- [182] Z. Zhang et al. “Deep learning-enabled triboelectric smart socks for IoT-based gait analysis and VR applications”. In: *npj Flex Electron.* 4.29 (July 2020). DOI: <https://doi.org/10.1038/s41528-020-00092-7>.
- [183] B. Zhang, P.E. Allen, and J.M. Huard. “A fast switching PLL frequency synthesizer with an on-chip passive discrete-time loop filter in 0.25-um CMOS”. In: *IEEE Journal of Solid-State Circuits* 38.6 (2003), pp. 855–865. DOI: 10.1109/JSSC.2003.811874.
- [184] Ming-Tao Zhang et al. “Design of Novel Reconfigurable Reflectarrays With Single-Bit Phase Resolution for Ku-Band Satellite Antenna Applications”. In: *IEEE Transactions on Antennas and Propagation* 64.5 (2016), pp. 1634–1641. DOI: 10.1109/TAP.2016.2535166.
- [185] Na Zhang et al. “Programmable Coding Metasurface for Dual-Band Independent Real-Time Beam Control”. In: *IEEE Journal on Emerging and Selected Topics in Circuits and Systems* 10.1 (2020), pp. 20–28. DOI: 10.1109/JETCAS.2020.2973310.
- [186] Boyi Zheng, Lu Jie, and Michael P. Flynn. “A 6-GHz MU-MIMO Eight-Element Direct Digital Beamforming TX Utilizing FIR H-Bridge DAC”. In: *IEEE Transactions on Microwave Theory and Techniques* 69.6 (2021), pp. 2832–2840. DOI: 10.1109/TMTT.2021.3064318.

INDEX

F

figures, 3, 7–13, 17–19, 21, 23, 24, 26, 27, 29, 31, 33–36, 38, 40, 42, 44–46,
48–50, 53–57, 59, 63–65, 68, 71, 73, 74, 76, 77, 79, 81, 82, 84, 85, 87, 88,
91, 92, 94, 95, 100, 101, 103, 105, 107, 111, 112, 114, 116–120, 122, 126,
128, 129, 132, 133, 135, 138, 140, 143, 144, 147, 148, 150–152

T

tables, 38, 39, 107, 111, 130, 132